Addendum

The following addresses corrections and qualifications which have been made subsequent to publication of this thesis. I would like to thank the thesis reviewers for bringing the following points to my attention.

Chapter 3

A note on Mode S'

From the results of the Floquet analysis described in chapter 3, a third mode of instability is identified (Mode S'). On page 106, it is mentioned that the real component of the Floquet multipliers (λ) are oscillatory, indicating that the Floquet multiplier for this mode of instability has complex-conjugate multipliers. Section 3.5 describes the spatio-temporal symmetry of all three modes, including Mode S'. In this section it has been assumed that Mode S' (referred to as Mode C in this subsection) is quasi-periodic. However, recent results (for example Blackburn & Lopez (2003)) indicate that instabilities with complex-conjugate pairs physically represent either a standing- or a travelling-wave pattern in the span-wise direction. As such, figure 3.20, and the surrounding text may not be a true representation of the structure of the Mode S' instabilty. Further analysis, using either a Floquet technique which stores the complex coefficients, or a fully three-dimensional direct numerical simulation would be required to verify the spatio-temporal structure of Mode S'.

Chapter 5

Page 159, line 1: *"From the definition,* $J = m \cdot L^2$*,..."*, should be replaced with: *"Following the work of Govardhan & Williamson (1997), the moment of inertia is defined as* $J = m \cdot L^2$*, (a more precise definition is given in chapter 7). From this definition,..."*

A note on the critical mass ratio for a tethered cylinder

The critical mass ratio as defined in Chapter 5 describes a mass ratio below which large amplitude oscillations are observed, up to and including the highest reduced velocity simulated. Owing to the definition of u^* for a tethered cylinder, only a finite reduced velocity may be reached for a given tether length and cylinder mass ratio (in contrast with a freely oscillating cylinder where $0 \leqslant u^* \leqslant \infty$). In all cases, simulations were run at a very large Froude number such that the mean layover angle was greater than 89^o, in order to check the definition of the critical mass ratio against that described in chapter 4. The link between the critical mass ratio for a tethered cylinder and that for a freely oscillating cylinder may be clearly defined by analysing the equations of motion for both the tethered- and freely-oscillating cylinder. This is the subject of future work.

Chapter 7

Page 226, line 6: *"if* $L^* >> 1/64$*..."*, should be replaced with:
"if $L^* >> 1/\sqrt{8}$*..."*

Page 227, paragraph 3, line 3: *"... frequency response as* $L^* \rightarrow 1/64$*..."*, should be replaced with: *"... frequency response as* $L^* \rightarrow 1/\sqrt{8}$*..."*

The Analysis of Wake Structures Behind Stationary, Freely Oscillating and Tethered Cylinders.

This thesis is submitted in fulfillment of
the requirements for the degree of Doctor of Philosophy,
Department of Mechanical Engineering
Monash University
January 2004.

Kris Ryan B.Eng. (Honours)

Declaration of Originality

I, Kris Ryan declare that this thesis is my own work and has not been submitted in any form for another degree or diploma at any university or institute of tertiary education. Information derived from the published and unpublished work of others has been acknowledged in the text and a list of references is given in the bibliography.

Kris Ryan January 14, 2004

Abstract

This thesis reports on the results of two distinct but related studies. The first study investigates the transition to three-dimensionality of fluid structures in the wake of a bluff body as a function of a systematic variation in body aspect ratio. The aim of the study is to determine if the transition to turbulence described for the wake of a circular cylinder is generic for all bluff bodies. A linear Floquet analysis is made of the wake of a variety of aspect ratio plates in order to determine the linear transition scenario to a three-dimensional wake.

For short bluff bodies $AR < 7.5$, the transition scenario observed agrees with that described for the circular cylinder. For larger aspect ratios, a three-dimensional instability with a spatial structure similar to the Mode B instability is the first mode to become critically unstable. Additionally, a third mode of instability is observed denoted as Mode S. The results conclude that for a bluff body with a large aspect ratio, the transition to turbulence follows a different path to that described for a circular cylinder.

The second part of the thesis studies the vortex-induced-vibration of both a cylinder held free to move transverse to the flow field, and a tethered cylinder.

The freely oscillating cylinder study aims to determine a critical mass ratio below which large amplitude oscillations occur. Previous studies suggest that such a mass ratio exists for moderate to high Reynolds numbers. The aim of this study is to determine the variation in the critical mass ratio at low Reynolds numbers.

A two-dimensional study is performed with $u^* = \infty$ for Reynolds numbers in the range $Re = [40, 300]$. Of note is that no critical mass ratio is observed in the Reynolds number range $Re = [100, 180]$, however on either side of this range, a critical mass ratio is obtained.

Further to the study of the freely oscillating cylinder, an analysis is made of the vortex-induced-vibration of a tethered cylinder. Three branches of oscillation are observed, an in-line branch, a transition branch and a transverse branch; the transverse branch compares favorably with the results of the freely oscillating cylinder. A negative mean lift is noted for a wide range of reduced velocities investigated; this coincides with a change in the fluid structures in the wake. The effect of mass ratio is investigated in the range $m^* = [0.1, 0.8]$, and a critical mass ratio, below which large amplitude oscillations are observed, is found. The tether length determines the value of the critical mass ratio for a particular case. For very large tether lengths, the critical mass ratio coincides with that found for the freely oscillating cylinder at the same Reynolds number.

Acknowledgements

I would like to thank both my supervisors, Professor Kerry Hourigan and Associate Professor Mark Thompson, for their guidance throughout my candidature. Since I began, both Kerry and Mark have provided continual enthusiasm, direction and support without which this work would not have been possible.

I gratefully acknowledge the support of the Department of Mechanical Engineering, for providing the resources and financial assistance (in the form of a Departmental scholarship) throughout my candidature. I would like to also acknowledge both the Victorian Partnership for Advanced Computing (VPAC) and the Australian Partnership for Advanced Computing (APAC), for providing the computational facilities which were essential to this work.

Thanks also for the assistance of John Sheridan and Josie Carberry, who together provided both the experimental facilities and experimental results which helped enormously in the validation of the numerical, tethered-cylinder, simulations.

I would also like to thank my two office mates, Craig and Greg for providing many memorable and often humorous office moments since my first day as a post-graduate (which I still remember with a laugh). These guys have made my work a joy, and have left me with many fond memories of post-graduate life.

I would like to take this opportunity to thank my family (Mum, Nan & Pop, and my brother Marc) for sticking with me from the very beginning, always trusting that I would be successful, whichever course I chose to travel. I am indebted to them for their support.

Thanks also to the Swalwell family (Terry, Janene, Katrina, Kim and Jeff), for the many enjoyable moments we have had together, and the constant encouragement which you have afforded me.

Finally, I would like to dedicate this work to Katrina: Thankyou for your constant support; your love, generosity and encouragement have never wavered.

Publications

Ryan, K., Thompson, M. C. & Hourigan, K., 2004 (to appear), Vortex Structures in the Wake of a Buoyant Tethered Cylinder at Moderate to High Reduced Velocities. *European Journal of Fuid Mechanics - B* .

Ryan, K., Thompson, M. C. & Hourigan, K., 2004 (to appear), Flow-Induced Vibrations of a Tethered Circular Cylinder *Journal of Fluids and Structures*.

Ryan, K., Thompson, M. C. & Hourigan, K., 2003, The Effect of Changed Mass Ratio on the Motion of a Tethered Cylinder. *in proceedings of IUTAM Symposium on Integrated Modelling of Fully Coupled Fluid-Structure Interactions using Analysis, Computations, and Experiments, 1 June - 6 June.*

Carberry, J., Ryan, K. & Sheridan, J., 2003, Experimental Study of a Tethered Cylinder in a Free Stream. *in proceedings of IUTAM Symposium on Integrated Modelling of Fully Coupled Fluid-Structure Interactions using Analysis, Computations, and Experiments, 1 June - 6 June.*

Pregnalato, C.J., Ryan, K., Thompson, M. C. & Hourigan, K., 2002, Numerical Simulations of the Flow-Induced Vibrations of Tethered Bluff Bodies. *in proceedings of IMECE 2002: 5th International Symposium on FSI, AE, FIV & N, 17-22 November 2002, New Orleans, LA, USA.*

Ryan, K., Thompson, M. C. & Hourigan, K., 2002, Energy Transfer in a Vortex Induced Vibrating Tethered Cylinder System. *in proceedings of Conference on Bluff Body Wakes and Vortex-Induced Vibrations, Port Douglas, Australia, 2002* , 57–60.

Ryan, K., Thompson, M. C. & Hourigan, K., 2001, Three Dimensional Flow Development in the Wake of Elongated Bluff Bodies. *14th Australasian Fluid Mechanics Conference Adelaide University, Adelaide, Australia 10-14 December*, 387–390.

Nomenclature

Symbol	**Parameter**
$\mathcal{B}_{\mathcal{L}}$	control volume boundary.
$\mathcal{B}_{\mathcal{S}}$	solid-fluid interface.
$\mathcal{V}$	control volume.
$\mathcal{V}_{\mathcal{S}}$	solid body volume.
α	oblique shedding angle.
α_q	Adams-Bashforth coefficients.
β	eccentricity parameter.
β_q	Adams-Moulton coefficients.
δ	boundary layer thickness.
δ_ω	vorticity thickness of separating shear layer.
ε	plane strain, relaxation parameter.
λ	span-wise wavelength.
μ	Floquet multiplier.
ν	kinematic viscosity.
$\boldsymbol{\omega}$	vorticity vector.
ω	oscillation frequency.
ω_x	stream-wise vorticity.
ω_y	transverse vorticity.
ω_z	span-wise vorticity.
ϕ	potential flow field.
ϕ	phase lag.
ρ	solid body density.
ρ_w	fluid density.
$\tilde{\rho}$	combined solid and fluid density.
σ	Floquet exponent.

σ_i	growth rate of most unstable perturbation.
θ	tethered cylinder layover angle
ζ	damping ratio.
A	dimensional amplitude of oscillation.
A^*	non-dimensional amplitude of oscillation in the direction of motion.
AR	plate aspect ratio.
B	buoyancy force.
C	chord length of plate.
c	damping coefficient.
c^*	normalized damping coefficient.
C_A	added mass coefficient.
C_D	drag coefficient.
C_L	lift coefficient.
C_T	tension coefficient.
C_{Tan}	force coefficient in the direction of motion.
C_{EA}	effective added mass.
$\overline{C_L}$	mean lift coefficient.
$\hat{C_Y}$	peak lift coefficient.
C_{PB}	base pressure coefficient.
D	cylinder diameter.
d'	H + twice the momentum thickness.
f	body oscillation frequency.
f_n	natural frequency.
f_o	wake shedding frequency of an oscillating cylinder.
f_{Drag}	drag trace frequency.
f_K, f_s	dimensional form of the Karman shedding frequency.
$f_S L$	Kelvin-Helmholtz instability frequency.
f^*	frequency ratio, f/f_N.
Fr	Froude number.
Fr'	modified Froude number.
F_A	aerodynamic force.
F_D	drag force.
F_L	lift force.

F_S	side force.
F_E	external (non fluid) forces.
F_g	force of gravity.
F_t	total force.
F_{tol}	force tolerance condition.
F_θ	force acting in the direction of motion.
g	acceleration due to gravity.
H	thickness of plate.
J	polar moment of inertia.
k	spring stiffness coefficient.
k^*	normalized spring stiffness coefficient.
l_i, l_h, l_w	inlet length, cross-flow length, out-flow length.
L	dimensional tether length.
$\mathbf{L}(\mathbf{u})$	linear diffusion term.
L^*	non-dimensional tether length.
L_c	cylinder span-wise length.
$\mathbf{n}$	normal vector.
m	solid body mass.
m_A	added mass.
m^*	mass ratio.
m^*_{crit}	critical mass ratio.
N	number of macro-elements.
$\mathbf{N}(\mathbf{u})$	non-Linear advection term.
p	interpolating polynomial order.
$\overline{p}$	pressure factor; base pressure field.
p'	perturbation pressure component.
r'	perturbation field.
Re	Reynolds number.
Ro	Roshko number.
St	Strouhal number.
S_g	Skop-Griffin parameter.
t	non-dimensional time.
T	Karman shedding period.

T	Mean tension force.
$\mathbf{u}$	velocity vector.
$\hat{\mathbf{u}}, \hat{\hat{\mathbf{u}}}$	intermediate velocity field.
u'_{rms}	RMS fluctuating velocity component.
U_∞	free-stream velocity.
u^*	reduced velocity.
u, v, w	velocity components in the x, y and z direction.
u_{tol}	velocity tolerance condition.
$\overline{u}, \overline{v}, \overline{w}$	base velocity components.
u', v', w'	perturbation velocity components.
x, y, z	Cartesian coordinates, inertial reference frame Cartesian coordinates.
x^*, y^*	normalized Cartesian coordinates.
y	oscillation time trace.
y^*	normalized oscillation time trace.
∇	gradient operator.
$\times$	curl operator.

Contents

Chapter 1

Background Information and Literature Review

1.1 Introduction to the Present Problem

This thesis reports on a study of two distinct but related topics in the field of the flow around a bluff body located within a uniform homogeneous Newtonian fluid.

The first problem deals with the transition to three-dimensionality of fluid structures in the wake of a blunt flat plate as a function of Reynolds number. Previous research indicates that transition of the fluid structures, from two-dimensionality to three-dimensionality, is the first step to a fully turbulent flow field in the wake of a nominally two-dimensional bluff body. Knowledge of this transition may develop our understanding of turbulent structures in general. This problem has been studied in detail specifically for the flow around a circular cylinder, however little research has been undertaken regarding flow transition for other bluff body geometries. The research reported herein aims to extend knowledge to incorporate the effect of a change in bluff body geometry to the phenomenon.

The second problem deals with the flow-induced vibration of a circular cylinder and may be broken into two separate parts, the second part being an extension of the first. Initially the flow-induced vibration of a hydro-elastically mounted, buoyant cylinder with low mechanical damping and spring stiffness is studied. The cylinder is restricted to move transverse to the flow field, as this motion has the greatest applicability to practical problems. This problem has practical applications in several fields, including: submerged pipelines, the motion of lighter-than-air craft, and submerged bodies, such as submarines. This study focuses on the effect of a change in mass ratio, with the ultimate aim to identify a critical mass ratio below which sustained peak to peak oscillations are observed beyond a finite reduced velocity.

As an extension to this problem, the flow-induced vibration of a buoyant cylinder tethered to a pivot point is studied. This geometry effectively negates mechanical damping and extends the vortex induced motion study to incorporate the effects of both in-line and transverse oscillations of the body. As with the hydro-elastically mounted cylinder case, the tethered cylinder has practical applications in submerged pipelines, however few (if any) previous studies into the motion of a tethered cylinder have been reported. Hence, of principal importance to this investigation is the effect of mass ratio and tether length to both the mean lay-over angle ($\overline{\theta}$) and the cylinder angle oscillations (θ') around this mean angle. It is anticipated that observed cylinder oscillations will mimic that already identified in the previous studies of the hydro-elastically mounted cylinder. Finally, this study aims to determine whether the reduced velocity (u^*) is the correct parameter against which to non-dimensionalize results.

Background information in the form of a literature review will be presented later in this chapter. Sections 1.2 and 1.3 will present previous research applicable to both problems presented in this thesis. Section 1.4 will present research in the area of three-dimensional flow instabilities. Section 1.6 will present prior research in the area of flow-induced vibration.

Chapter 2 presents both the numerical and experimental techniques used in the present investigation. Validation of the methods used will also be covered within this chapter.

Chapter 3 discusses the findings of the Floquet analysis on three dimensional flow instabilities in the wake of a blunt flat plate. Three modes are identified and compared to those found in previous studies.

In chapter 4, two-dimensional simulations of the flow-induced vibration of a circular cylinder are presented. In section 4.2.2, a critical mass ratio is found below which sustained peak to peak oscillations are observed.

In chapter 5, the system described in chapter 4 will be extended to a tethered cylinder, and findings of two-dimensional simulations will be presented. The effect of changing mass ratio is presented in chapter 6 and the effect of changed tether length ratio is presented in chapter 7. In chapter 6, the numerical findings will be compared with the results of an experimental investigation. From this comparison, the choice of using a two-dimensional domain may be validated. Finally in chapter 8, conclusions are drawn and possible future work is cited.

1.2 Vorticity and fluid forces acting on bodies

Vorticity fields are used throughout this thesis to visualize the fluid structures in the wake of the bluff body of interest. For the second problem studied, the fluid flow induces forces on the body which in turn induce body motion. The fluid forces acting on the body have been mathematically related to the fluid structures in the wake through the concept of vorticity (for example see Lighthill (1963), Batchelor (1967), Morton (1984), Wu (1981), and Wu & Wu (1996)).

1.2.1 Vorticity Defined

Vorticity is defined as the the local angular velocity of the fluid (Danielson (1997)) and is mathematically defined as the curl of the velocity vector ($\mathbf{u}$),

$$\boldsymbol{\omega} = \nabla \times \mathbf{u}. \tag{1.1}$$

Equation 1.1 may be decomposed into Cartesian components as:

$$\omega_x = \frac{\partial w}{\partial y} - \frac{\partial v}{\partial z}, \quad \omega_y = \frac{\partial u}{\partial z} - \frac{\partial w}{\partial x}, \quad \omega_z = \frac{\partial v}{\partial x} - \frac{\partial u}{\partial y}. \tag{1.2}$$

This thesis is only concerned with the vortex shedding from nominally two-dimensional bodies, and as such the three components of vorticity will be referred to as:

ω_x : stream-wise vorticity,

ω_y : transverse vorticity,

ω_z : span-wise vorticity.

Fully three dimensional flow fields (i.e. flow fields having components of each of ω_x, ω_y, and ω_z) occur in general for all bluff body wakes when the Reynolds number is beyond a critical threshold (see section 1.3). For low Reynolds number flows, it is possible to assume that the flow field is two-dimensional and from equation 1.2 the vorticity field can be completely described by ω_z.

For an incompressible homogenous fluid, vorticity can only be generated at solid-fluid boundaries (Morton (1984), Wu & Wu (1996)). Morton (1984) further found that vorticity generation results from a tangential acceleration of the boundary and its generation is instantaneous with this acceleration. After the vorticity has been generated, it diffuses into the fluid domain and is transported away from the solid-fluid boundary by both convection and diffusion (Wu (1981)). Morton (1984) further found that vorticity can only decay in the fluid interior due to diffusion although circulation is conserved; the boundary plays no role in the decay of vorticity.

By taking the curl of the momentum equations for an incompressible homogeneous fluid, the Helmholtz equation may be written as:

$$\frac{\partial \omega}{\partial t} = \boldsymbol{\nabla} \times (\mathbf{u} \times \boldsymbol{\omega}) + \nu \nabla^2 \boldsymbol{\omega} \tag{1.3}$$

From this equation, vorticity can only decay in the interior of a viscous fluid (Wu (1981)). As each term in equation 1.3 is proportional to vorticity, if $\boldsymbol{\omega} = 0$ then it will remain zero. Coupled with a solution for the pressure field, a solution to equation 1.3 is all that is required for a complete understanding of a fluid flow. Several numerical techniques (vortex methods) have been developed to solve fluid problems by solving equation 1.3, for examples see Leonard (1985) and Shiels (1998) among many others.

1.2.2 Vorticity and the fluid forces acting on a body

The force acting on a body due to the surrounding fluid flow may be determined in terms of vorticity, as was shown by Wu (1981). A sufficiently large control volume ($\mathcal{V}$) is chosen to encompass both the body and fluid of interest such that there is a very small net transfer of momentum through the control volume boundary ($\mathcal{B}_{\mathcal{L}}$). The body has volume $\mathcal{V}_{\mathcal{S}}$ and the solid-fluid interface is defined by $\mathcal{B}_{\mathcal{S}}$ (see figure 1.1).

The total force, F_t acting on $\mathcal{V}$ can be determined from the integral form of momentum theory (which is derived in many fluid dynamics text books, for example White (1999)) as:

$$F_t = \frac{d}{dt} \int_{\mathcal{V}} \tilde{\rho} \mathbf{u} d\mathcal{V} + \oint_{B_L} \rho_w \mathbf{u} (\mathbf{u} \cdot \mathbf{n}) d\mathcal{B}_{\mathcal{L}} \tag{1.4}$$

The first integral on the right hand side of equation 1.4 defines the momentum generated within the control volume. The term $\tilde{\rho}$ is either the density of the fluid ρ_w or the density of the solid ρ_s depending on the area of interest within $\mathcal{V}$. The second integral defines the net flux of momentum into the control volume, where $\mathbf{n}$ is the vector normal to the control volume boundary, $\mathcal{B}_{\mathcal{L}}$. Assuming that $\mathcal{V}$ is sufficiently large, the second term on the right hand side of equation 1.4 is negligible, equation 1.4 can be simplified and assuming there is only one solid body in the control volume, written as:

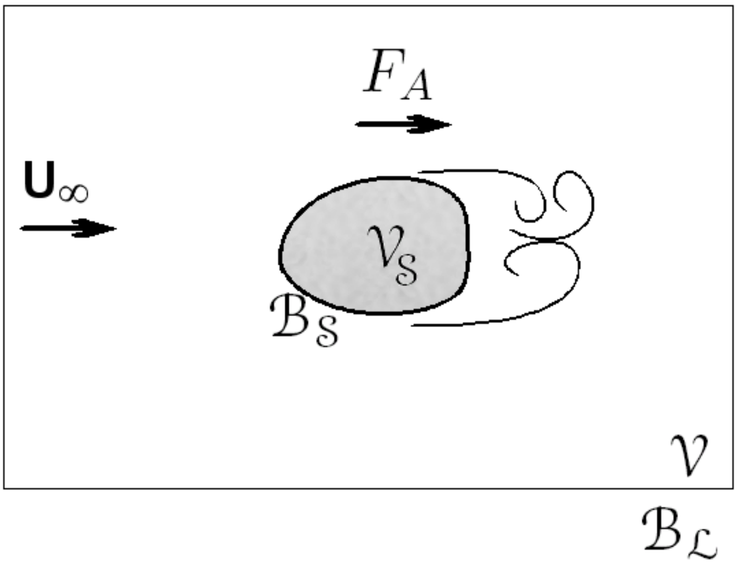

Figure 1.1: Control volumes and control volume boundaries used in relating vorticity to fluid forces acting on the body.

$$F_t = \frac{d}{dt}\int_{\mathcal{V}} \rho_w \mathbf{u} d\mathcal{V} + \frac{d}{dt}\int_{\mathcal{V}_\mathcal{S}} \rho_s \mathbf{u} d\mathcal{V}_\mathcal{S} - \frac{d}{dt}\int_{\mathcal{V}_\mathcal{S}} \rho_w \mathbf{u} d\mathcal{V}_\mathcal{S} \tag{1.5}$$

The first term on the right hand side of equation 1.5 describes the momentum generated within the fluid region of the control volume. The next two terms describe the momentum generated by the motion of the solid body within the control volume. From Newton's second law, the second term in equation 1.5 is the total force acting on the body ($F_{T_{body}}$).

Equation 1.5 describes the total force acting on the control volume, which includes forces due to the fluid flow (the aerodynamic force, F_A) and external forces which may act to control the motion of the body within the fluid, F_E. The effect of the external forces may be written in terms of a pressure force acting on the body from the inviscid "far field" by rewriting the inviscid momentum equations such that the pressure term is the subject and integrating over the surface of the body:

$$F_E = \rho_w \oint_{\mathcal{B}_\mathcal{L}} \left[\frac{\partial \phi}{\partial t} - \frac{u^2}{2} + \frac{f(t)}{\rho_w} \right] \mathbf{n} d\mathcal{B}_\mathcal{L} \tag{1.6}$$

In the above equation, the second term may be neglected as $\mathbf{u}$ decays asymptotically to zero (see Wu (1981)) and does not contribute to the surface integral; the function

$f(t)$ is also neglected as it is independent of position.

The aerodynamic force, F_A, is finally determined by negating the external force (from Equation 1.6) from the total force acting on the body ($F_{T_{body}}$):

$$F_A = \rho_w \oint_{\mathcal{B}_{\mathcal{L}}} \frac{\partial \phi}{\partial t} \mathbf{n} d\mathcal{B}_{\mathcal{L}} - \frac{d}{dt} \int_{\mathcal{V}} \rho_w \mathbf{u} d\mathcal{V} + \frac{d}{dt} \int_{\mathcal{V}_{\mathcal{S}}} \rho_w \mathbf{u} d\mathcal{V}_{\mathcal{S}} \tag{1.7}$$

This equation is written in terms of the velocity vector, however, by use of the Biot-Savart law:

$$u = \nabla \times \int_{\mathcal{V}_\infty} \boldsymbol{\omega} \cdot \frac{1}{2\pi} ln \frac{1}{|r - r_o|} d\mathcal{V}, \tag{1.8}$$

equation 1.7 may be rewritten in terms of the vorticity. In equation 1.8, r and r_0 are position vectors (r_0 is the initial position of a vortex core).

The above derivation is largely taken from Wu (1981) who provided a complete derivation relating both the aerodynamic force and moment acting on a body to the vortex structures in the surrounding fluid. Independent work by Noca (1997) has extended this idea to allow for finite control volume sizes. By allowing a net flux of momentum through the control volume and by using Stokes theorem to transform the volume integrals in equation 1.7 to surface integrals; Noca (1997) allows information from finite control volumes, in conjunction with experimental techniques such as DPIV to provide quantitative forces acting on the body. His derivations have been successfully applied to both numerical and experimental studies in the related papers of Noca *et al.* (1997) and Noca *et al.* (1999) at both low and high Reynolds numbers.

1.2.3 Vorticity and fluid structures in the wake

Fluid structures in the wake of a bluff body are generally depicted in terms of vorticity for several reasons. The vorticity vector is Galilean invariant (hence the wake structure is the same regardless of the reference frame of the observer). Regions of high vorticity only occupy a finite space, and the observer may restrict attention to the rotational region of the wake (Wu & Thompson (1973)). Regions of the wake may be classified as regions of diffusion and regions of convection.

1.2.4 Summary: Vorticity and the current problem

For both studies undertaken in this project, vortex fields have been used extensively to depict the flow field around nominally two-dimensional bluff bodies.

In the first study, the individual Cartesian components of vorticity are used as a representation of the three-dimensional wake, and "vortex structures" are used to visually identify different stability modes which occur during the onset of three-dimensional instability in the wake of bluff plates.

In the second study, the property of Galilean invariance allows the study of the fluid structures in the wake of the moving body regardless of the reference frame. By analyzing the vorticity field, one is able to relate the force acting on the body to the surrounding flow structure.

1.3 Introduction to the Flow Around Bluff Bodies

Roshko (1955) defined a bluff body by describing two critical features of the flow past the body:

> "The main feature(s) of flow past a bluff body is its separation from the body surface, well ahead of the rear stagnation point, and the formation of a large wake."

This study is restricted to the flow past nominally two-dimensional bluff bodies (cylinders). The first part of this project is confined to the intrinsic wake transition from two- to three-dimensional flow, for cylinders of varying cross-sectional geometry. For a circular cylinder, these intrinsic transitions occur in the range $Re \gtrsim 180$ (Williamson (1996b)). The second part of the project concerns the flow-induced vibration of a tethered circular cylinder at low Reynolds numbers.

The formation of vortex structures in the wake of two-dimensional bluff bodies has been the subject of intense study and debate for close to a century, e.g, Karman (1911), Roshko (1954), Berger & Wille (1972) and Williamson (1996c).

Much of this work has focused on the circular cylinder, due in part to the geometric simplicity, engineering practicality, and variation in results obtained over a wide range of investigations (to be discussed herein). Several comprehensive review articles exist on the topic (for example Gerrard (1978), Berger & Wille (1972), Williamson (1996c) and many others).

In the second part of this project, all simulations were carried out using a two-dimensional domain, and as such were restricted to low Reynolds number flows ($Re \leq$

200). Direct comparisons were made between this work and experimental work conducted in collaboration with Josie Carberry in the Monash FLAIR water channel (see section 6.7) which was conducted up to $Re \simeq 10000$.

As a result of the requirements of the two studies, flow phenomena up to $Re = 10000$ will be examined in detail, however phenomena occurring at higher Reynolds numbers will only be briefly examined.

1.3.1 2D Transition

For very low Reynolds number flow fields, $Re \lesssim 47$, the flow around a circular cylinder is steady-state in nature. Above $Re = 4$, the wake consists of two recirculating vortices attached to the rear surface of the cylinder and symmetrically placed about the centreline; together they form the recirculation region. Within this Reynolds number range, the size of the recirculation region varies in proportion to Reynolds number (Coutanceau & Bouard (1977), Gerrard (1978)).

Taneda (1956) observed irregular perturbations forming within the recirculation region for $Re > 35$. These perturbations convected downstream and were quickly damped out. However, oscillations of the wake 'trail' further downstream were observed for Reynolds numbers as low as 30. He further found a critical Reynolds number of $Re_{cr1} = 45$ beyond which the recirculation region of the wake became unstable. Coutanceau & Bouard (1977) found a critical Reynolds number, $Re_{cr1} = 39.5$, beyond which the size of the two vortex cores varied independently of each other. The discrepancy between Taneda (1956)'s and Coutanceau & Bouard's findings may in part be explained by the highly sensitive nature of the recirculation region and wake to perturbations. Taneda (1963) found slight oscillations of the cylinder cause near-wake oscillations for Reynolds numbers as low as 1. A comprehensive summary of the flow structures in the wake of a cylinder at these low Reynolds numbers is given by Gerrard (1978).

As the Reynolds number increases beyond Re_{cr1}, there is a Hopf bifurcation of the near wake, and a transition in the flow structures in the wake of the cylinder. Re_{cr1} has been found by Shair *et al.* (1963) and Provansal *et al.* (1987) to vary between $47 \leq Re_{cr1} \leq 123$ inversely with the cylinder aspect ratio (defined as the ratio of span length to cylinder diameter), however the generally accepted, experimentally-determined value of Re_{cr1} (for "infinite cylinders") is between 47 and 49 (Norberg

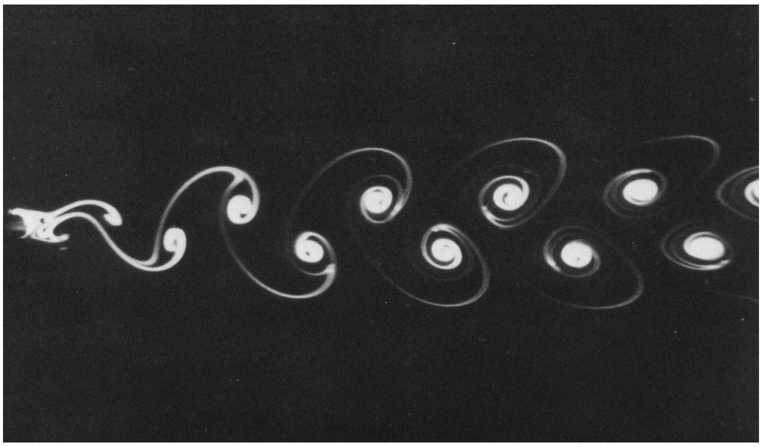

Figure 1.2: Karman vortex street in the wake of a circular cylinder at $Re = 105$; Van Dyke (1982)

(1994) and Williamson (1996c)). For $Re > Re_{cr1}$, the recirculation region becomes unstable and the two vortices begin to shed alternately. The steady wake is replaced with a pattern of alternating negative and positive vortex cores convecting downstream. The wake structure is described as a Karman vortex street, after von Karman (1911) (see Lamb (1932)) who analytically described the stability of the wake structure. An example of the Karman vortex street is shown in figure 1.2. von Karman (1911) found that the spatial arrangement of the observed vortex cores exhibits neutral stability. The vortex formation and shedding mechanism is described in detail by Perry *et al.* (1982). They found that viscous diffusion was not part of the basic shedding mechanism. This explains why the Karman type instability is observed over a very wide range of Reynolds numbers.

For Reynolds numbers in the range $Re \simeq [49, 140]$, the wake flow field is intrinsically two-dimensional in nature. The vortex shedding mechanism in this Reynolds number regime is commonly referred to as laminar shedding.

1.3.2 Extrinsic 3D transition

In the Reynolds number range of $[50, 150]$ Roshko (1954) observed a continuous curve describing the variation in the Strouhal number as a function of the Reynolds number given by the following equation:

$$Re \cdot St = 0.212Re - 4.5, \tag{1.9}$$

where the term on the left hand side of the equation is commonly referred to as the 'Roshko' number. Several investigators have since found different relationships between St and Re, see for example figure 1.3.

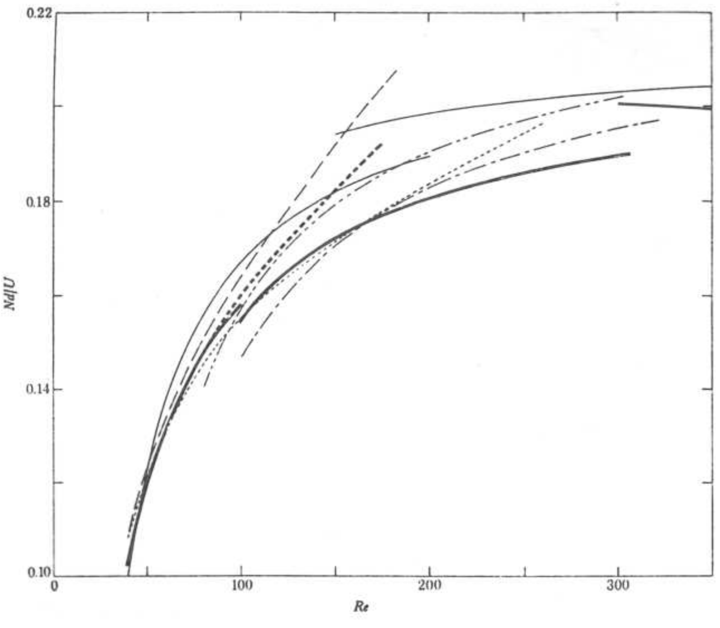

Figure 1.3: Comparison of results of measured Strouhal number as a function of Reynolds number; Gerrard (1978); results from: —, Roshko (1954); $- \cdot \cdot -$, Tritton (1959); $- - -$, — —; from Berger (1964).

Tritton (1959) found a discontinuity in the Strouhal-Reynolds relation resulting in a reduction in the Strouhal number of around 5% for Reynolds numbers above the discontinuity (Re_s). The transition occurred in the range $Re_s = [90, 100]$ for his wind tunnel experiments and $Re_s = 70$ in his water channel experiments. He proposed that the low speed mode arose from an instability of the wake, whereas the high speed mode arose as a direct result of the flow interaction with the cylinder surface. His findings were confirmed by Berger (1964) (see Tritton (1971)). Tritton (1971) repeated his experiment in a new facility in order to establish the repeatability of his findings, here he found $Re_s = 110$. Friehe (1980) found qualitative agreement with Berger and Tritton for cylinders with aspect ratios $L/D > 150$.

In his investigation of vortex shedding behind tapered cones, Gaster (1969) found no evidence of the discontinuity in the Strouhal-Reynolds number relationship. Gaster (1971) found a number of span-wise cells of constant shedding frequency. From the evidence of these two papers, Gaster (1971) suggested that observations of a discontinuity were due to a non-uniformity in the flow field of Tritton's facility. The repeatability of the phenomenon found across experimental setups in Tritton's (1959,1971) work questioned this conclusion.

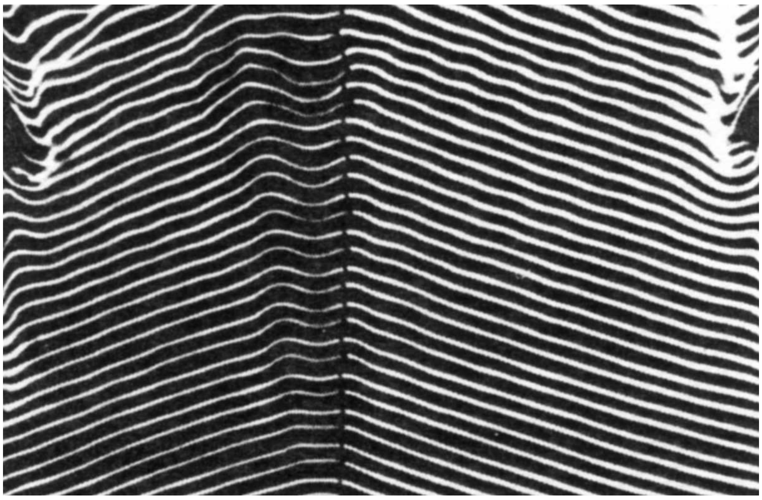

Figure 1.4: A chevron pattern of oblique shedding, $Re = 90$, induced by end (span-wise) boundary conditions; from Williamson (1996c)

A related observation is the phenomenon of oblique shedding (that is, vortex shedding at an angle α to the span direction - for example see figure 1.4) observed in this Reynolds number regime, even for exceptionally long cylinders (Norberg (1994) found oblique shedding for $L_c/D \leq 2000$). This phenomenon was found to be related to the choice of end conditions by Gerich & Ecklemann (1982) who hypothesized a connection between their findings and the observed Strouhal-Reynolds number discontinuity. They found a region of low frequency shedding ranging from 6 to 15 cylinder diameters from the cylinder ends. The extent of this low frequency region depended on the choice of end conditions, however with $L_c/D < 30$, the low frequency region extended across the entire span.

Ramberg's (1983) study of the flow past yawed cylinders allowed him to characterize the Strouhal frequency by taking the velocity component perpendicular to the cylinder. He noted an interdependence between the Strouhal frequency and the cylinder yaw. He also found that the addition of end-plates angled to be in-line with the flow influenced the shedding angle near the cylinder ends.

Williamson (1988a) extended Ramberg's (1983) work to the flow past a circular cylinder with no yaw angle to the flow. He observed a universal, continuous Strouhal-Reynolds number curve by relating the Strouhal number measured from flow with a oblique shedding angle α to a universal Strouhal number St_U using following equation:

$$St_U = St_\alpha / \cos(\alpha). \tag{1.10}$$

He found St_U corresponded almost exactly with the Strouhal number measured experimentally for the flow past a circular cylinder with induced parallel shedding, achieving a continuous Strouhal-Reynolds number relationship up to $Re \simeq 178$ (see figure 1.5).

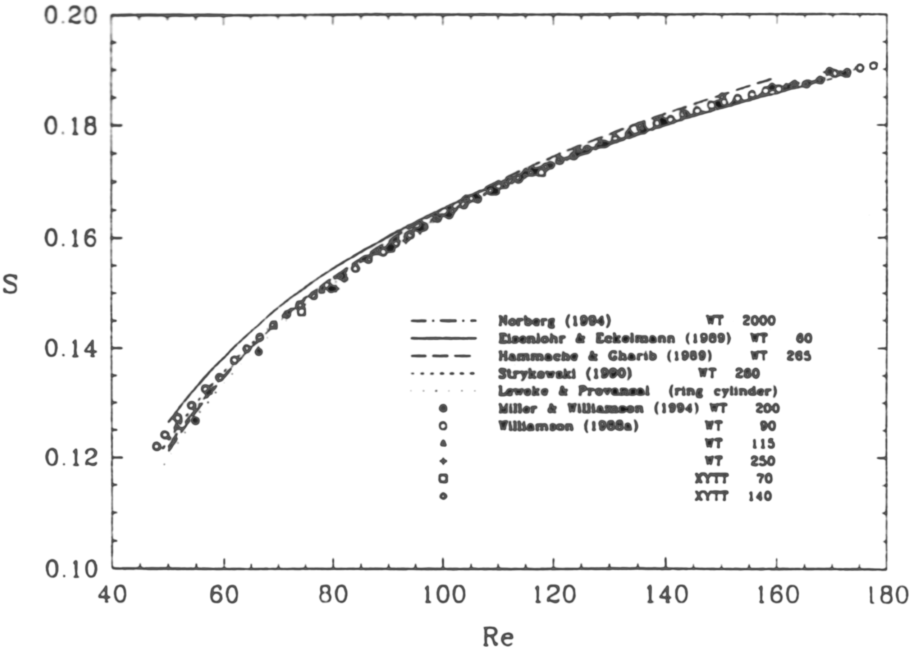

Figure 1.5: The continuous universal Strouhal Reynolds number relationship proposed by Williamson (1988a); data from laminar parallel shedding using different techniques agrees within 1%; from Williamson (1996c)

Williamson (1988a, 1989) further found that α could be controlled by changing the end conditions and parallel shedding could be induced across a majority of the span. This finding has been observed also by Hammache & Gharib (1989), Miller & Williamson (1994), Eisenlohr & Eckelmann (1989) and others. By using a Ginzburg-Landau equation to model the flow, Albarede & Monkewitz (1992) found that in general a slight increase in the local Reynolds number near the cylinder ends acts to induce the observed parallel shedding.

The two-dimensional simulations used throughout this project do not incorporate extrinsic (i.e. external forcing) three-dimensional effects, and the shedding is modelled as being parallel to the span dimension. The first part of the project does not concern the three-dimensional transitions caused by extrinsic effects. Extrinsic effects continue beyond the laminar regime and are apparent up to and including $Re = O(10^4)$ (Norberg (1994)) and they must be taken into consideration when comparing numerical results to experiments.

1.3.3 Intrinsic 3D transition

In his study of the flow past a circular cylinder, Roshko (1954) found transition occurred in the Reynolds number range $Re = [150, 300]$. Velocity measurements in the wake featured irregular bursts of energy accompanied by low frequency fluctuations. Within this range, as the Reynolds number was increased, these irregular bursts became more frequent and more intense. Beyond the transition range, no irregular bursts were observed. Dye visualizations of the wake flow field by Hama (1957) in the Reynolds number range $Re = [80, 300]$ indicated that the transition range corresponded with the appearance of an irregular transverse waviness in the near wake which became more intense and violent with increased Reynolds number. By taking time traces of velocity fluctuations within the wake, Bloor (1964) showed that the transition range is not associated with transition to turbulence in the free shear layers.

Further dye visualization by Gerrard (1978) showed ‘fingers of dye’ emanating from the newly shed primary vortex and orientated in the stream-wise direction. The ‘fingers of dye’ were observed to connect between the cores of successive Karman vortices. The span-wise distance between neighboring stream-wise structures was found to vary across the length of the cylinder span, however observation of his figures 25-28 indicates that the distance between the neighboring structures decreases with increasing Reynolds number.

Williamson (1988b) was able to distinguish two distinct three-dimensional flow instabilities within the transition region. He found a discontinuous drop in the Strouhal number marking the inception of the first instability as the Reynolds number was increased above the critical Reynolds number ($Re_{c2} = [140, 194]$). Williamson & Roshko (1990) noted a discontinuous drop in the base suction coefficient ($-C_{PB}$) at the same Reynolds number, as shown in figure 1.6. Associated with this drop is the observa-

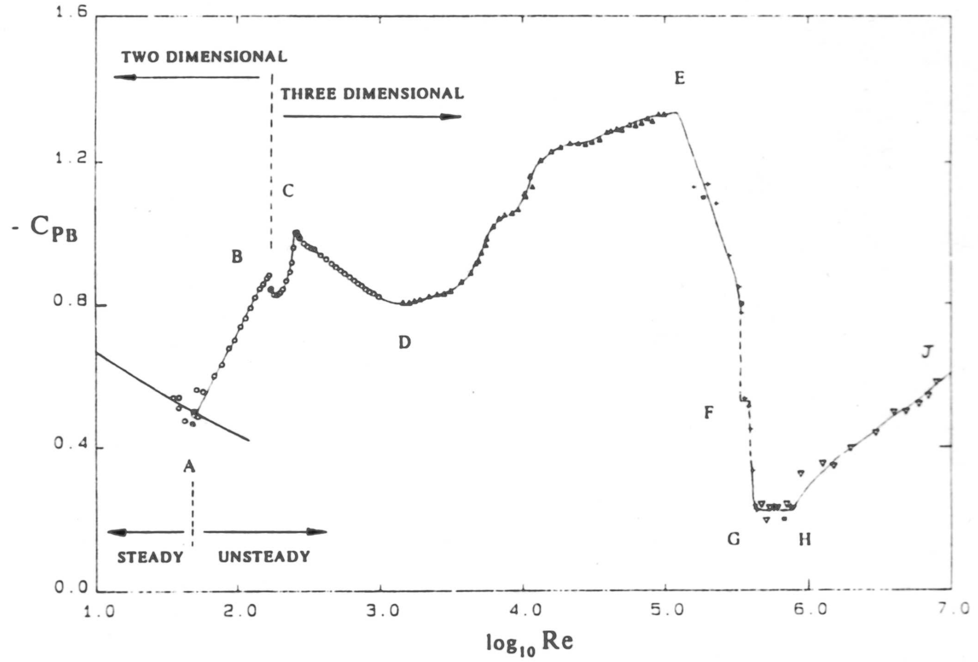

Figure 1.6: Plot of the base suction coefficient over a wide range of Reynolds numbers; from Williamson (1996c)

tion that the primary Karman vortices undergo sinusoidal span-wise perturbations (in agreement with the findings of Hama (1957)). The perturbations have a span-wise wavelength of 3-4 cylinder diameters (Williamson (1996b), Brede *et al.* (1994)). Over several shedding cycles, the initial span-wise waviness grows until vortex loops, pulled out of the deforming primary vortices, are stretched in the braid regions to form counter-rotating stream-wise vortex pairs. These vortex pairs occur with the same span-wise wavelength as the initial sinusoidal perturbations. Over successive primary Karman vortex cycles, stream-wise vortex structures form at the same span-wise location as their predecessors, however their vorticity is of opposite sign; that is, the mode exhibits out of phase symmetry. The structure described above has been termed “Mode A” shedding by Williamson (1988b) and is shown in figure 1.7. Similar wake patterns have been observed experimentally by Brede *et al.* (1994) and Hammache & Gharib (1989).

A relatively large range of critical Reynolds numbers ($Re_{c2} = [180, 194]$) have been experimentally recorded for Mode A transition. This is partly due to the hysteretic (or sub-critical) nature of the transition. Free stream turbulence (Bloor (1964)), cylinder

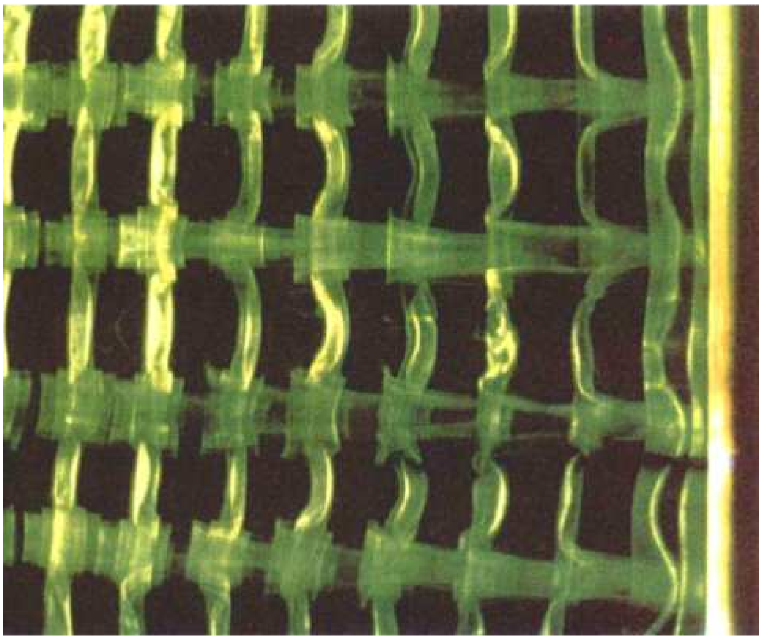

Figure 1.7: Dye visualization of the Mode A instability in the wake of a circular cylinder, $Re = 200$, $\lambda/D = 4.01$; flow is from right to left; from Williamson (1996c)

aspect ratio (Norberg (1994)) and end conditions (Williamson (1996b)) all affect the transition Reynolds number. The use of end plates to exclude extrinsic effects has enabled researchers to study intrinsic transition in isolation (for example Williamson (1988b)). However, the inclusion of end-plates induces large scale vortex dislocations (Williamson (1996b)) which disturb the Karman vortex shedding at the cylinder ends and effectively reduces the span over which parallel shedding is observed, an example of which is shown in figure 1.8. Miller & Williamson (1994), using non-mechanical end conditions, yielded “clean” end conditions, and observed the critical Reynolds number for Mode A transition as $Re_{c2} = 194$. This was taken as the critical Reynolds number for purely intrinsic transition to three-dimensional flow.

As the Reynolds number is further increased to $Re = [230, 250]$, a new mode of instability is intermittently observed (Mode B (Williamson (1988b))). With increasing Reynolds number, Mode B is established as the dominant mode and Mode A is no longer observed. For a circular cylinder, Mode B has a span-wise wavelength of 1 diameter and is shown in figure 1.9. From this observation, Williamson (1996c) has suggested that Mode B scales on the vorticity thickness in the braid shear layer. The span-wise wavelength remains constant over a broad Reynolds number range; Mode B has been

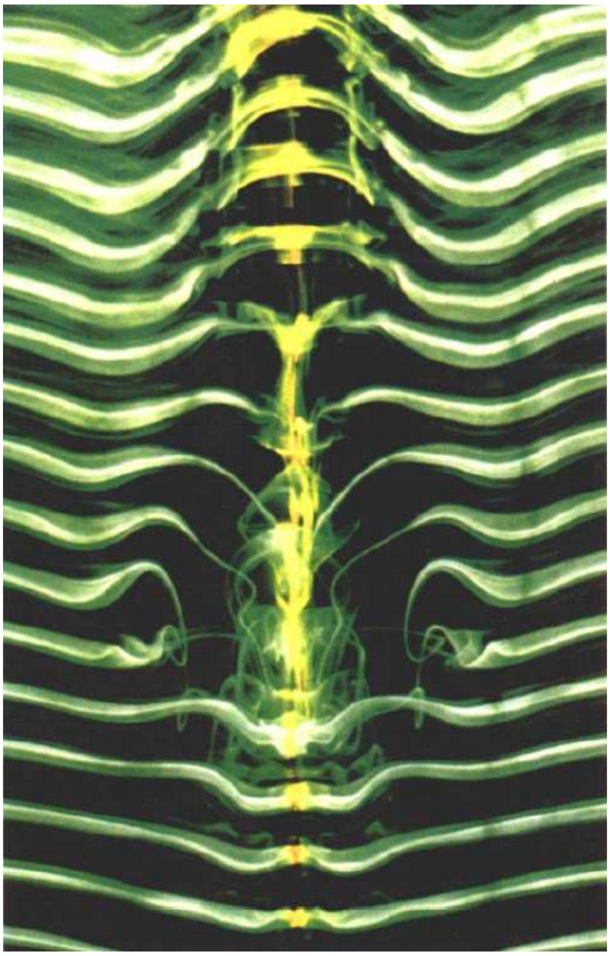

Figure 1.8: Dye visualization of a two-sided vortex dislocation in the wake of a circular cylinder, $Re = 140$, $x/D = 18$ to 60 (vertically); from Williamson (1996c)

observed experimentally at Reynolds numbers up to 10 000. Mode B exhibits in-phase symmetry; that is, successive stream-wise vortex structures have the same sign.

Miller & Williamson's (1994) results correspond very well with the numerical Floquet stability analysis performed by Barkley & Henderson (1996). Barkley & Henderson (1996) confirmed the critical span-wise wavelengths for both Mode A and Mode B. They found critical Reynolds numbers of 188.6 for Mode A, and 259 for mode B, corresponding well with experimental findings. Due to the nature of Floquet stability analysis, only intrinsic linear instabilities may be deduced.

Williamson (1996) has associated the reduction in both Strouhal number and base pressure coefficient with the spontaneous formation of large-scale vortex dislocations, which occur experimentally at the same critical Reynolds number as for mode A. These

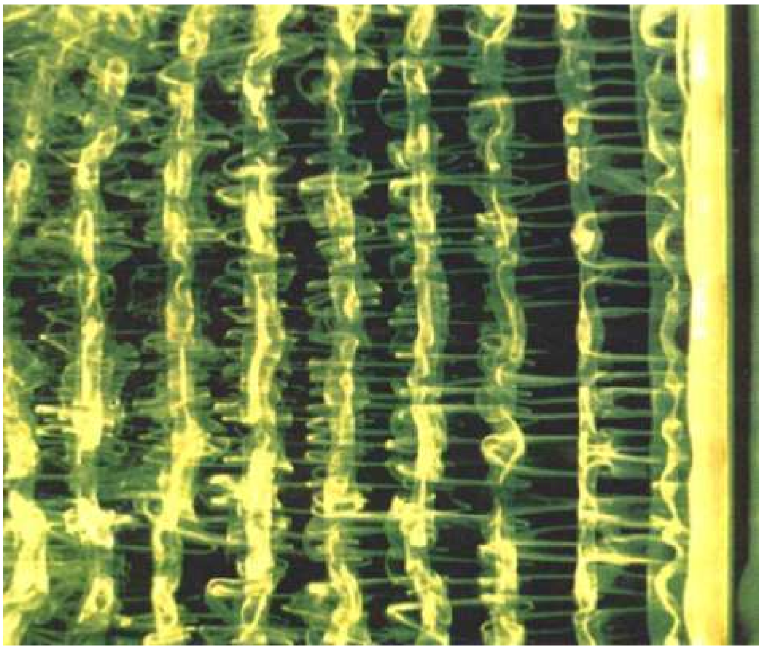

Figure 1.9: Dye visualization of the Mode B instability in the wake of a circular cylinder, $Re = 270$, $\lambda/D \simeq 1.0$; flow is from right to left; from Williamson (1996c)

large-scale vortex dislocations appear to be due to a nonlinear instability and occur naturally once the Mode A instability has reached a non-linear saturated state. The linear analysis performed by Barkley & Henderson (1996) could not predict the large-scale instabilities or the associated reduction in St and C_{bp}.

Figure 1.10: Iso-surface visualization of a Mode A instability from a direct numerical simulation; the yellow surface represents positive ω_x; the blue surface represents negative ω_x; the red surface represents ω_z; from Thompson *et al.* (1994)

Williamson's (1998b,1996a) observations have been verified both experimentally and numerically by a number of authors. Thompson *et al.* (1996) conducted (DNS) computational studies of the flow around a circular cylinder using a three-dimensional flow field. Their work verified the existence, and critical span-wise wavelength, of both Mode A and Mode B (see, for example figure 1.10). Henderson (1997), Zhang *et al.* (1995), Brede *et al.* (1994) and Hammache & Gharib (1989) have, through independent experiments, verified the existence of both Mode A and Mode B in the wake of a circular cylinder.

1.3.4 Transition to Turbulence

As the Reynolds number is increased further, the fine scale three dimensional structures constituting Mode B become increasingly more disordered. Associated with this is an increase in the base suction coefficient, $-C_{PB}$ (Williamson (1996b)) which peaks at $Re \simeq 260$. A corresponding peak is observed in both the formation length (Unal & Rockwell (1988)) and in the parameter:

$$\frac{u'_{rms}}{U_\infty}. \tag{1.11}$$

This implies a maximum value in the instantaneous velocity fluctuations in the near wake and is inferred by Williamson (1996b) as an increase in the near-wake Reynolds stresses, (defined as $-\rho u'v'$). As the Reynolds number is increased beyond 260, the base suction coefficient gradually decreases (Williamson & Roshko (1990)), as does u'_{rms}/U_∞ (Williamson (1996b)).

Two theories have been suggested in order to explain the local peak at $Re \simeq 260$. Barkley & Henderson (1996) find that this corresponds to the Reynolds number at which Mode B becomes linearly unstable to the two-dimensional flow field. The inception of Mode A would appear to allow Mode B to become unstable at lower Reynolds numbers experimentally. Williamson (1996c) suggests that this finding may explain the distinctly ordered patterns observed at this Reynolds number. He further proposes that the local peak may be due to a resonance between the Karman frequency and Kelvin-Helmholtz instabilities in the shear layer, based on the following equation proposed by Prasad & Williamson (1997):

$$\frac{f_{SL}}{f_K} = \left(\frac{Re}{262}\right)^{0.67}, \tag{1.12}$$

where f_{SL} is the frequency of the Kelvin-Helmholtz instability within the shear layer and f_k is the Karman shedding frequency.

Kelvin-Helmholtz instabilities in the shear layer of a circular cylinder were analyzed in detail by Bloor (1964), who found a critical Reynolds number equal to 1300 below which instabilities were not observed. A more recent study by Prasad & Williamson (1997) found that the Kelvin-Helmholtz instabilities in the shear layer are only observed for $Re > 1200$ for parallel shedding and $Re > 2600$ for oblique shedding. They relate this finding to the requirement that at least one spatial wavelength of the Kelvin-Helmholtz instability must propagate within the formation length. From these findings it seems difficult to use equation 1.12 at $Re \simeq 260$; the origin of the base suction maxima at $Re \simeq 260$ remains unresolved.

As the Reynolds number is increased beyond the critical Reynolds number marking the onset of the shear layer instability ($Re \simeq [1200, 1600]$) the base suction coefficient increases once more (Norberg (1994)) and the Strouhal number gradually decreases. Consistent with these findings, Schiller & Linke (1933) found that the formation length decreases with increasing Reynolds number beyond the onset of the shear layer instability. They also found the turbulent transition point in the separating shear layers moves upstream with increasing Reynolds number. Visualization of the wake by Unal & Rockwell (1988) and Lin *et al.* (1995) confirms the findings of Schiller & Linke (1933). Braza *et al.* (1986) found the shear layer instability is principally two-dimensional in nature and contributes to the rise of the 2-D Reynolds stresses and the base suction pressure coefficient.

The base suction coefficient continues to increase with Reynolds number in the Reynolds number range $Re = [1000, 100\,000]$ (Norberg (1987) and Bearman (1969)).

1.3.5 Higher Reynolds number flows

As the Reynolds number is increased beyond $Re \simeq 100\,000$, both C_{PB} and C_D decrease dramatically in the well known ‘drag crisis’ or ‘Critical Transition’. This is due to the turbulent transition point in the boundary layer moving sufficiently upstream that a separation-reattachment bubble forms on the sides of the cylinder resulting in a dramatic reduction in the width of the downstream wake (see Roshko (1993) and references cited therein). As the Reynolds number is increased beyond $Re \simeq 200\,000$, the turbulent transition only occurs on one side of the cylinder which acts to generate a net mean circulation inducing a mean lift (Schewe (1983)).

In the Reynolds number range $0.5 \times 10^6 \lesssim Re \lesssim 1 \times 10^6$, the flow is symmetric again. The drag coefficient is extremely low; Bearman (1969) detects fluctuations in the wake however it is unknown if vortices still form and shed in the traditional Karman manner. This Reynolds number region is known as the 'supercritical regime'

As the Reynolds number is increased beyond 1×10^6, the drag begins to increase with increasing Reynolds number. The boundary layer is now turbulent upstream of the separation point. See Roshko (1961) for further details.

1.4 Instability theory and intrinsic flow transition

In sections 1.2-1.3, previous work has been reviewed which pertains to both problems analyzed in this thesis. This section is restricted to analyzing previous work pertaining to the first problem (i.e. intrinsic flow transition in the wake of blunt flat plates with elliptic leading edges). Section 1.6 reviews previous work in relation to the second problem in the thesis.

As stated in section 1.3, a majority of research into the flow past bluff bodies has focused on the flow past a circular cylinder. This section will focus on intrinsic flow transition in the wake of bluff bodies of non-circular cross-section. Following this will be a review of stability theory for each instability mode identified, which allows comparison of the flow transition in the wake of a wide range of bluff bodies.

1.4.1 Flow Transition in the Wake of Non-Circular Cylinders

Zhang *et al.* (1995) experimentally observed the existence of a Mode C instability in the wake of a circular cylinder when a tripwire was placed adjacent to the cylinder in a direction transverse to the fluid flow. The Mode C instability was found to have a span-wise wavelength of 1.8 cylinder diameters (between the wavelength of the other modes), and was found to occur when the tripwire was located within 1 diameter of the cylinder. No information of the symmetry of the Mode C instability was provided. They hypothesized that the suppression of the flow field near the boundary layer results in a Mode C instability occurring in preference to Mode A and Mode B. Numerical calculations performed by Zhang *et al.* (1995) supported their experimental observations. Williamson (1996b) suggested that Mode C was only present due to the forcing on the two dimensional wake by the trip-wire and did not represent a “natural” instability of the Karman vortex street.

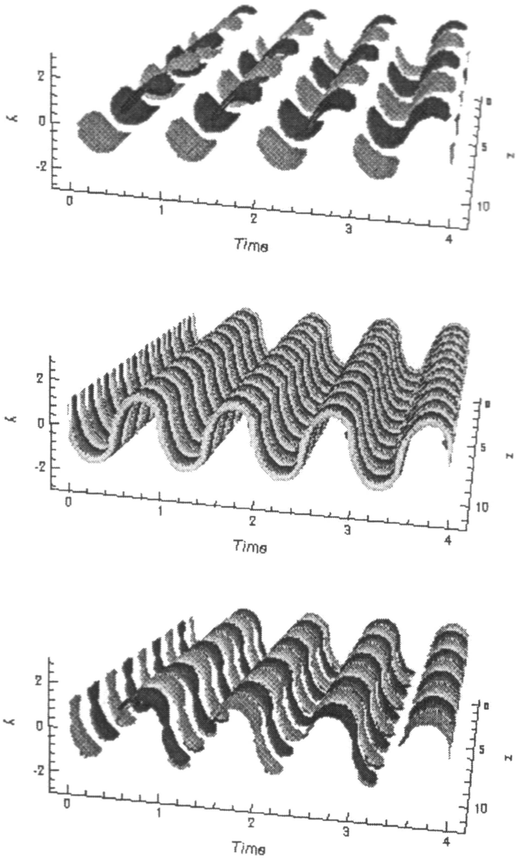

Figure 1.11: Space-time reconstruction of ω_z, of normalized Floquet modes for Modes A, B, and S. Dark contours represent negative vorticity, light contours represent positive vorticity; from Robichaux *et al.* (1999)

Robichaux *et al.* (1999) performed a Floquet stability analysis on a cylinder of square cross-section. Their model predicted the existence of a third mode of instability, which they denoted Mode S. While many physical features of this instability mode corresponded to those of Zhang *et al.*'s (1995) experimental and numerical work, Robichaux *et al.* (1999) did not refer to this instability as Mode C as a trip wire was not required to artificially break the planar symmetry and trigger the instability. The wake of the square cylinder was found to be unstable to Mode S for Reynolds numbers beyond 200. However, at this Reynolds number, the wake is already unstable to both Mode A and Mode B and hence the two-dimensional wake may not adequately model the fully three-dimensional wake observed experimentally at this Reynolds number. Due to the restriction of using linear analysis, their research did not indicate if Mode S would be observed experimentally. The structure of the three modes they identified are shown in figure 1.11.

Recently, Blackburn & Lopez (2003) repeated a Floquet analysis of both a square and circular cross-section cylinder. They found a third mode of instability with a critical wavelength between that of Mode A and Mode B ($\lambda \simeq 2.5$), coinciding with the critical wavelength found by Robichaux *et al.* (1999) for the flow past a square cross-section cylinder. This mode of instability was found to have complex conjugate Floquet multipliers (for a discussion of the Floquet method see section 2.3) with the direct implication that the mode represents either standing or travelling waves. They refer to this instability mode as the quasi-periodic (or QP) mode. This finding is in agreement with Barkley & Henderson's (1996) finding for a circular cylinder but it contradicts the findings of Robichaux *et al.* (1999) for the wake of square cylinder. Blackburn & Lopez (2003) demonstrated that the Floquet multipliers approach the negative real axis with increasing Reynolds numbers and suggested that Robichaux *et al.* (1999), by looking at Reynolds numbers above the onset for the QP mode, confused what they saw for a subharmonic instability, as at these higher Reynolds numbers, the imaginary component is comparatively small.

Blackburn & Lopez (To Appear) demonstrated that three-dimensional structures consistent with Mode A, Mode B and Mode QP existed for the case of a periodic driven cavity flow. They found that, for their geometry, many of the properties of mode QP were similar to those of Mode B. From this evidence, they hypothesize that mode QP is an example of a centrifugal instability. Blackburn *et al.* (To Appear) postulate that the QP mode becomes unstable via a Niemark-Sacker bifurcation. They further postulate that the QP mode is an example of a centrifugal type instability.

Meiburg & Lasheras (1987, 1988) conducted combined experimental and numerical investigations of the flow in the wake of a very thin flat plate held parallel to the flow. In these investigations they perturbed the flow in the span-wise direction generating several three-dimensional structures, two of which appear to have similar spatial symmetry to Mode A and Mode B in the wake of a circular cylinder. Julien *et al.* (2003a) experimentally investigate the flow over very thin flat plates. They find, in the case with no external forcing, that the two modes of three-dimensional transition corresponding with Mode A and Mode B of a circular cylinder occur naturally in the wake.

Previous studies have been conducted on the wake of blunt flat plates with elliptical leading edges (which is the subject of the first problem discussed in the thesis). Tan (2001) studied the flow around a blunt flat plate with elliptic leading edges both with and without imposed three-dimensional perturbations, using three-dimensional DNS. He found for a plate aspect ratio $C/H = 7.5$ (where C is the chord length of the plate and H is the plate thickness), a Mode A like instability for $Re = 500$. He found no three-dimensional instabilities below this Reynolds number, however the next lowest Reynolds number investigated was 400.

For a shorter plate, $C/H = 2.5$, he found a Mode A instability at $Re = 300$ and a Mode B type instability at $Re = 350$. For both plate C/H values, the critical wavelength of Mode A is uncertain, as only one complete wavelength was captured in the span-wise domain. Details of these findings are also presented in Hourigan *et al.* (2001).

1.4.2 Theory of wake transition

In the previous section, three instability modes have been identified, and it has been shown that each of these modes may grow in a wide range of flow geometries. By modelling each of these modes analytically in terms of an instability theory, similarities in many flow field types can be related, and the complex problem of three-dimensional transition may be simplified. The current theories for the growth of each of the modes are presented briefly here.

Mode A

Mode A transition has been studied by numerous authors, and several transition mechanisms have been suggested. Leweke & Provansal (1995) used a Ginzburg-Landau model to model the flow in the wake of a circular cylinder and from their findings proposed that Mode A was a form of a Benjamin-Feir instability. The wake dynamics of a Mode A instability are consistent with this finding, however the Benjamin-Feir instability has a vanishing span-wise wave-number which is inconsistent with experimental and numerical observations of Mode A (e.g. Williamson (1988b), Barkley & Henderson (1996)).

Brede *et al.* (1996) suggested that the strong curvature of the streamlines observed in the wake was consistent with a centrifugal type instability, however no conclusive evidence exists to support their theory.

Williamson (1996b) suggested that Mode A was associated with an elliptic instability of the primary Karman vortex cores, Leweke & Willimson (1998) concurred.

The theory of elliptic instability was originally developed for the idealized flow field consisting purely of elliptic streamlines in an unbounded region. Several authors, including Pierrehumbert (1986), Bayly (1986), Landman & Saffman (1987) and Waleffe (1990) have contributed to the development of elliptic instability theory within this idealized flow field.

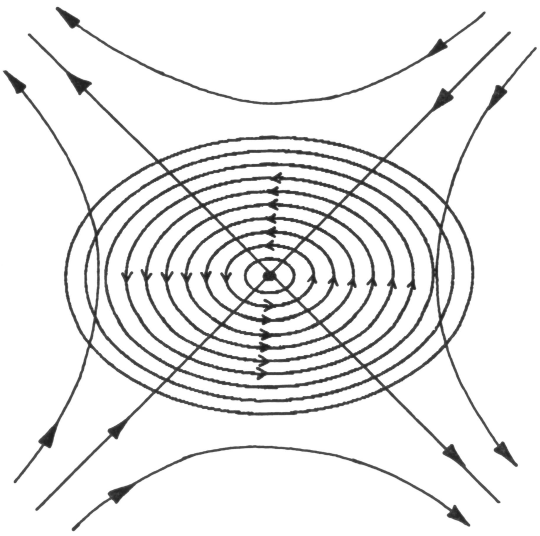

Figure 1.12: Elliptic flow stream-lines; from Williamson (1996c)

The elliptic streamlines of the idealized flow are created by the superposition of a solid body rotation of constant vorticity ω and a plane strain ε to give the following equation for the flow field:

$$\boldsymbol{U} = \begin{pmatrix} 0 & -\frac{1}{2}\omega - \varepsilon & 0 \\ -\frac{1}{2}\omega - \varepsilon & 0 & 0 \\ 0 & 0 & 0 \end{pmatrix} \begin{pmatrix} x \\ y \\ z \end{pmatrix} \tag{1.13}$$

(see Leweke & Williamson (1998)) which results in the flow field depicted in figure 1.12. For values of the eccentricity parameter, $\beta = 2\varepsilon/|\omega| < 1$ the flow is elliptic; for $\beta > 1$

the flow is hyperbolic. In either case, the flow is unstable to perturbations acting in the z direction (that is, normal to the elliptic streamlines).

The instability of the elliptic flow field is due to an amplification of inertial waves in the rotational frame of reference of the base flow (Waleffe (1990)), and for inviscid flows, the growth rate, σ_i of the most unstable perturbations is:

$$\frac{\sigma_i}{\varepsilon} \simeq \frac{9}{16}(1-\beta^m)^n \qquad \text{for } 0 < \beta < 1 \text{ (elliptic flow)} \tag{1.14}$$

where the values of $m = 2.811$ and $n = 0.3914$ have been found by Landman & Saffman (1987). Importantly, in the idealized case, all the perturbation wavelengths, λ_z, are equally unstable.

Both elliptic and hyperbolic regions can be observed locally in the wake of a bluff body, where the local hyperbolic regions correspond to the braid regions and the local elliptic regions correspond to the primary vortex cores. Here, the extent of either the local hyperbolic or local elliptic region is clearly finite and is restricted by adjacent wake structures. However, Waleffe (1990) showed that there were localized modes of elliptic instability which would grow within the primary vortices in the same fashion as the idealized unbounded elliptic fields.

Eloy & Le Dizes (1999) and Eloy & Le Dizes (2001) found analytically that the perturbation length scale in the span-wise direction is coupled to the length scale in the cross-stream plane. Therefore, as the size of the elliptic region of the flow is restricted to the primary vortex core region, there is an upper limit of allowed span-wise perturbation wavelengths, λ_z. Further, the addition of viscosity imposes a lower a limit to the span-wise wavelength.

Leweke & Willimson (1998) find that the most unstable span-wise wavelength is $\lambda_z \simeq 3D$ given that $\beta \simeq 0.6$. They further find that there is an invariant stream-tube which is not disturbed by the growing perturbation. These findings are in agreement with experimental and numerical observations for a Mode A instability in the wake of a circular cylinder. However Henderson (1997) questioned this finding, as the most significant growth for Mode A is not found in the vortex core as would be expected for an elliptic instability, but in the hyperbolic braid region.

Recently Thompson *et al.* (2001c) proposed that Mode A is due to a co-operative elliptic instability between two adjacent primary Karman vortices. Using numerical techniques, they were able to separate span-wise perturbations growing in the braid region from perturbations growing within the vortex core, and perform three-dimensional

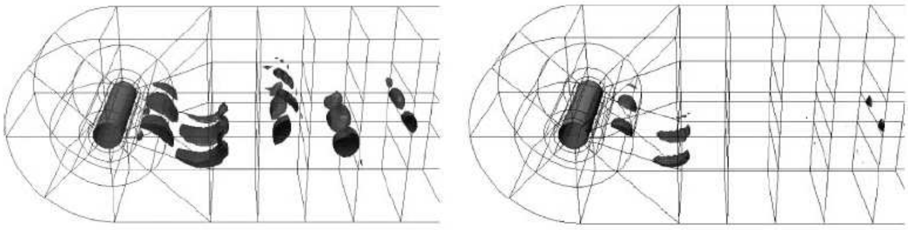

Figure 1.13: Iso-surface visualization of the perturbation ω_z after removing (left) the hyperbolic or (right) the elliptic component of the Floquet mode and evolving the flow for 2.4 shedding periods; from Thompson *et al.* (2001c)

DNS simulations to evolve both solutions separately. They found a topology similar to Mode A evolved for the simulation initially disturbed by vortex core perturbations. The simulation perturbed only in the braid region took longer to evolve back to the Mode A field. From this they concluded that perturbations occurring in the elliptic vortex core region are essential to generate a Mode A instability (see figure 1.13). The higher growth rate noted in the braid region by Henderson (1997) appears to be due to the elliptic perturbations being amplified in the highly strained braid region. These results agree with Leweke & Williamson (1998) who found a co-operative elliptic instability occurred in the flow of two interacting counter-rotating vortices.

Mode B

Williamson (1996b) related the span-wise wavelength of the Mode B instability with the vorticity thickness of the separating shear layer, δ_ω. He found for the wake of a circular cylinder that δ_ω measured one diameter downstream of the cylinder could be related to the Reynolds number by:

$$\frac{\delta_\omega}{D} = \frac{4.2}{\sqrt{Re}}. \tag{1.15}$$

For Re = 230, marking the critical Reynolds number beyond which Mode B occurs, $\delta_\omega/D \simeq 0.28$ and $\lambda_z = 0.98D \simeq 4\delta_\omega$. He related this finding to studies on mixing layers by Corcos & Lin (1984) who find that the most unstable wavelength of an instability in a shear layer is $\lambda \simeq 3\delta_\omega$. Williamson (1996b) suggests that a system of counter rotating vortices may have a critical wavelength of twice this value (i.e. $\lambda_z \simeq 6\delta_\omega$), close to his observed value. Williamson (1996b) proposed that Mode B may be a result of a hyperbolic instability in the braid region. However as a hyperbolic instability has no preferred perturbation wavelength, this suggestion does not agree with the very consistent wavelength observed for a Mode B instability.

More recently, Ryan *et al.* (To appear) have suggested that Mode B is due to a centrifugal instability. They find that Mode B has the greatest growth between the hyperbolic saddle point found in the braid region, and the elliptic flow field of the vortex core. They quantified the maximum perturbation amplitude of Mode B as approximately $7.2(U_\infty/D)^2$, where U_∞ is the free stream velocity.

In order to test the theory of a centrifugal instability, the profile of a primary vortex core was isolated from the surrounding flow field creating an idealized flow field. A linear stability analysis was conducted on the idealized vortex core which found a maximum growth rate of $10(U_\infty/D)^2$ with a preferred span-wise wavelength of $0.6D$. This is close to the growth rate and span-wise wavelength observed for the Mode B instability.

They propose that the amplitude of the perturbation is maintained over time and that the perturbation remains in the braid region which is then convected downstream. They further propose that the perturbation is sufficiently large to influence the upstream production of the Mode B instability and the process is repeated.

Ryan *et al.* (To appear) are careful to emphasize that the proposed centrifugal mechanism may only be applicable to the wake of a circular cylinder. For the wake behind a blunt flat plate with an elliptic leading edge, a Mode B' was found which was subtly different in topology to Mode B for a circular cylinder (see chapter 3). This may be due to the elliptic instability playing a more dominant role for this bluff body geometry when compared to a circular cylinder.

Mode QP

Considerably less research has been devoted to the existence and generation mechanism governing mode QP. However Blackburn *et al.* (To Appear) suggest that it is an example of a centrifugal instability. However, at this stage there is little evidence to support or reject this suggestion.

1.5 Scope of First Investigation

Despite intrinsic transition being noted for a range of cylinder cross-sectional geometries, to the author's knowledge, no study has been conducted which systematically alters the bluff body aspect ratio, C/H, and observes the effect of this alteration on the intrinsic transition to three dimensionality discussed in sections 1.3.3 and 1.4. That is, it has generally been believed that the circular cylinder transition scenario is fairly generic. A primary aim here is to test this hypothesis (with a body geometry which can be specified by a simple parameter).

The aim of this study is to quantify the characteristics of the three-dimensional instabilities in the wake of a nominally two-dimensional bluff cylinder. The leading-edge geometry is chosen to be streamlined to prevent any vortex shedding into the boundary layer as it convects along the plate surface and into the wake. Experiments with a semi-circular leading edge showed that small boundary layer vortices could occur at Reynolds numbers of order 1000 and possibly less. An elliptical leading edge prevents this from occurring. For all numerical experiments described in this paper, the elliptic leading-edge has a major to minor axis ratio of 2.5:1. The cylinders have a square trailing edge such that vortices are shed at the same spatial location regardless of the Reynolds number. In each investigation the cylinder is modelled as being immersed within a uniform homogeneous incompressible Newtonian fluid with constant inlet velocity U.

There are two parameters governing the flow behaviour. The first is the aspect ratio, $AR = C/H$, and the second is the Reynolds number, $Re = UH/\nu$, where ν is the kinematic viscosity. Within the scope of this investigation, four aspect ratios were studied ($AR = 2.5$, 7.5, 12.5, 17.5), encompassing a non-equilibrium boundary layer at small aspect ratio to a near-universal boundary layer (prior to flow separation) for the larger aspect ratio studies. Through the course of the investigation it was found that the critical Reynolds number range for three-dimensional transition increased substantially with aspect ratio. Hence, it was necessary to use higher Reynolds numbers for the larger aspect ratios.

Numerical modelling was performed in two stages. Initially, the time-dependent two-dimensional flow field around the cylinder is predicted by solving the time-dependent Navier-Stokes equations in two dimensions. Above the critical Reynolds number, Re_{c1} two-dimensional instabilities saturate to form the familiar periodic flow field in the form of a Karman vortex street of period T. The stability of this periodic, two-dimensional, *base* flow field to three-dimensional disturbances is then determined using Floquet stability analysis.

1.6 Vortex-Induced-Vibration

As discussed in section 1.2, fluid forces acting on a body may be directly related to the vortex structures in the surrounding fluid. For the case of a bluff body, the vortices in the wake form periodic fluid structures referred to collectively as the Karman vortex street (discussed in section 1.3.1). These structures induce periodic forcing on the body. Depending on the mass of the body, its mechanical damping and its spring stiffness, the periodic forcing can induce vibrations of the body. Vortex-induced-vibration of circular cylinders is comprehensively reviewed by Sarpkaya (1979), Griffin & Ramberg (1982), Bearman (1984) and the books by Blevins (1990) and Naudascher & Rockwell (1993), as well as many others.

Studies of vortex-induced-vibration of bluff cylinders generally consider either the motion of a stiff, flexibly-mounted cylinder which has the same motion along the entire length of the span; or a flexible cylinder, in which vortex-induced vibration creates travelling modes along the span. A flexible cylinder generally exhibits vortex-induced-vibration along part of the span which subsequently forces oscillations at different spanwise locations. This review will focus on stiff, flexibly-mounted, circular cylinders.

Variations in the inlet velocity are quantified by the reduced velocity $u^* = U_\infty / f_n D$, where U_∞ is the inlet velocity, D is the cylinder diameter and f_n is the natural frequency of the flexibly mounted cylinder.

Flexibly mounted bluff bodies generally exhibit vortex-induced-vibrations with components in-line and transverse to the flow field. Across a wide range of u^*, the largest amplitude of the transverse component of oscillations is typically an order of magnitude greater than the largest amplitude of the in-line component Bearman (1984). It could be anticipated that large amplitude transverse oscillations, excited by the lift force, occur when the shedding frequency, f_s, approaches the natural frequency of the system, f_n (i.e. a peak in the transverse component of oscillation occurs as $u^* \rightarrow 1/St$).

As the Strouhal number for a fixed circular cylinder can be assumed to be roughly equal to 0.2 over a wide range of Reynolds number, a peak amplitude in transverse oscillations should occur as $u^* \rightarrow 5$; this phenomenon has been widely reported (see for example Griffin & Ramberg (1982)). Similarly for in-line oscillations, it may be anticipated that a peak in the amplitude will occur as $f_{Drag} = 2 \cdot f_s \rightarrow f_n$, as the drag force is now driving the oscillation. Appreciable in-line oscillations have been reported in the range $u^* = [1.5, 4]$, by King (1974).

1.6.1 In-Line Oscillations

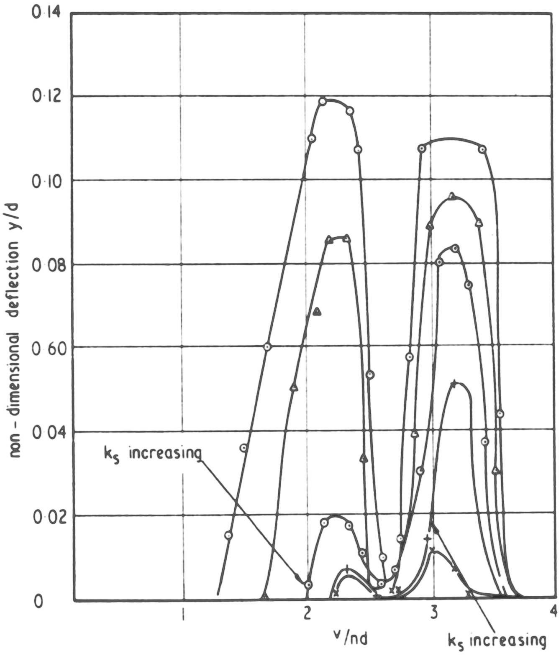

Figure 1.14: Amplitude response of a cylinder free to oscillate in the in-line direction; as a function of reduced velocity; from King (1974)

King (1974), by restricting the cylinder to only oscillate in-line with the flow, observed oscillations up to 0.15 diameters in amplitude in the Reynolds number range 6×10^4 to 6×10^5. He observed two modes of shedding. The first is a symmetric mode, where both positive and negative vortices are shed from the cylinder for each oscillation cycle and convect downstream symmetrically. Further downstream, the symmetric structure becomes unstable and the wake reverts to the staggered Karman type. The symmetric mode was found to occur in the range, $u^* = [1, 2.5]$. A local minimum in the in-line oscillation amplitude was noted at $u^* \simeq 2.5$, however in the range $u^* = [2.5, 4]$, a second mode of shedding was observed (see figure 1.14). In this mode, a single vortex is shed per oscillation cycle, and the wake resembles the traditional Karman arrangement.

King (1974) further speculated that a critical Reynolds number existed, in the range $Re = 1200 - 1500$, below which in-line oscillations were not observed. King's (1974) results have been qualitatively verified by Jauvtis & Williamson (2002).

1.6.2 Transverse Oscillations

Many studies have analyzed the freely oscillating cylinder, restricted to oscillate transverse to the free-stream. Of these studies, several have considered the case of a rigid, spring-mounted cylinder. This will be of principal interest in this review, as it represents the geometry which most closely resembles that investigated in the second part of this thesis. The equations of motion for this system will be briefly discussed. Non-dimensional groups arising from the linearized solution of the equations of motion form the basis of much discussion in the literature. The equations of motion governing an elastically-mounted cylinder system may be written in Cartesian form as:

$$m \cdot \ddot{y} + c \cdot \dot{y} + k \cdot y = F_L, \tag{1.16}$$

where m is the mass of the cylinder, c is the mechanical damping acting on the cylinder, k is the mechanical spring stiffness of the supporting springs, and F_L is the lift force acting on the system (see figure 1.15).

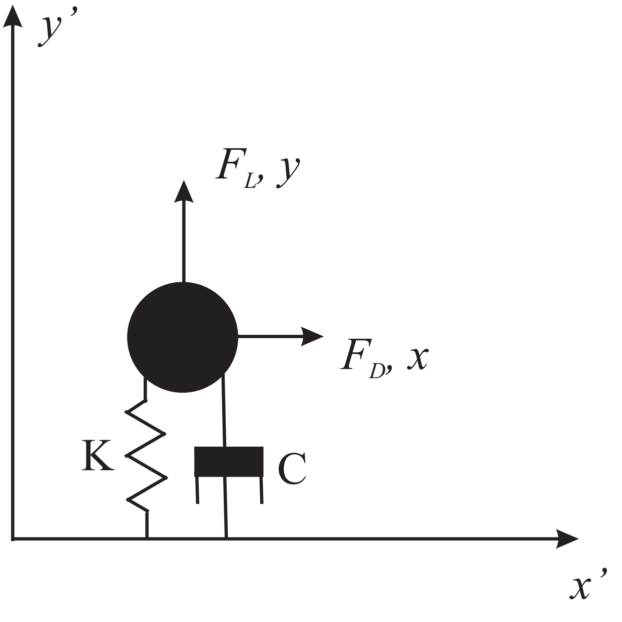

Figure 1.15: Hydro-elastically mounted, transversely oscillating, cylinder system.

In the case where both the wake shedding frequency, f_o, of the oscillating cylinder, and the oscillation frequency, f, coincide (referred to as 'lock-in' by Khalak & Williamson (1999) and Sarpkaya (1995)); both the cylinder oscillation and the lift force acting on the cylinder may be modelled as the sinusoidal functions:

$$
\begin{aligned}
y &= A \cdot \sin(\omega t) && (1.17)\\
F_L &= \hat{F_L} \cdot \sin(\omega t + \phi) && (1.18)
\end{aligned}
$$

where A represents the peak amplitude, and $\hat{F_L}$ represents the peak lift force. From standard vibration analysis (for example Rao (1995)), the forcing signal (F_L) must precede the cylinder oscillation signal (y); this is commonly referred to as the 'lag'. This is accounted for by the inclusion of the phase lag term (ϕ). For positive work to be done by the fluid on the cylinder, ϕ must be in the range 0^o to 180^o as pointed out by Blackburn & Henderson (1999). The phase lag may be related to the structural damping, spring stiffness, and cylinder mass by the equation:

$$\phi = \tan^{-1}\left(\frac{c \cdot \omega}{k - m \cdot \omega^2}\right), \tag{1.19}$$

where $\omega = 2\pi \cdot f$ is the oscillation frequency of the cylinder system.

Substituting equations 1.17 and 1.18 into equation 1.16, and using the trigonometric identity:

$$\sin(a + b) = \sin(a) \cdot \cos(b) + \cos(a) \cdot \sin(b), \tag{1.20}$$

the equation of motion may be reduced to,

$$
\begin{aligned}
&-m\omega^2 A \sin(\omega t) + c\omega A \cos(\omega t) + kA \sin(\omega t)\\
&\qquad = \hat{F_y} \cdot [\sin(\omega t)\cos(\phi) + \cos(\omega t)\sin(\phi),
\end{aligned} \tag{1.21}
$$

or in non-dimensional terms as,

$$
\begin{aligned}
&-\pi^3 m^* \left(\frac{f^*}{u^*}\right)^2 A^* \sin(\omega t) + 2\pi^3 \zeta \frac{(m^* + C_A)}{u^{*2}} A^* f^* \cos(\omega t) + \pi^3 \frac{(m^* + C_A)}{u^{*2}} A^* \sin \omega t\\
&\qquad = \frac{1}{2} \hat{C}_Y \cdot [\sin(\omega t)\cos(\phi) + \cos(\omega t)\sin(\phi)],
\end{aligned} \tag{1.22}
$$

where definitions of the non-dimensional parameters are listed in table 1.1.

Two identities may be derived from equation 1.22 (following Bearman (1984) and Khalak & Williamson (1999)):

$$A^* = \frac{C_Y \sin(\phi)}{4\pi^3 (m^* + C_A)\zeta} \left(\frac{u^*}{f^*}\right)^2 f^*, \tag{1.23}$$

$$f^* = \sqrt{\frac{m^* + C_A}{m^* + C_{EA}}}, \tag{1.24}$$

Mass Ratio	m^*	$\dfrac{m}{\pi \rho_w D^2 L_c/4}$
Damping ratio	ζ	$\dfrac{c}{2\sqrt{k(m+m_A)}}$
Reduced velocity	u^*	$\dfrac{U_\infty}{f_N D}$
Amplitude Ratio	A^*	$\dfrac{A}{D}$
Frequency Ratio	f^*	$\dfrac{f}{f_N}$
Peak Lift Coefficient	$\hat{C}_Y$	$\dfrac{\hat{F}_Y}{\frac{1}{2}\rho_w U_\infty^2 D L_C}$

Table 1.1: Non-Dimensional parameters used to normalize the equations of motion of a freely oscillating cylinder.

where the term C_{EA} is defined as,

$$C_{EA} = \frac{1}{2\pi^3} \cdot \frac{C_Y \cos(\phi)}{A^*} \left(\frac{u^*}{f^*}\right)^2 . \tag{1.25}$$

Prior research has considered three fundamental questions in relation to vortex-induced-vibrations of cylinders:

- Can the maximum amplitude of oscillation (A^*_{max}) be characterized by one plot for a range of system parameters?
- What modes of oscillation response exist for cylinders constrained to oscillate transverse to the flow field?
- What vortex structures exist in the wake of the oscillating cylinder as it approaches synchronization?

Two further questions have relevance to this thesis, and shall also be addressed:

- What is the effect of Reynolds number on the cylinder response?
- What are the implications of the limiting case of zero spring stiffness and zero damping on the system?

Each of these questions shall be considered in turn.

Characterizing the Maximum Amplitude Response

For large mass ratio cylinders ($m^* >> 1$), Bearman (1984) found that, under resonance conditions, the oscillation frequency f approached both the shedding frequency of the fixed cylinder (f_o) and the natural frequency of the cylinder system (i.e. $f \sim f_o \sim f_n$). This implies that (for large m^*) $f^* \rightarrow 1$ and $u^* \rightarrow 1/St$. As the Strouhal number $St \simeq 0.2$ for a wide Reynolds number range, resonance should occur as $u^* \rightarrow [5, 6]$, yielding large response amplitudes, A^*. This phenomenon has been observed by Griffin & Ramberg (1982) for $m^* = 4.8$ and 43. Therefore, for resonance, both u^* and f^* approach constant values, and from equation 1.23, the amplitude of oscillation may be written:

$$A^* \propto \frac{C_Y \sin(\phi)}{(m^* + C_A)\zeta} \tag{1.26}$$

Further, from equation 1.23, if u^* and f^* are constant, $C_Y \sin(\phi)$ is purely a function of A^*. The conclusion drawn by several investigators (for example Vickery & Watkins (1964), Scruton (1965) and Skop & Griffin (1973)), is that for large mass ratios under resonance conditions:

$$A^* \propto \frac{1}{(m^* + C_A)\zeta}. \tag{1.27}$$

Several parameters have been developed in order to plot against A^*_{max} such that the amplitude data collapse over a wide range of m^* and ζ. The best known of these is a term developed by Skop & Griffin (1973) and Skop (1974) who modelled the vortex-induced-vibration of an elastically mounted cylinder using a Van-der-Pol equation; they suggested the term,

$$S_g = 2\pi^3 St^2 \cdot (m^* \zeta). \tag{1.28}$$

Griffin *et al.* (1982) compiled several sets of results from separate studies, plotting A^*_{max} as a function of S_g, and found an overall trend was evident across the experiments. An example Skop-Griffin plot is shown in figure 1.16. Griffin (1980) and Skop & Balasubramanian (1973) have provide updated versions of this plot.

Considerable scatter was noted for results where $S_g < 1.0$. Sarpkaya (1978, 1979) reported variations in A^*_{max} of between 50-100% by varying m^* independently of $m^* \cdot \zeta$ at $S_g \simeq 2.0$. Bearman (1984) found that for the case of small mass ratio, f^* will be affected by both mass ratio and damping constant independently. Analysis of equation 1.24 agrees with Bearman's (1984) conclusion, for small mass ratios, the value of C_{EA} begins to dominate the right hand side and f^* varies accordingly.

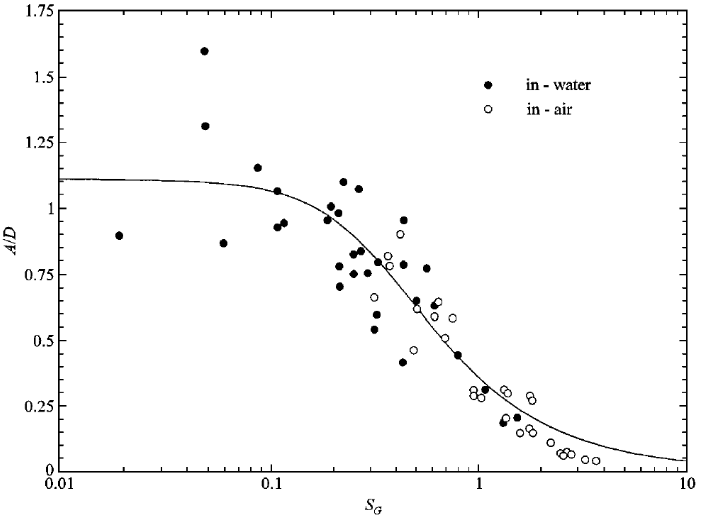

Figure 1.16: Skop-Griffin plot showing peak amplitude A^* versus the Skop-Griffin parameter S_g; from Khalak & Williamson (1999)

Sarpkaya (1993, 1995) concluded that the A^*_{max}, S_g plot could only be used to give an approximate indication of the maximum amplitude observed; Zdravkovich (1982) concurred.

Ramberg & Griffin (1981) reviewed two sets of experimental results for $m^* = 3.8$ and $m^* = 34.0$ respectively at $S_g = 0.5 - 0.6$. They found two results of interest; first, A^*_{max} was found to be roughly equal to 0.5 for both mass ratio values; second, the range of u^* for which large amplitude, synchronous oscillations were observed was larger for the lower mass ratio case.

Khalak & Williamson (1999) found A^*_{max} remained reasonably constant for the values $m^* = 2.4, 10.3$ and 20.6, when A^* was plotted against S_g. For low mass ratios, they found a mode of oscillation not observed at higher mass ratios (the upper mode) which explained the variation in amplitude for low S_g ($S_g < 1.0$, see 1.17) as the mass ratio was varied.

Finally, the maximum amplitude that could be obtained in the limiting case of zero damping has been estimated as $A^*_{max} \simeq 1.1$ by Skop & Balasubramanian (1973) from evidence of prior investigations. Bearman (1984) suggested a value of $A^*_{max} \simeq 1.5$. Experimental evidence from Hover *et al.* (1997, 1998) gave $A^*_{max} \simeq 0.8$ for zero mass-damping. Khalak & Williamson (1999) point out that this large scatter of results is probably due to the wide variety of experimental setups used (including cantilevers,

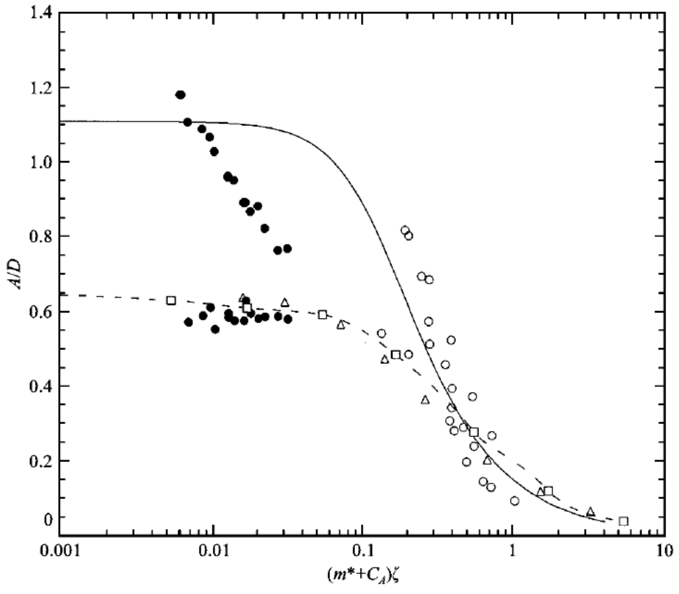

Figure 1.17: Griffin plot of the present peak amplitude data, compared with data compiled by Griffin (1980). •, Khalak & Williamson (1999); ∘, data compiled by Griffin (1980); —— Skop & Balasubramanian (1973); △, Blackburn & Karniadakis (1993); – – □ – –, Karniadakis (1996); from Khalak & Williamson (1999).

pivoted cylinder and elastically mounted cylinders), they found no experiment which has found $A^*_{max} > 1.13$ for an elastically mounted cylinder, and conclude that this value approximates the value of A^*_{max} with no damping.

Modes of Oscillation for the Elastically Mounted Cylinder

Feng (1968) investigated the flow past an elastically-mounted, low-damped, freely-oscillating cylinder with $m^* \simeq 250$. He found two branches of oscillations (see 1.18). As the oscillation frequency approached the natural frequency of the cylinder system. As the reduced velocity was increased from $u^* \simeq 5$, the maximum amplitude of oscillation increased rapidly with reduced velocity reaching a maximum value of $A^*_{max} \simeq 0.6$. A hysteretic jump was noted in the amplitude in a very narrow reduced velocity range ($u^* \simeq 6.0$). As the reduced velocity was further increased, the amplitude decreased gradually. Khalak & Williamson (1997) have termed the first mode of oscillation the “initial branch”, and the second mode of oscillation the “lower branch”. Brika & Laneville (1993) found qualitatively similar results for the case of a vibrating cable, as

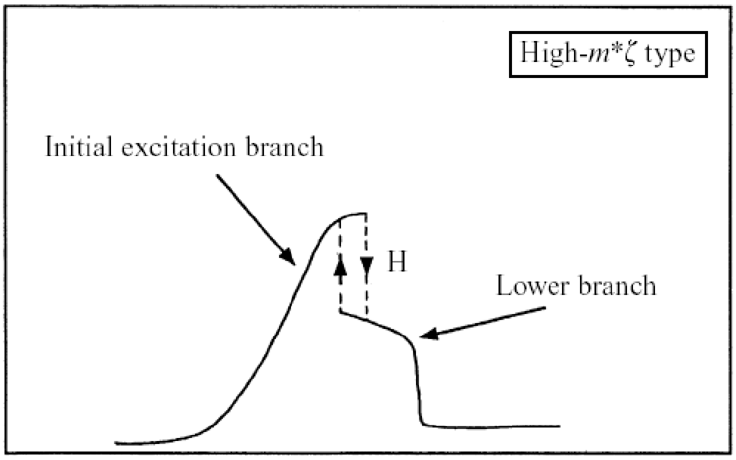

Figure 1.18: Schematic of the large mass-damped response of a freely oscillating cylinder, showing the initial and the lower branch; from Khalak & Williamson (1999).

did Saltara *et al.* (1998), and Pesce & Fujarra (2000), who independently investigated the response of flexible cantilevers.

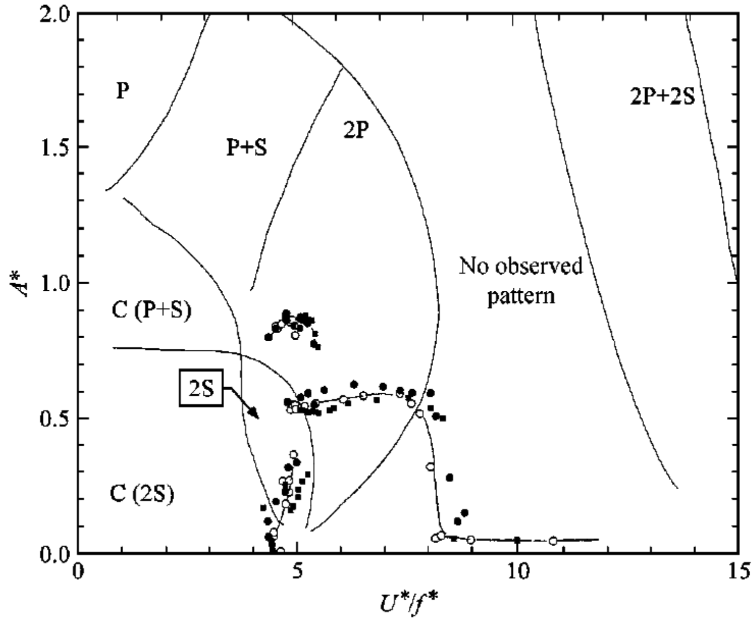

Figure 1.19: Amplitude response for constant $m^*\zeta$, but for different values of m^*, plotted as a function of u^*/f^*. Data: $\bullet, m^* = 2.4$ and $m^*\zeta = 0.014$; $\square, m^* = 10.3$ and $m^*\zeta = 0.017$; $\blacksquare, m^* = 20.6$ and $m^*\zeta = 0.019$; from Khalak & Williamson (1999).

Khalak & Williamson (1999) considered much lower values of mass ratio ($m^* \sim 10$), and mass damping values ($m^* \cdot \zeta \sim 4\%$ of Feng's (1968) value). They found a third branch of oscillation, referred to as an "upper branch" which exhibited much larger amplitude oscillations ($A^*_{max} \sim 1.0$) when compared to Feng's (1968) findings. They also found the extent of reduced velocity over which significant amplitudes were observed varied inversely with m^*. In Khalak & Williamson's (1999) results, the upper branch occurred for low mass ratios, between the initial branch and the lower branch (see figure 1.19). The jump between the initial and upper branch was found to be hysteretic, whereas the jump between the upper branch to the lower branch was found to occur intermittently.

In the author's opinion, the hysteretic jump between the initial and upper branches may contribute to the large scatter found when A^* is plotted against S_g for low mass ratio cylinders. This conclusion is supported by Khalak & Williamson (1999), who found the A^*_{max} values collapsed when plotted against S_g for mass ratios in the range $m^* = 1.2 - 20.6$ for both the upper and lower branch. Their results coincide with previous experimental findings.

Khalak & Williamson's (1999) findings were confirmed and extended by Govardhan & Williamson (2000). Govardhan & Williamson (2000) studied mode transitions for oscillating cylinders of low m^* and $m^* \cdot \zeta$. They split the lift force into a potential force and a vortex force (following Lighthill (1986). In a fashion similar to that described in section 1.2, where,

$$\begin{aligned} F_{vortex} &= -\frac{1}{2}\rho_w \left(\frac{d}{dt}\right) \int (\mathbf{x} \times \boldsymbol{\omega_a}) dV = F_{Total} - F_{Potential}, & (1.29) \\ F_{Potential} &= -C_A \cdot \pi \rho_w D^2 L_c / 4 \cdot \ddot{y}(t), & (1.30) \end{aligned}$$

and L_c is the span of the cylinder; they rewrote the equations of motion in the form,

$$(m + m_A)\ddot{y} + c\dot{y} + ky = F_{Vortex} \sin(\omega t + \phi_{Vortex}), \qquad (1.31)$$

$$m\ddot{y} + c\dot{y} + ky = F_{Total} \sin(\omega t + \phi_{Total}). \qquad (1.32)$$

In equation 1.31, ϕ_{Vortex} represents the phase lag of the vortex component of the force and in equation 1.32, ϕ_{Total} represents the phase lag of the total force, both with respect to the cylinder displacement.

By rewriting equation 1.19, both ϕ_{Total} and ϕ_{Vortex} can be represented by the damping coefficient, and the frequency ratio as:

$$\tan(\phi_{Vortex}) = \left[\frac{2\zeta \cdot f^*_{fluid}}{1 - f^{*2}_{fluid}}\right] \tag{1.33}$$

$$\tan(\phi_{Total}) = \left[\frac{2\zeta \cdot f^*_{vacuum}}{1 - f^{*2}_{vacuum}}\right] \tag{1.34}$$

where $f^*_{vacuum} = f/f_{n_{vacuum}}$ and $f^*_{fluid} = f/f_{n_{fluid}}$; $f_{n_{vacuum}}$ is the natural frequency of the oscillating cylinder in a vacuum, and $f_{n_{fluid}}$ is the natural frequency of the cylinder in the fluid in which it is immersed.

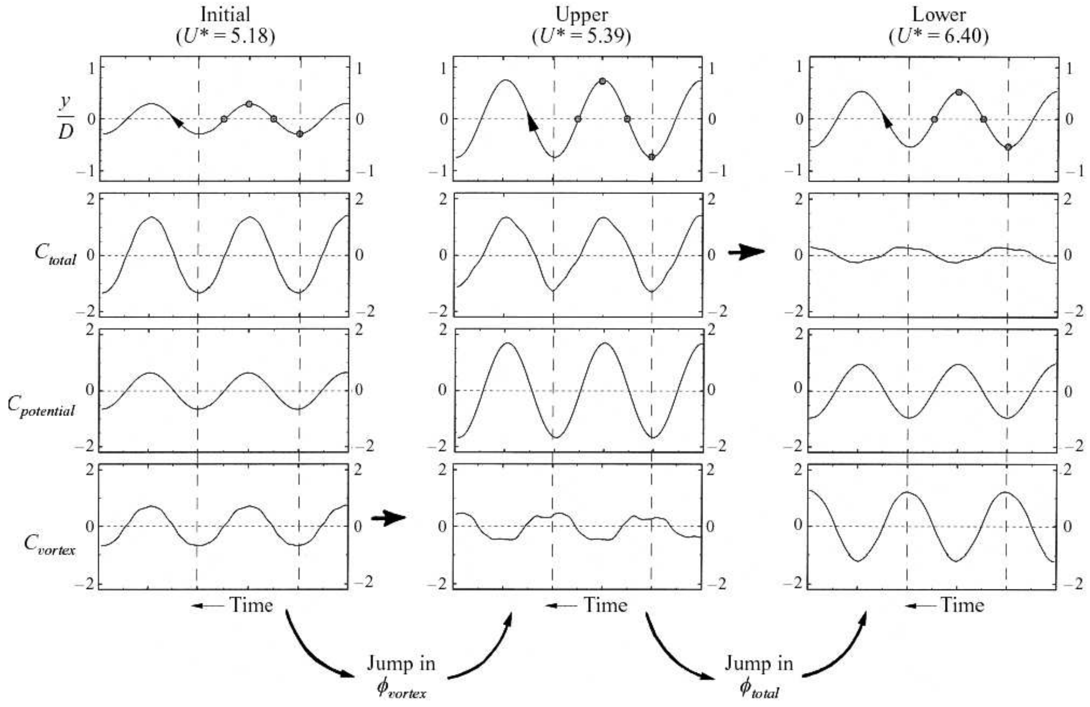

Figure 1.20: Relationship between total transverse force (C_{total}), the potential added mass force ($C_{potential}$), and the vortex force (C_{vortex}) in the initial, upper and lower branches. ($m^* = 8.63, \zeta = 0.00151$); from Govardhan & Williamson (2000).

Govardhan & Williamson (2000) found that the transition from the initial to the upper branch occurred when $f^*_{fluid} \to 1$, and involved a jump in ϕ_{Vortex} from $\phi_{Vortex} \simeq 5^o$ to $\phi_{Vortex} \simeq 175^o$, as predicted from equation 1.33. They further found the transition from the upper to the lower branch occurred as $f^*_{Vacuum} \to 1$, corresponding to a jump in ϕ_{Total} from $\phi_{Total} \simeq 5^o$ to $\phi_{Total} \simeq 175^o$. For large mass ratios $f^*_{vacuum} \to f^*_{fluid}$, and no distinct upper branch was observed, the transition in ϕ_{Total} and ϕ_{vacuum} occurring simultaneously (as shown in figure 1.20).

Govardhan & Williamson (2000) found a good collapse of amplitude data across a wide range of mass ratio $m^* = 1.19 - 8.63$ when plotted against the term $(u^*/f^*_{fluid}) \cdot St$. They concluded from observation of equation 1.25 that, since A^* was independent of m^* in the lower branch when plotted against $(u^*/f^*_{fluid}) \cdot St$, C_{EA} must also be independent of m^* for the lower branch. They also concluded that as f^* was constant for a given m^* in the lower branch; from equation 1.25, C_{EA} must be a constant value. Combining these observations, they found that for a cylinder oscillating in the lower branch, C_{EA} should be the same constant value regardless of cylinder mass ratio. They found this value to be $C_{EA} = -0.54$.

Substituting this into equation 1.24 for the lower branch, they obtained,

$$f^*_{lower} = \sqrt{\frac{m^* + C_A}{m^* - 0.54}} \tag{1.35}$$

From equation 1.35, they conclude that a critical mass ratio exists ($m^*_{crit} = 0.54$), below which the lower branch cannot exist. They confirmed this result by observing oscillations of a cylinder with $m^* = 0.52$ which oscillates in the upper branch up to the highest reduced velocity measured by their experimental setup. Finally they derived two equations which described the extent of u^* over which the lower branch was observed,

$$\begin{aligned} u^*_{start} &\simeq 5.75\sqrt{\frac{m^* + C_A}{m^* - 0.54}}, && (1.36) \\ u^*_{finish} &\simeq 9.25\sqrt{\frac{m^* + C_A}{m^* - 0.54}}. && (1.37) \end{aligned}$$

In light of their findings of a critical mass ratio, Carberry (2003) questioned the validity of the jump between the upper and lower branch being associated with f^*_{fluid}. Clearly, for the case of $m^* \leqslant 0.54$ the cylinder oscillation frequency passes through f^*_{fluid}, and yet no jump between the upper and lower branch is observed, their results are shown in figure 1.21.

Vortex Structures in the Wake of a Freely Oscillating Cylinder

Each branch of oscillation described in the previous subsection is associated with a different vortex pattern in the wake. Khalak & Williamson (1999) associate this with the sharp changes in ϕ_{Total} and ϕ_{Vortex} associated with the jump between oscillation branches. The change in vortex structures coincides with a switch in the timing of the vortex shedding with the body displacement, This was first shown by Zdravkovich (1982). His findings were confirmed by Griffin & Ramberg (1994) who studied the forced

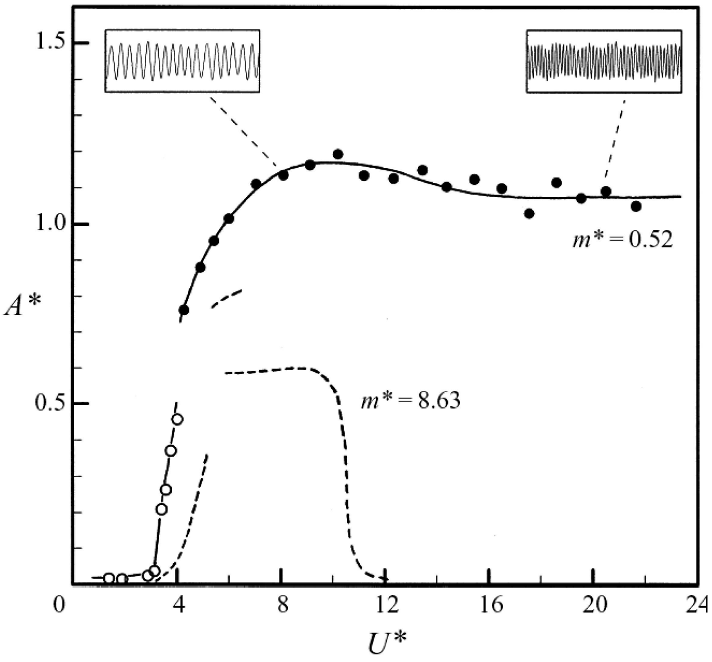

Figure 1.21: Amplitude of oscillation response for a low mass-damped cylinder for two mass ratios; the smaller mass ratio is less than the critical mass ratio found for this Reynolds number range; from Govardhan & Williamson (2000).

oscillation of a cylinder at low amplitudes. Simulations by Meneghini & Bearman (1995) and Lu & Dalton (1996) also agree with this finding.

Griffin & Ramberg (1974) found an asymmetric shedding mode associated with forced in-line oscillations. Here, two positive vortex cores and one negative vortex core were shed over each oscillation cycle. Williamson & Roshko (1988), by studying the forced oscillation of a circular cylinder, found three wake types which they referred to as the 2S, 2P, and P + S modes. The 2S mode corresponded to a single positive vortex and a single negative vortex being shed over each oscillation cycle; the 2P mode corresponded to a pair of negative vortices and a pair of positive vortices being shed per oscillation cycle; and the P+S mode corresponded to the asymmetric wake structure observed by Griffin & Ramberg (1974). Their results have been confirmed by Sheridan *et al.* (1998), and by Brika & Laneville (1993) who were the first to observe both the 2P and 2S modes for the case of a freely oscillating cylinder.

Govardhan & Williamson (2000) found that the initial branch of oscillation corresponds to a 2S mode (see figure 1.22), whereas both the upper branch and the lower

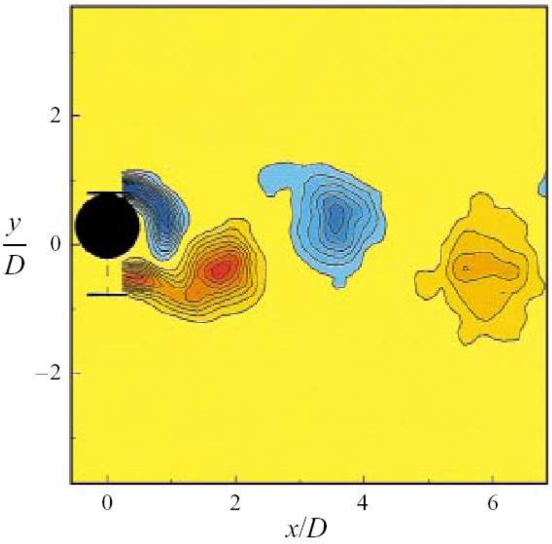

Figure 1.22: Vortex structures in the wake of a low-mass damped hydro-elastically mounted cylinder, for oscillations in the initial branch; the cylinder is at the top of its oscillation cycle. $\omega_z \cdot D/U = \pm 0.4, \pm 0.8, \pm 1.2...$ $u^* = 5.18$, $Re \simeq 3000$; from Govardhan & Williamson (2000).

branch corresponds to the 2P mode (see figure 1.23 and 1.24). For the upper branch, they found that the second vortex in the 2P mode was considerably weaker than its neighbor, and was very quick to dissipate; further downstream, the wake resembled a 2S mode.

To the author's knowledge, the 2P mode has not been observed numerically. Evangelinos & Karniadakis (1999) simulated a freely vibrating cable at $Re = 1000$, and found a transient P + S mode corresponding to the lower branch of oscillation. A study by Blackburn *et al.* (2001) compared two-dimensional and three-dimensional simulations with experimental results for a freely oscillating cylinder. Their two-dimensional study did not find either the 2P or P+S wake modes for any of the modes of oscillation. However, their amplitude response, while significantly lower than A^*_{max} found either experimentally or by the three-dimensional simulations, did find an initial, lower and upper branch. By taking the span-wise average of the span-wise vorticity of their three-dimensional simulations, they found a vortex pattern which resembles the 2P mode for the lower branch of oscillations, as shown in figure 1.25.

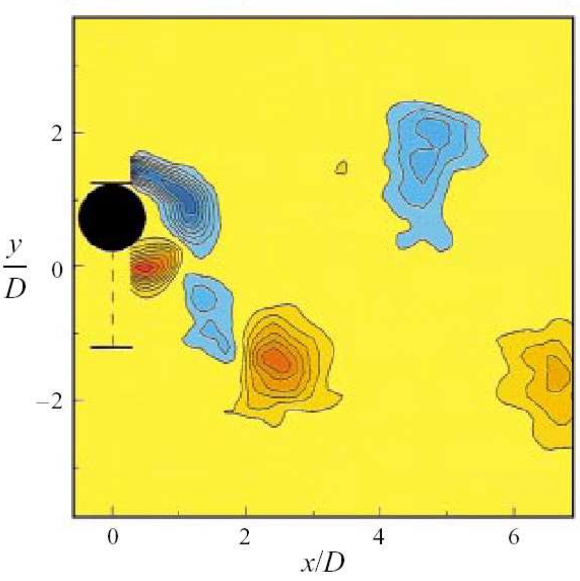

Figure 1.23: Vortex structures in the wake of a low-mass damped hydro-elastically mounted cylinder, for oscillations in the upper branch, showing the 2P mode of shedding; the cylinder is at the top of its oscillation cycle. $\omega_z \cdot D/U = \pm 0.4, \pm 0.8, \pm 1.2...$ $u^* = 5.39$, $Re \simeq 3100$; from Govardhan & Williamson (2000).

The Effect of Reynolds Number

As discussed in the previous subsection, two-dimensional numerical simulations have not managed to capture a 2P mode of shedding. Numerical simulations have also consistently found lower A^*_{max} values when compared to experimental results. This is most likely due to the limited Reynolds number range which numerical algorithms can accurately simulate the flow field. To the author's knowledge, all direct numerical simulations conducted to date have considered $Re \leqslant 1000$. Most experiments have considered a higher Reynolds number range, for example Govardhan & Williamson (2000) considered $Re \sim [1000, 10000]$, as did Khalak & Williamson (1999).

Anagnostopoulos & Bearman (1992) experimentally investigated the case of a freely oscillating cylinder at low Reynolds number ($Re = 90 - 150$); in this range, from section 1.3.1, the flow is laminar. They found, for $m^* = 150$ and $m^*\zeta = [0.18, 0.228]$, a maximum oscillation amplitude of $A^* \simeq 0.6$. This value occurred very close to the lower limit of the lock-in region. A slight variation in the amplitude is noted in comparing the case of an increasing u^* to a decreasing u^*, indicating a possible hysteresis between

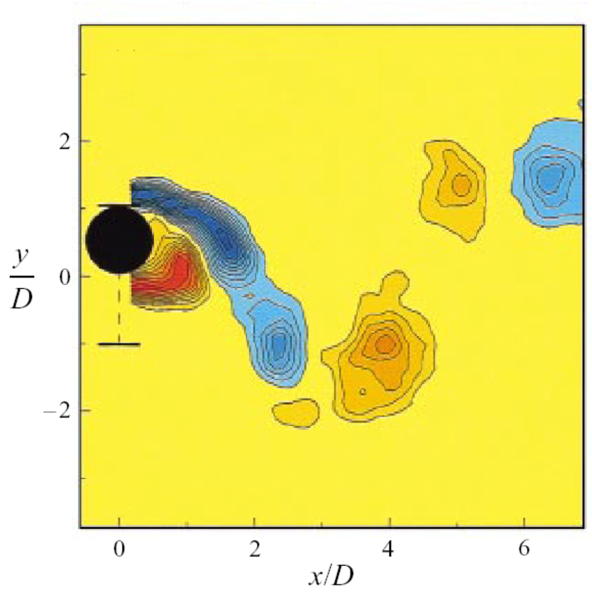

Figure 1.24: Vortex structures in the wake of a low-mass damped hydro-elastically mounted cylinder, for oscillations in the lower branch, showing the 2P mode of shedding; the cylinder is at the top of its oscillation cycle. $\omega_z{\cdot}D/U = \pm 0.4, \pm 0.8, \pm 1.2...$ $u^* = 6.40$, $Re \simeq 3700$; from Govardhan & Williamson (2000).

the initial and lower branch similar to that reported by Feng (1968) and many others. Finite element simulations performed by Anagnostopoulos (1989) at $Re = 106$ and 115 were in good agreement with Anagnostopoulos & Bearman's (1992) experimental findings. All vortex structures observed in the wake of the oscillating cylinder in the numerical simulations were 2S in nature.

Shiels (1998) and Shiels *et al.* (2001) considered the flow past a freely oscillating cylinder at the limiting case of $\zeta = 0$ and with $k \to 0$ and $m \to 0$, at a Reynolds number of 100. Their results agreed qualitatively with Anagnostopoulos & Bearman's (1992) experimental findings, despite the significant difference in mass ratio values investigated. Govardhan & Williamson (2003) re-interpreted Shiels *et al.* (2001) data to find a critical mass ratio, $m^*_{crit} = 0.25$, below which appreciable oscillations were observed for $u^* = \infty$. This value was compared to the experimental finding of $m^*_{crit} = 0.54$ at higher Reynolds number.

To the author's knowledge no systematic investigation has taken place which investigates the effect of Reynolds number on the critical mass ratio, or indeed if such a

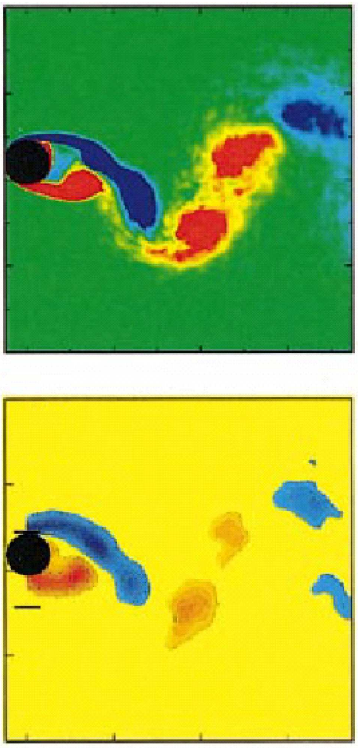

Figure 1.25: Phase and span-wise average contours of span-wise vorticity for a cylinder oscillating in the lower branch, (top), numerical simulations; (bottom), experimental results; from Blackburn *et al.* (2001).

critical mass ratio exists for all Reynolds numbers.

The Effect of Zero Damping and Zero Spring Constant

Shiels (1998) and Shiels *et al.* (2001) both considered the case of a freely oscillating cylinder with no mechanical damping. From equation 1.33 and equation 1.34, this restricts the phase lag ϕ_{Total} and ϕ_{Vortex} to 180^o for finite amplitudes of oscillation, or 0^o for no oscillation. From Govardhan & Williamson's (2000) findings, oscillations are therefore restricted to the lower branch of oscillation near the resonance condition, as no phase jump can occur. However, relatively high amplitude oscillations, reminiscent of the upper branch, were found by Govardhan & Williamson (2003) when re-interpreting Shiels *et al.*'s (2001) data, and from this data they determined a critical mass ratio (as discussed in the previous subsection). Therefore, the dramatic change in amplitude noted as $m^* < m^*_{crit}$ is not necessarily associated with a jump in the phase lag angle.

Govardhan & Williamson (2003) extended the findings of Govardhan & Williamson (2000) by determining the response of a elastically-mounted cylinder at an infinite reduced velocity. They obtained an infinite reduced velocity by setting the mechanical spring constant, k, to zero. This allowed for $u^* = \infty$ through,

$$k = 0; \quad f_n = \sqrt{\frac{k}{m}} = 0; \quad u^* = \frac{u}{f_n D} = \infty. \tag{1.38}$$

They found a jump in A^* as a function of m^*, such that large peak-to-peak oscillations were observed for all mass ratios $m^* < 0.54$ (as shown in figure 1.26). They used this result to support their hypothesis that large peak to peak oscillations (corresponding in Govardhan & Williamson (2000) to the upper branch) continue up to and including $u^* = \infty$ for $m^* < m^*_{crit}$.

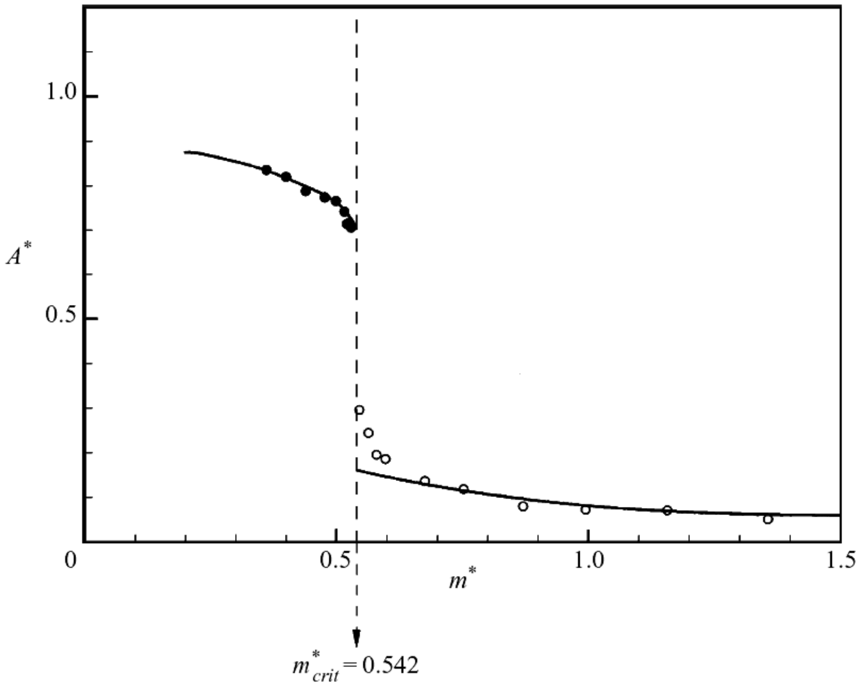

Figure 1.26: Amplitude response (A^*) of a hydro-elastically mounted cylinder at $u^* = \infty$, as a function of mass ratio; from Govardhan & Williamson (2003).

It would appear from casual observation that this result corresponds to the upper branch discussed in Govardhan & Williamson (2000). However, by rewriting the equation of motion (equation 1.16) with a zero spring constant, the author has concluded that a jump in ϕ_{Total} (associated with the transition from the upper branch to the lower branch) is not possible at an infinite reduced velocity. This conclusion is drawn from the following 'Amplitude' equation:

$$A^* = \frac{-\hat{C}_Y \cos(\phi_{Total}) u^{*2}}{2\pi^3 m^*}. \tag{1.39}$$

For a finite amplitude, the $\cos(\phi_{Total})$ must be negative, and therefore $\phi_{Total} = [90^0, 180^0]$ for finite A^*. As $\phi_{Total} \rightarrow 0^o$ in the upper branch (Govardhan & Williamson (2000)), the upper branch cannot be reached for an infinite reduced velocity.

This conclusion was confirmed in private communication with Govardhan and Williamson. Govardhan concluded that the large peak to peak oscillations observed in Govardhan & Williamson (2003) corresponded to large peak to peak oscillations within the lower branch. This was also observed in Govardhan & Williamson (2000) when f^*_{Vacuum} is marginally greater than 1.

In conclusion, both the initial branch and the upper branch (as described by Govardhan & Williamson (2000) can only exist with a finite spring stiffness and mechanical damping. However, when k and/or c are set to zero a critical mass ratio below which large amplitude oscillations are observed, has been confirmed to exist for the Reynolds number range, $Re \sim [1000, 10000]$ and $Re = 100$.

1.6.3 Combined In-Line and Transverse Oscillations

Two distinct areas of research have involved cylinders with oscillation components in both the in-line and transverse directions.

The first area restricts the cylinder to oscillate at an angle α inclined to the free stream. Ongoren & Rockwell (1988) investigated the forced oscillation of a cylinder at an angle to the free-stream. They found that phase locking between the cylinder oscillations and the cylinder wake was possible for all oscillation angles investigated ($\alpha = [0^o, 90^o]$). Kocabiyik (2003) numerically investigated the case of a freely oscillating cylinder oscillating at an angle to the free-stream. She found a net positive lift for all positive angles of attack.

The second area of research allows the cylinder to freely oscillate with components in the in-line and transverse directions. Moe & Wu (1990) studied this case, however, due to their experimental setup, the in-line mass ratio was different to the transverse mass ratio. The experimental setup also gave distinct in-line and transverse natural frequencies. They found a broad range of reduced velocity over which large peak to peak oscillations were observed. However, they did not find any evidence of the distinct branches of oscillation discussed previously. Sarpkaya (1995), using a similar experimental setup, found that the response of a cylinder allowed to oscillate with components in both the in-line and transverse directions could, in certain circumstances, behave substantially differently to the freely oscillating cylinder, restricted to transverse oscillations discussed earlier.

Jauvtis & Williamson (2002) and Jauvtis & Williamson (2003) investigated the case of a cylinder allowed to freely oscillate in both the in-line and transverse directions, where the mass ratio and natural frequency was the same in both the in-line and transverse directions. They investigated the mass ratio range, $m^* = [5, 25]$ and the reduced velocity range, $u^* = [2, 12]$. For $u^* \gtrsim 5$, they found remarkably little difference in the results between their experimental setup and the transverse oscillating cylinder discussed in the previous section. For low reduced velocities the cylinder oscillated similarly to that described by King (1974) for the case of a cylinder oscillating in-line with the flow field.

1.6.4 Tethered Bodies

As an extension to the case of the flow-induced vibration of a hydro-elastically mounted cylinder in a uniform flow field, a study has been performed on the flow-induced vibration of a buoyant tethered cylinder. This system geometry has practical applications in submerged pipelines, ocean spars, and tethered lighter-than-air craft. It is also of interest as it exhibits flow-induced oscillation where the combined effects of in-line oscillation and transverse oscillation may be observed. Finally, both numerically and analytically, the tethered cylinder provides a simplification to the fully three-dimensional problem of a tethered sphere, which has been the subject of recent investigation (Govardhan & Williamson (1997), Williamson & Govardhan (1997), Jauvtis *et al.* (2001)).

For the case of a tethered body, for large tether lengths, the natural frequency may be related to the tension in the tether through the equation,

$$f_N = \frac{1}{2\pi}\sqrt{\frac{T}{m}} \tag{1.40}$$

where T is the tension force acting through the tether. The mean tension force may be related to the fluid forces acting on the body through the equation,

$$\overline{T} = \sqrt{\overline{F}_D^2 + (\overline{F}_L + B)^2 + \overline{F}_S^2}, \tag{1.41}$$

where B is the buoyancy force acting on the body, and $\overline{F}_S$ is the mean side force acting on the body.

The reduced velocity defined earlier is now implicitly a function of the fluid forces acting on the body, and in general is equal to,

$$u^* = \frac{8\pi\sqrt{\mathcal{V}_{\mathcal{S}} \cdot D(m^*+1) \cdot L^*}}{D \cdot \mathcal{A}_{\mathcal{S}} \cdot \sqrt{\overline{C}_D^2 + \overline{C}_S^2 + \left(\overline{C}_L + (1-m^*) \cdot \frac{g\mathcal{V}_{\mathcal{S}}}{1/2 \cdot U_\infty^2 \mathcal{A}_{\mathcal{S}}}\right)^2}}, \qquad (1.42)$$

where $\mathcal{V}$ is the volume of the body, $\mathcal{A}$ is the cross-sectional area normal to the flow field, D is the characteristic length of the body (corresponding to the diameter for the case of a tethered cylinder or sphere), and $L^* = L/D$ is the normalized tether length. The term, $g\mathcal{V}_{\mathcal{S}}/(1/2U_\infty^2\mathcal{A}_{\mathcal{S}})$, is effectively the reciprocal of the Froude number squared, where the Froude number is defined as $Fr = U_\infty/\sqrt{g \cdot D}$.

Most previous work regarding tethered bodies has focused on the free surface interaction with tethered buoys (Harlemann & Shapiro (1961), Shi-Igai & Kono (1969), and Ogihara (1988)). In each of these studies the tethered bodies oscillate due to the combined effect of a uniform (or sheared) free stream and free surface wave effects. This combination, incorporating the interaction of a free surface, has made interpretation of results complex and conclusions difficult to draw.

The Tethered Sphere in a Uniform Flow-Field

The related work of Williamson & Govardhan (1997), Govardhan & Williamson (1997), and Jauvtis *et al.* (2001) deal purely with the action of a tethered sphere in a uniform flow. In these investigations, the definition of the reduced velocity was simplified by neglecting the mean force coefficients in equation 1.42, giving the equation,

$$u^*_{GW} = \left(\frac{1}{2\pi}\right) \cdot \frac{1}{Fr^2}\sqrt{\frac{1-m^*}{(m^*+C_A)L^*}}, \qquad (1.43)$$

This simplification was justified by assuming a maximum Froude number in the order 0.45 in any practical application; however this simplification does limit the applicability of their findings.

Williamson & Govardhan (1997) studied two positively buoyant spheres with $m^* = 0.73$ and $m^* = 0.082$, in the Reynolds number range $Re = [500, 14000]$ for three tether lengths, $L^* = 3.8, 8.9$ and 9.3.

When plotted against u^*_{GW}, their amplitude data collapsed independently of mass ratio and tether length (see figure 1.27). Two local peaks in the amplitude of transverse

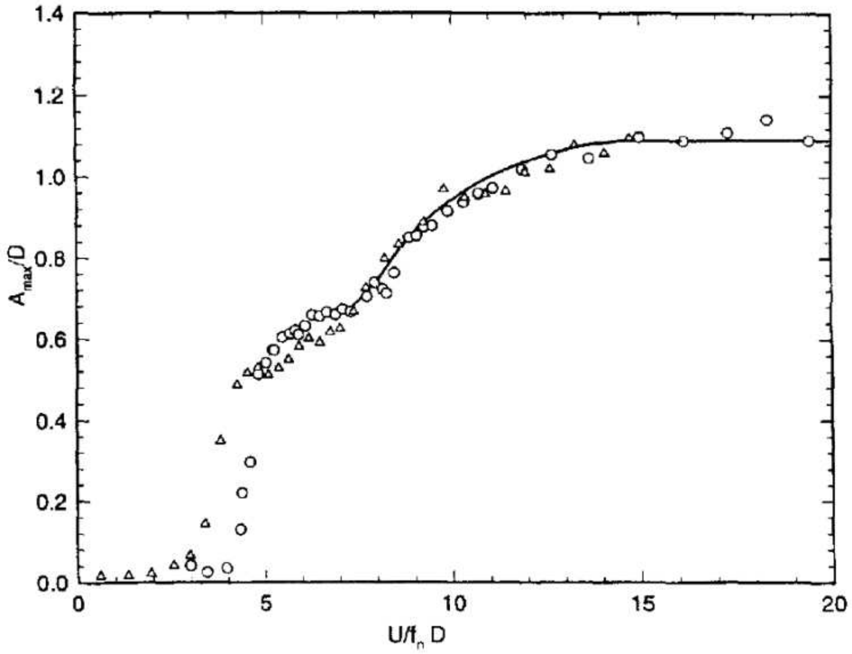

Figure 1.27: Tethered sphere results; A_Y^* as a function of reduced velocity for the case of $\triangle$, $m^* = 0.26$; and $\circ$, $m^* = 0.76$; from Govardhan & Williamson (1997).

oscillation were observed. The first, at $u^* \simeq 5$, had an amplitude $A_Y^* = 0.4$. Williamson & Govardhan (1997) hypothesize that this local maximum was due to a lock-in effect as the frequency of oscillation approached the shedding frequency of a fixed sphere (see the results of Sakamoto & Haniu (1990) for fixed sphere data).

A second mode was found for $u^* \gtrsim 10$ with considerably larger amplitudes ($A_Y^* = 0.8$). For both modes, the same amplitude was noted regardless of tether length. However, the maximum transverse oscillation amplitude varied inversely with mass ratio, the sphere with $m^* = 0.082$ only exhibiting maximum amplitudes of $A_Y^* = 0.6$ in the second mode. Govardhan & Williamson (1997) found that despite the variation in the transverse amplitude, the maximum amplitude in the direction of oscillation was $A_{max}^* \simeq 1.1$ regardless of either the sphere mass ratio or tether length.

Williamson & Govardhan (1997) found that the mean drag measured was considerably higher for all Reynolds numbers investigated when compared to that measured for a fixed sphere.

Jauvtis *et al.* (2001) extended the findings of Govardhan & Williamson (1997) and Williamson & Govardhan (1997) by investigating a tethered sphere with mass ratios

$m^* = [0.1, 1000]$ and reduced velocities $u^*_{GW} = [0, 300]$. They characterized mode one and mode two as analogous to the 2S and 2P modes discussed in the case of a freely oscillating cylinder (see section 1.6.2). They found two further modes of oscillation: mode three, which existed in the reduced velocity range $u^*_{GW} \simeq [20, 40]$ and which exhibited extremely sinusoidal oscillations; and a fourth mode which existed for all reduced velocities investigated above $u^*_{GW} \gtrsim 100$. The fourth mode was characterized by intermittent bursts of high amplitude oscillations.

Pregnalato (2003) and Pregnalato *et al.* (2003a,b) numerically investigated the case of a tethered sphere for the much lower Reynolds number range, $Re = [200, 500]$. In these investigations, the first mode of oscillation was not found. The numerical results compared well with experiments performed in the same Reynolds number range (see Pregnalato (2003)).

The Tethered Cylinder in a Uniform Flow-Field

Apart from the work reported by the author in collaboration with colleagues at Monash University and the work discussed herein, almost no studies have been conducted for the case of the tethered cylinder. The only work found was by Meier-Windhorst (1939) (see Khalak & Williamson (1999)) who investigated the case of a tethered cylinder using a water table. The cylinder had a very small span/diameter aspect ratio, $AR = 1.8$. Due to the experimental setup, the buoyancy force discussed earlier was exactly equal to zero. They found the existence of an initial, upper and lower branch for tethered cylinders with sufficiently small damping.

1.6.5 Scope of Second Investigation

For the case of a low mass-damped cylinder, free to oscillate transverse to the free-stream, Govardhan & Williamson (2000) found a critical mass ratio, and in Govardhan & Williamson (2003), they expanded their findings to include the numerical results of Shiels *et al.* (2001), performed at a much lower Reynolds number. No systematic investigation has taken place which investigates the effect of Reynolds number (and especially low Reynolds numbers) on the amplitude response of a freely oscillating cylinder. Therefore, an initial investigation is made of the amplitude response of a positively buoyant cylinder restricted to oscillate transverse to the flow field at an infinite reduced velocity (with spring constant and damping coefficient set to zero) both as a function of mass ratio and Reynolds number. The mass ratio range investigated was $m^* = [0.075, 0.7]$ and the Reynolds number range investigated was $Re = [30, 300]$. All simulations used the two-dimensional spectral-element method. A major aim was of the determination of a critical mass ratio m^*_{crit}, as described by Govardhan & Williamson (2000), as a function of Reynolds number. Also of interest was the peak amplitude response and the frequency characteristics of the oscillating cylinder system.

Despite practical applications existing for the tethered cylinder (the most recent example found being the PELAMIS 750 kilowatt power generation system, which harnesses ocean wave energy, see Knott (2003)), to the author's knowledge, there is almost no research in existence which quantifies the amplitude response of a tethered cylinder system. The second component of this study investigates the flow around a positively buoyant, tethered cylinder system. Once again the simulations used a two-dimensional spectral-element method which restricted the Reynolds number to less than or equal to 200. All simulations were conducted at $Re = 200$. Initially a constant mass ratio and tether length were investigated as a function of changing flow inlet conditions. Subsequently the mass ratio and tether length were independently changed in order to investigate the effect of both these parameters. The results are compared with the experimental findings conducted by Josie Carberry. The experimental and numerical findings have qualitatively good agreement.

Chapter 2

Numerical and Experimental Methods

The numerical component of this project comprises two distinct investigations. The three-dimensional growth of flow field structures in the wake of a blunt flat plate, and the flow induced motion of a circular cylinder. The second component of this project is further subdivided into the flow around a hydro-elastically mounted cylinder and a tethered cylinder. Both components utilize a Galerkin spectral-element method to discretize the spatial domain in two dimensions. The Galerkin spectral-element method is a well known, high-order technique, and has been described by several researchers (for example see Karniadakis & Henderson (1998) and references therein).

Section 2.1 discusses techniques used for the temporal advancement of the governing equations. Section 2.3 presents the Floquet stability technique to analyze the stability of the flow in the wake of blunt flat plates. Section 2.4 discusses both the equations of motion and the predictor-corrector technique required for simulating the flow-induced vibration of circular cylinders. Validation of each aspect of the code, along with grid independence studies are presented in section 2.5.

2.1 Numerical Method: 2D Flow Fields

The equations governing the fluid flow are the incompressible form of the Navier-Stokes equations. These are comprised of the momentum and continuity equations, which in non-dimensional form are:

$$\frac{\partial \mathbf{u}}{\partial t} = -\nabla p + \frac{1}{Re}\boldsymbol{L}(\mathbf{u}) + \boldsymbol{N}(\mathbf{u}), \qquad (2.1)$$

$$\nabla \cdot \mathbf{u} = 0, \qquad (2.2)$$

where $\mathbf{u} = \mathbf{u}(\mathbf{x}, \mathbf{y}, \mathbf{t}) = (u, v)$ is the normalized velocity field, p is the normalized kinematic pressure field, Re is the Reynolds number, $\boldsymbol{N}(\mathbf{u})$ is the non-linear advection term defined as:

$$\boldsymbol{N}(\mathbf{u}) = -(\mathbf{u} \cdot \nabla)\mathbf{u} \tag{2.3}$$

and $\boldsymbol{L}(\mathbf{u})$ is the linear diffusion term defined as:

$$\boldsymbol{L}(\mathbf{u}) = \nabla^2 \mathbf{u} \tag{2.4}$$

The techniques used for solving the above form of the Navier-Stokes equations are addressed in the following sections. The spatial derivatives are evaluated using spectral-element discretizations. Temporal derivatives are evaluated using a classical three step splitting scheme. The basic code was developed largely by Mark C. Thompson and Kerry Hourigan (Both at the Department of Mechanical Engineering, Monash University), and has been validated extensively for several geometric configurations (see for example: Thompson *et al.* (1996), Pregnalato (2003) and Tan (2001)).

2.1.1 Time-advancement of the Governing Equations

Many techniques exist for integrating the Navier-Stokes equations forward in time (for examples see Karniadakis *et al.* (1991) and references cited therein). In general, these techniques inherently contain splitting errors which result in divergence errors to propagate at the domain boundaries (Karniadakis *et al.* (1991)). Splitting errors lead to temporal inaccuracy in the zeroth order pressure. This also manifests as a divergence error of the pressure field at the domain boundaries. Typically, temporal error is proportional to $1/Re$.

The time-splitting algorithm employed in this thesis uses a pressure boundary condition reducing the divergence error at the boundaries to $O(\delta t/Re)^J$, where J is the order of the time-integration employed, the scheme was developed by Karniadakis *et al.* (1991). They demonstrated that the time-splitting algorithm produced time-splitting errors in the velocity, one order smaller in δt than in the divergence error. The scheme divides the coupled Navier-Stokes equations (equations 2.1 and 2.2) into three separately solvable sub-steps for the pressure and velocity terms. Each sub-step is solved using a mixture of high-order implicit and explicit techniques.

The first of the three sub-steps (the non-linear convective step) solves an intermediate velocity field $\hat{\mathbf{u}}$ as follows. For the first iteration through the time integration loop

$\hat{\mathbf{u}}$ is solved using an explicit third order Adams-Bashforth technique:

$$\frac{\hat{\mathbf{u}} - \mathbf{u}^{(n)}}{\Delta t} = \sum_{q=0}^{J-1} \alpha_q \boldsymbol{N}(\mathbf{u}^{(n-q)}), \tag{2.5}$$

subsequent sub-step iterations are performed explicitly using a third-order Adams-Moulton technique:

$$\frac{\hat{\mathbf{u}} - \mathbf{u}^{(n)}}{\Delta t} = \sum_{q=0}^{J-1} \beta_q \boldsymbol{N}(\mathbf{u}^{(n+1-q)}). \tag{2.6}$$

The parameters α_q and β_q are the Adams-Bashforth and Adams-Moulton coefficients, the values of which are presented in table 2.1 (see Chapra & Canale (1998) and Gerrard (1978) for further details). The value of $\mathbf{u}^{(n+1)}$ is an approximation from the previous iterate.

J	α_0	α_1	α_2	β_0	β_1	β_2
1	1					
2	3/2	-1/2		1/2	1/2	
3	23/12	-16/12	5/12	5/12	8/12	-1/12

Table 2.1: Values for the Adams-Bashforth and Adams-Moulton coefficients

In general, the update equation is applied to the entire domain, including the boundary nodes (see Canuto *et al.* (1988)). No boundary conditions are imposed in this sub-step, with the direct consequence that $\hat{\mathbf{u}}$ is not forced to a prescribed value at the boundaries.

The second sub-step is the pressure correction step which is written as:

$$\frac{\hat{\hat{\mathbf{u}}} - \hat{\mathbf{u}}}{\Delta t} = -\nabla \overline{p}^{n+1}, \tag{2.7}$$

where $\hat{\hat{\mathbf{u}}}$ is the second intermediate velocity field and $\overline{p}$ is related to the pressure term in equation 2.1 by (see Karniadakis *et al.* (1991)):

$$\int_{t_n}^{t_{n+1}} \nabla p dt = \Delta t \nabla \overline{p}^{n+1}. \tag{2.8}$$

A Poisson equation for the pressure term is obtained by taking the divergence of equation 2.7 and forcing the second intermediate velocity $\hat{\hat{\mathbf{u}}}$ to satisfy the incompressibility condition (equation 2.2) to form:

$$\nabla^2 \overline{p}^{n+1} = \frac{1}{\Delta t} \cdot \nabla \hat{\mathbf{u}}. \tag{2.9}$$

This requires that the pressure boundary condition for this sub-step be chosen to ensure continuity is satisfied at the boundaries. Karniadakis *et al.* (1991) suggested the following Neumann pressure boundary condition be imposed for this sub-step:

$$\frac{\partial \overline{p}^{(n+1)}}{\partial n} = \mathbf{n}\dot{\sum}_{q=0}^{J-1}\beta_q \left[\boldsymbol{N}(\mathbf{u}^{n-q}) - \frac{1}{Re}\nabla \times \nabla \times \mathbf{u}^{n-q}\right] \text{on } \Gamma, \tag{2.10}$$

where $\mathbf{n}$ is the unit normal vector to the boundary surface Γ. This formulation proposed by Karniadakis *et al.* (1991) uses the flow field from the previous time steps to form a condition for the normal pressure gradient at the boundary. Karniadakis *et al.* (1991) showed that the order of the time-advancement scheme can only be one order above the order of extrapolation used to find the pressure boundary condition. As the scheme requires at least first order accurate boundary conditions for the pressure field, this gives second order accurate boundary conditions for the velocity fields. Higher order boundary conditions can be used for the pressure field, however this reduces stability.

The third sub-step is the diffusion step and is written as:

$$\frac{\mathbf{u}^{n+1} - \hat{\hat{\mathbf{u}}}}{\Delta t} = \frac{1}{Re}L(\mathbf{u}), \tag{2.11}$$

which is solved implicitly using a second order Crank-Nicholson technique, combined with a theta scheme modification. This results in a Helmholtz equation which is solved by inverting the equation matrix. Boundary conditions are imposed on the final velocity field, $\mathbf{u}^{n+1}$ in this sub-step, ensuring that the velocity boundary condition is satisfied at the end of this time step and at the start of the next. Also, since $\hat{\hat{\mathbf{u}}}$ is divergence free, $\mathbf{u}^{n+1}$ remains divergence free (provided that $\mathbf{u}^{n}$ is divergence free).

The above scheme has been shown by Karniadakis *et al.* (1991) to produce time-differencing errors in the velocity field one order smaller in Δt than the corresponding boundary divergence error. The numerical scheme used in this study uses a first-order pressure boundary condition results in an overall second order time-accurate scheme.

2.2 Three-dimensional Method

In chapter 3 a fully three dimensional simulation was performed to verify the flow structures determined using the Floquet technique. The three-dimensional simulations were undertaken using a Fourier/spectral-element code documented and validated in Thompson *et al.* (2001a) and Thompson *et al.* (1996).

The three-dimensional method extends the two-dimensional spectral element method by using a global Fourier spectral discretization in the third dimension. This approach has been employed previously for the case of the flow past a circular cylinder by Karniadakis & Trintafyllou (1992) and Thompson *et al.* (1996). The global spectral approach has the advantage of spectral convergence, however the boundary conditions in the span-wise direction are restricted to be periodic.

The spatial discretization consists of f equi-spaced planes in the span-wise direction, each consisting of an identical spectral-element mesh. The flow variables are transformed into Fourier space in the span-wise direction for each node on the spectral element mesh using a fast Fourier transform. This decouples the problem into a set of F Fourier modes which are then solved independently for the linear operators.

2.3 Floquet Analysis

The first part of the project analyzes the linear stability of the two-dimensional von Karman vortex street in the wake of blunt flat plates to minute disturbances. The growth of these disturbances along the cylinder span indicates a transition to a three-dimensional wake. In order to do this, a Floquet method is employed. In general, Floquet theory is used to analyze the linear stability of a periodic solution. The general development of Floquet theory is described in several texts (for example Iooss & Joseph (1990)), and we will restrict ourselves to the case of the stability of the periodic solution in the wake of bluff bodies given by the two-dimensional Navier-Stokes equations (referred to herein as the base flow field).

Two variables determine the stability of the solution, these are the Reynolds number and span-wise wavelength (λ). The same spectral-element code used to calculate the two-dimensional base flow field was extended to include the Floquet stability analysis technique.

The velocity components and the kinematic pressure are expanded as the base field plus a perturbation:

$$u(t,x,y,z) = \overline{u}(t,x,y) + u'(t,x,y)\sin(2\pi z/\lambda), \tag{2.12}$$

$$v(t,x,y,z) = \overline{v}(t,x,y) + v'(t,x,y)\sin(2\pi z/\lambda), \tag{2.13}$$

$$w(t,x,y,z) = w'(t,x,y)\cos(2\pi z/\lambda), \tag{2.14}$$

$$p(t,x,y,z) = \overline{p}(t,x,y) + p'(t,x,y)\sin(2\pi z/\lambda). \tag{2.15}$$

The chosen sinusoidal z (spanwise) variation of the perturbation fields is appropriate to satisfy the linearised (and constant coefficient with respect to z) time-dependent three-dimensional Navier-Stokes equations for the perturbation fields exactly. Alternatively, complex forms for the z variation could be incorporated into the expansions which would automatically determine the phase information, however, this is only of consequence if the Floquet multiplier is complex at transition (such as for Mode S for the square cylinder). These cases can be detected since the real Floquet multiplier will be oscillatory. However further analysis would require the complex form of the Floquet multiplier (see Blackburn & Lopez (2003)).

The equations for the time evolution of the perturbation fields is given by linearizing the full three-dimensional Navier-Stokes equations

$$\frac{\partial u'}{\partial t} + (\overline{\mathbf{u}} \cdot \boldsymbol{\nabla}_{xy})u' + (\mathbf{u}' \cdot \boldsymbol{\nabla}_{xy})\overline{u} = -\frac{\partial p'}{\partial x} + \nu(\nabla^2_{xy}u' - (\frac{2\pi}{\lambda})^2 u'), \tag{2.16}$$

$$\frac{\partial v'}{\partial t} + (\overline{\mathbf{u}} \cdot \boldsymbol{\nabla}_{xy})v' + (\mathbf{u}' \cdot \boldsymbol{\nabla}_{xy})\overline{v} = -\frac{\partial p'}{\partial y} + \nu(\nabla^2_{xy}v' - (\frac{2\pi}{\lambda})^2 v'), \tag{2.17}$$

$$\frac{\partial w'}{\partial t} + (\overline{\mathbf{u}} \cdot \boldsymbol{\nabla}_{xy})w' = -\frac{\partial p'}{\partial z} + \nu(\nabla^2_{xy}w' - (\frac{2\pi}{\lambda})^2 w'), \tag{2.18}$$

$$\frac{\partial u'}{\partial x} + \frac{\partial v'}{\partial y} + \frac{\partial w'}{\partial z} = 0. \tag{2.19}$$

According to Floquet theory, the velocity and pressure perturbations satisfy the relationship:

$$r'(t+T, x, y) = \exp(\sigma T) r'(t, x, y), \tag{2.20}$$

where r' represents any of the perturbation fields (u', v', w' or p'). That is, the perturbations grow or decay exponentially from period to period. The coefficient $\exp(\sigma T)$ is often grouped to form the parameter μ (the Floquet multiplier). If the Floquet multiplier is greater than unity, a perturbation at that wavelength will be exponentially amplified and hence result in three-dimensional flow. In reality there are an infinite number of different modes with different Floquet multipliers, but the mode(s) of most interest is that/those corresponding to the largest Floquet multiplier, since it is that mode that grows fastest or decays slowest and hence will dominate. The Reynolds number corresponding to $\mu = 1$ is said to be the critical Reynolds number of inception (Re_{crit}). In experiments, this is the lowest Reynolds number above which the instability will be observed provided the Reynolds number is increased from below. (The three-dimensionality may be maintained below this critical Reynolds number if it is decreases from above if the transition is hysteretic, as it is for Mode A in the wake of a circular cylinder (Williamson (1988b))).

Initially the perturbation fields, r' are randomized and the perturbation equations are stepped forward in time using the same temporal technique described in sections 2.1.1. The perturbation fields are re-normalized at the end of each base flow period. After many cycles only the dominant Floquet mode remains. At this point, the ratio of the mode amplitude to the amplitude exactly one period prior is equal to the Floquet multiplier for the dominant mode. (Here the amplitude is measured by the L_2 norm of any of the velocity perturbations). The number of integration periods required depends on the ratio of the Floquet multipliers of the two most dominant modes. At the end of each period the amplitude of the dominant Floquet mode relative to all others increases by at least this factor. Typically, in the simulations reported in this paper, 30–100 base flow periods were required to obtain results accurate to at least three significant figures.

In the computational code, both the base flow and the perturbation field are simultaneously integrated forward in time. This is slightly inefficient, since the base flow can be calculated independently and a Fourier time decomposition used to supply the base flow fields to the linearized perturbation equations (Barkley & Henderson (1996)). However, it has the advantage of examining the pseudo-stability of non-periodic base flows. In addition, it has been implemented for a parallel computer cluster so that the base flow is calculated on one node and the Floquet modes corresponding different wavelengths are simultaneously calculated on many other nodes, thus the inefficiency is reduced considerably.

2.4 Methodology of Moving Body Simulations

2.4.1 Equations Governing the Motion of a Freely Oscillating Cylinder

For the case of the freely oscillating cylinder, the motion of the cylinder is restricted to move in a direction transverse to the flow field.

Given these restrictions, the only force acting on the cylinder is the lift force (F_L). The equations of motion have been determined by writing Newton's second law of motion, relating the instantaneous acceleration of the cylinder to the forces acting on the cylinder:

$$m\ddot{y} + c\dot{y} + ky = F_L \tag{2.21}$$

The following non-dimensional parameters may be used to rewrite equation 2.21 in

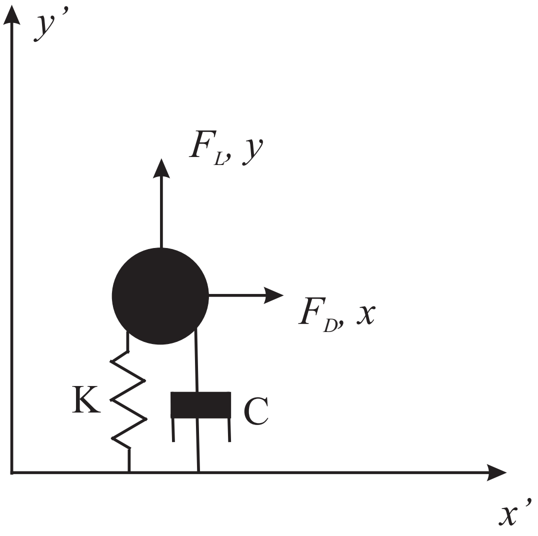

Figure 2.1: Freely oscillating cylinder geometry and coordinate system.

non-dimensional form:

$$m^* = \frac{\rho}{\rho_W}; \quad y^* = \frac{y}{D}; \qquad C_L = \frac{F_D}{\frac{1}{2}\rho_w U_\infty^2 D L_C}; \quad k^* = \frac{k}{\frac{1}{2}\rho_w U_\infty^2 L_C};$$

$$\dot{y}^* = \frac{\dot{y}}{D}; \qquad \ddot{y}^* = \frac{\ddot{y}\pi D}{2U_\infty^2}; \quad c^* = \frac{C}{\frac{1}{2}\rho_w U_\infty D L_C};$$

Using these non-dimensional definitions, we may rewrite the equations of motion in the following non-dimensional form:

$$m^* \ddot{y}^* + c^* \dot{y}^* + k^* y^* = C_L \tag{2.22}$$

Equation 2.22 is solved numerically using the predictor-corrector technique which is described in section 2.4.3.

2.4.2 Equations Governing the Motion of a Tethered Cylinder

Both experimentally and numerically, the motion of the cylinder is restricted to a two-dimensional domain such that the effects of side forces acting in the span-wise direction are neglected. The cylinder is further restricted to move along a circular arc around a specified pivot point. The radius of the arc is referred to as the tether length. Experimentally, the restrictions on the cylinder motion are achieved by tethering the cylinder to a pivot point such that its motion is restrained in the span-wise direction. In the present numerical study, the restraining tether is assumed to be massless. The calculations further assume that the tether has significantly smaller dimensions than the cylinder such that the fluid loading forces acting directly on the tether may be ignored.

The cylinder is attached to the tether such that it remains fixed during its motion along the arc, that is the cylinder cannot “nod” about the tether attachment point. The tether is assumed to have a fixed length, and is further assumed to be in-elastic. Wall and floor effects are not considered in this study. This final point is especially important for both cylinder end effects) and also, in the case of large cylinder lay over angles, floor effects have been neglected in this study. Experimentally, this implies that the pivot point cannot be attached to a floor when the cylinder's layover angle is large and the span-wise dimension of the cylinder is significantly greater than the cylinder diameter such that end effects can be neglected.

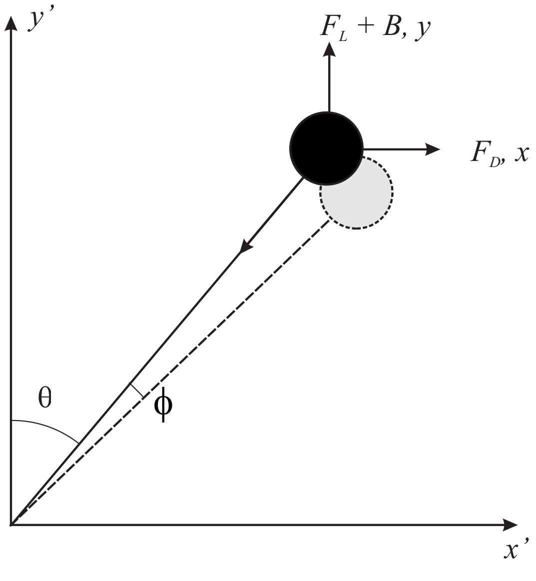

Figure 2.2: Tethered cylinder geometry and coordinate system.

Given these restrictions, the only forces acting on the cylinder are the tether tension (T), drag, lift and buoyancy forces (F_D, F_L, B). Examination of figure 2.2 shows that the tension in the tether is related to buoyancy and fluid forces by:

$$T = F_D \sin(\theta) + (F_L + B) \cos(\theta) \tag{2.23}$$

The equations of motion have been determined by writing Newton's second law of motion, relating the instantaneous acceleration of the cylinder to the forces acting on the cylinder; in Cartesian coordinates this is written as:

$$m\ddot{x} = F_D - T\sin(\theta) \tag{2.24}$$

$$m\ddot{y} = (F_L + B) - T\cos(\theta) \tag{2.25}$$

By substituting the definition of the T (equation 2.23) into the equations of motion (equations 2.24 and 2.25) and gathering like terms we may rewrite the equations of motion as:

$$m\ddot{x} = F_D\cos^2(\theta) - (F_L + B)\cos(\theta)\sin(\theta) \tag{2.26}$$

$$m\ddot{y} = (F_L + B)\sin^2(\theta) - F_D\sin(\theta)\cos(\theta) \tag{2.27}$$

The parameter θ can be rewritten in terms of x and y, using this the equations of motion may be simplified and rewritten in the form:

$$m\ddot{x} = F_D(\frac{y^2}{L^2}) - (F_L + B)\frac{xy}{L^2} \tag{2.28}$$

$$m\ddot{y} = (F_L + B)\cdot(\frac{x^2}{L^2}) - F_D\frac{xy}{L^2} \tag{2.29}$$

The following non-dimensional parameters may be used to rewrite equations 2.28 and 2.29 in non-dimensional form:

$$C_D = \frac{F_D}{\frac{1}{2}\rho_w U_\infty^2 D L_C} \qquad C_L = \frac{F_L}{\frac{1}{2}\rho_w U_\infty^2 D L_C} \qquad m^* = \frac{\rho}{\rho_W}$$

$$Fr = \frac{U}{\sqrt{gD}} \qquad x^* = \frac{x}{D} \qquad y^* = \frac{y}{D}$$

$$L^* = \frac{L}{D} \qquad \ddot{x}^* = \frac{\ddot{x}\pi D}{2U_\infty^2} \qquad \ddot{y}^* = \frac{\ddot{y}\pi D}{2U_\infty^2}$$

These non-dimensional definitions, combined with the definition of the buoyancy force:

$$B = (\rho_w - \rho)\cdot g \cdot \frac{\pi D^2 L_C}{4} \tag{2.30}$$

allows us to rewrite the equations of motion in the following non-dimensional form:

$$\frac{m^*}{2}\ddot{x}^* = C_D\left(\frac{y^{*2}}{L^{*2}}\right) - \left(C_L + \frac{\pi}{2Fr^2}\cdot(1-m^*)\right)\frac{x^*y^*}{L^{*2}} \tag{2.31}$$

$$\frac{m^*}{2}\ddot{y}^* = \left(C_L + \frac{\pi}{2Fr^2}\cdot(1-m^*)\right)\cdot\frac{x^{*2}}{L^2} - C_D\frac{x^*y^*}{L^{*2}} \tag{2.32}$$

Equations 2.31 and 2.32 are coupled and non-linear, they are solved numerically using the predictor-corrector technique which is described in section 2.4.3.

2.4.3 Solution of the Governing Equations: The Predictor-Corrector Technique

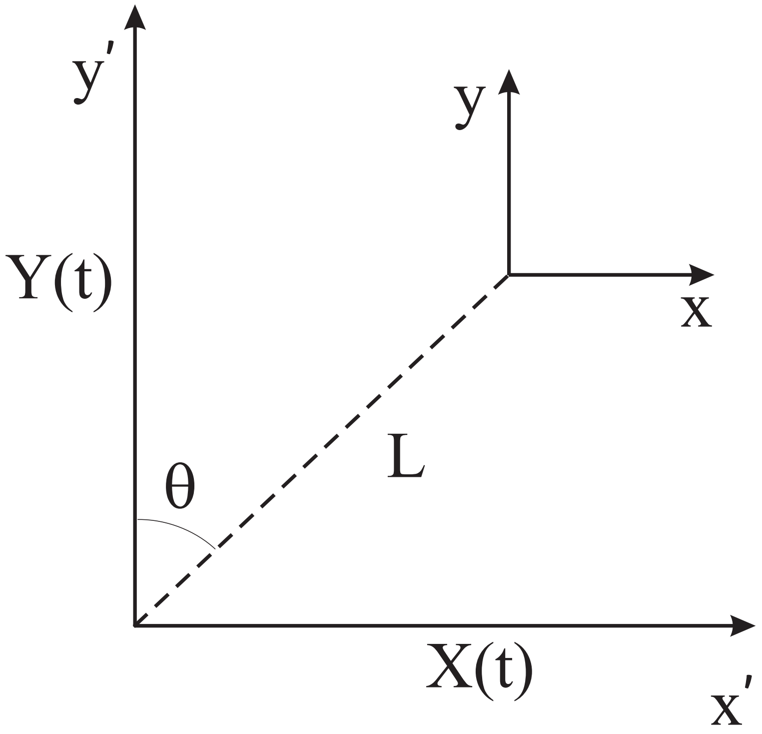

Figure 2.3: Transformation used to map from inertial to non-inertial reference frame.

Solving fluid-structure interaction problems generally involves the use of deforming and/or moving meshes. Figure 2.3 shows the transformation used to map the inertial reference frame to the time-independent reference frame. This mapping is described by the following transformation:

$$\boldsymbol{x} = \boldsymbol{x'} - \boldsymbol{X}(t), \tag{2.33}$$

where $\boldsymbol{X}(t)$ is the normalized displacement of the cylinder and is described in terms of $\theta + \phi$ as:

$$\boldsymbol{X}(t) = L^* \sin(\theta + \phi(t)), \quad \boldsymbol{Y}(t) = L^* \cos(\theta + \phi(t)). \tag{2.34}$$

In the transformed system of coordinates the cylinder appears stationary, although it is free to rotate. Given the transformation (2.33), the Navier-Stokes and continuity equations (2.1), (2.2) become:

$$\begin{aligned} \frac{\partial \mathbf{u}}{\partial t} &= -\boldsymbol{\nabla} p + \frac{1}{Re}\boldsymbol{L}(\mathbf{u}) + \boldsymbol{N}(\mathbf{u}) + \boldsymbol{A} \ , & (2.35) \\ \boldsymbol{\nabla} \cdot \mathbf{u} &= 0, & (2.36) \end{aligned}$$

where the forcing term $\boldsymbol{A}$ is an additional dimensionless acceleration term introduced by the coordinate transformation, Equation (2.33), and is the acceleration of the cylinder normalized by the inlet velocity and the cylinder diameter. Due to the attachment of the coordinate system to the cylinder, the cylinder will rotate as it moves about the base pivot.

The addition of the acceleration term, A^* in the Navier-Stokes equations, alters the time stepping scheme used for the fixed body calculations discussed in section 2.1.1. The first of the three sub-steps (the non-linear convective step) solves an intermediate velocity field $\hat{\mathbf{u}}$ as follows. For the first iteration through the time integration loop $\hat{\mathbf{u}}$ is solved using an explicit third order Adams-Bashforth technique:

$$\frac{\hat{\mathbf{u}} - \mathbf{u}^{(n)}}{\Delta t} = \sum_{q=0}^{J-1} \alpha_q \boldsymbol{N}(\mathbf{u}^{(n-q)}) - \left(\mathbf{u}_B^{(n+1)} - \mathbf{u}_B^{(n)}\right), \tag{2.37}$$

subsequent sub-step iterations are performed implicitly using a third-order Adams-Moulton technique:

$$\frac{\hat{\mathbf{u}} - \mathbf{u}^{(n)}}{\Delta t} = \sum_{q=0}^{J-1} \beta_q \boldsymbol{N}(\mathbf{u}^{(n+1-q)}) - \left(\mathbf{u}_B^{(n+1)} - \mathbf{u}_B^{(n)}\right). \tag{2.38}$$

The parameters α_q and β_q are the Adams-Bashforth and Adams-Moulton coefficients, the values of which have been previously presented in table 2.1. The bracketed terms on the right hand side of equation 2.37 and equation 2.38 is due to the motion of the cylinder relative to the tether attachment point. Here the velocity of the cylinder is denoted by $\mathbf{u}_B$ and the displacement of the cylinder is denoted by $\mathbf{x}_B$. The current best estimate of the cylinder velocity is denoted by $\mathbf{u}_B^{(n+1)}$. The pressure and diffusion substeps remain unchanged in the moving body scheme, however the diffusion equation (equation 2.11) requires the velocity of the reference frame at the boundaries which again comes from the current best estimate of $\mathbf{u}_B^{(n+1)}$.

From the solution of the Navier-Stokes equations at the $(n+1)^{st}$ timestep we have estimates of the fluid velocities and the pressure field. We then use these to calculate the fluid forcing coefficients, C_D and C_L, acting on the body at the $(n+1)^{st}$ time step. The acceleration of the cylinder is then calculated using equation 2.22 for the freely oscillating cylinder and equations 2.31 and 2.32 for the tethered cylinder. Initially, the displacement of the cylinder (required in the equations of motion) is unknown and the equations of motion (Equations 2.22 or 2.31-2.32) use a linear interpolation of the position at the $(n-1)^{st}$ and n^{st} timesteps in order to provide a current best guess of the position at the present (i.e. the $(n+1)^{st}$) timestep. This prediction of the acceleration is then substituted into a predictor-corrector scheme as detailed below.

The predictor-corrector method uses $\kappa \leq K$ substeps in an iterative process which calculates convergent values of the cylinder displacement and velocity to satisfy the following convergence criterion:

$$\begin{aligned} \frac{\Delta \mathbf{u}_B}{|\mathbf{u}_B|} &< u_{tol}, \qquad (2.39) \\ \frac{\Delta \mathbf{u}_{max}}{|\mathbf{u}_{max}|} &< u_{tol}, \qquad (2.40) \\ \frac{\Delta \boldsymbol{F}_B}{\boldsymbol{F}_B} &< F_{tol}. \qquad (2.41) \end{aligned}$$

Equation 2.39 states that the normalized change in the velocity of the cylinder between predictor-corrector substeps must be less than some tolerance u_{tol}. Equation 2.40 states that the normalized maximum change in the velocity field between substeps must be less than the tolerance u_{tol} at any point in the entire domain. The last convergence criterion ensures that the normalized change in the force of the body between substeps is less than some tolerance F_{tol}. For all of the simulations, the values of u_{tol} and F_{tol} were kept at 0.0001 and 0.01 respectively.

The first substep of the predictor-corrector method calculates the velocity and displacement of the cylinder at the $(n+1)^{st}$ timestep as:

$$\begin{aligned} \mathbf{u}_B^{(n+1)^*} &= \mathbf{u}_B^{(n)} + \frac{25\ddot{\mathbf{x}}^{(n+1)} - 2\ddot{\mathbf{x}}^{(n)} + \ddot{\mathbf{x}}^{(n-1)}}{24}\Delta t \qquad (2.42) \\ \mathbf{x}_B^{(n+1)^*} &= \mathbf{x}_B^{(n)} + \frac{5\mathbf{u}_B^{(n+1)} + 8\mathbf{u}_B^{(n)} - \mathbf{u}_B^{(n-1)}}{12}\Delta t \qquad (2.43) \end{aligned}$$

where the asterisk denotes that the solution is from the first substep in the predictor-corrector scheme. Subsequent substeps calculate the velocity and displacement of the cylinder as:

$$\begin{aligned} \mathbf{u}_B^{(n+1)^{**}} &= \mathbf{u}_B^{(n)} + \frac{25\ddot{\mathbf{x}}^{(n+1)^*} - 2\ddot{\mathbf{x}}^{(n)} + \ddot{\mathbf{x}}^{(n-1)}}{24}\Delta t \qquad (2.44) \\ \mathbf{u}_B^{(n+1)'} &= \mathbf{u}_B^{(n+1)^*} + \varepsilon\left(\mathbf{u}_B^{(n+1)^{**}} - \mathbf{u}_B^{(n+1)^*}\right) \qquad (2.45) \\ \mathbf{x}_B^{(n+1)^{**}} &= \mathbf{x}_B^{(n)} + \frac{5\mathbf{u}_B^{(n+1)'} + 8\mathbf{u}_B^{(n)} - \mathbf{u}_B^{(n-1)}}{12}\Delta t \qquad (2.46) \end{aligned}$$

where the double asterisk denotes the velocity and displacement predicted at the current substep. In equation 2.45, we improve the convergence characteristics by employing underrelaxation, in which ε is the relaxation parameter. The primed velocity term, $\mathbf{u}_B^{(n+1)'}$, denotes prediction of the predictor-corrector scheme at the current sub-step. The underrelaxation parameter was introduced after extensive testing without it found that for some parameter combinations, the method was unstable except for very small timesteps. The introduction of underrelaxation improves the convergence quality considerably. The choice of an optimal value for ε is highly problem specific and, because we are solving a very large system of PDE's that arise when modelling continuous variations of variables, the efficiency introduced by a wise choice of ε can be extremely important (see Chapra & Canale (1998)). This will be further discussed in section 2.5.7.

At the conclusion of each sub-step, the equations of motion are evaluated (equation 2.22 or equations 2.31 and 2.32), which allows a current evaluation of the force and acceleration acting on the cylinder. These results, along with the current best guess of the velocity is substituted into equations 2.39 - 2.41 and the solution is tested for convergence. If the convergence criteria are not met, then the process restarts at the first sub-step, i.e. the solution of equation 2.37 However, if equations 2.39 - 2.41 are satisfied, then we can continue to the next time step.

The local truncation errors introduced by the approximations are typically of the order (Δt^3) for both the third-order Adams-Bashforth predictors and the Adams-Moulton correctors used in the present method, although overall the combined problem is second-order accurate. Even though the errors are small, the position of the cylinder drifts away from the surface defined by the tether, although only marginally over a single time step. However when considering the long time traces that are needed for accurate determinations of oscillation amplitudes and frequencies for example, this position drifting is no longer insignificant. Accordingly, for the tethered cylinder, the position of the cylinder $\mathbf{x}_B^{(n+1)^{**}}$ is projected onto the surface defined by the tether and, for consistency, the velocity of the sphere is also projected. This stabilizes the scheme without affecting the accuracy.

2.4.4 The Tethered Cylinder: Differences between Experiments and Numerical Simulations

When comparing the two-dimensional, low Reynolds number results from this study with results of experiments performed at much higher Reynolds numbers (as is discussed in section 6.7), a problem arises in the need to characterize the motion of the cylinder in terms of a suitable parameter. For a tethered sphere, Govardhan & Williamson (1997) and Williamson & Govardhan (1997) elected to use the reduced velocity as the flow field controlling parameter. As described in section 1.6.4, when plotting their results against the reduced velocity, their data from tethered sphere setups with several different tether lengths and mass ratios collapsed onto a single line. The reduced velocity has similarly been used in studies of the flow past a freely oscillating cylinder as is also discussed in section 1.6.

Experimentally, the reduced velocity is changed by increasing the flow velocity, U_∞. Numerically, this is undesirable, as it inherently increases the Reynolds number Re, which would severely restrict the parameter space which could be investigated numerically. For example, Josie Carberry (private communications), examined the reduced velocity range, $u^* = [0, \simeq 20]$ for a range of cylinder mass ratios. This reduced velocity range coincided with a Reynolds number range of $Re = [2000, 14000]$. The entire Reynolds number range falls well outside the possible range that could be investigated using direct numerical simulations at this time. Direct numerical simulations using two-dimensional domains further require that the Reynolds number be of the order $Re = 200$ or less.

By numerically simulating the flow around a tethered cylinder at $Re = 200$, the vortex dynamics in the near wake is also significantly different when compared to higher Reynolds number flows, which exhibit essentially inviscid flow fields in the near wake. As the proportion of viscous force is greater for the low Reynolds number simulations, it is impossible to know a priori if similar modes of response will be observed numerically.

As previously mentioned, a range of reduced velocity is obtained experimentally by by increasing the flow velocity (and hence increasing the Reynolds number). When performing the computations, however, it is desirable to keep the Reynolds number fixed at a suitable value. As the Reynolds number is increased, smaller scale structures are gradually introduced into the flow field, as the flow undergoes transition to turbulence. In order to accurately capture these small scales, a finer mesh density is required, which translates to much higher computational cost. It was therefore investigated whether the reduced velocity could be altered without altering the Reynolds number.

The equation for the reduced velocity (which is derived in section 5.2) is reproduced below,

$$u^* = \frac{2\pi^{3/2}}{\sqrt{2}} \left(\frac{(m^* + C_A) \cdot L^*}{2\sqrt{C_D^2 + \left[C_L + \frac{\pi}{2}\frac{(1-m^*)}{Fr^2}\right]^2}.} \right)^{1/2} \tag{2.47}$$

Here, C_A is the added mass for a cylinder and is equal to 1.0. For any given numerical simulation or experiment performed, both the mass ratio and tether length must be held constant. The drag and lift forces acting on the cylinder are due to the flow interaction with the cylinder and cannot be predetermined, either experimentally or numerically. Therefore, the only parameter which can vary the reduced velocity either numerically or experimentally is the Froude number. The Froude number is defined as:

$$Fr = \frac{U_\infty}{\sqrt{gD}} \tag{2.48}$$

where g is the gravitational acceleration. Evidentally, g cannot be altered experimentally, so the only way to alter the Froude number experimentally is by altering the flow velocity U_∞. However, numerically, the Froude number can be altered by changing the g in place of U_∞, this allows a wide range of reduced velocities to be investigated at a single Reynolds number. By altering g, a much higher range of reduced velocity is attainable, when compared to experimentally altering the flow velocity, as the experimental range of U_∞ is limited by the experimental facility.

Altering the gravity term in equation 2.48 effectively decouples the reduced velocity from the Reynolds number. An obvious question is whether decoupling these two parameters will affect the response of the tethered cylinder appreciably. In their investigations of the tethered sphere, Govardhan & Williamson (1997) found that the vibrational response of the tethered sphere was essentially independent of the Reynolds number, but was a strong function of the reduced velocity. Numerical investigations into the wake of a tethered sphere by Pregnalato (2003) found this assumption to be reasonable. It is therefore likely that the tethered cylinder geometry will also be invariant to Reynolds number within a reasonable range.

The next question is what Reynolds number should be used in the simulations? As the simulations are conducted on a two-dimensional domain, the Reynolds number should be restricted to values $Re \leqslant 200$.

The $Re = 200$ was chosen as it is the highest Reynolds number which can be justifiably simulated on a two-dimensional domain. Beyond this Reynolds number, experimental and numerical investigations conclude that three-dimensional structures in the wake of a stationary cylinder act to alter the wake characteristics when compared to the results obtained from two-dimensional simulations (Williamson (1996a)). While large amplitude oscillations act to increase the correlation length along the span of a cylinder, and as such two-dimensional simulations of these systems may be used to study higher Reynolds number flows (for example Blackburn & Henderson (1999)), Koopman (1967), in his investigation of forced cylinder oscillation, found that $Re = 200$ is the highest Reynolds number with a two-dimensional field regardless of the amplitude of oscillation.

When considering the flow past a fixed cylinder, both the mean drag coefficient and the Strouhal number remain relatively constant in the range $200 \leq Re \leq 10000$. Within the Reynolds number range, $Re = 200$-10000, both the formation length, and the ratio of viscous to pressure drag terms alter when comparing the flow past a fixed cylinder at $Re = 200$ to that at a higher Reynolds numbers. Clearly, these discrepancies will alter the body-fluid interaction when comparing the numerical results to the experimental results, in particular, the amplitude of cylinder oscillation will be greatly affected by the ratio of viscous to pressure drag terms.

2.5 Validation

Rigorous validation of the numerical techniques, domain size analysis, and mesh independence studies were performed for each of the configurations investigated further in the thesis (results of which are presented in chapters 3 - 7).

Section 2.5.1 reports on a domain analysis study, which studies the effects of the location of inlet and outlet conditions on the flow around a stationary cylinder. From this study, an acceptable domain size, free of any substantial blockage and outflow effects is determined. Section 2.5.2 reports on an '$h-p$' grid resolution study performed on the domain chosen from the study in section 2.5.1 at both $Re = 200$ and 500, once again for a stationary cylinder. From this study, the effect of the mesh refinement was determined and a grid independent result was obtained. The results of this study provided a mesh for subsequent investigations of the flow around a circular cylinder.

Section 2.5.3 details the results of a combined domain analysis and '$h-p$' grid resolution study for the flow past a blunt flat plate. Mesh independent results for three blunt flat plates, of varying aspect ratio, were obtained from this study.

The Floquet technique, described in section 2.5.4 was validated for the flow past a stationary circular cylinder at various Reynolds numbers $Re \leqslant 259$; the results of the validation were compared against the findings of Barkley & Henderson (1996), as well as the experimental findings of Williamson (1996b). From this investigation, the Floquet technique was validated for subsequent studies on the flow past blunt flat plates.

Simulations of the flow past a freely oscillating cylinder were validated against the existing results of Blackburn & Henderson (1996). In section a grid independence study was performed for the case of the flow past a tethered cylinder, both at low and high reduced velocities, to ensure a mesh independent result was obtained in subsequent simulations. The effect of the relaxation parameter, ε and convergence criteria was investigated in section 2.5.7 for both a tethered and freely oscillating cylinder.

In chapter 5 of the results, the tethered cylinder results are compared with the results of experiments performed by Josie Carberry (private communications), the experimental setup was jointly designed by Josie Carberry and the author, and is described in section 2.5.8.

2.5.1 Domain Analysis: The Flow Around a Stationary Cylinder

The flow around a circular cylinder at $Re = 200$ was tested for sensitivity to domain size using the range of meshes shown in figure 2.4, with domain size parameters defined in table 2.2; where l_i is the in-flow length, l_o is the out-flow length, and l_h is the cross-flow length. Due to the design of the domain, $l_i \equiv l_h$ for all the meshes considered. As can be seen from figure 2.4, each mesh considered is an exact subset of $M6$, the largest mesh considered, therefore any variation in flow-field parameters is due solely to the domain size.

Within each macro-element, a Lagrange interpolant polynomial order, $p = 8$ was chosen to investigate the effects of changed domain size. As is shown in the next section, $p = 8$ is sufficient to resolve the near wake flow structures in the $M3$ domain. As the macro-element mesh in the near wake is identical for all meshes considered in this study, $p = 8$ is sufficient to analyze the effect of changed domain size parameters.

In each case, the shedding frequency (in the form of a Strouhal number), mean drag coefficient and fluctuating lift and drag coefficients were established for each domain size investigated, and used to evaluate the effect of domain size. The results are presented in table 2.3, and the percentage difference of each of the evaluating parameters for each

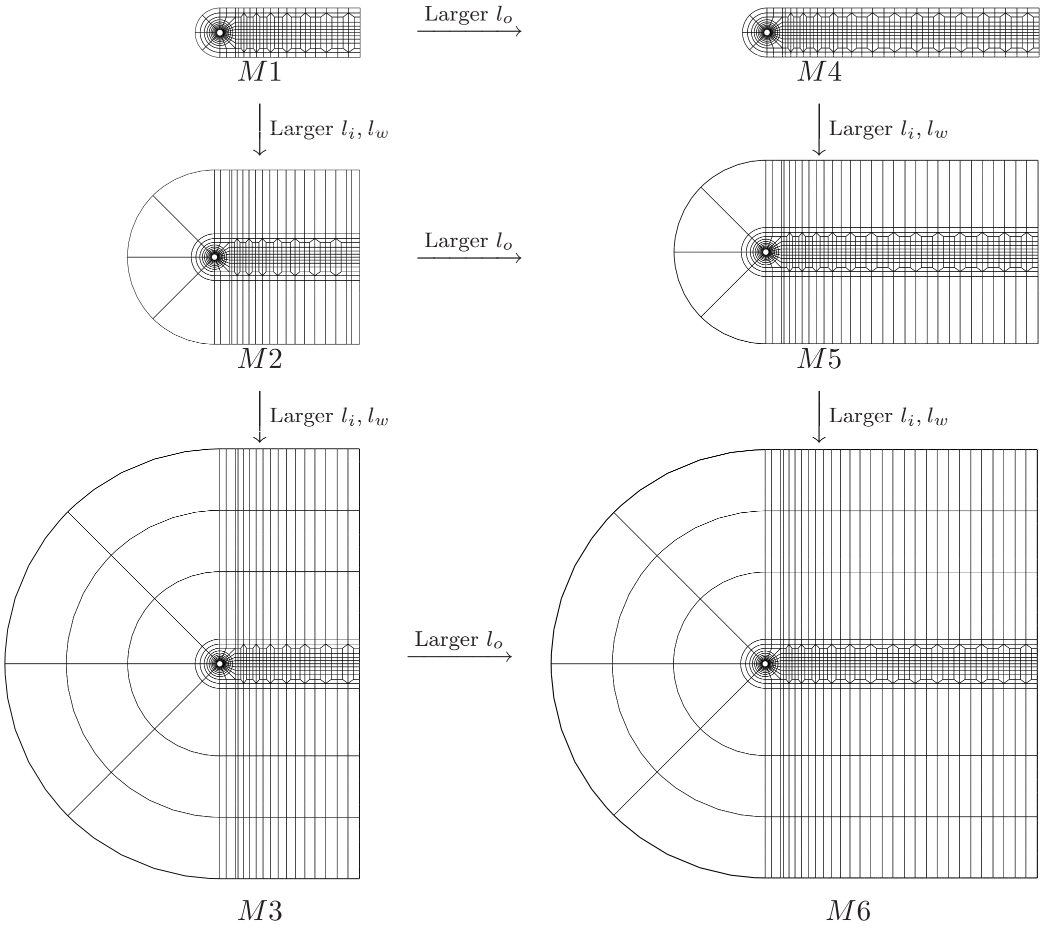

Figure 2.4: Family of spectral element meshes used for domain analysis.

Dimension	$M1$	$M2$	$M3$	$M4$	$M5$	$M6$
l_i/D	$4.0D$	$15.0D$	$35.0D$	$4.0D$	$15.0D$	$35.0D$
l_h/D	$4.0D$	$15.0D$	$35.0D$	$4.0D$	$15.0D$	$35.0D$
l_o/D	$23.0D$	$23.0D$	$23.0D$	$44.5.0D$	$44.5D$	$44.5D$
N	452	518	566	692	754	878

Table 2.2: Mesh parameters for the different domain sizes investigated.

domain is compared in table 2.4 with the findings of the $M6$ domain.

	$M1$	$M2$	$M3$	$M4$	$M5$	$M6$
St	0.2154	0.1985	0.1958	0.2154	0.1986	0.1963
$\overline{C_D}$	1.5473	1.3595	1.3299	1.5472	1.3601	1.3330
C'_D	0.0555	0.0453	0.0443	0.0555	0.0454	0.0457
C'_L	0.7893	0.6949	0.6770	0.7894	0.6950	0.6790

Table 2.3: Variation of global quantities as a function of domain size for domains $M1$ to $M6$ at $Re = 200$

	$M1$	$M2$	$M3$	$M4$	$M5$
St	9.70%	1.14%	0.26%	9.71%	1.17%
$\overline{C_D}$	16.07%	1.96%	0.24%	16.07%	2.03%
C'_D	21.38%	0.83%	3.16%	21.39%	0.17%
C'_L	16.24%	2.12%	0.30%	16.25%	2.36%

Table 2.4: Percentage difference of global quantities between domains $M1$ to $M5$ with the $M6$ domain, at $Re = 200$

When comparing all the results, a distinct blockage effect is noted for both the $M1$ and $M4$ meshes. When compared to the $M6$ mesh, the Strouhal number for both the $M1$ and $M4$ meshes was approximately 10% larger. The blockage effect is also apparent when comparing the other global parameters.

For most global parameters (all except C'_D), the $M3$ mesh exhibited the least difference when compared with the $M6$ mesh. However the $M2$ mesh was chosen as the domain for further investigations as it had a reasonably small difference in all the global quantities when compared to the $M6$ mesh and was significantly more computationally efficient.

2.5.2 Mesh Independence: The Flow Around a Stationary Cylinder

A detailed grid resolution study was performed to establish the suitability of the mesh used for all simulations involving a circular cylinder. The study was performed on the $M2$ grid which was selected in the previous section following a domain analysis study.

Two Reynolds numbers were chosen to measure mesh independence; $Re = 200$ and $Re = 500$. The former value was chosen as it was the Reynolds number selected for analysis of the tethered cylinder (section 2.4.4), and it may be compared directly with the following numerical results of previous investigations, Barkley & Henderson (1996) and Blackburn & Karniadakis (1993). Previous experimental and numerical research concludes that the wake is intrinsically three-dimensional at this Reynolds number, therefore differences exist between prior experimental findings and the numerical results discussed herein.

Some results presented in chapter 4 were conducted at higher Reynolds numbers, up to $Re = 300$. To accommodate this, a further grid resolution study was performed at $Re = 500$ as this value lies beyond the highest Reynolds number considered and the results of the grid resolution study may be directly compared with the numerical findings of Blackburn & Henderson (1999) who conducted two-dimensional simulations at this Reynolds number. It is inherently assumed that mesh independence at $Re = 500$ implies mesh independence at lower Reynolds numbers.

The grid resolution study employed two techniques; an 'h' type refinement, where the spatial size and number of macro-elements over the domain are altered, and a 'p' type refinement, where the order of the polynomial interpolants within each element, p is increased.

The 'h' type refinement involved reducing the size of the macro-elements in regions of high velocity gradient, in order to capture the structures within the cylinder boundary layer and wake. Once an acceptable macro-element mesh was created, a 'p' type refinement study was conducted in order to determine the most suitable value of p to use in further simulations.

2.5.2.1 Re = 200

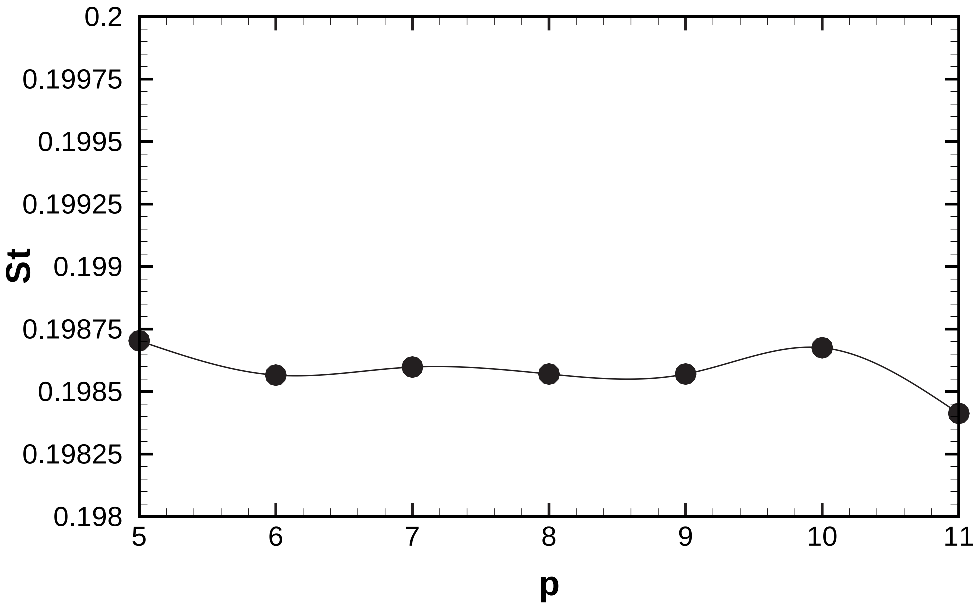

Figure 2.5: Variation in the shedding Strouhal number as a function of the p, for the $M2$ mesh at $Re = 200$.

The 'p' refinement study conducted at a Reynolds number of 200, monitored the viscous and pressure components of fluid force, as well as the shedding frequency (expressed as a Strouhal number) for a range of p values, $5 < p < 11$. Grid-independent values of these parameters were measured and these values were then compared to accepted values from previous studies (Barkley & Henderson (1996), Williamson (1988a), Norberg (1994), and Henderson (1995)). When comparing with previous studies, the results from simulations of a slightly lower Reynolds number ($Re = 190$) was chosen.

Figure 2.5 shows the results of the mesh independence study for the vortex shedding Strouhal frequency as a function of p. The percentage difference difference of the Strouhal number calculated for each value of p and that calculated for $p = 11$ were determined. The results are presented in table 2.5. For all values of p investigated, the percentage difference in the Strouhal number was found to be 0.2%. Given the marginal difference in the Strouhal number, it was concluded that a value of $p = 5$ is sufficient to provide reliable shedding frequency results at $Re = 200$.

Figure 2.6 shows the maximum viscous and pressure components of drag as a func-

p	5	6	7	8	9	10	11
St	0.1987	0.1985	0.1986	0.1985	0.1986	0.1986	0.1985
$\overline{C_D}$	1.3624	1.3592	1.3598	1.3595	1.3592	1.3593	1.3591
C'_D	0.0456	0.0454	0.0454	0.0453	0.0454	0.0455	0.0457
C'_L	0.6967	0.6955	0.6956	0.6950	0.6937	0.6940	0.6943

Table 2.5: Convergence of global quantities with polynomial order p on mesh $M2$ at $Re = 200$

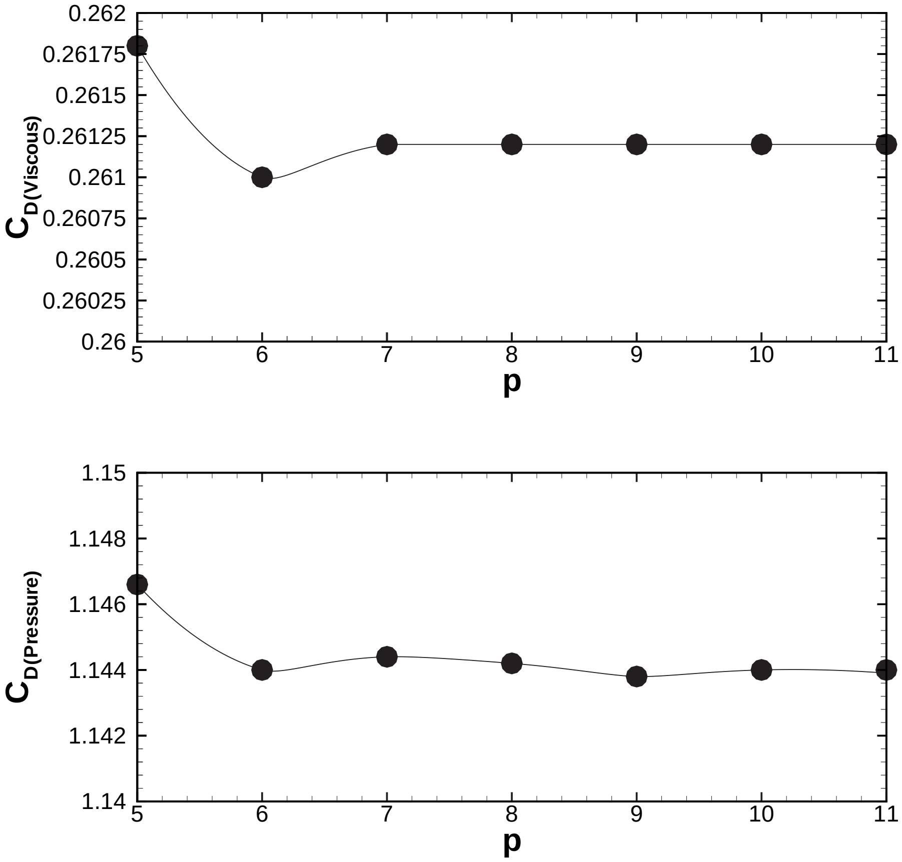

Figure 2.6: Variation in the (top) viscous component of the drag coefficient and (bottom) pressure component of the drag coefficient, as a function of the p, for the $M2$ mesh at $Re = 200$.

tion of p. As with the shedding frequency results, percentage differences were calculated for the drag components as a function of p when compared to the values obtained at

$p = 11$. These findings are presented in table 2.5. These results indicated that for $p \geq 8$, the percentage difference in the viscous and pressure drag components was reduced below 1% when compared to $p = 11$. The viscous component of drag was found to have the most variation as a function of p. It was considered that variations of less than 1% represented mesh independent result, and from this data the smallest value of p which would provide reliable drag data was $p = 8$.

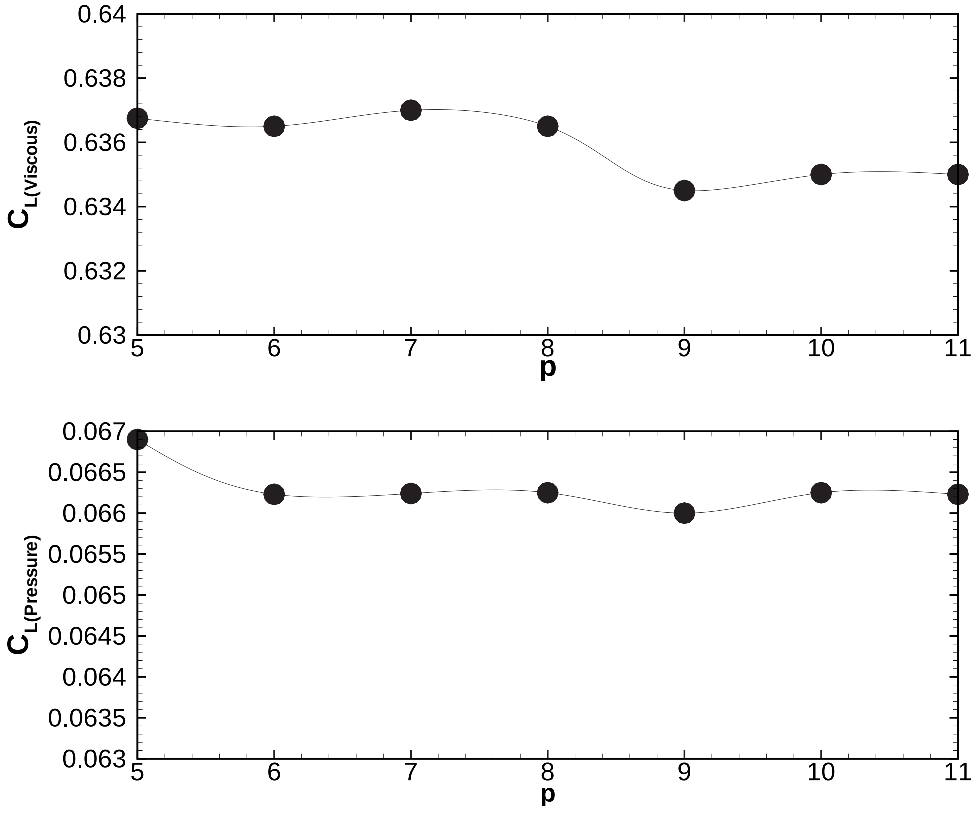

Figure 2.7: Variation in the (top) viscous component of the lift coefficient and (bottom) pressure component of the lift coefficient, as a function of the p, for the $M2$ mesh at $Re = 200$.

Figure 2.7 shows the maximum viscous and pressure components of lift as a function of p. percentage differences were once again calculated, and are presented in table 2.5. These results indicated that the percentage difference was less than 1% for all values of p considered. However, variations in the percentage difference are minimized for $p \geq 6$. It was therefore considered that the smallest value of p which would provide reliable lift data was $p = 6$.

Given the results summarized in table 2.5 and 2.6 and detailed in the previous para-

	St	$\overline{C_D}$
Current Results	0.1966	1.3558
Barkley & Henderson (1996)	0.1954	1.3442
Henderson (1995)		1.3386
Williamson (1988a)	0.1945	
Norberg (1994)	0.1940	

Table 2.6: Comparison of Strouhal number and mean drag coefficient with prior studies at $Re = 190$.

graphs, the most cost-effective case is obtained when $p = 8$. This is cost effective in the sense that all scales observed in the flow for Reynolds numbers up to and including $Re = 200$ are clearly resolved, and running the simulations using $p = 8$ are considerably more efficient than corresponding simulations at higher values of p, with only marginal benefits in the flow-field resolution. For these reasons, all simulations up to and including Reynolds numbers of $Re = 200$ were simulated using $p = 8$ as the order of the Lagrange polynomial interpolants.

Finally, the results from simulations computed at $Re = 190$ are compared with published values. In this case, only the Strouhal number and mean drag coefficient are compared. The results are presented in table 2.6. The results computed here compare to within 1.5% of established values.

2.5.2.2 Re = 500

A second detailed resolution study was performed on a stationary cylinder at $Re = 500$ to verify grid independence at this Reynolds number. A Reynolds number of $Re= 500$ was chosen for two reasons; first it represents the highest Reynolds number considered for this (and other) investigations and therefore represents the most rigorous grid resolution study possible; secondly the grid resolution results may be compared against the findings of Blackburn & Henderson (1999) in their numerical study, where their grid resolution was conducted at the same Reynolds number. The order of the interpolating polynomials increased from $p = 5$ to $p = 9$. Flow quantities such as the Strouhal number, lift and drag coefficients were measured and compared to previous research. The results are summarized in Table 2.7.

p	5	6	7	8	9
C'_L	1.1873	1.1809	1.1817	1.1818	1.1822
C'_D	1.5897	1.5792	1.5798	1.5793	1.5795
$\overline{C_D}$	1.4561	1.4457	1.4462	1.4461	1.4459
St	0.2270	0.2264	0.2267	0.2267	0.2267

Table 2.7: Convergence of global quantities with polynomial order p on mesh $M2$ at $Re = 500$

For all measures employed, the variation between the values at $p = 7$ and $p = 9$ is less than 1%. Furthermore, the values of all measures for $p = 8$ (used in all simulations) compare to within 1% of the numerical values of Blackburn & Henderson (1999), and Henderson (1995) (see table 2.8).

	St	C'_L	$\overline{C_D}$
Current Results	0.2267	1.182	1.446
Blackburn & Henderson (1999)	0.2280	1.200	1.460
Henderson (1995)			1.445

Table 2.8: Comparison of Strouhal number, fluctuating lift coefficient and mean drag coefficient with prior studies at $Re = 500$.

2.5.3 Flow Around a Blunt Flat Plate

Four spectral-element meshes were used for the calculations, each corresponding to a different cylinder aspect ratio. The meshes were composed of N quadrilateral conforming macro-elements. Within each element, a tensor-product of Lagrangian polynomial interpolants of order p were used to approximate the solution variables. The front and side boundaries of the domain were set to a uniform background flow in the x direction ($\overline{u} = U_\infty$). Zero normal velocity derivatives were used at the outlet boundary (While this can cause problems at higher Reynolds numbers, where it can prevent vortices from leaving the domain, it does not cause any degradation of the solution accuracy in the neighborhood of the cylinder for the Reynolds numbers considered here). The boundary conditions for the perturbation velocity components are: u', v', w' set to zero at the upstream and side boundaries; and zero normal velocity gradient at the downstream boundary. The inlet length (l_i) and the sidewall boundary width (l_w) were held constant across all plate geometries. The outlet boundary length (l_o) was increased for larger aspect ratios. The number of macro-elements within each mesh was varied between the different geometries, such that longer plates were modelled with more macro-elements. The meshes used for the investigation are shown in Figure 2.8. The geometrical parameters defining each mesh are listed in Table 2.9.

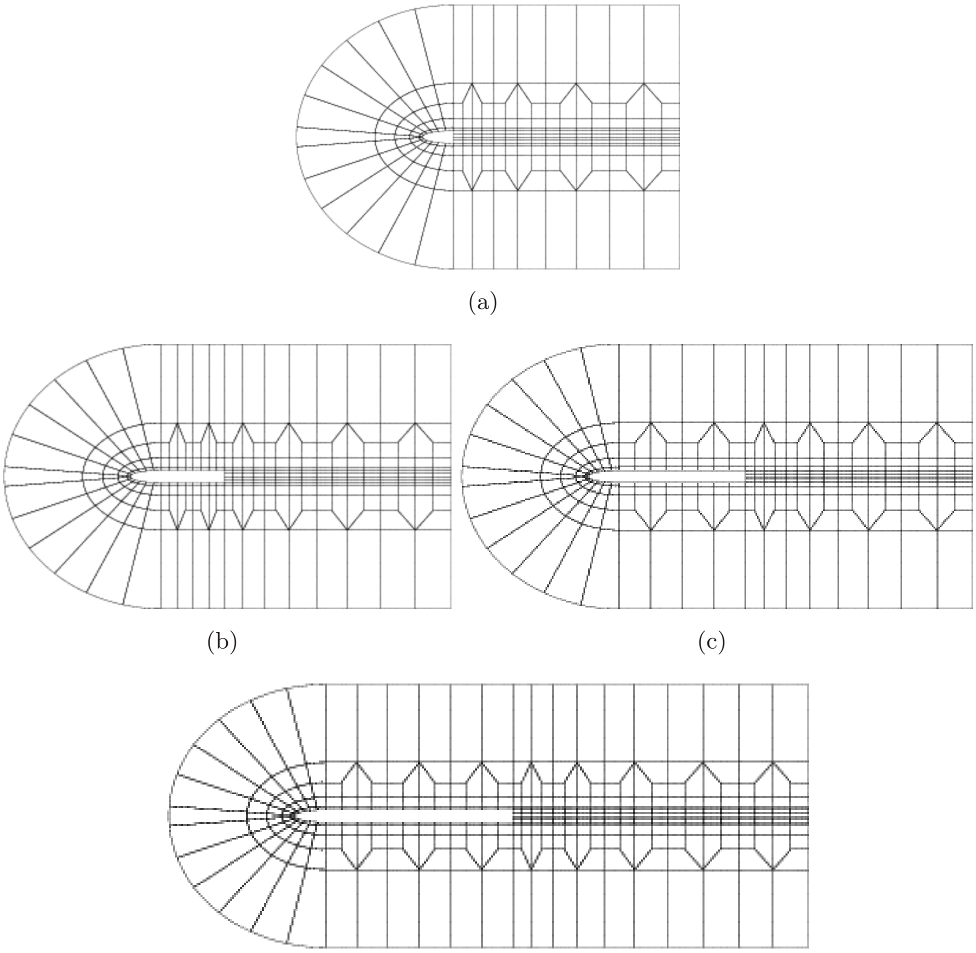
(a)

(b)

(c)

(d)

Figure 2.8: Macro element meshes used for simulations, Top to bottom ((a)–(d)) correspond to $AR = 2.5$, 7.5, 12.5, 17.5 respectively.

Mesh independence was established by performing a p-type resolution study. The order of the Lagrangian polynomial interpolants within each element was successively

Dimension	$AR = 2.5$	$AR = 7.5$	$AR = 12.5$	$AR = 17.5$
l_i/H, l_w/H	10	10	10	10
l_o/H	18	18	18	23.5
N	321	321	321	401

Table 2.9: Mesh parameters for the different aspect ratios considered.

increased until the solution was mesh independent. A separate grid resolution study was performed for each mesh. The Reynolds number employed in the grid resolution study was the highest Reynolds number examined in further computations. The Strouhal number, lift and drag coefficients were measured and compared across the range of n investigated. The results for the aspect ratio $AR = 17.5$ grid at a Reynolds number $Re = 700$ are summarized in Table 2.10. For all measures employed, the variation between the values at $p = 10$ and $p = 12$ is less than 1% which is representative of all the grids employed in this study. Ninth-order ($p = 10$) Lagrangian polynomial interpolants were used for the tensor-product expansion basis for all subsequent calculations.

p	5	6	7	8	9	10	11	12
$C_{L(P)}$	2.8585	1.5516	1.7550	1.6231	1.6824	1.6684	1.6845	1.6874
$C_{D(P)}$	1.4252	0.9609	1.0598	0.9942	1.0231	1.0095	1.0159	1.0156
$C_{D(m)}$	1.4252	0.9609	1.0317	0.9661	0.9933	0.9806	0.9854	0.9853
St	0.2261	0.1752	0.1948	0.1840	0.1880	0.1861	0.1865	0.1865

Table 2.10: Convergence of global quantities with polynomial order p for the plate aspect ratio $AR = 17.5$ grid at $Re= 730$.

A domain study was performed to evaluate blockage effects. As anticipated, the Strouhal number was found to be sensitive to the sidewall boundary width. Results from the p-type resolution study were crosschecked against a mesh with a larger inlet length $l_i = 22$, side wall domain length $l_w = 22$, outlet length $l_o = 35$, and $N = 603$ elements. The study was only performed on the $AR = 17.5$ case, as this is the most sensitive to boundary location. The tests were performed at the highest Reynolds number examined in further computations for this mesh ($Re= 700$). The Strouhal number was found to vary by 3.5% from the results from the grid for the smaller domain, and mean and peak drag forces were found to vary by 6%. Despite this, the smaller domain sizes listed in Table 2.9 were used in this study, principally for computational efficiency as it was felt that the physical mechanism governing the mode transition would not be affected by the smaller domain mesh size. In order to test this hypothesis, the Floquet multipliers over the full range of span-wise wavelengths, λ/H, reported in this study were calculated for the large mesh domain. The mode transition order and topology were found to be the same as that calculated for the smaller mesh domain size, as was the critical wavelength for each three-dimensional instability. The critical Reynolds number describing the transition from two- to three- dimensional flow was found to vary slightly with mesh domain size, in the order $\Delta Re = 5$.

2.5.4 Floquet Analysis of the Flow Around a Fixed Cylinder

The Floquet technique described in section 2.3 was used to determine the linear transition to three-dimensionality of the wake of a blunt flat plate (the results of which appear in chapter 3). To validate the Floquet technique, the transition to three-dimensionality of the wake of a circular cylinder was calculated at sever Reynolds number, such that the critical Reynolds number can be compared with the previous findings of Barkley & Henderson (1996), Williamson (1996b), and Brede *et al.* (1996).

The Reynolds numbers, $Re = 140, 180, 220$, and 259 were investigated at wavelengths, $\lambda = [0.5, 4.5]$. The wavelengths were chosen to correspond with to the wavenumber β, (where $\beta = 2\pi/\lambda$), investigated by Barkley & Henderson (1996).

The results are presented in figure 2.9, and are compared with the findings of Barkley & Henderson (1996). The results for each Reynolds number investigated, compare very well between the two studies. The greatest variation between any two data points for $\mu > 0.55$, between the two studies being 3.5%. For values of $\mu < 0.55$ the error was somewhat greater, however the convergence of the Floquet multipliers at such low values is not as accurate when compared to $\mu \to 1$. The critical Reynolds number was determined from the present results using a third order polynomial fit. These results found a critical Reynolds number $Re_{crit1} = 188.1$ at a critical span-wise wavelength of $\lambda = 3.93$ for the transition of the wake to a Mode A instability; and $Re_{crit2} = 259$ at a critical span-wise wavelength of $\lambda = 0.79$ for a Mode B instability. These values compare to within 0.2% of Barkley & Henderson (1996)'s results and agrees well with Williamson

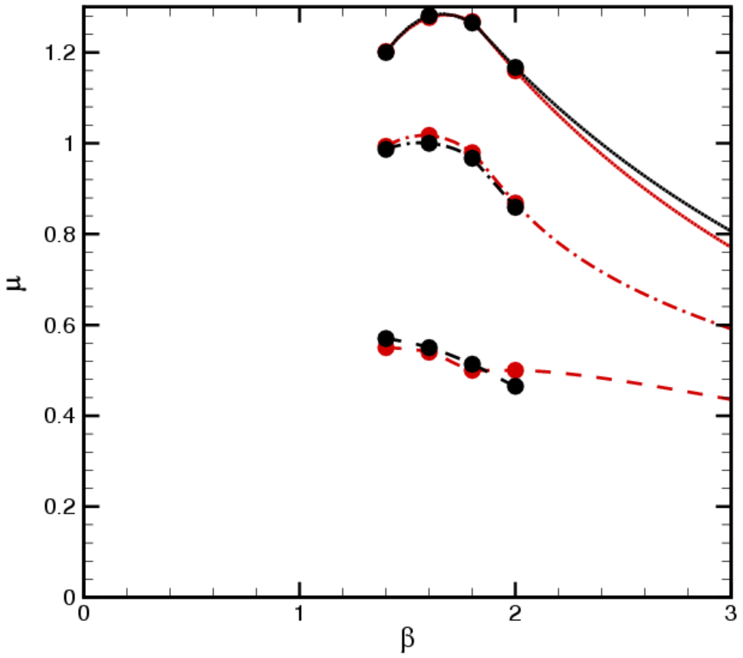

(a)

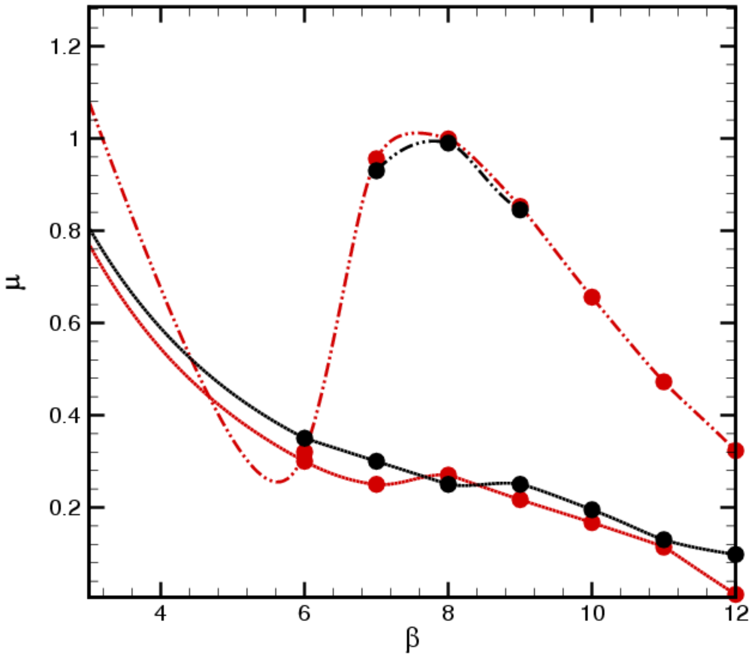

(b)

Figure 2.9: Comparison of Floquet multiplier results for the flow around a circular cylinder with the findings of Barkley & Henderson (1996) for, (a) $\beta = [0, 3]$, for the case of: $--$, $Re = 140$; $-\cdot\cdot-$, $Re = 180$; —, $Re = 220$; (b) $\beta = [6, 12]$, for the case of: —, $Re = 220$; $-\cdot\cdot-$, $Re = 259$; the red lines indicate the present results.

	This Study	I	II	III
Re_{crit}				
Mode A	188.1	188.5	[180, 194]	$\simeq 170$
Mode B	259	259	[230, 260]	
λ_{crit}				
Mode A	$3.93D$	$3.96D$	$[3,4]D$	$\simeq 4$
Mode B	$0.79D$	$0.822D$	$\simeq 1D$	

Table 2.11: Comparison of critical Reynolds numbers and critical wavelengths for Mode A and Mode B between the present results and previous findings; (I), Blackburn & Henderson (1996); (II), Williamson (1996b); (III), Brede *et al.* (1994).

(1996b)'s and Brede *et al.* (1994)'s experimental findings of $Re_{crit1} = [180, 194]$ for mode A and $Re_{crit2} = [230, 260]$ for Mode B. The results are summarized in table 2.11.

2.5.5 Flow around a Freely Oscillating Cylinder

A few studies have been performed, which investigate the flow past a freely oscillating cylinder at low Reynolds number. The best known, Anagnostopoulos & Bearman (1992) investigated the flow past a freely oscillating cylinder in the Reynolds number range $Re = [90, 150]$. However, this Reynolds number range is smaller than the one investigated in the present work (see chapter 4), and their mass ratio is comparatively high ($m^* = 150$) as is their mass-damping parameter ($m^*\zeta = [0.18, 0.228]$) when compared to the parameters investigated in this study. Therefore, comparison with their study was not conducted to validate the freely oscillating code. Validation was performed by comparing the results of a freely oscillating simulation with the findings of Blackburn & Henderson (1996). Blackburn & Henderson (1996) performed a two-dimensional study on a freely oscillating cylinder at a Reynolds number, $Re = 250$. In all cases, their mass ratio, $m^* = 12.785$, and their mass damping coefficient, $\zeta = 0.1278$, which is closer to the values of interest studied in chapter 4. The higher Reynolds number allows the present code to be validated up to $Re = 250$.

Blackburn & Henderson (1996) used a similar technique to the one described in section 2.4.3 to simulate the motion of the freely oscillating cylinder which was combined with a spectral-element technique for spatial discretization. They found results similar to previous investigations by Blackburn & Karniadakis (1993) and observed a region of 'lock-in' oscillation behavior.

The current freely oscillating technique was compared to their results in the 'lock-in' region, which corresponds to the normalized frequency range $f_n/St = [0.8, 1.2]$, where f_n is the natural frequency of the freely oscillating cylinder system, measured in a vacuum, and St is the Strouhal number of the fixed cylinder case, measured at the same Reynolds number (computed as $St = 0.2077$ on a two-dimensional domain).

The following quantities were used to evaluate the accuracy of the present simulations in comparison with the findings of Blackburn & Henderson (1996):

- f_o/St, the ratio of the oscillation frequency to the vortex shedding frequency,
- $\overline{C_D}$, the mean drag coefficient and,
- RMS A^*, the root mean square amplitude of oscillation.

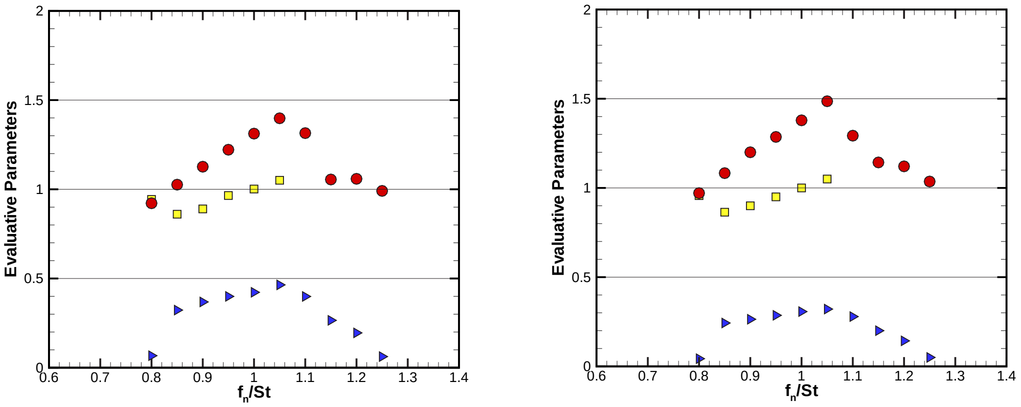

Figure 2.10: Comparison of flow field parameters for a freely oscillating cylinder with the results of Blackburn & Henderson (1996) as a function of the ratio of f_n/St, where f_n is the natural frequency of the freely oscillating cylinder, and St is the Strouhal shedding frequency from a fixed cylinder; (left) Blackburn & Henderson (1996); (right), present results. ○, $\overline{C_D}$; ▷, RMS A^*; □, f_o/St.

A comparison of the two results is presented in figure 2.10. For all the parameters investigated, there was very little discrepancy between the two studies. The largest discrepancy between the two studies occurs for the amplitude of oscillation which was found to be 57% higher then for Blackburn & Henderson at $f_n/St = 0.8$. This discrepancy between the two results decreased as f_n/St was increased further, however the current results exhibited larger RMS amplitude oscillations for all values of f_n/St considered. Given the small amplitude of oscillation at $f_n/St = 0.8$ the discrepancy was considered insignificant; and the trend between the two results is consistent across the parameter space. As with the amplitude response, the mean drag coefficient exhibited a similar trend when comparing the two results. The largest discrepancy for the mean drag was 7%. Finally, the normalized frequency of oscillation, f_o/St was also found to be extremely similar when comparing both cases. The maximum discrepancy in f_o/St was only 1.5%. The region of 'lock-in' behaviour was found to be the same as that reported by Blackburn & Henderson (1996).

In conclusion, the trend in the results was found to agree very well with the results reported by Blackburn & Henderson (1996). While quantitative discrepancies were found, these are reasonably small and may be due to domain and/or boundary effects or insufficient spatial resolution in the study performed by Blackburn & Henderson (1996). No details of a domain or resolution analysis were provided by Blackburn & Henderson (1996), and the their domain width was quite small ($l_w = 11D$), which was found to cause significant blockage effects for the case of a fixed cylinder in section 2.5.1.

2.5.6 Flow around a Tethered Cylinder

While the results of the tethered cylinder simulations will be compared with the experimental findings of Josie Carberry (private communications), these experiments were performed at much higher Reynolds numbers, and the author was unable to find either experimental or numerical results from a tethered cylinder at low Reynolds numbers ($Re = 200$ in this case).

However, a mesh independence study was conducted for the tethered cylinder with $m^* = 0.833$ and $L^* = 5.5$ for the two Froude numbers, $Fr = 0.08$ and $Fr = 1.25$.

The lower Froude number case corresponds to a low mean layover angle (where the cylinder is essential vertical). While not known *a priori*, it was assumed (and has further been verified) that at this low Froude number, the cylinder is essentially stationary. The $Fr = 1.25$ case corresponds to a much higher mean layover angle, and the system exhibits larger amplitude oscillations.

In this study, the mean layover angle, mean drag coefficient, fluctuating lift and drag coefficients, and calculated mean reduced velocity were used as evaluation parameters. The results are presented in table 2.12 ($Fr = 0.08$) and table 2.13 ($Fr = 1.25$). In both cases, for $p \geqslant 8$, all parameters monotonically approached the results for $p = 10$ (which was the most refined case investigated).

p	5	6	7	8	9	10
$\overline{\theta}$	1.851	1.849	1.849	1.849	1.849	1.849
$\overline{C_D}$	1.349	1.348	1.347	1.347	1.347	1.347
C'_L	-0.676	-0.674	-0.674	-0.674	-0.674	-0.674
C'_D	-0.00031	-0.00030	-0.00031	-0.00015	-0.00016	-0.00015
$\overline{u^*}$	0.673	0.673	0.674	0.673	0.673	0.673

Table 2.12: Convergence of global quantities with polynomial order p for the case of a tethered cylinder with $m^* = 0.833$, $L^* = 5.5$ and $Fr = 0.08$.

For $Fr = 0.08$ (table 2.12), no difference was noted up to three significant figures, when comparing the results for the case where $p = 8$, to the case where $p = 10$. A small difference of 7% was noted in the fluctuating drag when comparing $p = 9$ to $p = 10$, however, this difference is only noted in the fifth significant figure, and given the extremely small values of C'_D, was considered negligible.

For $Fr = 1.15$ (table 2.13), it was anticipated that a larger difference would exist when comparing the results for different cases of p, as the amplitude of oscillation is significantly greater. When comparing the results for the case where $p = 8$, to the case where $p = 10$, the greatest variance was found for C'_L, which exhibited a 0.45% difference between the two cases. It was considered that this difference is negligibly small, and a interpolant polynomial order, $p = 8$ was chosen for all subsequent simulations.

2.5.7 Moving Body Simulations: Effect of relaxation parameter and Convergence Criteria

Section 2.5.2 has provided grid independent results for a fixed cylinder. This grid was then used to provide convergent results for both the flow around a freely oscillating cylinder and the flow around a tethered cylinder, with all simulations performed at $Re \leqslant 200$ (Sections 2.5.5 and 2.5.6). The technique described in section 2.4.3 employed

p	5	6	7	8	9	10
$\overline{\theta}$	81.952	81.701	81.385	83.390	83.309	83.252
$\overline{C_D}$	1.220	1.218	1.217	1.255	1.256	1.257
C'_L	0.157	0.157	0.157	0.164	0.164	0.164
C'_D	-1.045	-1.037	-1.028	-1.070	-1.068	-1.066
$\overline{u^*}$	22.519	22.528	22.524	22.210	22.194	22.182

Table 2.13: Convergence of global quantities with polynomial order p for the case of a tethered cylinder with $m^* = 0.833$, $L^* = 5.5$ and $Fr = 1.25$.

the use of both a relaxation parameter, ε and convergence criteria. We now examine the effect of altering these terms. We look at a typical tethered cylinder simulation, in this case with parameters $m^* = 0.8$ and $L^* = 5$ at two different reduced velocities, $u^* = 10$ and $u^* = 15$. Further to this, we look at a freely oscillating cylinder simulation with $m^* = 0.4$ and $u^* = \infty$.

For the case of the tethered cylinder, the parameters used to evaluate the relaxation parameter independence were the mean layover angle, $\overline{\theta}$, the mean drag coefficient, $\overline{C_D}$, the root-mean-square (RMS) θ' amplitude response of the cylinder as well as the RMS drag and lift coefficients. For the case of the freely oscillating cylinder, the parameters used to evaluate the relaxation parameter independence were amplitude of oscillation response of the cylinder, $\overline{C_D}$, and the RMS drag and lift coefficients. In all cases a sampling period of $\Delta t^* = 1000$ time units has been used to calculate all quantities.

Relaxation parameters in the range $0.2 < \varepsilon < 0.8$ were investigated for all simulations considered. From section 2.4.3, the purpose of ε in the moving body simulations is to improve the convergence rate of the solver, rather than to improve the converged solution. As a result, increasing ε from 0.2 to 0.8 is not expected to significantly alter the vibration response, either for the case of the tethered, or freely oscillating cylinder. The results of the tethered cylinder study is shown in table 2.14 and 2.15. The results of the freely oscillating cylinder study is shown in table 2.16.

For the tethered cylinder with a low reduced velocity ($u^* = 10$), all the evaluation parameters are reasonably independent of ε with the greatest variation being for RMS C_D. The greatest percentage difference in RMS C_D was found to be 0.066% between

ε	$\overline{\theta}$	$\overline{C_D}$	θ'_{RMS}	$C_{D(RMS)}$	$C_{L(RMS)}$
0.2	14.253429	1.361509	0.554347	0.101249	0.470917
0.3	14.253372	1.361504	0.554346	0.101184	0.470773
0.4	14.253339	1.361500	0.554343	0.101244	0.470906
0.5	14.253333	1.361505	0.554348	0.101244	0.470904
0.6	14.253476	1.361507	0.554306	0.101244	0.470906
0.7	14.253446	1.361511	0.554331	0.101246	0.470908
0.8	14.253575	1.361527	0.554107	0.101182	0.470771

Table 2.14: Effect of changing ε for a tethered cylinder with $u^* = 10, m^* = 0.8, L^* = 5.0$.

ε	$\overline{\theta}$	$\overline{C_D}$	θ'_{RMS}	$C_{D(RMS)}$	$C_{L(RMS)}$
0.2	35.15486	1.37803	1.23779	0.19345	0.40419
0.3	35.15449	1.37801	1.23776	0.19344	0.40418
0.4	35.15440	1.37802	1.23763	0.19333	0.40413
0.5	35.15440	1.37801	1.23763	0.19333	0.40413
0.6	35.15423	1.37801	1.23770	0.19333	0.40413
0.7	35.15464	1.37803	1.23763	0.19333	0.40413
0.8	35.15445	1.37802	1.23768	0.19344	0.40417

Table 2.15: Effect of changing ε for a tethered cylinder with $u^* = 15, m^* = 0.8, L^* = 5.0$.

$\varepsilon = 0.2$ and 0.8. For practical applications, the variation in the evaluation parameters at $u^* = 10$ was considered negligible.

For the tethered cylinder with a high reduced velocity, $u^* = 15$ the cylinder is oscillating with a much greater amplitude and it would be anticipated that the variation in evaluation parameters should vary more significantly when compared to the $u^* = 10$ case. However this is not the case, the parameter exhibiting the greatest variation was once again RMS C_D, and for this case it has a maximum percentage difference of 0.057% between $\varepsilon = 0.2$ and 0.4. As was the case with $u^* = 10$, it was considered that for practical applications, the variation in the evaluation parameters at $u^* = 15$ was negligible.

ε	A^*	$\overline{C_D}$	$C_{D(RMS)}$	$C_{L(RMS)}$
0.2	0.107495	1.174596	0.012977	0.051169
0.3	0.107466	1.174598	0.012977	0.012977
0.4	0.107499	1.174598	0.012977	0.051172
0.5	0.107422	1.174561	0.012967	0.051171
0.6	0.107342	1.174477	0.012965	0.051171
0.7	0.107362	1.174415	0.012957	0.051171
0.8	0.107426	1.174380	0.012954	0.051169

Table 2.16: Effect of changing ε for a freely oscillating cylinder with $u^* = \infty$ and $m^* = 0.4$.

Table 2.16 lists the results for the freely oscillating cylinder. As with the case of the freely oscillating cylinder, all the evaluation parameters are reasonably independent of ε. In this case the parameter exhibiting the greatest variation is A^*. The greatest percentage difference in A^* was found to be 0.15% between $\varepsilon = 0.3$ and 0.5; for practical applications, this variation in the evaluation parameters is considered negligible.

Finally, the results should be theoretically independent of the relaxation parameter if they are converged. To test this, two simulations were performed where the convergence criteria was decreased an order of magnitude from $u_{tol} = 0.0001$ and $F_{tol} = 0.01$ to $u_{tol} = 0.00001$ and $F_{tol} = 0.001$. This was performed for the tethered cylinder case with parameters, $m^* = 0.8$, $L^* = 5$, $u^* = 15$, and $\varepsilon = 0.5$. The results are presented in table 2.17.

u_{tol}/F_{tol}	$\overline{\theta}$	$\overline{C_D}$	θ'_{RMS}	$C_{D(RMS)}$	$C_{L(RMS)}$
0.0001/0.01	35.15440	1.361527	1.23763	0.19333	0.40413
0.00001/0.001	35.15446	1.360751	1.23686	0.19324	0.40406

Table 2.17: Effect of changing u_{tol}/F_{tol} for a freely oscillating cylinder with $u^* = \infty$ and $m^* = 0.4$.

From table 2.17, it is evident that the evaluation parameters remained independent of the convergence criteria, as the convergence criteria was decreased by an order of magnitude as described. The largest percentage difference occurred for θ'_{RMS}, which exhibited a percentage difference of 0.06%.

In conclusion, it was found that a relaxation parameter anywhere in the range of $\varepsilon = 0.2 - 0.8$ was acceptable, however, for low mass ratio simulations, the upper limit of ε was restricted in order to ensure a converged result. In general ε was set equal to the mass ratio of interest. The convergence criteria were always $u_{tol} = 0.0001$ and $F_{tol} = 0.01$.

2.5.8 Experimental Equipment and Setup

The numerical findings presented in section 6.7 were compared to the experimental findings of J. Carberry (Private Communications). The experimental and numerical findings were compared for three reasons. First, the results were compared to qualitatively assess the numerical findings and determine if the same modes of cylinder motion discussed in chapter 5 and 6 are observed experimentally. Second, the comparison allowed us to determine the effect of Reynolds number on the response of the tethered cylinder system, the experiments being performed at significantly higher Reynolds numbers, as discussed below. Finally, the numerically simulated flow field structures were analyzed such that hypotheses regarding the fluid forces acting on the cylinder both experimentally and numerically could be formed. Combined, these three reasons assess the ability of the low Reynolds number simulations to qualitatively predict the response of the tethered cylinder system at higher Reynolds numbers.

All experiments were obtained using the FLAIR water channel facility, located in the department of Mechanical Engineering, Monash University. The water channel has a cross section of 60cm by 80cm and a maximum speed of 40cm/s. The Reynolds number range investigated was $Re = [2800, 14000]$, corresponding to a calculated reduced velocity range of $u^* = [3.5, 21]$.

For all cases the cylinder tether length was held constant at $L^* = 5$, and the mass ratio was varied in the range $m^* = [0.54, 0.97]$. The cylinders span-to-diameter aspect ratio was 20 diameters, and the sidewalls of the channel were used as end conditions. In all cases the clearance between the cylinder ends and the side walls was less than 1mm. The tether attachment point was raised above the bottom surface of the channel to avoid boundary layer effects. Care was taken to ensure that the cylinder was sufficiently immersed below the free surface such that free-surface effects were negligible and could be ignored.

The cylinder motion was captured using an 'off-the-shelf' PAL video camera. Preliminary PIV data was obtained of the wake field directly behind the cylinder, for his a digital (4 mega-pixel) camera was used, which in combination with PIV software, allowed 16,256 individual flow vectors to be analyzed in the field of interest, this corresponds to a resolution of 0.97 mm. The PIV images were taken such that the motion of the cylinder could be correlated with the instantaneous flow-field structures observed in the wake.

The cylinder was not instrumented to measure forcing or displacement. The mean lift was assumed to be negligible, and from this assumption, the mean drag could be calculated from knowledge of the cylinder mass ratio and mean layover angle from equation 2.49.

$$\overline{\theta} = \tan^{-1}\left(\frac{\overline{C_D}}{\overline{C_L} + (1-m^*)\cdot \pi/2 \cdot 1/Fr^2}.\right) \tag{2.49}$$

Numerical findings presented in section 5.5 suggest that the mean lift is not negligible for a wide range of mean layover angles. Assuming this effect is also observed experimentally, the calculations performed to determine the experimental reduced velocity, and the mean drag acting on the cylinder can only be approximations of the actual values. This point is further discussed in section 6.7. Future work aims to instrument the tethered cylinder to directly measure the lift and drag acting on the body.

Chapter 3

Three Dimensional Instabilities in the Wake of an Elongated Blunt Flat Plate

3.1 Introduction

Despite little supporting evidence, there appears to be an implicit assumption that the wakes of two-dimensional bluff bodies undergo transition to three-dimensional flow, and eventually turbulence, through the same sequence of transitions observed for a circular cylinder wake. Previous studies of a square cylinder wake support this presumption. In this paper, the transition to three-dimensional wake flow is examined for an elongated cylinder (or plate) with an aerodynamic leading edge and square trailing edge. The three-dimensional instability modes are determined for a range of aspect ratio ($AR \equiv$ chord / thickness). Floquet analysis reveals that three distinct instabilities occur. These are referred to as Mode A, B$'$ and S$'$ through analogy with the modes for circular and square cylinders. For aspect ratios less than approximately 7.5, Mode A is the most unstable mode. For aspect ratios greater than this, the most unstable mode switches to Mode B$'$. This mode has the same spatio-temporal symmetry as Mode B for a circular cylinder, but a span-wise wavelength and near-wake features more in common with Mode S for a square cylinder. The dominant wavelength for this mode is approximately 2 plate thicknesses, much longer than that of Mode B for a circular cylinder. It is found that the critical Reynolds number for the onset of the Mode A instability varies approximately with the square root of the aspect ratio. On the other hand, the critical Reynolds number for the onset of Mode B$'$ is almost independent of aspect ratio. For large aspect ratios, the separation in Reynolds number between the critical Reynolds numbers is substantial; for instance, for $AR = 17.5$, these values are approximately 450 and 700. In fact, for this aspect ratio, the onset of the third instability mode, Mode S$'$, occurs at a lower Reynolds number than Mode A. These results suggest that the transition scenario for similar bluff bodies may be distinctly different to that for short bodies such as circular or square cylinders. At the very least, the dominant span-wise wavelength in the turbulent wake is likely to be much longer than that for a circular cylinder wake. In addition, the reversal of the ordering of appearance of the two modes with the different spatio-temporal symmetries is likely to affect the development of spatio-temporal chaos as a precursor to fully turbulent flow.

3.2 Two-Dimensional Base-Flow Field Results

While not the main focus of this study, a summary of the base flow field results are presented in this section, in order to facilitate comparison of the Floquet results with previous studies.

3.2.1 Vortex Structures in the wake

Figures 3.1 to 3.3 show equispaced contours of vorticity in the range $\omega_z = \pm 1$ for the case of $AR = 7.5, 12.5$ and 17.5. The Reynolds number for each case is $Re = 400$, based on the plate thickness. This particular Reynolds number was chosen because, based on the current study, it represents the highest Reynolds number prior to transition to three-dimensionality for all of the aspect ratios considered. As shall be quantitatively discussed in section 3.2.2, the shedding frequency clearly decreases with plate aspect ratio.

Figure 3.4 shows d' as a function of Reynolds number for each plate in the range $Re = [300, 650]$. Here, d' is defined as $H + 2\ \delta$, where δ is the momentum thickness of the boundary layer, measured at the trailing edge of the plate. For all plates, H contributes at least 97% of d'. There is very little variation between $AR = 7.5$ and 12.5; d' for both aspect ratios decreases slightly as a function of Reynolds number. For the case of $AR = 17.5$, d' is $\simeq 3\%$ smaller than for the other plates at all Reynolds numbers investigated. This is a significant decrease, as it requires an approximately 7% decrease in the boundary layer thickness of the plate with $AR = 17.5$ when compared to the case with $Ar = 12.5$.

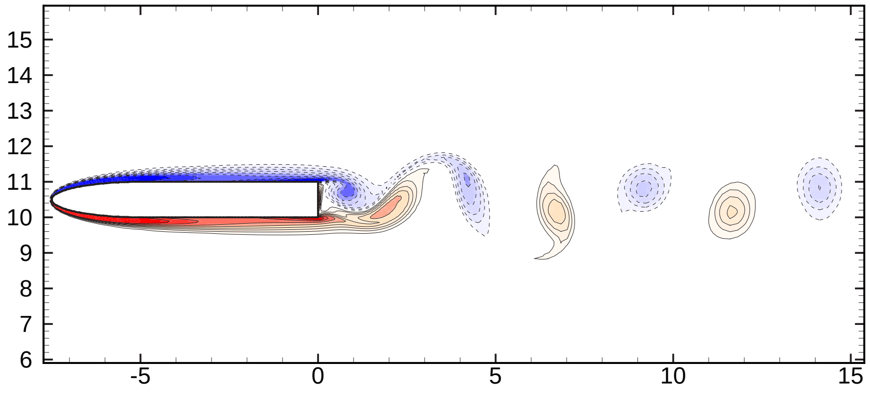

Figure 3.1: Span-wise vorticity field $\omega_z = \pm 1$ for $AR = 7.5$ and $Re = 400$. Contours are evenly spaced over the range (blue) $-4.0 \leqslant \omega_z \leqslant 4.0$ (red); with $\Delta\omega_z = 0.5$.

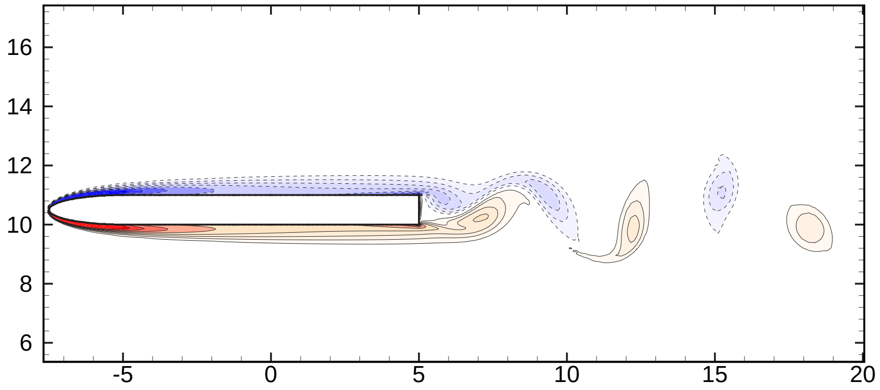

Figure 3.2: Span-wise vorticity field $\omega_z = \pm 1$ $AR = 12.5$ and $Re = 400$. Contours are evenly spaced over the range (blue) $-4.0 \leqslant \omega_z \leqslant 4.0$ (red); with $\Delta\omega_z = 0.5$.

3.2.2 Wake Shedding Frequency Analysis

Eisenlohr & Eckelmann (1989) experimentally investigated the flow past thin flat plates with blunt trailing edges. They found a linear relationship between the Roshko number ($Ro_{d'} = Re_{d'} \cdot St_{d'}$) and the Reynolds number ($Re_{d'}$ based on d'). This choice of d' allows direct comparison between all plates considered as it contains a combination of plate length (in the form of the momentum thickness) and plate thickness. Results of $Ro_{d'}$ as a function of $Re_{d'}$ are shown in figure 3.5 for plate aspect ratios $AR = 7.5, 12.5$ and 17.5, along with the experimental results of Eisenlohr & Eckelmann (1989). The results for all aspect ratios simulated lie within the experimental scatter of Eisenlohr

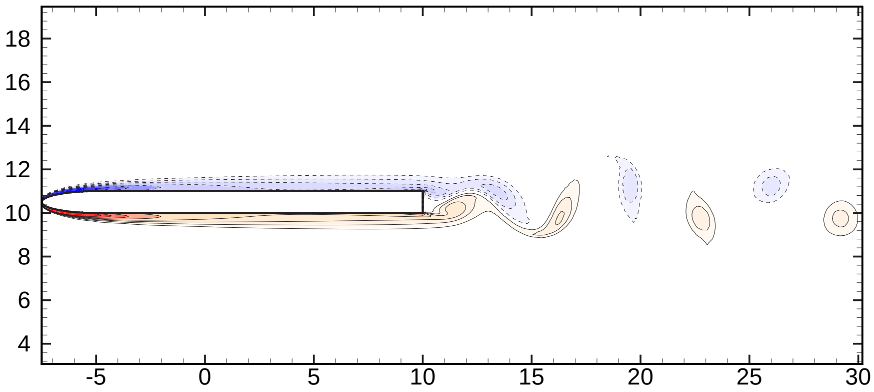

Figure 3.3: Span-wise vorticity field $\omega_z = \pm 1$ $AR = 17.5$ and $Re = 400$. Contours are evenly spaced over the range (blue) $-4.0 \leqslant \omega_z \leqslant 4.0$ (red); with $\Delta\omega_z = 0.5$.

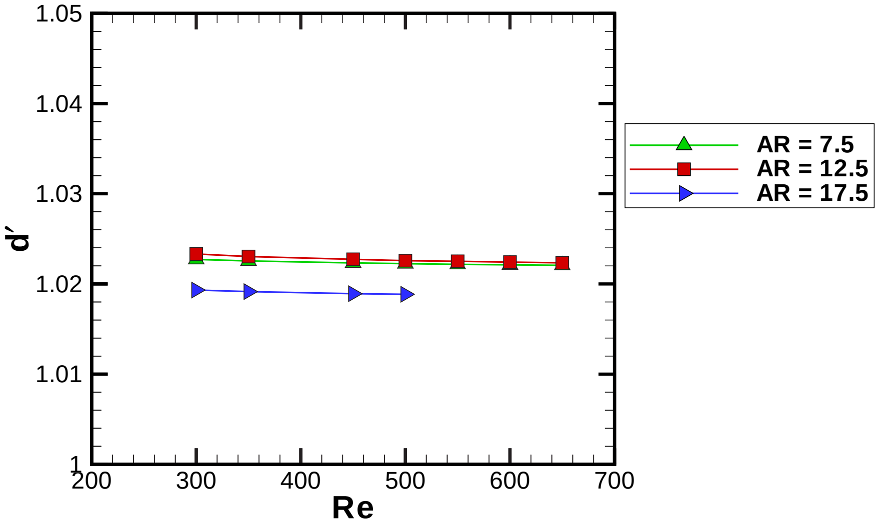

Figure 3.4: Effective thickness, d', as a function of Reynolds number for plates with aspect ratios, $AR = 7.5, 12.5$ and 17.5; where d' is defined as H + twice the momentum thickness.

& Eckelmann (1989) results.

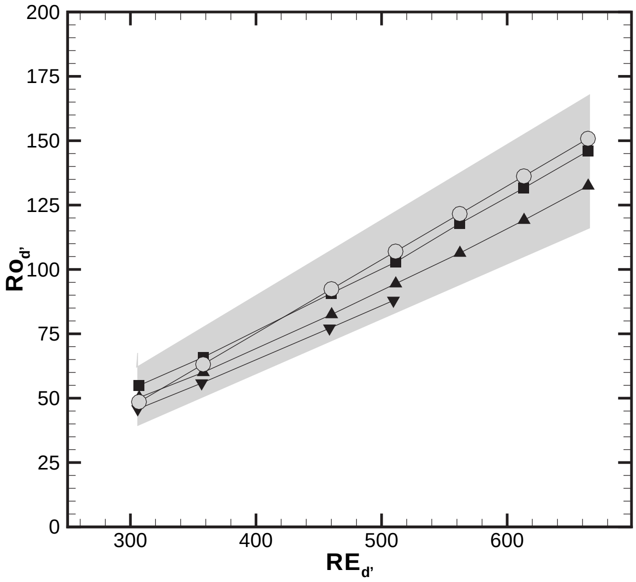

Figure 3.5: The shedding frequency, expressed as the Roshko number ($Ro = Re \cdot St$), where both the Strouhal number and Reynolds number use d' as the length scale. –○–, experimental results of Eisenlohr & Eckelmann (1989); –■– $AR = 7.5$ results; –▲–, $Ar = 12.5$ results; –▼–, $Ar = 17.5$ results. The shaded region is indicative of the spread in Eisenlohr & Eckelmann's experimental data.

3.2.3 Fluid Force Analysis

Both the mean Drag and the fluctuating lift and drag forces were calculated for plates with aspect ratios, $Ar = 7.5, 12.5$ and 17.5.

Mean Drag

Figure 3.6 shows the mean drag as a function of Reynolds number in the range $Re = [300, 650]$ for each plate. Over this Reynolds number range, the plate with $AR = 7.5$ exhibited a dramatic increase in drag with Reynolds number as the Reynolds number was increased beyond $RE \simeq 400$. Between $Re = 400$ and $Re = 650$ the mean drag increases by $\simeq 80\%$. By contrast, no dramatic increase was noted in the mean drag as a function of Reynolds number for either the $AR = 12.5$ or 17.5 case. The $AR = 12.5$ plate showed a small decrease in mean drag with increasing Reynolds number up to a local minimum at $Re \simeq 450$, beyond this the mean drag coefficient increased with Reynolds number up to the highest Reynolds number investigated. A significant drop in the mean drag of $\overline{C_D} \simeq 20\%$ was noted when comparing $AR = 17.5$ with $AR = 12.5$

over the same Reynolds number range. The drag to Reynolds number relationship for $AR = 17.5$ had a very similar profile to the $AR = 12.5$ case up to $Re = 450$; beyond this Reynolds number, the mean drag continued to decrease with increasing Reynolds number.

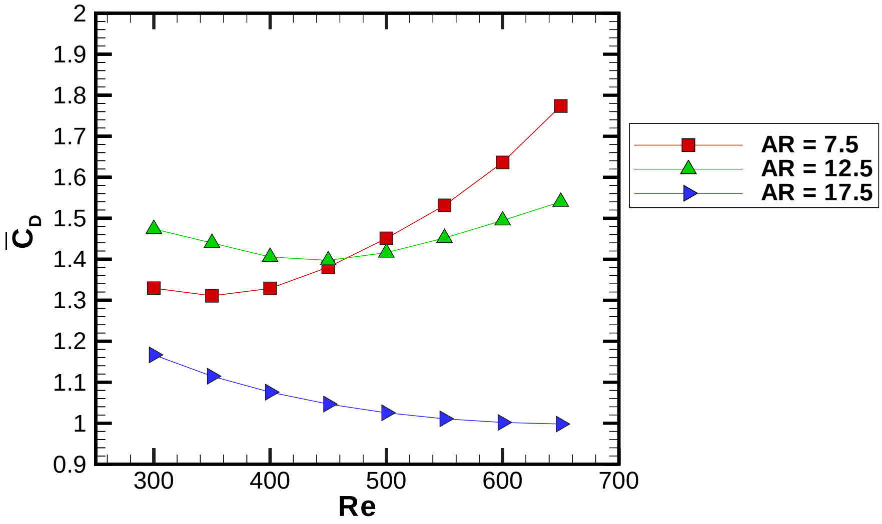

Figure 3.6: Time mean Drag as a function of Reynolds number, for Reynolds numbers in the range $Re = [300, 650]$.

The above description shows a dramatic difference in the mean drag as a function of Reynolds number depending on the aspect ratio of the plate. A 66% increase in the plate aspect ratio between $AR = 7.5$ and 12.5 has dramatically reduced the drag at highest Reynolds number investigated. A further increase of 40% between $Ar = 12.5$ and 17.5 has resulted in a further reduction in the drag.

Peak Lift and Drag Forces

The peak values of the fluctuating components of the lift and drag forces are shown in figure 3.7 and 3.8 respectively as a function of Reynolds number for plate aspect ratios $AR = 7.5, 12.5$ and 17.5. The peak lift coefficient increases linearly with Reynolds number for all aspect ratios considered. The results for $AR = 7.5$ and 12.5 are very similar, with $Ar = 7.5$ exhibiting a slightly greater gradient in C'_L with increasing Re when compared with $AR = 12.5$. By contrast, the peak lift for $AR = 17.5$ is dramatically greater for all Reynolds numbers considered, and C'_L increases far more rapidly with Reynolds number when compared to the other plates considered.

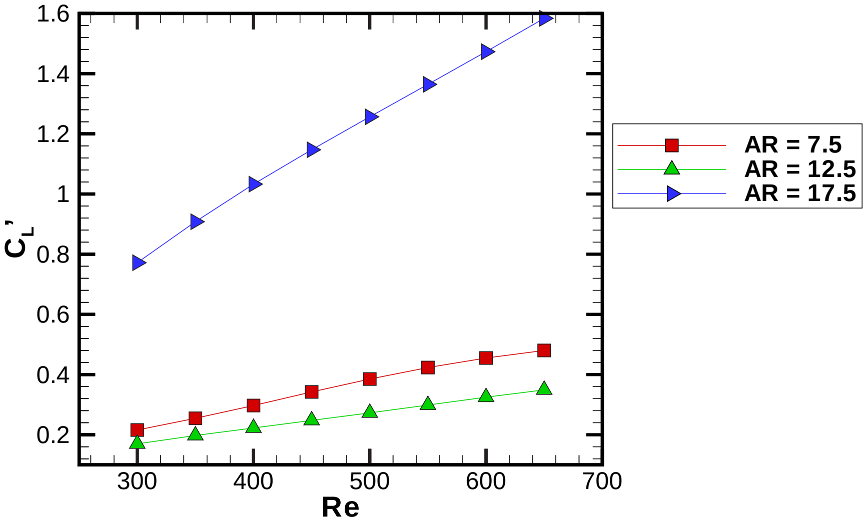

Figure 3.7: Peak fluctuating lift coefficient as a function of Reynolds number, for plate aspect ratios $AR = 7.5$, 12.5 and 17.5.

For both $AR = 7.5$ and 12.5, a small amount of scatter was observed in the peak value of the fluctuating drag coefficient, C'_D, as a function of Reynolds number. However, within the bounds of this scatter, both aspect ratio plates exhibited a very similar C'_D to Reynolds number relationship. By contrast, for plate $AR = 17.5$, the peak drag was significantly reduced for all Reynolds numbers considered, and there was no scatter away from a linear relationship between C'_D and Reynolds number for this plate.

In summary, the change in aspect ratio from $AR = 12.5$ to 17.5 appears to have a considerable influence on the fluctuating lift and drag response. While the results are consistent, they were unexpected (for example the marked reduction in $\overline{C_D}$ with increasing Reynolds number, for the case of $AR = 17.5$). Further work is needed to relate the fluid force behaviour with vortex structures in the wake.

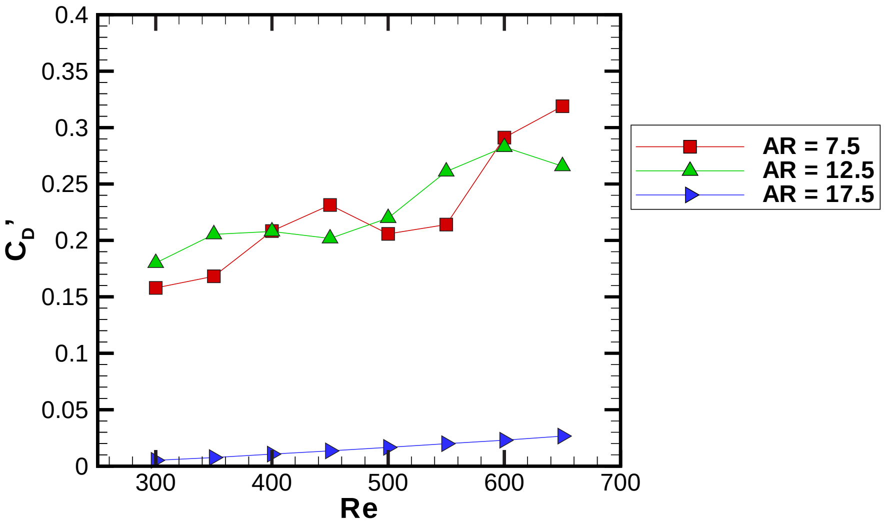

Figure 3.8: Peak fluctuating drag coefficient as a function of Reynolds number, for plate aspect ratios $AR = 7.5$, 12.5 and 17.5.

3.3 Floquet Stability Analysis of the Flow Past Blunt Flat Plates

Floquet analysis was performed for each aspect ratio over a range of Reynolds numbers. For each Reynolds number, a range of span-wise wavelengths was considered, including at least $0.5 < \lambda/H < 4.0$. Some simulations were performed for longer wavelengths to ensure that the dominant modes were captured. Once the critical Reynolds number for each mode was bracketed, interpolation was used to refine the estimate of the critical Reynolds numbers and corresponding wavelengths.

Figures 3.9 - 3.12 show the Floquet multipliers for the dominant modes for a range of span-wise wavelengths and Reynolds numbers. The figures refer to aspect ratios AR = 2.5, 7.5, 12.5 and 17.5, respectively.

Local maxima in these figures correspond to topologically different wake instability modes for the corresponding wavelength ranges. If the magnitude of the Floquet multiplier, μ, at a local peak exceeds unity, then the flow field is critically unstable to the mode at the particular wavelength. This means that its amplitude will grow

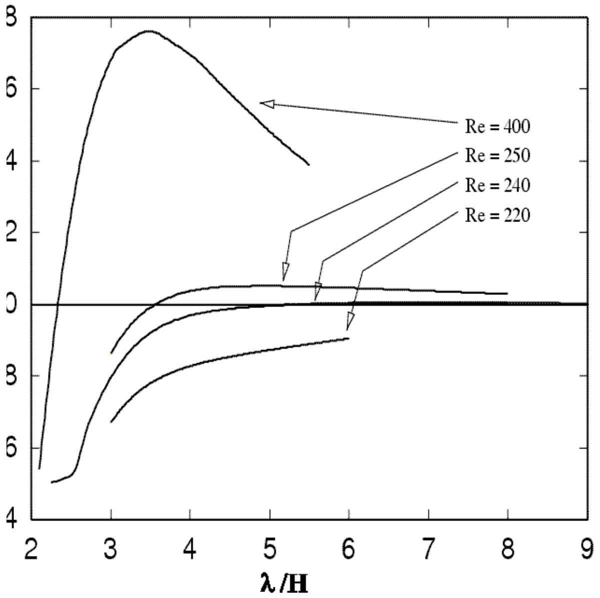

Figure 3.9: Floquet multipliers (μ) for the dominant mode at each span-wise wavelength (λ/H) for different Reynolds numbers, and for plate aspect ratio, $AR = 2.5$.

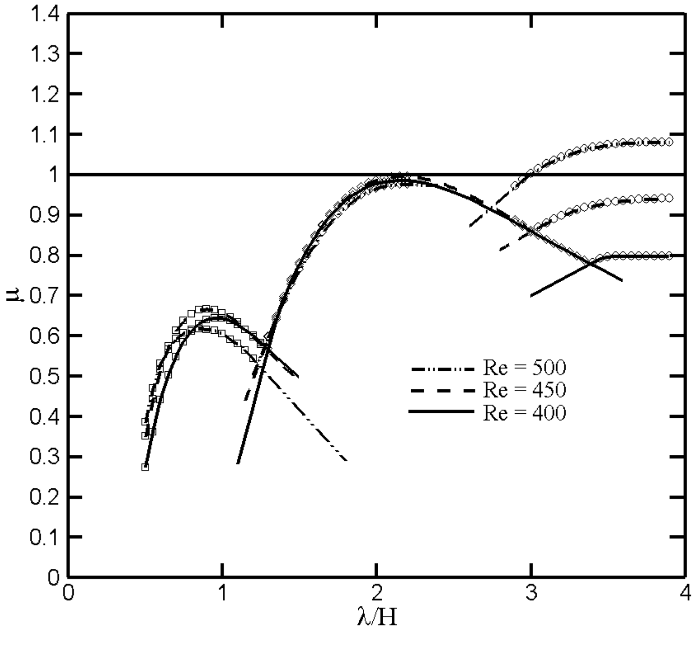

Figure 3.10: Floquet multipliers (μ) for the dominant mode at each span-wise wavelength (λ/H) for different Reynolds numbers, and for plate aspect ratio, $AR = 7.5$.

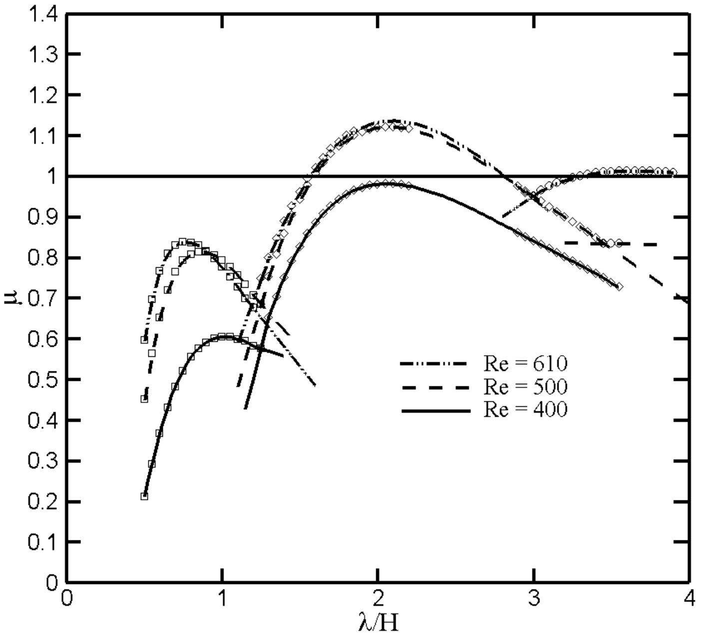

Figure 3.11: Floquet multipliers (μ) for the dominant mode at each span-wise wavelength (λ/H) for different Reynolds numbers, and for plate aspect ratio, $AR = 12.5$.

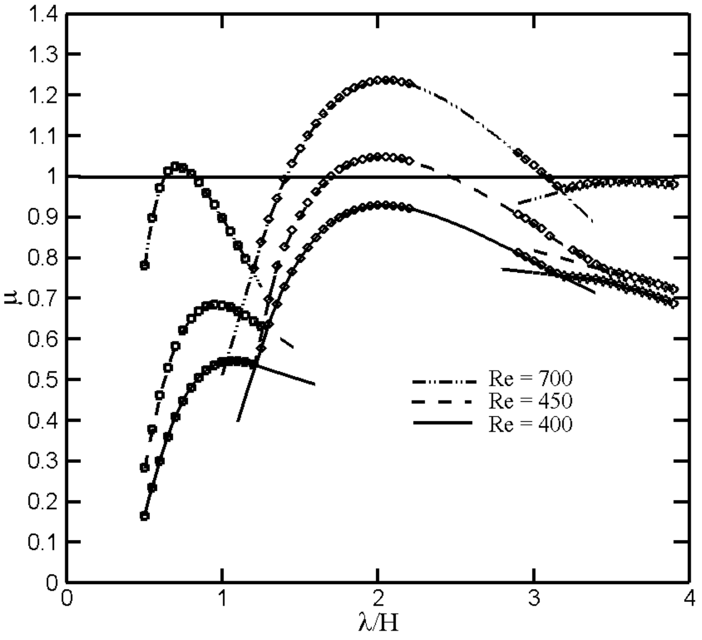

Figure 3.12: Floquet multipliers (μ) for the dominant mode at each span-wise wavelength (λ/H) for different Reynolds numbers, and for plate aspect ratio, $AR = 17.5$.

exponentially from background noise resulting in transition to three-dimensional flow.

Aspect Ratio 2.5

Figure 3.9 shows Floquet multipliers for the $AR = 2.5$ case. For wavelengths in the range $0.5 \leq \lambda/H \leq 2.0$, no clearly dominant ($T-$ periodic) Floquet mode emerged from the iteration procedure after 100 cycles for $Re \leq 500$. For higher wavelengths, the procedure converged quickly (typically within 30 cycles for four significant figure accuracy) and the Floquet multiplier variation corresponding to the dominant mode is shown on the figure for different Reynolds numbers. The instability mode first becomes unstable for $\lambda/H \simeq 7$ at a Reynolds number of approximately 240. However the instability is fairly broadband, and for $Re = 250$, the unstable range lies between $3.5 < \lambda/H < 10$. The upper limit is likely to be greater than this value, but no computations have been performed to confirm this. As the Reynolds number is increased the most unstable wavelength is reduced so that for $Re = 400$ it is approximately $3.5H$.

The spatio-temporal symmetry and the perturbation field distribution for this mode are analogous to those of the Mode A instability for the circular cylinder (Williamson (1988b)). Figure 3.13 shows a comparison between coloured contours of span-wise perturbation vorticity for the Mode A circular cylinder wake at $Re = 190$ at $\lambda/H = 4$, and the $AR = 2.5$ plate wake for $Re = 400$ and $\lambda/H = 4$. The circular cylinder Floquet mode shown here has been calculated independently and agrees with the mode structure found by Barkley & Henderson (1996). Both wake instabilities show similar near and far wake structure and the same span-wise/stream-wise vorticity topology. That is, at the same span-wise location, the span-wise/stream-wise vorticity swaps sign between each Karman vortex pair.

Aspect Ratio 7.5

Figure 3.10 depicts the Floquet multipliers for a plate of aspect ratio of $AR = 7.5$. Three distinct stability branches are observed for this case corresponding to three topologically different instability modes. For the Reynolds number range investigated, the mode corresponding to the longest wavelength instability becomes critical at $Re \approx 470$ for $\lambda/H = 3.9$. Again, this mode is topologically similar to Mode A of the circular cylinder wake and the critical wavelength is similar. In addition, as for the circular cylinder, the instability quickly becomes relatively broadband as the Reynolds number is increased.

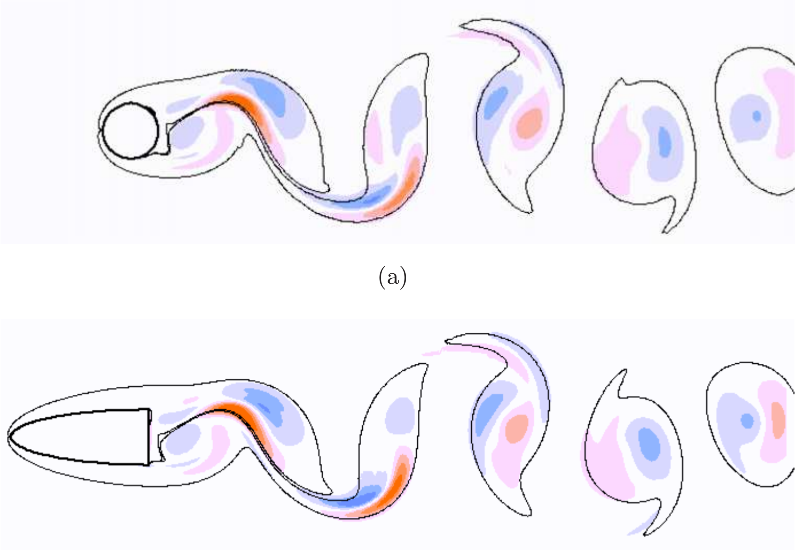

(a)

(b)

Figure 3.13: Comparison of the wake span-wise vorticity field of the Floquet mode for (a) a circular cylinder ($Re = 190, \lambda = 4D$) and (b) short plate ($AR = 2.5, Re = 240, \lambda = 4H$) showing the longer wavelength instability for the short plate is analogous to the Mode A instability of the circular cylinder. The spatial structure of the perturbation field relative to the position of the Karman vortices is highlighted by the contours of span-wise vorticity with $\omega_z = \pm 0.2$. Both images are at approximately the same phase in the shedding cycle.

At $\lambda/H = 2.2$, another local maximum is observed. For $AR = 7.5$, this mode is approximately neutrally stable over the Reynolds number range simulated in this study ($400 \leq Re \leq 500$). Its spatio-temporal symmetry is analogous to that of the Mode B instability described by Williamson (1988b). In Figure 3.14, the spatial structure of the stream-wise vorticity of the perturbation field is compared with that of Mode B for a circular cylinder wake ($Re = 259$ and $\lambda/H = 0.82$) at a similar point in the shedding cycle. The symmetry is such that the sign of stream-wise vorticity is maintained from one half cycle to the next. This is true of Mode B for a circular cylinder. However, there are some important differences in the perturbation field distributions. For the circular cylinder, the perturbation vorticity decays downstream much more quickly than for the plate. This is not surprising given the lower critical Reynolds number and hence higher relative viscous diffusion for the case of the circular cylinder. In addition, because the mode for the circular cylinder has a considerably shorter relative span-wise wavelength than that for the plate, the structures will be subject to more rapid diffusion anyway.

The difference in span-wise wavelength is surprising, especially given that the wavelength predictions for the square cylinder (Robichaux *et al.* (1999)) are similar to those for a circular cylinder if the length scale for the square cylinder is taken as the diagonal length. For both the flow past a circular cylinder and a square cylinder, the ratio of the Mode B to Mode A wavelength is between 22 and 23%. For the case of a blunt flat plate, this ratio is greater than 50%. If fact examination of Figure 3.15, which shows the perturbation stream-wise vorticity in the neighbourhood the newly-forming vortices, reveals that the near field spatial structure of the perturbation field has some important differences relative to the circular cylinder case. In the newly-forming vortex in the top half of the vortex street, the perturbation field is of a different sign for the case of the plate and the circular cylinder. This is indicated by the circles overlaid on the plots. One result of this sign reversal for the plate wake is that half a cycle later, the stream-wise vorticity of opposite sign to the dominant stream-wise vorticity pervading the braids is amplified, leading to a different local spatial structure at the corresponding downstream position. This is indicated by the arrows on the figure. Because of the differences in the near wake perturbation field and the span-wise wavelength, we will refer to this mode as Mode B$'$.

At λ/H =0.9–1.0, another local peak corresponding to a third instability mode is observed in figure 3.12. This mode remains clearly subcritical up to the highest

Reynolds number simulated for this plate aspect-ratio case. The value of λ/H corresponding to maximum growth varies with Reynolds number; a higher Reynolds number corresponds to a slightly smaller critical span-wise wavelength. The Floquet multipliers (μ) for this mode are oscillatory, indicating that the Floquet multiplier (corresponding to an analysis assuming complex eigenmodes) is actually complex. The Floquet analysis method described above cannot extract complex coefficients directly. However, the analysis was repeated assuming a complex perturbation field. Like the situation for the square cylinder (Robichaux *et al.* (1999)), the mode has a complex Floquet multiplier close to -1, and hence appears to be almost a subharmonic mode. However, as pointed out by Blackburn & Lopez (2003), a true subharmonic is extremely unlikely, and does not occur in this case either.

Interestingly, the wavelength of this mode is similar to that of Mode B for a circular cylinder wake, although the spatio-temporal symmetry is different. Figure 3.16 shows the stream-wise perturbation field close to the end of the plate, similar to the snapshots revealing Mode B and B$'$ in Figure 3.15. While the mode is time-varying from one shedding period to the next, this snapshot shows that the perturbation field structure in the newly-forming vortex structure at the top of the trailing edge, and in the near wake region, is more reminiscent of Mode B than is the intermediate wavelength Mode B$'$ instability discussed above. Thus, it may be argued this instability has more in common with Mode B than Mode S (Robichaux *et al.* (1999)) or Mode C (Zhang *et al.* (1995)), even though the spatio-temporal symmetry is different. We will refer to this mode as Mode S$'$ (even though the mode is not a subharmonic) to relate it to the time-varying mode for a square cylinder (Robichaux *et al.* (1999)).

Aspect Ratio 12.5

As the plate aspect ratio is increased to 12.5 (figure 3.11), Mode B$'$ is observed to become unstable at a lower Reynolds number than Mode A. Mode B$'$ is found to become critically unstable at a critical Reynolds number of $Re_{crit} \simeq 410$ for a critical wavelength, $\lambda/H \simeq 2.2$, whereas Mode A has a much higher critical Reynolds number of $Re_{crit} \approx 600$. This has interesting experimental ramifications. It indicates that Mode B$'$ will be the first three-dimensional wake mode observed experimentally for long aspect-ratio elliptical leading-edge cylinders. For the circular cylinder wake, it appears that the rapid transition to a chaotic wake state is due to the nonlinear interaction of the

(a)

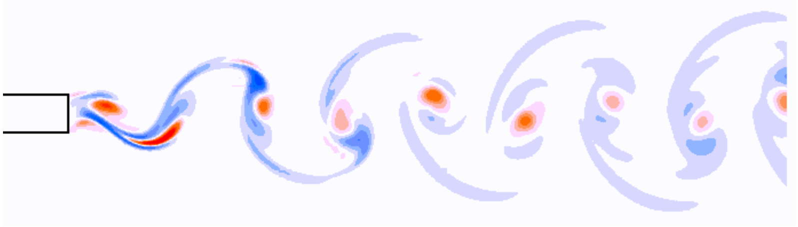

(b)

Figure 3.14: Comparison of the wake stream-wise vorticity field of the Floquet mode for the circular cylinder ($Re = 259$, $\lambda = 0.8D$) and the elliptical leading-edge plate ($AR = 7.5$, $Re = 450$, $\lambda = 2.2H$) showing the same spatio-temporal symmetries.

A and B instability modes (Henderson (1997)). Experimentally, Williamson (1996c) has shown that Mode A, unlike Mode B, is not periodic in its saturated state even for Reynolds number not far in excess of the critical value. Mode B has a relatively narrow instability wavelength band and is non-hysteretic. Therefore, for the geometry studied here, the swapping of the order of occurrence of two modes with different spatio-temporal symmetries may mean that the initial transition to three-dimensional flow is much cleaner than for a circular cylinder. Even at higher Reynolds numbers, the spectrum of wake wavelengths may be quite different to that found for a circular cylinder. This is because of the order of transition and interactions between the modes, and the different apparent dominance of the intermediate wavelength mode which does not exist for the circular cylinder wake.

As for the $AR = 12.5$ plate, Mode S$'$ remains subcritical for the range of Reynolds numbers simulated. Once again, the amplification of the perturbation field has an oscillatory component indicative of a complex Floquet multiplier. The wavelength corresponding to the slowest decay rate was found to decrease slightly with increasing Reynolds number.

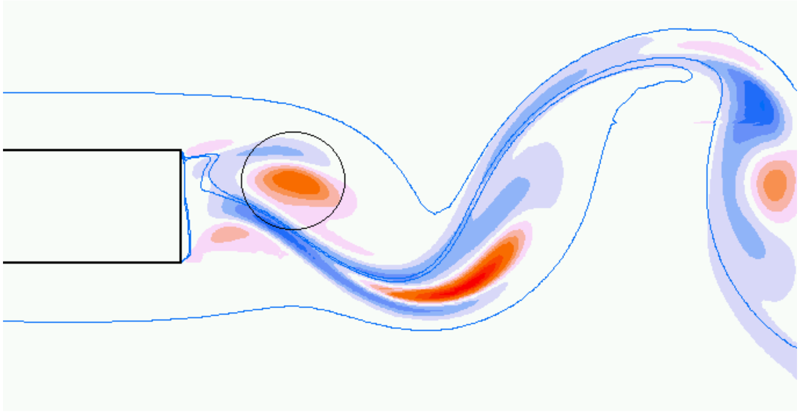

(a)

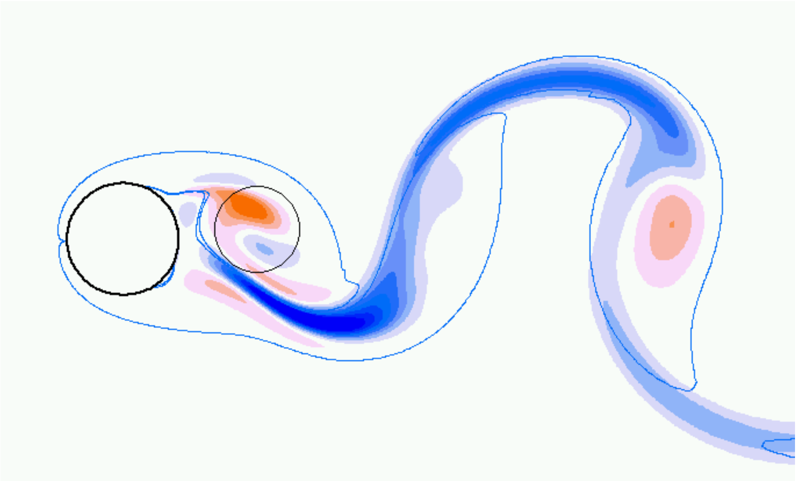

(b)

Figure 3.15: Enhanced view of stream-wise vorticity field of the Floquet mode for the elliptical leading-edge plate ($AR = 7.5$, $Re = 450$, $\lambda = 2.2H$) and the circular cylinder ($Re = 259$, $\lambda = 0.8D$). The circles overlaid on the contour plots highlight the change to the spatial distribution of the vorticity in the newly-forming vortices.

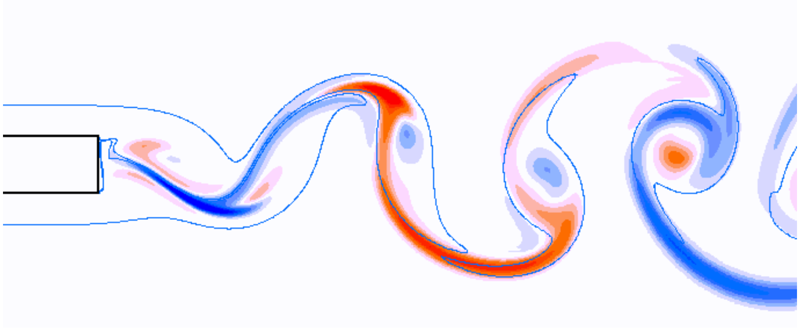

Figure 3.16: stream-wise vorticity field of the Mode S′ instability ($AR = 7.5$, $Re = 500$, $\lambda = 1.0H$). The positions of the Karman vortices are highlighted by the contours of span-wise vorticity of the base flow at $\omega = \pm 0.2$.

Aspect Ratio 17.5

The Floquet multipliers for $AR = 17.5$ are shown in Figure 3.12. Once again Mode B$'$ is found to become unstable first at a critical Reynolds number of $Re_{crit} \approx 430$. Mode A becomes unstable for $Re > 700$, with a preferred wavelength of approximately $3.5H$. Interestingly, Mode S$'$ was found to become critically unstable at $Re_{crit} \approx 690$ for $\lambda/H \approx 0.7$. Thus, both Mode B$'$ and S$'$ are more unstable than Mode A for this aspect ratio.

3.4 Comparison of Plate Aspect Ratio Results

The current choice of body geometry allows a wider parameter space study than has been presented in previous work, focusing on the effect of variation of bluff body aspect ratio, and by implication boundary layer characteristics at separation, to the wake flow field. A previous study (Roshko (1955)) indicates that different bluff body geometries generally have very similar *primary* wake structures. In this section we analyze the nature of the instabilities, the possible effect of the different orderings of critical Reynolds numbers for the onset of the instabilities, and the relationship to previous studies.

3.4.1 Critical Reynolds Numbers for Transition

Figure 3.17 depicts the critical Reynolds numbers for each three-dimensional mode transition as a function of plate aspect ratio. The curves represent approximate fits to the data. For Mode A, it was found that a relationship of the form $Re_{crit} \propto AR^{0.5}$ was found to fit the data well. For Mode B$'$, the transition Reynolds number remains approximately constant independent of aspect ratio. Note that for $AR = 7.5$, Mode B$'$ only reached approximately neutral stability ($\mu = 0.995$) at $Re = 440$. At higher Reynolds numbers, the maximum Floquet multiplier decreased slightly. Mode S$'$ becomes critical for $AR = 17.5$ but this is not shown on the figure.

3.4.2 Mode A

For all aspect ratios examined, Mode A is critically unstable at approximately the same span-wise wavelength of $3.5H$. This compares well with the experimentally observed wavelength of 3–4H (Williamson (1996c)) and the predicted critical wavelength of 3.96H (Barkley & Henderson (1996)) for a circular cylinder wake. Also, as found for the circular cylinder, at Reynolds numbers not far in excess of critical, amplification of this

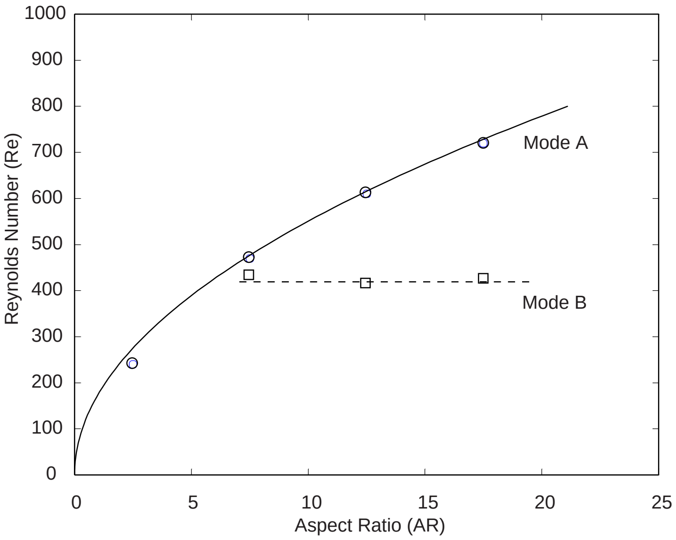

Figure 3.17: Critical Reynolds number for the different mode transitions as a function of plate aspect ratio. Here, □ indicates a Mode B′ transition and ∘ indicates a Mode A transition. The curves represent an approximate fit to the data.

mode occurs over a broad wavelength band. On the other hand, the critical Reynolds number increases significantly with aspect ratio: from $Re_{crit} \approx 240$ for $AR = 2.5$ to $Re_c \approx 700$ for $AR = 17.5$. The trend is shown in Figure 3.17. As noted, a fit to the data points is shown assuming a relationship of the form $Re_{crit} \propto (AR)^{1/2}$. While this is not perfect, it fits the data reasonably well.

It has been suggested (e.g., Williamson (1996c), Leweke & Willimson (1998), Thompson *et al.* (2001b)) that Mode A is predominantly an elliptical instability with the spanwise wavelength scaling on the length scale of the vortex cores. For a circular cylinder wake, the vortex perturbation pattern in the vortex cores appears to be clearly elliptical in nature in the wake downstream from the body. However, there has been considerable debate in the literature (*e.g.*, Henderson (1997), Thompson *et al.* (2001b)) on whether the elliptical instability mechanism is the cause of the instability in the near wake. The results for different aspect ratios are interesting in that the wavelength of the Mode A instability is approximately independent of aspect ratio and similar to that for a circular cylinder wake. For both circular cylinders and elliptical leading-edge plates, the length scale of the vortices is determined primarily by the body cross-section; the wake visualizations in this paper confirm this by showing that the vortex cores are similar in size for the different geometries. This is consistent with the hypothesis that the instability is an elliptic instability of the vortex cores.

According to standard laminar boundary layer theory, the boundary layer thickness (δ) can be approximated by (for example see Lamb (1932))

$$\delta = 5.0\left(\frac{x}{Re}\right)^{1/2},$$

where x is the distance from the (virtual) origin and the Reynolds number is based on thickness H. Thus, if the transition required that the boundary layer profile was similar as the flow enters the wake at the trailing edge, this should mean that the transition Reynolds number should vary in proportion to aspect ratio. This is clearly not the case as indicated by the approximate fit described above. On the other hand, theory suggests (see for example Le Dizes & Laporte (2002)) that the growth rate (σ) of an elliptic instability is given by

$$\sigma = \sigma_{\text{inviscid}} - \Delta\sigma_{\text{viscous}}.$$

Here the inviscid growth rate is a function of the ellipticity of vortices. Now suppose that the ellipticity of shed vortices is mainly dominated by convective effects rather than viscosity, once the vortices are shed. It would follow that if the transition Reynolds number did vary in proportion to the aspect ratio, the boundary layer thickness at the trailing edge would remain constant5, hence the elliptical form of the vortex structures in the wake should be similar and the first term contributing to the growth rate should be similar. The viscous correction is

$$\Delta\sigma_{\text{viscous}} \propto \frac{1}{Re(\lambda/H)^2},$$

where λ is the span-wise wavelength. This term reduces the amplification of short wavelength modes providing a short wavelength cutoff. An interpretation of Mode A in terms of elliptic instability theory is that Reynolds number must be high enough so that the viscous correction term does not prevent the wavelength based on the core size from growing. We have seen that the inviscid contribution to the growth rate suggests the transition Reynolds number should be approximately proportional to aspect ratio, and that the viscous correction term is inversely proportional to Reynolds number. Hence, the theory suggests that the critical Reynolds number dependence on aspect ratio should be less than linear. While this is not conclusive evidence that an elliptical instability is the controlling generic instability mechanism for Mode A, it is at least consistent.

3.4.3 Order of Appearance of Mode A, Mode B$'$ and Mode S$'$

An increase in the aspect ratio can alter the preferred mode of instability. For an aspect ratio of $AR = 7.5$, the initial instability is Mode A with a critical Reynolds number of approximately 475. As the aspect ratio is increased to 12.5, the critical Reynolds number for three-dimensional transition is approximately 450, however Mode B$'$ is now the initial mode of instability, in preference to Mode A. As the aspect ratio is further increased to 17.5, the critical Reynolds number remains close to 450, and once again Mode B$'$ is the initial instability mode. As the aspect ratio is increased still further, the critical Reynolds numbers for the Mode A and Mode B$'$ instabilities presumably become increasingly separated. Further increases in the aspect ratio may result in Mode A not becoming critical at all, or at least, the development and saturation of Mode B may lead to a distinctly different transition to turbulent flow which may not involve Mode A. For the largest aspect ratio studied ($AR = 17.5$), even Mode S$'$ becomes unstable prior to Mode A, also suggesting a further possible alteration to the transition scenario.

3.4.4 Mode B$'$

For aspect ratios between 7.5 and 17.5, a distinct instability mode with the same spatio-temporal symmetry as Mode B was found to become unstable. We have referred to this mode as Mode B$'$ based on its spatio-temporal symmetry. The critical wavelength was found to be approximately 2.2 plate thicknesses over the range of aspect ratios studied. Interestingly, the critical Reynolds number does not vary significantly with aspect ratio. Visualizations in the neighbourhood of the trailing edge reveal that the perturbation field for Mode S$'$ has more in common with Mode B than Mode B$'$. An interpretation may be that the spatio-temporal symmetry is perhaps not an ideal classification scheme. In this case, Mode S$'$ and Mode B also share a common relative span-wise wavelength, even though their spatio-temporal properties are different.

3.4.5 On the Nature of Modes

A possible interpretation of the spatial structure of the perturbation field for each of the instability modes is that one can view these instability modes as a combination of idealized generic instability types such as elliptic, hyperbolic and centrifugal, with feedback from one cycle to the next to sustain the mode, but with possibly one mechanism governing the growth rate and wavelength selection. There is reasonable circumstantial evidence that this is the case for Mode A for a circular cylinder wake (e.g., Leweke & Willimson (1998), Thompson *et al.* (2001b)) although dissenting views exist (Barkley & Henderson (1996), but also consider the discussion above). Numerical simulations and experimental visualizations of Mode A produce invariant stream-tubes as predicted by elliptic instability theory, and are consistent with the predicted span-wise wavelength and the growth rate in the core. Recently, Julien *et al.* (2003b) have shown that the primary instability modes for an idealized Bickley wake also show strong elliptical character, in that the measured local growth rate is well predicted by elliptical instability theory, even though the perturbations migrate to, and are amplified in, the braid regions where the flow is hyperbolic. Conversely, the growth rates predicted by hyperbolic instability theory do not match the observed amplification rates. Julien *et al.* (2003b) and others have suggested that the hyperbolic instability is *slaved* to the elliptic instability which controls the growth rate and wavelength selection.

There is more doubt as to the nature of the Mode B. Williamson (1996c) and Leweke & Willimson (1998) suggest that the hyperbolic instability is the dominant mechanism especially given that the mode appears to be located in the braids. Brede *et al.* (1996) have suggested that a centrifugal instability is involved in the transition. In the case here, as noted, the mode is mostly concentrated initially between the forming vortices and in the braids between the vortices as the flow convects downstream. However, given the considerably longer span-wise wavelength of Mode B$'$ for the case of a blunt flat plate than for Mode B for the circular cylinder, the elliptical instability probably plays a stronger role in the cores and may support the maintenance of the instability.

3.5 Spatio-Temporal symmetry of the Floquet modes

In the previous sections, each mode has been defined in terms of its spatio-temporal wake structures when compared to previous research. As both Mode A and B are T periodic, their symmetry over $T/2$, along with their time history over one base flow field period, T, has previously been used to distinguish them. The spatio-temporal symmetry of each mode has been summarized in Barkley & Henderson (1996) and extended in Robichaux *et al.* (1999) (described as Reflection-Translation or RT symmetry in Robichaux *et al.* (1999)). By referring to the temporal history of each mode the spatio-temporal symmetry may be inferred and compared with these previous findings.

Figure 3.18 shows contours of the temporal evolution of stream-wise vorticity, $\overline{\omega}_x$,

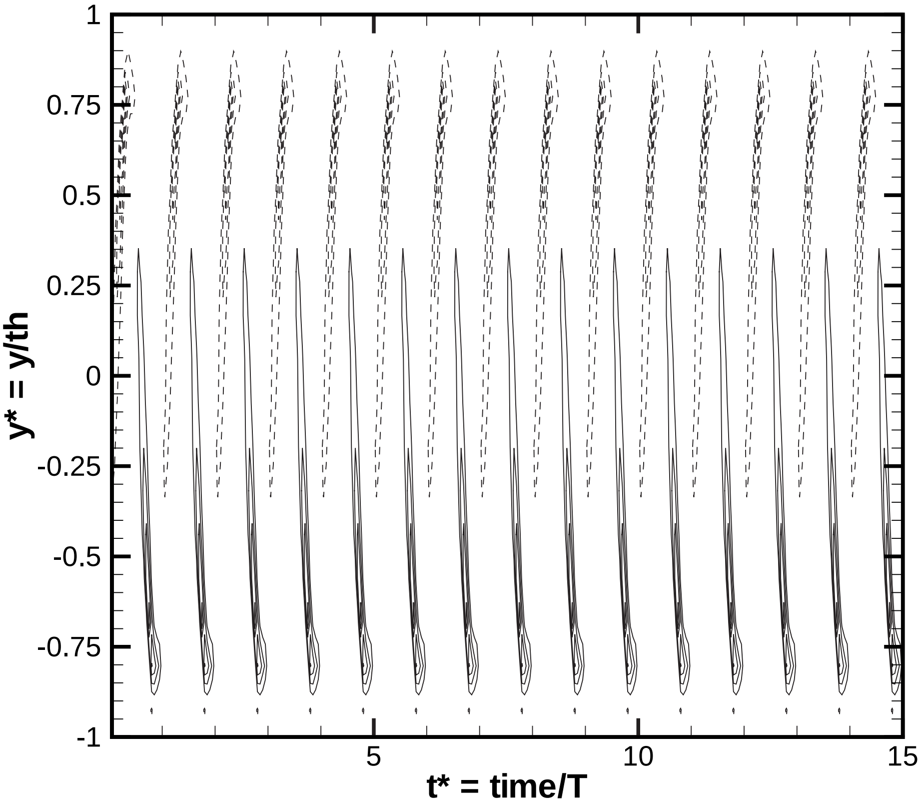

Figure 3.18: Contours of $\overline{\omega_x}$ for Mode A in the $y^* - t^*$ plane, calculated two plate thicknesses downstream of the plate trailing edge ($AR = 7.5$). Contours are evenly spaced over the range $-0.5 \leqslant \omega_x \leqslant 0.5$ with $\Delta\omega_x = 0.1$. Dashed lines indicate negative contour values.

for a plate aspect ratio, $AR = 7.5$ at a Reynolds number Re= 500, for an instability wavelength $\lambda/H = 3.9$, corresponding to a Mode A instability. The temporal evolution of $\overline{\omega}_x$ is measured along an imaginary vertical line placed 2 plate thicknesses downstream of the trailing edge for Mode A. This may be compared to figure 11a in Robichaux *et al.* (1999) which depicts Mode A for a square cylinder, along with the numerical findings of Thompson *et al.* (1996) for the flow past a circular cylinder and the experimental findings of Williamson (1988b), again for the flow around a circular cylinder. From analysis of figure 3.18, the following symmetry for Mode A may be inferred, in agreement with the findings of Williamson (1996c), Barkley & Henderson (1996) and Robichaux *et al.* (1999):

$$\overline{\omega}_x(x, y, z, t) = -\overline{\omega}_x(x, -y, z, t + T/2) \tag{3.1}$$

Figure 3.19 depicts the temporal evolution of $\overline{\omega}_x$ for the same plate aspect ratio case and Reynolds number, for an instability wavelength $\lambda/H = 2.2$ corresponding to a Mode B instability. Comparison with the findings of Robichaux *et al.* (1999), Williamson (1996b) and Barkley & Henderson (1996), show a temporal symmetry corresponding to Mode B for a circular cylinder. This is despite the span-wise critical wave-length for Mode B in this study having roughly twice the span-wise wavelength of Mode B for a circular or square cylinder ($\lambda/H \approx 2.2$ for all plate aspect ratio cases investigated in this study). From Figure 3.19, the following symmetry for Mode B may be inferred, in agreement with Robichaux *et al.* (1999), Williamson (1996b) and Barkley & Henderson (1996):

$$\overline{\omega}_x(x, y, z, t) = \overline{\omega}_x(x, -y, z, t + T/2) \tag{3.2}$$

An instability corresponding to a Mode C type has not been found for a circular cylinder, unless the geometry has been affected by the addition of a trip wire placed above the cylinder surface, and parallel to the axis of the cylinder, within the boundary layer region (Zhang *et al.* (1995)). Robichaux *et al.* (1999) found a similar mode structure in the wake of a square cylinder (with no additional trip wires) and referred to it as Mode S which was found to repeat once every second base flow field period (i.e. it was $2T$ in nature). The structure of Mode C found in the current study corresponds closely to the findings of Robichaux *et al.* (1999). The stream-wise vorticity for $AR = 7.5$ and $Re = 500$, for an instability wavelength $\lambda/H = 0.9$ corresponding to a Mode C instability is depicted in Figure 3.20. Comparison to Figure 11c in Robichaux *et al.* (1999) indicates that the temporal symmetry of Mode C corresponds very closely to the Mode S case that they found. However, as discussed in the previous section, and as is clearly evident from figure 3.20, Mode C is not $2T$ periodic as was found for Mode S for a square cylinder, as there is an imposed low frequency nT component, where $n > 2$.

For the case depicted in figure 3.20, the long period component was found to have a period $n = 12$, therefore Mode C has a $12T$ component and repeats every twelve base flow field periods; this is evident in figure 3.20. The value of n was found to vary with Reynolds number and plate aspect ratio, and the nT component does not appear to greatly affect the $2T$ component of the wake field structures. For this reason, Mode C is viewed as quasi $2T$ periodic in nature with an imposed low frequency component.

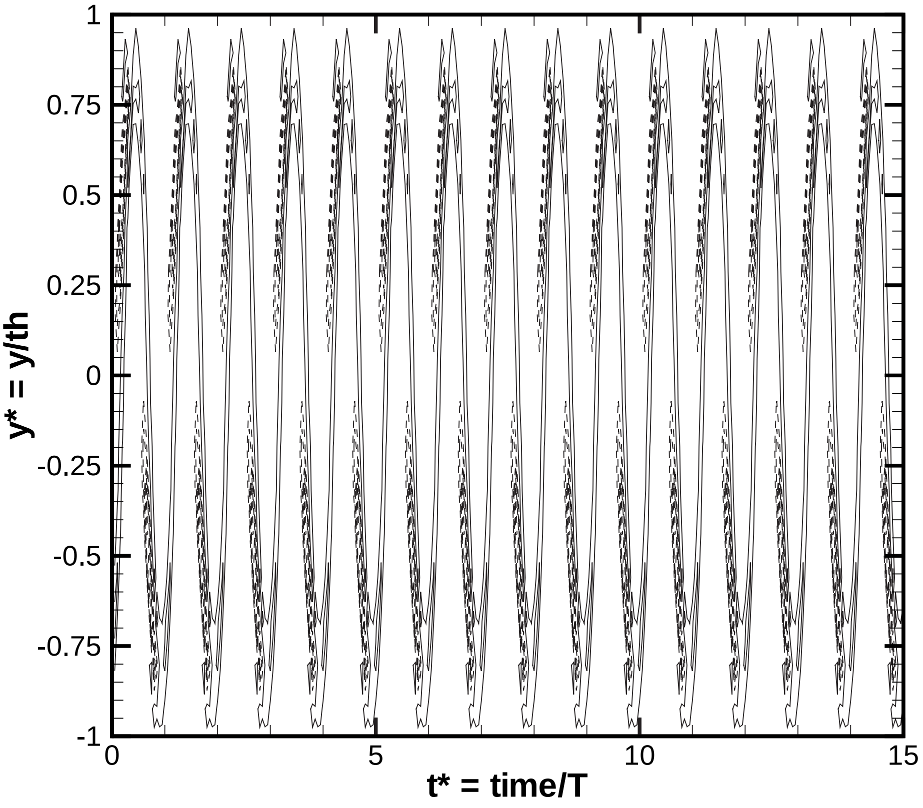

Figure 3.19: Contours of $\overline{\omega_x}$ for Mode B in the $y^* - t^*$ plane, calculated two plate thicknesses downstream of the plate trailing edge ($AR = 7.5$). Contours are evenly spaced over the range $-0.5 \leqslant \omega_x \leqslant 0.5$ with $\Delta\omega_x = 0.1$. Dashed lines indicate negative contour values.

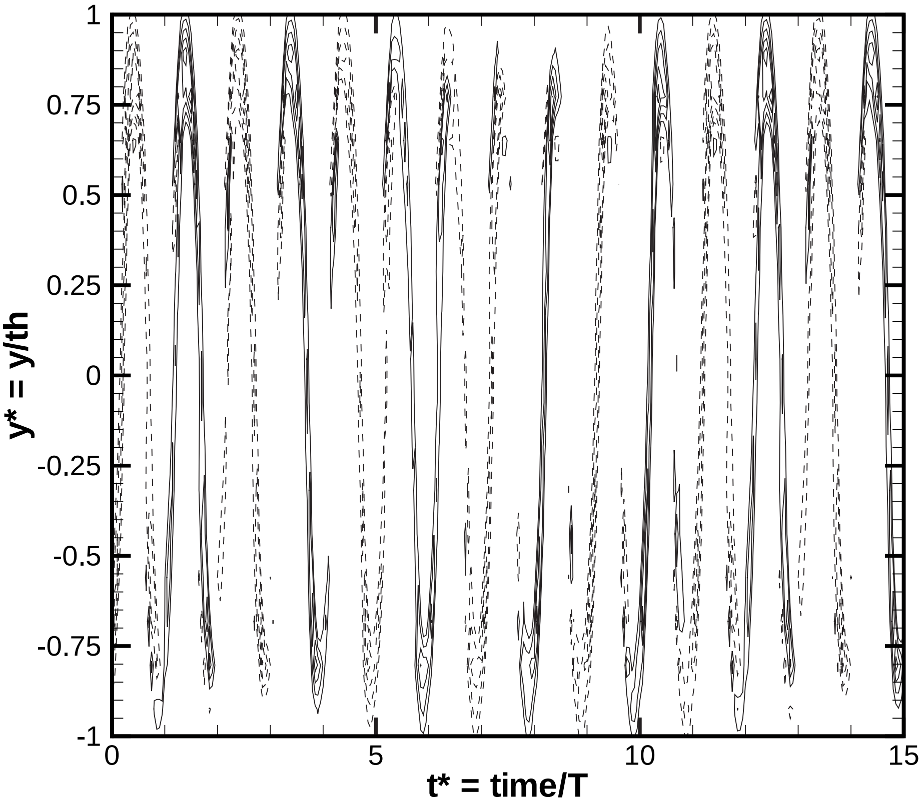

Figure 3.20: Contours of $\overline{\omega_x}$ for Mode C in the $y^* - t^*$ plane, calculated two plate thicknesses downstream of the plate trailing edge ($AR = 7.5$). Contours are evenly spaced over the range $-0.5 \leqslant \omega_x \leqslant 0.5$ with $\Delta\omega_x = 0.1$. Dashed lines indicate negative contour values.

As Mode C is quasi $2T$ periodic, its symmetry may be inferred as: :

$$\overline{\omega}_x(x, y, z, t) \simeq -\overline{\omega}_x(x, y, z, t + T) \tag{3.3}$$

In agreement with Robichaux *et al.* (1999), however, in order to include the low frequency term, the symmetry for Mode C is written as:

$$\overline{\omega}_x(x, y, z, t) = -\alpha\overline{\omega}_x\left(x, y, z, t + T\right) - \beta\overline{\omega}_x\left(x, y, z, t + \frac{nT}{2}\right) \tag{3.4}$$

where α and β are weighting coefficients and $n > 2$ ($n = 12$ for the case represented by figure 3.20). The parameters, $\alpha + \beta = 1$, such that the cycle repeats every nT.

Information regarding each of the two periods represented in equation 3.4 may be obtained from analysis of the Floquet multipliers. Here, the contributions of the $2T$ and nT components are discussed separately. In order to clearly show the effect of a periodic cycle on the Floquet multiplier, equation 2.20 has been rewritten as:

$$\mu = \frac{r'(t + T, x, y)}{r'(t, x, y)} = \exp(\zeta T)\left[\cos(\xi T) + i\sin(\xi T)\right], \tag{3.5}$$

where r' represents any of the perturbation fields (u', v', w' or p'), and ζ and ξ are the real and imaginary components, respectively, of the Floquet exponent, σ.

For the dominant $2T$ wavelength, equation 3.5 implies that the Floquet multiplier, μ, must be real and negative. The Floquet exponent, σ, must be complex, with an imaginary component $\xi = \pm\frac{\pi}{T}$; this finding is in agreement with Robichaux *et al.* (1999).

The nT wavelength implies that the Floquet multiplier, μ, representing this wavelength must be imaginary, such that the real component can be periodic with a period of nT. From analysis of equation 3.5, it may be observed that for the flow to be nT periodic, the imaginary component of σ must equal $\frac{\pi n}{2T}$.

As both the $2T$ and nT frequencies are present for Mode C, the characteristics of the Floquet multiplier should contain aspects of each wavelength. Here, the real component of the Floquet multiplier should be sinusoidally oscillating about a negative constant with a period of nT. This is indeed the case.

3.6 Three-Dimensional Topology of the Floquet Modes

The three modes found have been described in the previous sections for each aspect ratio investigated. In order to compare the topology of each mode directly, the three-dimensional structure of the wake flow field for each mode is presented for the specific case of plate aspect ratio, $AR = 7.5$, and Reynolds number, $Re = 400$. The Floquet mode topology for this case is representative of that found for other plate aspect ratio cases.

For each mode, the Floquet velocity field was computed and this was added as a small perturbation to the base flow to produce a flow field representative of the three-dimensional mode in the linear regime. In order to be able to represent Modes A, B$'$ and S$'$, perturbation fields were calculated for imposed span-wise wavelengths of $4H$, $2H$ and $1H$, respectively. For uniformity in the visualizations, the span-wise domain has been extended out to $12H$. This allows the span-wise variation to be observed and compared more easily.

Iso-surfaces of positive and negative stream-wise vorticity for Mode A are presented in Figure 3.21. The span-wise vorticity is also plotted ($\omega_z = \pm 0.2 U_\infty / D$) to highlight the position of the vortical structures instability field relative to the span-wise rollers in the wake. The swapping of the sign of stream-wise vorticity from one half cycle to the next is clearly apparent. As previously observed for Mode A, the perturbation field is strong in the braid regions between the rollers, although it is also strong inside the roller cores, but this is more difficult to discern from the plots.

Figure 3.22 shows similar isosurfaces for Mode B$'$. Twice as many span-wise structures are shown because of the reduced span-wise wavelength. At a given span-wise position, stream-wise vorticity ω_x of a given sign is generated in a fashion similar to that found for a circular cylinder (Williamson (1996c)). The sign of ω_x, at a given span-wise location, remains constant over successive shedding cycles, leading to the formation of a continuous chain of stream-wise vorticity of the same sign. The similarity to the Mode B topological structure for a circular cylinder (Williamson (1996c)) is apparent despite the much longer relative wavelength.

Figure 3.23 shows stream-wise vorticity isosurfaces for Mode S$'$. This mode is distinctly different to Mode A and B$'$ as the span-wise wavelength is much smaller in comparison and the stream-wise vorticity appears to swap sign approximately every full shedding period, which is why the corresponding mode for a square cylinder has been mistakenly identified with a subharmonic mode previously. (Note that this Floquet mode structure was obtained from a complex Floquet mode calculation, which allows for travelling modes as well as spatially stationary modes (see Blackburn & Lopez

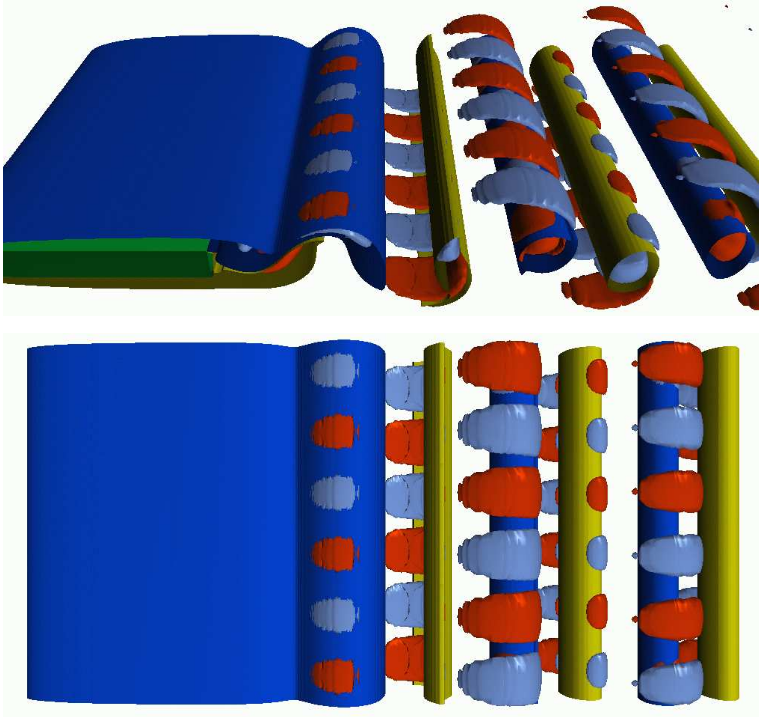

Figure 3.21: Isosurfaces of the stream-wise vorticity field for the Floquet Mode A. Isosurfaces of span-wise vorticity ($\omega_z = \pm 0.2$) are also shown to indicate the positions of the Karman vortices. ($Re = 400$, $AR = 7.5$).

(2003)).

3.7 Three-Dimensional DNS Calculations

Floquet analysis has uncovered two important features of the Mode B′ instability in the wake of a aerodynamic leading-edge, blunt trailing-edge flat plate. Mode B′ was found to have a consistent critical wavelength $\lambda/H = 2.2$ across all aspect ratio plates investigated; this value varies markedly from that for small aspect bodies studied previously, i.e., either circular or square cylinders. Also, for sufficiently large plate aspect ratio, Mode B′ was found to precede the transition to Mode A, once again in contrast to the observed ordering for circular and square cylinders. There was also evidence presented that the perturbation field in the near wake, and the span-wise wavelength, have more in common with Mode S of a square cylinder than Mode B. In order to verify these findings, and investigate the transition towards the saturated state, a three-dimensional direct numerical study was performed for an aspect ratio where Mode B′ is dominant and Mode A is also unstable. The Floquet analysis shows these criteria occur for $AR = 12.5$ and $Re = 600$.

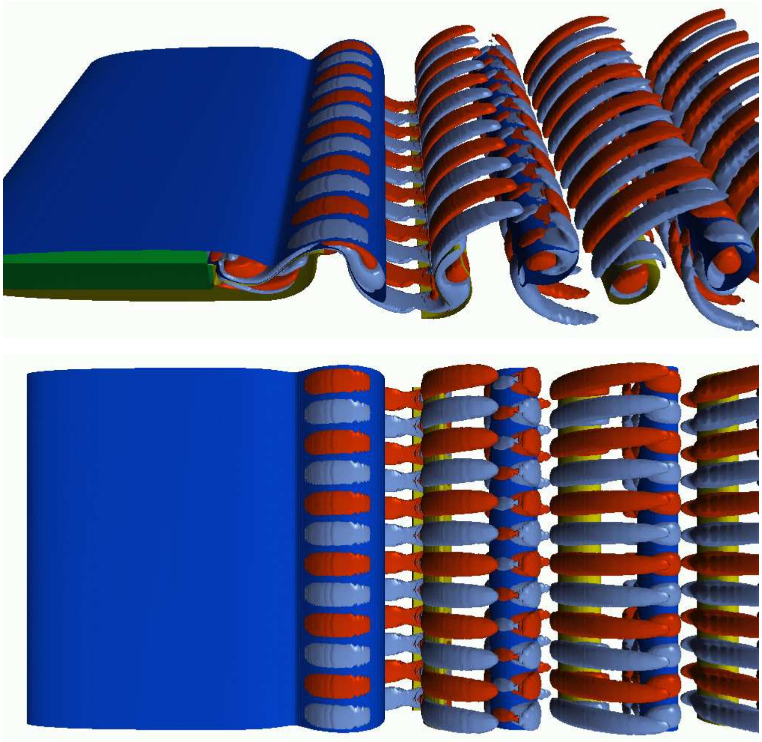

Figure 3.22: Isosurfaces of the stream-wise vorticity field for the Floquet Mode B′. Isosurfaces of span-wise vorticity ($\omega_z = \pm 0.5$) are also shown to show the positions of the Karman vortices. The selected span-wise wavelength is $2H$ with 6 wavelengths are shown. ($Re = 400$, $AR = 7.5$).

Figure 3.23: Isosurfaces of the stream-wise vorticity field for the Floquet Mode S$'$. Isosurfaces of span-wise vorticity ($\omega_z = \pm 0.5$) are also shown to show the positions of the Karman vortices. Span-wise wavelength is $1H$ and 12 wavelengths are shown. ($Re = 400$, $AR = 7.5$).

Full three-dimensional simulations were undertaken using a Fourier/spectral-element code documented and validated in Thompson *et al.* (2001a) and Thompson *et al.* (1996) to explore the wake evolution from two-dimensional periodic flow to a fully three - dimensional saturated wake flow. This calculation assumes a Fourier series representation in the span-wise direction and hence periodicity is enforced. This places a restriction on the allowable span-wise wavelengths, determining both the upper wavelength limit and the discrete wavelength spectrum. For the parameters discussed above, a span-wise domain size of $12H$ was chosen. This allows three Mode A wavelengths to fit inside the domain (and approximately six and twelve Mode B$'$ and S$'$ wavelengths). Sixty-four Fourier planes were used for the computation, corresponding to about 12 planes (six modes) per Mode B$'$ wavelength. Whilst this is somewhat minimal, these full three-dimensional simulations are still computationally expensive. Previous experience indicates that this discretisation should still provide reasonable resolution for the saturated mode.

Figure 3.24 shows stream-wise and span-wise vorticity isosurfaces for the DNS investigation once the flow has reached a quasi-asymptotic state. The simulation was continued for approximately 30 shedding cycles after the wake saturated; however, at the end of this time there was still some irregularity in downstream velocity traces at selected points. The simulation was discontinued at this time without resolving whether the final state would become truly periodic. The stream-wise vortex structures shown here resemble the Mode B$'$ isosurfaces shown in Figure 3.22. The main difference is the pinching together of the opposite signed vortex structures at their heads in line with many other studies (e.g., Henderson (1997)). The spatio-temporal symmetry of the saturated mode is clearly identical to that of Mode B$'$. There are six wavelengths shown in the figure, indicating a selected span-wise wavelength of $2H$, consistent with the preferred wavelength of the Floquet mode. There is no visual evidence of any remnant of Mode A in the visualisation, although perhaps this is not surprising given the relative amplification of Mode A and B$'$ at the Reynolds number of the simulation. This simulation supports the findings of the Floquet analysis.

3.8 Conclusions

Floquet stability analysis has been presented quantifying the three-dimensional instability modes associated with the two-dimensional periodic base flow of an elliptical

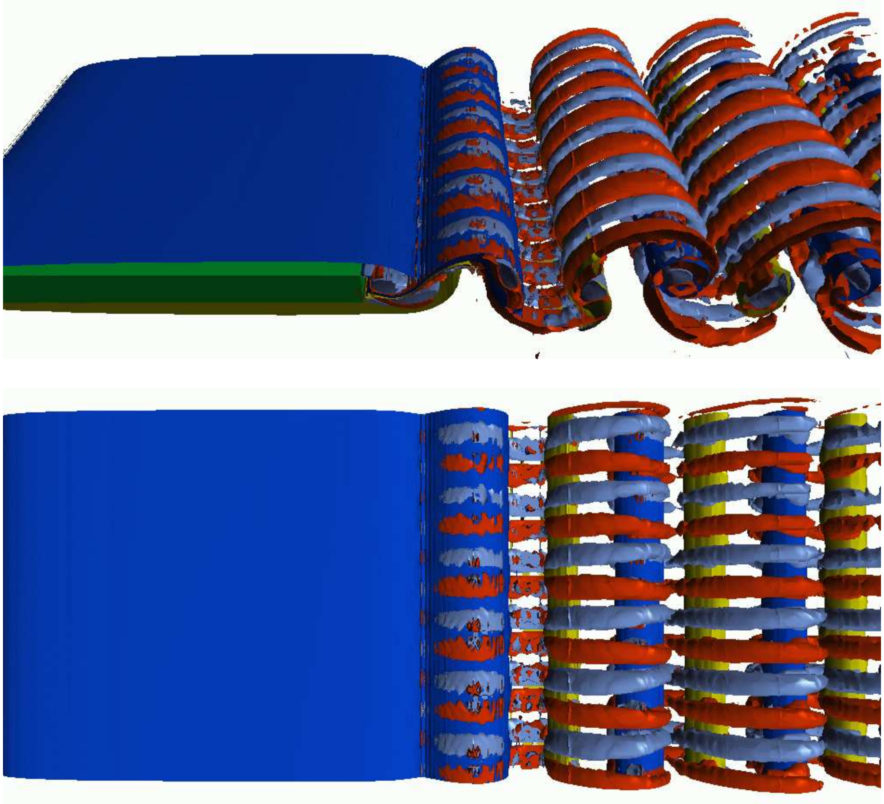

Figure 3.24: Stream-wise vorticity contours from three-dimensional DNS calculation for $AR = 12.5$ and $Re = 600$ showing Mode B instability. Red and Blue iso-surfaces represent ω_x, yellow iso-surfaces represent ω_z the plate is shown as green.

leading-edge, square trailing-edge plate. The three modes show both some similarities to, and differences from, the three instability modes, A, B and S, previously identified for compact bodies. For very short bodies, Mode A is clearly dominant and it is expected that the transition scenario may be similar to that for a circular cylinder. For intermediate aspect ratio bodies ($AR > 7.5$) the intermediate wavelength instability mode, Mode B$'$, undergoes transition at the lowest Reynolds number, This has the same spatio-temporal symmetry of Mode B for a circular cylinder but a much longer wavelength ($2.2H$ compared to $0.8D$), and there is evidence that these instabilities are distinctly different in the near field. For very long aspect ratio bodies, the difference in critical Reynolds numbers for Modes B$'$ and A becomes more substantial, potentially indicating that Mode A may play a very much reduced role, if any, in the transition to turbulence. For $AR = 17.5$, the shortest wavelength instability mode is even more unstable than Mode A, again possibly affecting the transition scenario.

A recent paper by Sheard *et al.* (2003) investigated the three-dimensional instability modes for flow past a toriod with its axis parallel to the oncoming flow. As the aspect ratio is varied, this geometry bridges the gap between the axisymmetric geometry of a sphere (small aspect ratio) and that of a two-dimensional circular cylinder (infinite aspect ratio). There were different sets of instability modes depending on the aspect ratio. For large aspect ratios, three important instability modes were found: Mode A and B, analogues of the circular cylinder mode; and Mode C, the intermediate wavelength mode which is a subharmonic. In this case, it is possible for a true subharmonic to exist since the group properties of the system are different from those governing flow past a circular cylinder (Blackburn & Lopez (2003)). Specifically, the symmetry about the cylinder centreplane no longer holds because of the curvature of the body. For intermediate aspect ratios, Mode C is the most unstable mode. Even though this is not strictly a two-dimensional cylindrical body, it is a related case and, like the situation for the bluff body considered in this paper, again indicates that transition may be less generic than previously assumed.

Finally, a full three-dimensional simulation was performed which produced a quasi-asymptotic state consistent with the findings of the Floquet analysis. Ideally, it would be advantageous to undertake simulations at significantly higher Reynolds numbers to investigate possible interactions between modes and transition to turbulence but this would require very long integration times and be very expensive computationally. We are planning to investigate this problem experimentally in the near future.

Chapter 4

A Freely Oscillating Cylinder at an Infinite Reduced Velocity and very low Reynolds Numbers

4.1 Introduction

This chapter investigates the vortex-induced vibration of a hydro-elastically mounted cylinder, free to oscillate transverse to the flow field. The specific case of an infinite reduced velocity was investigated for a range of mass ratios, $m^* = [0.075, 0.7]$, and a Reynolds number range, $Re = [30, 300]$. All simulations were conducted using a two-dimensional domain as discussed in section 2.5. The case of an infinite reduced velocity corresponds to setting the mechanical spring stiffness, k, to zero. The damping constant was set to zero.

While an infinite reduced velocity represents an impractical case, Govardhan & Williamson (2000) and Govardhan & Williamson (2003) found a critical mass ratio $m^*_{crit} \simeq 0.54$ for $Re \sim [1000, 10000]$, below which large peak-to-peak oscillations were observed up to and including $u^* = \infty$, as discussed in section 1.6. Govardhan & Williamson (2003) further found that prior numerical simulations by Shiels *et al.* (2001) at $Re = 100$ exhibited a critical mass ratio of $m^*_{crit} \simeq 0.25$. It is clear therefore that the critical mass ratio varies with Reynolds number. The principal aim of this study is to determine the variation in the critical mass ratio as a function of Reynolds number in the range $Re = [30, 300]$. The mass ratio range has been chosen in order to accurately establish a critical mass ratio in the Reynolds number range of interest. The technique used (see sections 2.4.1 and 2.4.3 for details) does not allow for the limiting case of $m^* = 0$, hence limiting the present investigation to finite mass ratio cylinders.

The results of this study may find direct application in nano-technology and biomechanical fields. Further to this, the amplitude response, fluid forcing, frequency response and flow field structures are established in order to classify the fluid-body interaction across a range of Reynolds numbers and mass ratio.

4.2 Oscillation Amplitude Results

The amplitude results, as a function of mass ratio, are presented in figures 4.1 to 4.3. The results have been separated into two distinct Reynolds number ranges; the viscous range corresponding to $Re = [40, \sim 100]$, and the higher Reynolds number range corresponding to $Re = [\sim 100, 300]$. While the higher Reynolds number range may extend beyond $Re = 300$, Reynolds numbers above this value are beyond the scope of this present study. No discernable cylinder oscillations were observed for $Re \lesssim 40$.

The Viscous Range

Figure 4.1 shows the amplitude as a function of m^* for the viscous range. In this range, the maximum incremental size of Reynolds number was $\Delta Re = 10$. For $Re = 40$, the lowest Reynolds number at which oscillations were observed, the amplitude was considerably lower for all mass ratios (mass ratios investigated for Re = 40 were $m^* = [0.2, 0.4]$) when compared to the higher Reynolds number cases ($Re = [60, 95]$), the largest oscillation amplitude being $A^*_{max} \sim 0.14$ for $m^* = 0.2$, this corresponds to the lowest mass ratio considered at $Re = 40$, and it is possible that larger amplitude oscillations may occur at still lower mass ratios for $Re = 40$.

The relationship between m^* and A^* for $Re = 40$ was different to that at higher Reynolds numbers, where the amplitude appears to exponentially decay to a finite value as m^* was increased. For $Re = 40$, the oscillation amplitude approaches zero as m^* is increased and does not appear to approach a constant amplitude for larger mass ratios in the range investigated.

As the Reynolds number is increased to $Re = [50, 60]$, the amplitude of oscillation appears to smoothly increase with decreasing mass ratio. For the case of $Re = 50$, the amplitude was somewhat greater than the case of $Re = 60$ for all mass ratios investigated, this offset increasing as $m^* \to 0$. The relationship between A^* and m^* was found to be best approximated by an equation of the form:

$$A^* = \alpha \cdot e^{-2.2m^*}, \qquad Re = [50, 60] \tag{4.1}$$

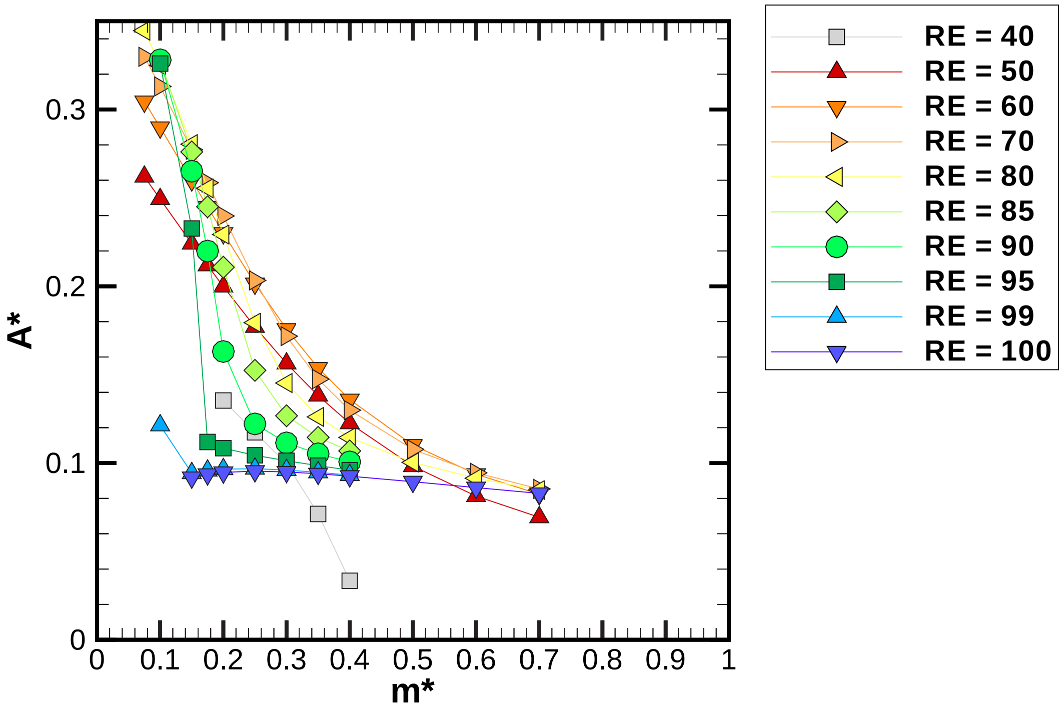

Figure 4.1: Cylinder oscillation amplitude as a function of mass ratio for Reynolds numbers in the viscous range ($Re = [40, 100]$).

with a coefficient of determination, $R^2 = 0.989$. Here the coefficient, α was found to be related to the Reynolds number as,

$$\alpha = 0.0045 \cdot Re, \qquad Re = [50, 60]. \tag{4.2}$$

Combined, equations 4.1 and 4.2 can be used to estimate the amplitude of oscillation in the limiting case of $m^* \to 0$. For $Re = 50$, this was found to be $A^*_{(m^* \to 0)} = 0.225$ and for $Re = 60$, this was found to be $A^*_{(m^* \to 0)} = 0.270$. From the form of equation 4.1, it is predicted that $A^*_{(m^* \to 0)}$ corresponds to the largest amplitude expected for the case of zero spring stiffness ($k = 0$) and zero damping ($\zeta = 0$). This is in qualitative agreement with the findings of Shiels *et al.* (2001).

At higher Reynolds numbers (but still within the viscous range), a sharp increase in the amplitude is observed as the mass ratio is decreased below a critical value. This was initially noted for $Re = 70$; here the amplitude of oscillation was slightly lower than for $Re = 60$ in the mass ratio range $m^* = [0.25, 0.6]$ and a change in gradient is observed at $m^* \simeq 0.35$. As the Reynolds number was increased above $Re = 70$, the mass ratio at which this change in gradient occurred decreased with increasing Reynolds number until at $Re = 100$, no discernable increase in A^* was observed for all mass ratios investigated ($m^* = [0.075, 0.7]$ for $Re = 100$).

In the range, $Re = [50, 99]$, a peak amplitude of $A^* = 0.35$ occurred at the lowest mass ratio investigated ($m^* = 0.075$), independent of Reynolds number. However at slightly higher Reynolds numbers, $Re = [95, 100]$, the peak amplitude rapidly decreases with Reynolds number. At $Re = 99$, the maximum amplitude observed, $A^*_{max} \simeq 0.15$ which was only observed for $m^* = 0.075$; and at $Re = 100$, $A^*_{max} \simeq 0.1$, which corresponds to roughly the same amplitude observed for all mass ratios investigated.

In summary, three observations are made for Reynolds numbers in the viscous range; the critical mass ratio (taken as the mass ratio below which large amplitude oscillations are observed) decreases with increasing Reynolds number, the maximum amplitude of oscillation also decreases with Reynolds number, and the maximum amplitude is always noted at the lowest mass ratio investigated, giving cause for speculation that the maximum amplitude possible occurs as $m^* \to 0$.

The Higher Reynolds Number Range

Figure 4.2 shows the amplitude of oscillations as a function of mass ratio for Reynolds numbers in the range $Re = [150, 200]$. The amplitude response of $Re = 100$ presented earlier is virtually identical to the case of $Re = 150$; for this reason intermediate Reynolds numbers were not investigated.

For Reynolds numbers in the range $Re = [150, 170]$, the amplitude increased gradually with mass ratio in the range investigated. However at $Re = 180$ a small increase in A^* was noted when $m^* \simeq 0.075$ when compared to higher mass ratio cases. At $Re = 190$ a slightly larger jump in A^* was noticed with $\Delta A^* = 0.013$ at $m^* \simeq 0.075$ when compared to higher mass ratios.

As the Reynolds number was increased to $Re = 200$, the size of the jump increased dramatically, and the mass ratio at which the jump was noted increased to $m^* \simeq 0.1$. This trend in both the size of the jump and the mass ratio at which the jump occurs (referred to here as the critical mass ratio, m^*_{crit}) continues for the cases $Re = 250$ and

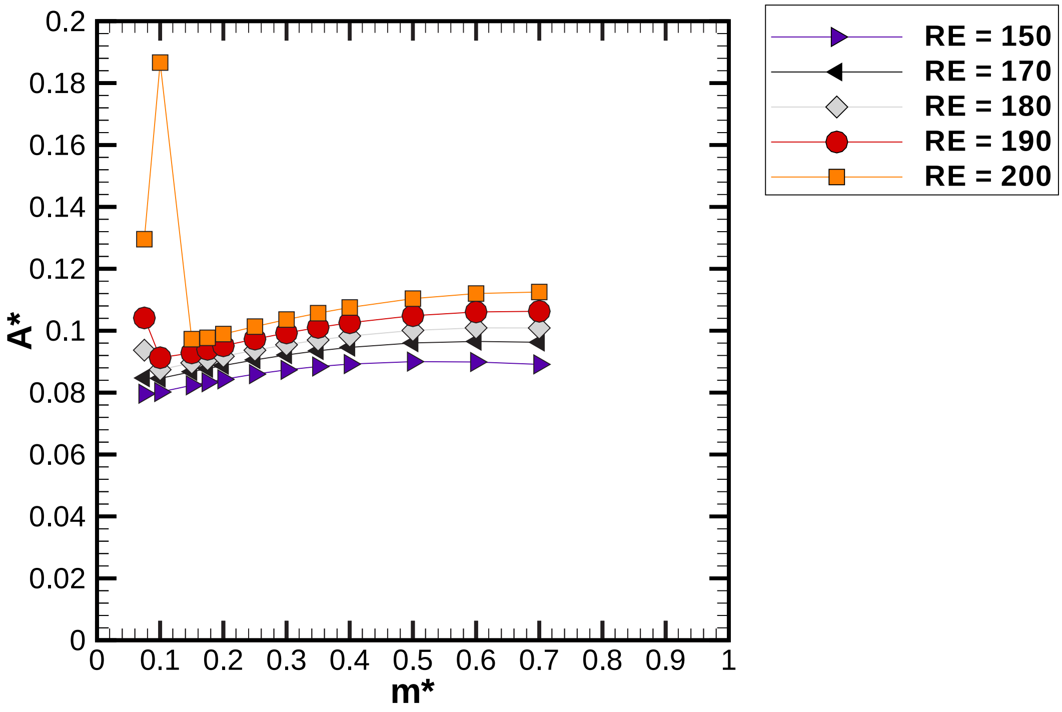

Figure 4.2: Cylinder oscillation amplitude as a function of mass ratio for Reynolds numbers in the higher Reynolds number range ($Re = [100, 200]$.

$Re = 300$ (see figure 4.3).

For both $Re = 250$ and $Re = 300$ the flow field is intrinsically three-dimensional in nature (see section 1.3.3) and the two-dimensional simulations model the flow field with considerably less accuracy then for lower Reynolds numbers. These two Reynolds numbers were considered to determine whether the trend noted in the amplitude response and critical mass ratio continues at higher Reynolds number. With this qualification, the trend of larger amplitude response and higher critical mass ratios continued up to $Re = 300$.

For both $Re = 200$ and 250 and for mass ratios below m^*_{crit}, the amplitude of oscillations fluctuated significantly with mass ratio. These fluctuations were not observed at any other Reynolds number investigated, and are shown in the time series data presented in section 4.3.

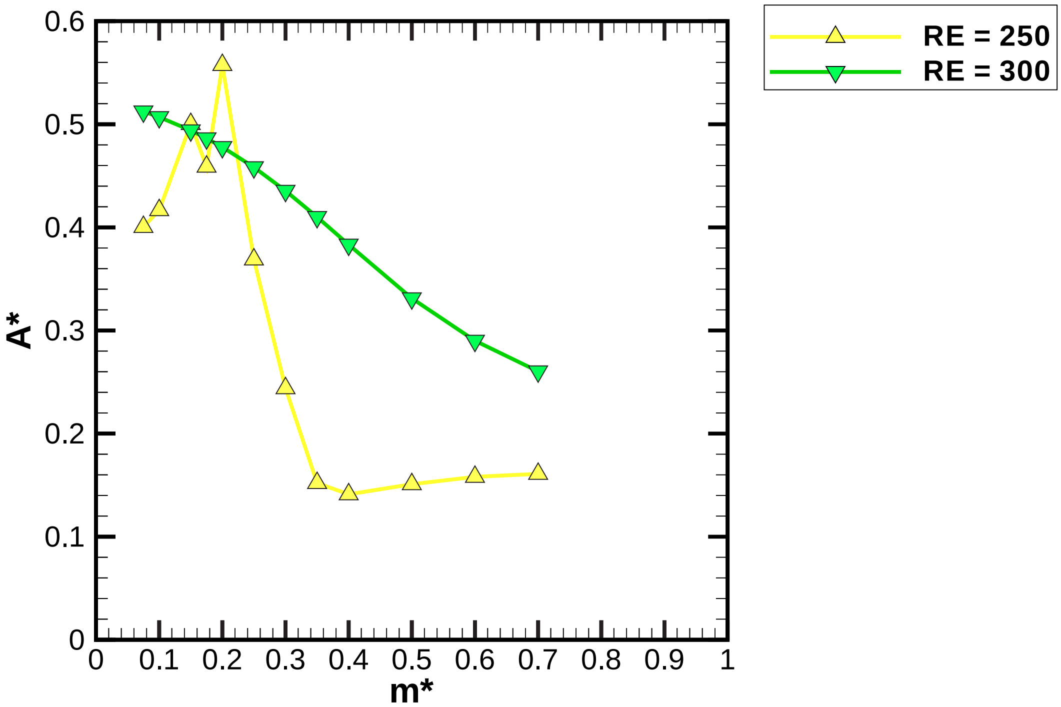

Figure 4.3: Cylinder oscillation amplitude as a function of mass ratio for Reynolds numbers in the higher Reynolds number range ($Re = [250, 300]$.

4.2.1 Maximum Amplitude Results

Figure 4.4 shows the maximum amplitude of oscillation as a function of Reynolds number in the range investigated ($Re = [40, 300]$). It should be stressed that A^*_{max} found here is only for the range $m^* = [0.075, 0.7]$. From the trends noted in A^* as a function of m^* in section 4.2, high amplitude results (with $A^* > A^*_{max}$ determined in this section) may be observed for $m^* < 0.075$. Again, from section 4.2, it is anticipated that for $m^* > 0.7$, $A^* < A^*_{max}$.

In the range, $Re = [40, 80]$, the maximum amplitude increases smoothly with Reynolds number, and was found to be best approximated by the cubic polynomial:

$$A^*_{max} = (6.14 \times 10^{-6})Re^3 - (1.28 \times 10^{-2})Re^2 + (8.97 \times 10^{-2})Re - 1.8, \qquad (4.3)$$

with a coefficient of determination, $R^2 = 0.988$. Equation 4.3 predicts that $A^*_{max} = 0$

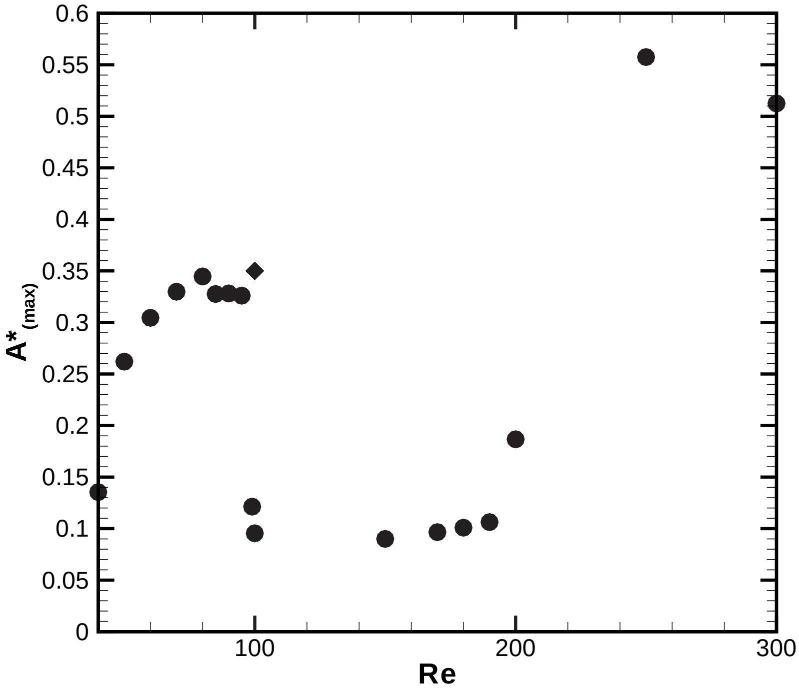

Figure 4.4: • Maximum oscillation amplitude as a function of Reynolds number for cylinder mass ratios in the range $m^* = [0.075, 0.7]$ and $Re = [40, 300]$. ♦ Oscillation amplitude results for Shiels *et al.* (2001) with $m^* = 0.16$, $k = 0$, $c = 0$, representing the highest oscillation amplitude reported for a finite m^*.

when $Re \simeq 34$ in agreement with the observations presented in section 4.2, which found no oscillations below $Re = 35$. This is also in good agreement with the findings of Taneda (1956) in his experimental examination of a the flow past a fixed cylinder at low Reynolds numbers. He found perturbations in the recirculation region for $Re \simeq 35$ as discussed in section 1.3.1. From section 1.2, any perturbations in the wake will result in a net force acting on the cylinder.

As the Reynolds number is increased from $Re = 80$ to $Re = 85$, a small discontinuous drop of $\Delta A^*_{max} = 0.017$ representing a 5% decrease in the maximum amplitude observed as the Reynolds number is increased. Beyond this discontinuity, the maximum amplitude of oscillation remains constant for the range $Re = [85, 95]$.

In the range $Re = [95, 100]$, a significant drop in A^*_{max} is noted from $A^*_{max} = 0.326$ at $Re = 95$ to $A^*_{max} = 0.0954$ at $Re = 100$, representing a 70% decrease in the maximum amplitude of oscillation over $\Delta Re = 5$. In this Reynolds number range, the largest amplitude was found to occur at $m^* = 0.075$ (i.e. $A^*_{max} \equiv A^*_{m^*=0.075}, Re = [95, 100]$). This result is somewhat different to the results obtained from simulations performed by Shiels *et al.* (2001), at $Re = 100$, of a freely oscillating cylinder with $m^* = 0.16$, $c^* = 0$ and $u^* = \infty$; where they found the amplitude of oscillation $A^* = 0.35$. For their limiting case of $m^* = 0$, Shiels *et al.* (2001) found an even higher amplitude of oscillation of $A^*_{max} = 0.47$ (representing the highest amplitude oscillation found in their study for the case of $u^* = \infty$). Their finding at $m^* = 0.16$ is shown for comparison in figure 4.4. Their finding at $m^* = 0$ falls outside the range of m^* considered in the present investigations.

When comparing the present results to Shiels *et al.* (2001)'s findings, two conclusions may be drawn. The first, as has been previously discussed, is that $m^* = 0$ would appear to represent the case of highest amplitude oscillation for all Reynolds numbers investigated in the current study. Their results at $m^* = 0$ exhibit significantly larger amplitudes than any found at $Re = 100$ in this study. It may therefore be concluded that by looking at $m^* < 0.075$, higher amplitude responses should be observed for all Reynolds numbers investigated. Second, Shiels *et al.*'s simulations employed a vortex method which approximates the Laplacian viscous term separately in the solution of the Navier-Stokes equations; these methods are best suited to low viscous (high Reynolds number) flow, where the viscous term does not significantly add to the total force acting on the cylinder. It is therefore unknown how accurately Shiels *et al.*'s technique can simulate the flow at $Re = 100$; indeed, their results are reminiscent of the present findings at $Re = 80$.

Studies characterizing the viscous and pressure components of force in the flow around a circular cylinder by Henderson (1995) indicate that dramatic changes in the viscous drag component as a function of Reynolds number occur at $Re \lesssim 100$. It is unclear from Shiels *et al.* (2001) how well these changes are captured using their vortex method.

In the range $Re = [100, 190]$, A^*_{max} is almost independent of Reynolds number, and remains very small. However a slight increase is observed as the Reynolds number is increased.

Between $Re = [190, 300]$, the maximum amplitude increases significantly with Reynolds number, up to $A^*_{max} \simeq 0.55$ for $Re \geqslant 250$. A decrease in the maximum amplitude is noted as the Reynolds number is increased from $Re = 250$ to 300. From time series analysis (see section 4.3), a beating phenomenon is observed for both $Re = 200$ and 250. This phenomenon was not observed for Re = 300. Comparing the root-mean-square amplitude at both $Re = 250$ and $Re = 300$, we found that at $Re = 250, A^*_{max-RMS} = 0.28$ and at $Re = 250, A^*_{max-RMS} = 0.36$. Therefore, while A^*_{max} undergoes a slight decrease as the Reynolds number is increased from $Re = 250$ to 300, the maximum RMS amplitude increases with increasing Reynolds number. It should again be noted that two-dimensional simulations for Reynolds numbers beyond 200 do not model the three-dimensional structures observed in the flow field experimentally, and may not reflect experimental time history and amplitude results.

4.2.2 Variation in the Critical Mass Ratio as a Function of Reynolds Number

As discussed in the previous section, a critical mass ratio has been found and below which large amplitude oscillations have been observed. This finding is in qualitative agreement with the findings of Govardhan & Williamson (2000) and Govardhan & Williamson (2003), as will be discussed below. Because the peak amplitude of oscillation varies with Reynolds number, the critical mass ratio is defined in these results as the mass ratio at which a jump (or change in gradient) is observed in the $[m^*, A^*]$ parameter space.

Figure 4.5 shows m^*_{crit} as a function of Reynolds number. As can be seen, two distinct regions exist where a finite critical mass ratio could be determined. The first region, existing in the Reynolds number range $Re = [40, 99]$, corresponds to the viscous range. For low Reynolds numbers ($Re = [50, 70]$), the amplitude response of the cylinder was very similar, and the critical mass ratio was found to be constant ($m^*_{crit} \simeq 0.5$). Still within the viscous range, but at slightly higher Reynolds numbers, the critical mass ratio decreases with increasing Reynolds number, such that, at $Re = 99$, the critical mass ratio is $m^*_{crit} \simeq 0.075$.

In the Reynolds number range $Re = [100, 170]$, no discernable critical mass ratio was observed in the mass ratio range investigated in this study, however it may be possible that a critical mass ratio exists below the range of mass ratios considered (i.e. $m^* < 0.075$). For Reynolds numbers in the range $Re = [180, 300]$, a critical mass ratio was determined, the value of which is observed to increase sharply with Reynolds number.

Figure 4.6 compares the present findings of the critical mass ratio with the findings

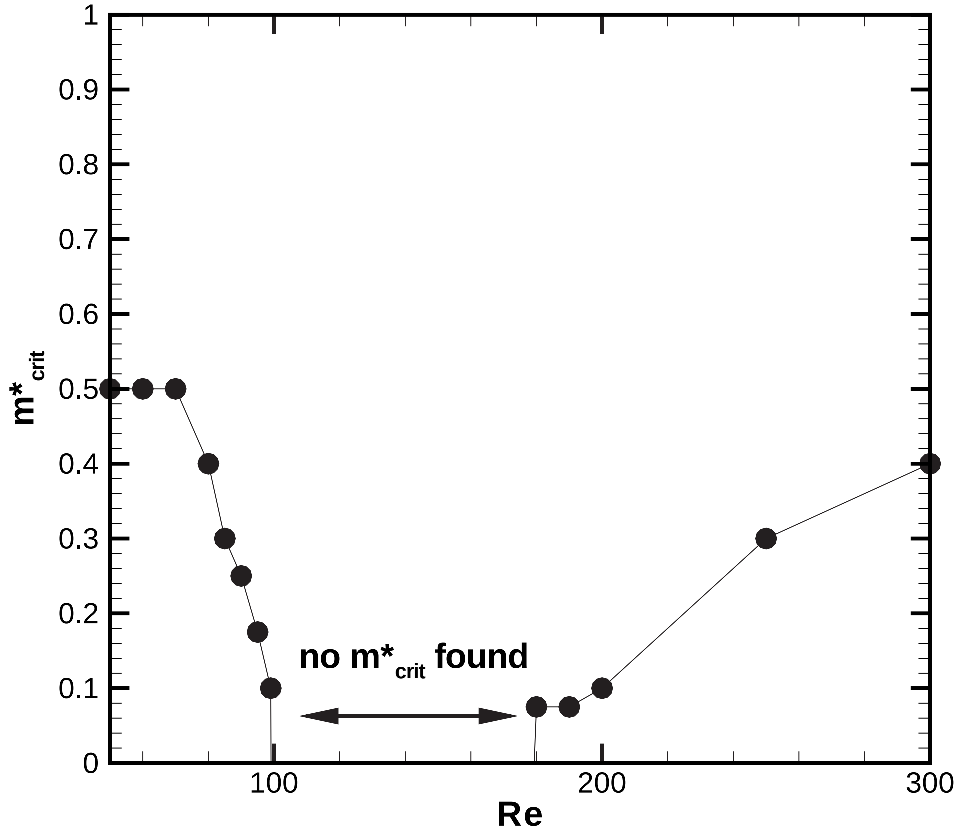

Figure 4.5: Variation of the critical mass ratio as a function of Reynolds number

of Govardhan & Williamson (2000) and Govardhan & Williamson (2003), where the results for $Re = 100$ are from simulations reported by Shiels *et al.* (2001). As can be seen, the critical mass ratio found from our simulations for $Re = [180, 300]$ appear to approach the value found by Govardhan & Williamson (2000, 2003) for higher Reynolds numbers. Govardhan & Williamson (2003), based on the simulations of Shiels *et al.* (2001), find a much higher value of $m^* \simeq 0.25$ at $Re = 100$ than that reported here. Figure 4.7 shows the amplitude results for $Re = 80, 100$ and the equivalent results of Shiels *et al.* (2001). From this figure, we can see that their results appear to more closely resemble the results obtained by this study at $Re = 80$ than at $Re = 100$.

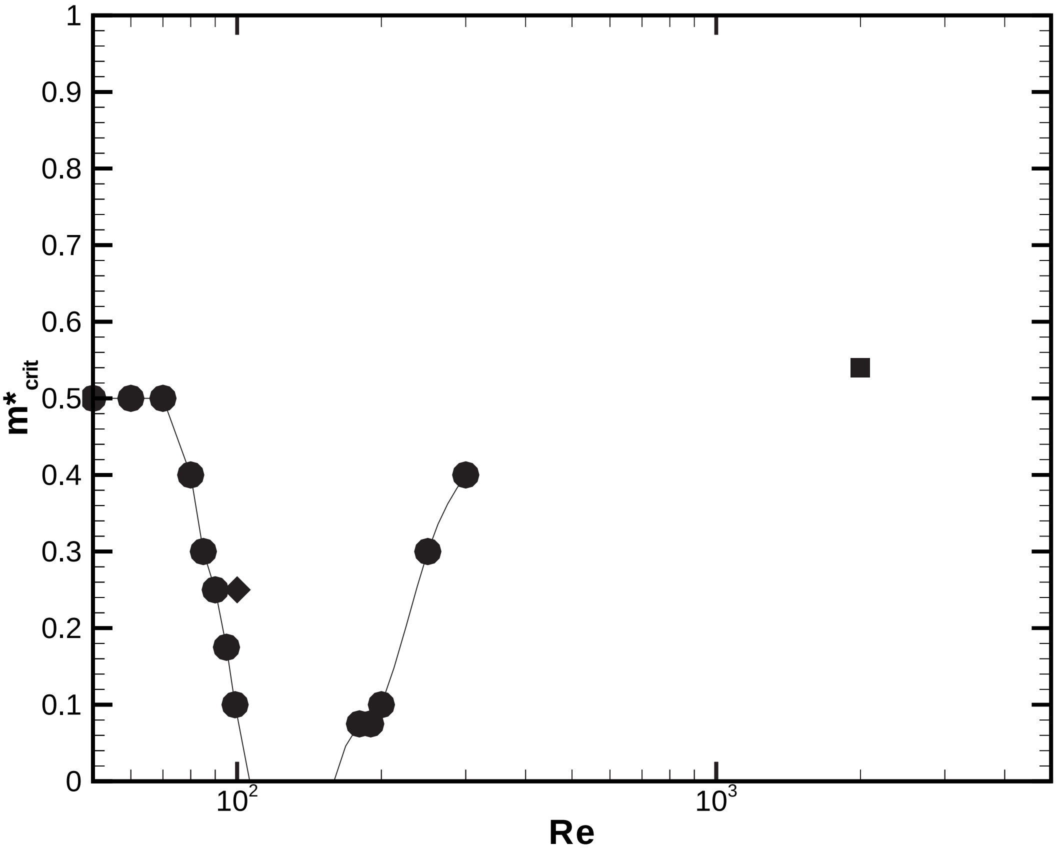

Figure 4.6: Comparison of the calculated critical mass ratio as a function for Reynolds number with ♦ Govardhan & Williamson (2003)'s estimate of Shiels *et al.* (2001)'s simulations and ■ Govardhan & Williamson (2003)'s results from experimental evidence at high Reynolds number.

4.3 Time History and Oscillation Frequency Analysis

The time history and frequency results are analyzed in this section. For a majority of the cases investigated, the cylinder oscillated sinusoidally at one oscillation frequency. However for the cases $Re = 200$ and $Re = 250$, a beating effect was noted for large amplitude oscillations. Results were plot against the frequency ratio parameter $f^* = f_{osc}/f$, where f_{osc} is the fundamental oscillation frequency, and f is the shedding frequency for a fixed cylinder at the same Reynolds number. From the frequency analysis, it was found that the beating occurred when the frequency ratio was between the values of 0.5 and 0.7.

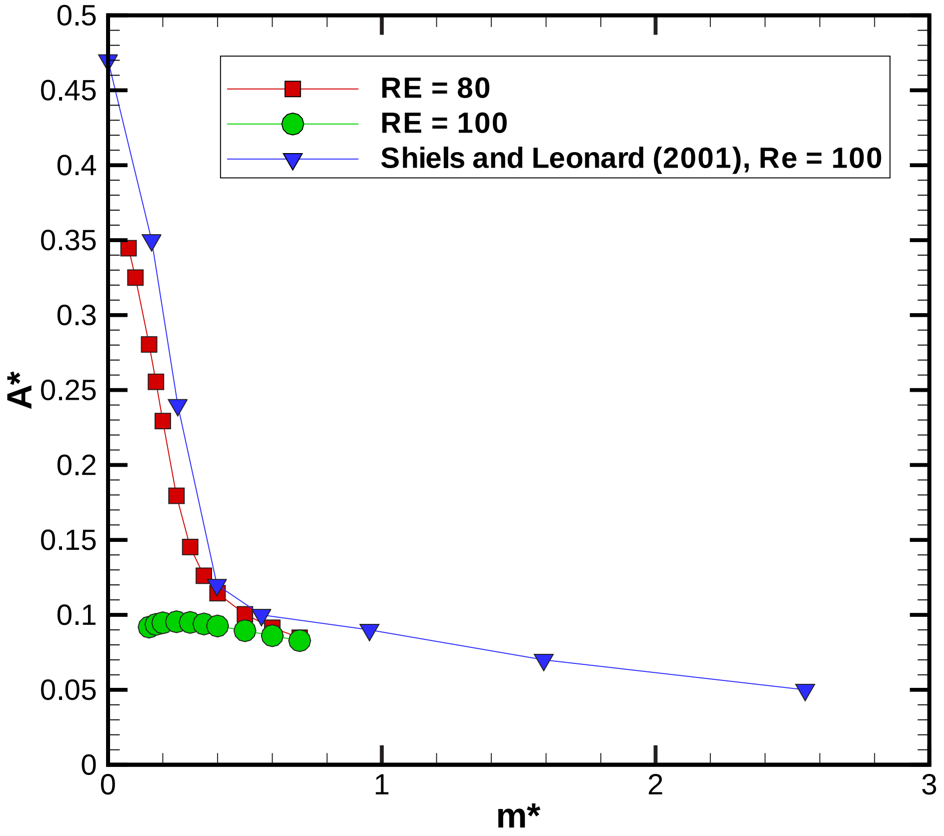

Figure 4.7: Comparison of oscillation amplitude results at $Re = 80$ and 100 with the results reported in Shiels *et al.* (2001) of simulations performed at $Re = 100$.

4.3.1 Time History Results

As the oscillation response was purely sinusoidal for Reynolds numbers in the range $Re = [40, 190]$ and for the particular case of $Re = 300$, oscillation traces at these Reynolds number will not be investigated in this section; the frequency response of these Reynolds numbers is discussed in the next section.

For the Reynolds numbers, $Re = 190, 200$ and 250 and for $m^* < m^*_{crit}$ a beating phenomena was noted in the oscillation response of the cylinder. A typical example time series is presented in figure 4.8(a). This time series is taken from simulations performed at $Re = 250$ and with a mass ratio just below the critical mass ratio for this Reynolds number ($m^* = 0.3$). For comparison, the case of $m^* > m^*_{crit}$ is also presented in figure 4.8(b), once again for $Re = 250$ (in this case $m^* = 0.4$). The time series indicate that for $Re = 190, 200$ and 250 the oscillations of cylinders with mass ratio below m^*_{crit} are no longer locked on to the shedding frequency. By contrast, as mentioned, all the high amplitude oscillations in the viscous regime, and at $Re = 300$, are locked on to the shedding frequency.

For $Re = 190$ and 200, the beating phenomenon was observed only for one or two mass ratios as the critical mass ratio was extremely low. For $Re = 250$, however, the beating phenomenon occurred over a range of mass ratios as m^*_{crit} was relatively high. The spectral density of the cylinder motion was determined and is plotted against frequency for a range of mass ratios in figure 4.9. In figure 4.9(a), representing the case of m^* slightly greater than m^*_{crit} ($m^* = 0.4$), the cylinder oscillates at only one frequency, corresponding to the vortex shedding frequency. As the mass ratio is reduced slightly to a value just below the critical mass ratio ($m^* = 0.3$), a significant amount of energy is noted at frequencies on either side of the wake shedding frequency (see figure 4.9(b)). However, two frequency components are dominant. The most dominant is at the wake shedding frequency, the second most dominant is at a frequency slightly below this; combined they account for the beating effect noted earlier. As the mass ratio is reduced further ($m^* = 0.2$ see figure 4.9(c)) the frequency range which exhibits significant energy levels increases such that energy is noted at all frequencies from just above the mean frequency to frequencies just above the wake shedding frequency. Three dominant frequencies are noted at the wake shedding frequency and at frequencies just above and below the wake shedding frequency. Interestingly, as the mass ratio is further reduced ($m^* = 0.1$ see figure 4.9(d)), the oscillation spectrum is cleaner with only one dominant frequency at the vortex shedding frequency. It therefore appears that for the Reynolds number range $Re = [190, 250]$ there is a range of mass ratios below the critical mass ratio where the cylinder does not 'lock in' to the wake shedding frequency. Further, at least for $Re = 250$, if the mass ratio is reduced sufficiently, the cylinder oscillation 'locks on' to the vortex shedding frequency.

4.3.2 Frequency Analysis

Figure 4.10 shows the oscillation frequency, represented as a Strouhal number ($St_{osc} = f_{osc} \cdot D/U_\infty$), as a function of Reynolds number. The oscillation frequency is found to increase asymptotically with increasing Reynolds number up to $Re = 190$. The variation of St_{osc} (varying with mass ratio) is also found to vary with Reynolds number,

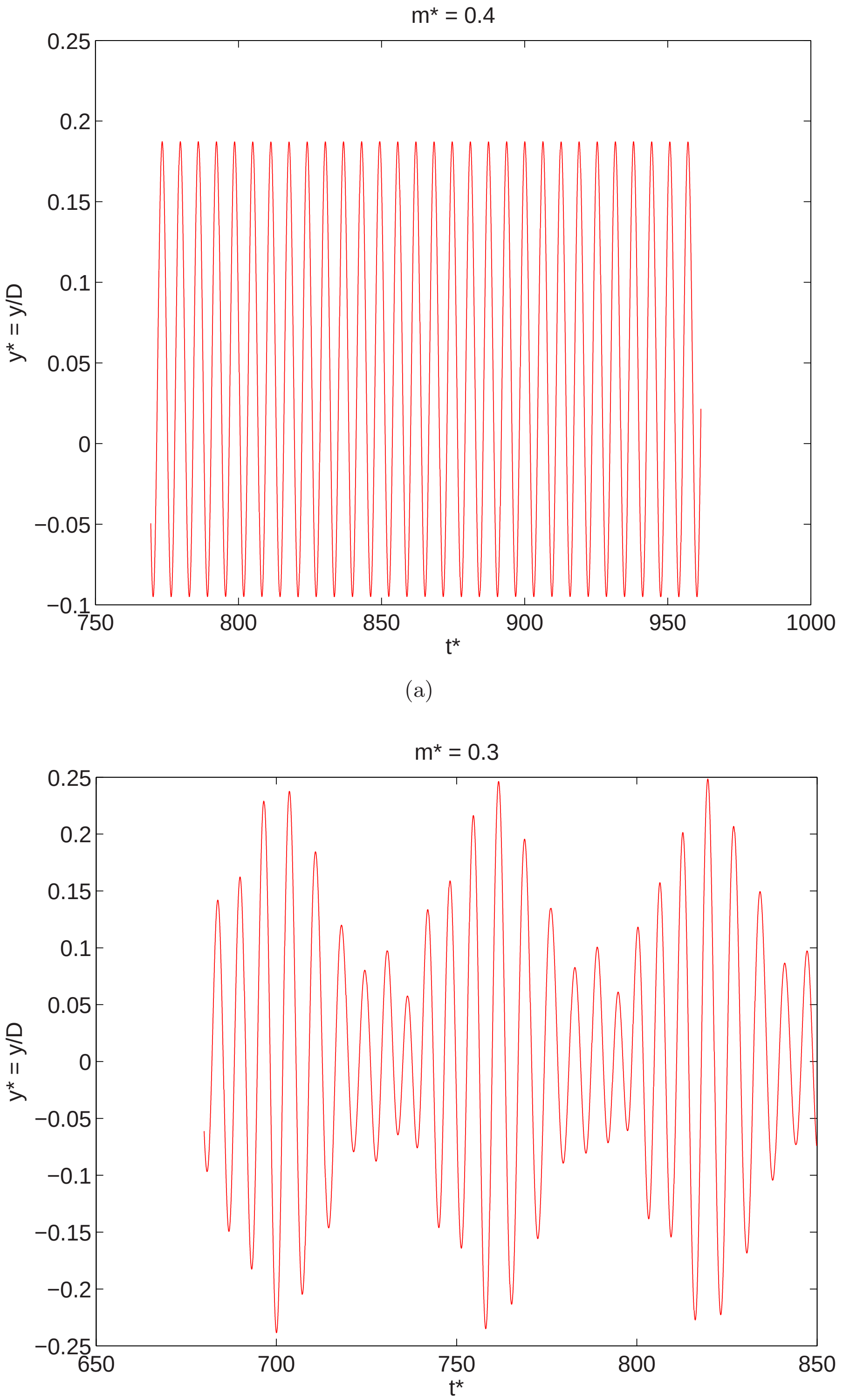

(a)

(b)

Figure 4.8: Time trace of cylinder oscillation for $Re = 250$, (a) $m^* = 0.4$, (b) $m^* = 0.3$.

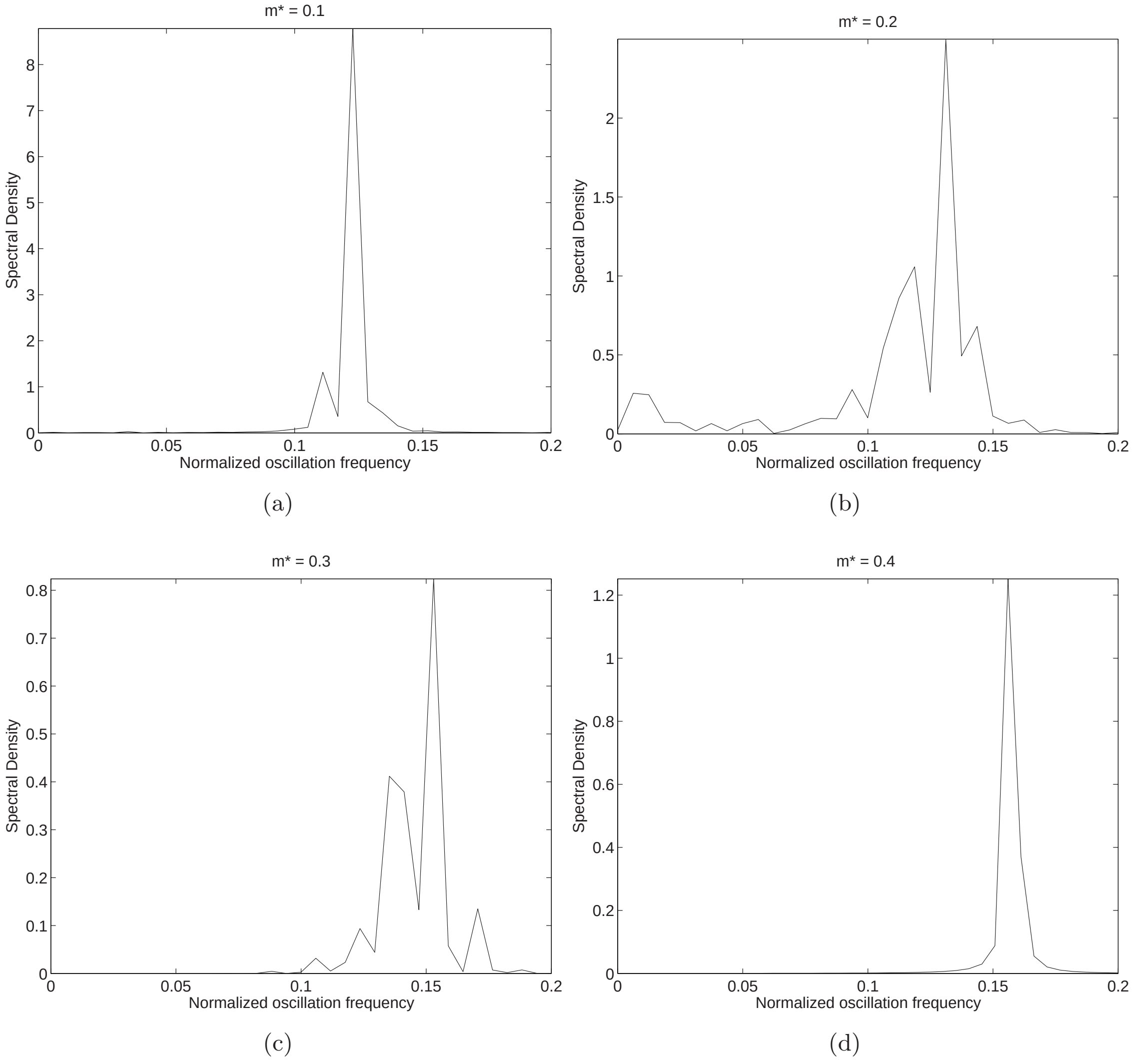

(a)

(b)

(c)

(d)

Figure 4.9: Spectral Density of the oscillation time trace as a function of frequency at $Re = 250$ for (a) $m^* = 0.1$, (b) $m^* = 0.2$, (c) $m^* = 0.3$, and (d) $m^* = 0.4$.

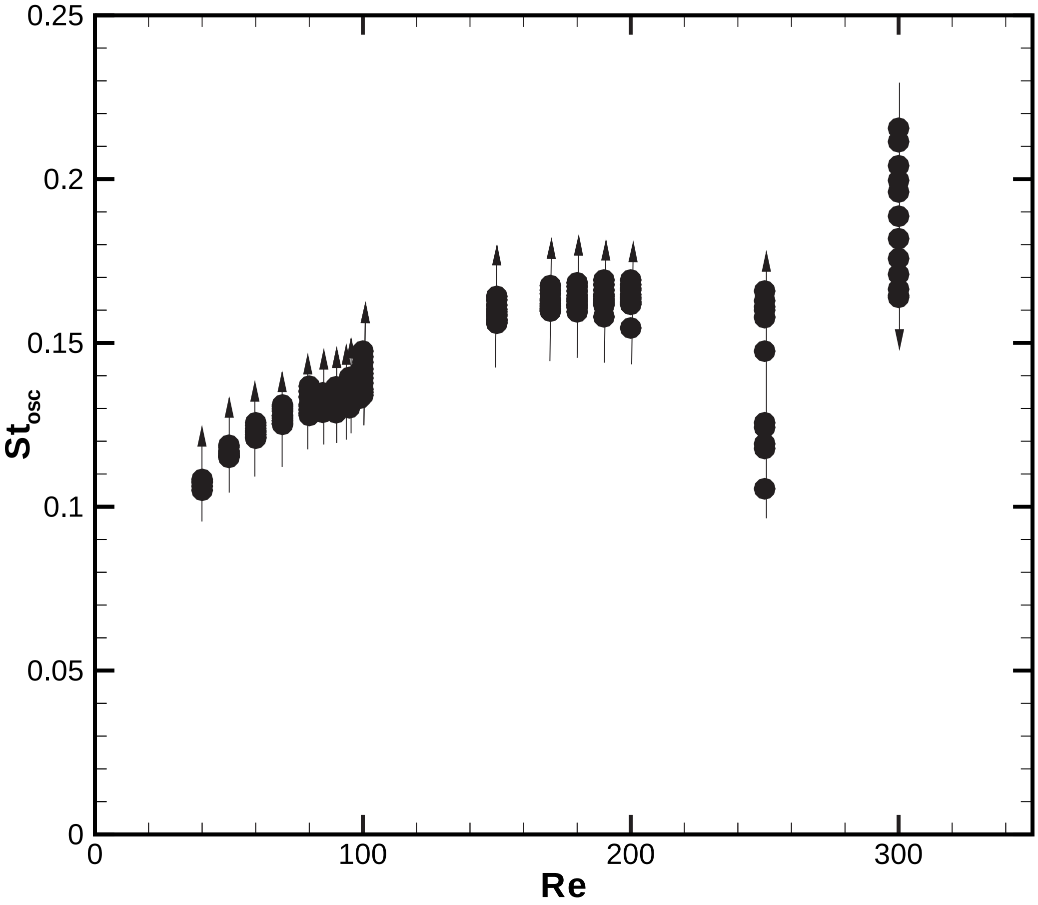

Figure 4.10: Frequency of oscillation (presented as a Strouhal number based on the fundamental oscillating frequency) as a function of Reynolds number. The arrows indicate increasing mass ratio.

the largest range of St_{osc} being found for $Re = 250$.

Figure 4.11 shows $f^* = f_{osc}/f$ (where f is the vortex shedding frequency from a fixed cylinder) as a function of Reynolds number. The parameter f^* has been shown by Khalak & Williamson (1999) to provide information on the 'lock-in' characteristics of an oscillating body. The case of $Re = 40$ represents the only case where $f^* > 1$ for all of the mass ratios investigated in this study. As the Reynolds number is increased, the average value of f^* across the mass ratios investigated decreases up to $Re \simeq 100$. In the range $Re = 100, 190$ the average value of f^* remains reasonably constant. As with figure 4.10, the frequency region for Reynolds numbers in the higher Reynolds number range where $m^* < m^*_{crit}$, has been shaded. This region corresponds to very low values of f^*. This is initially a surprising discovery, however it may be explained by the beating

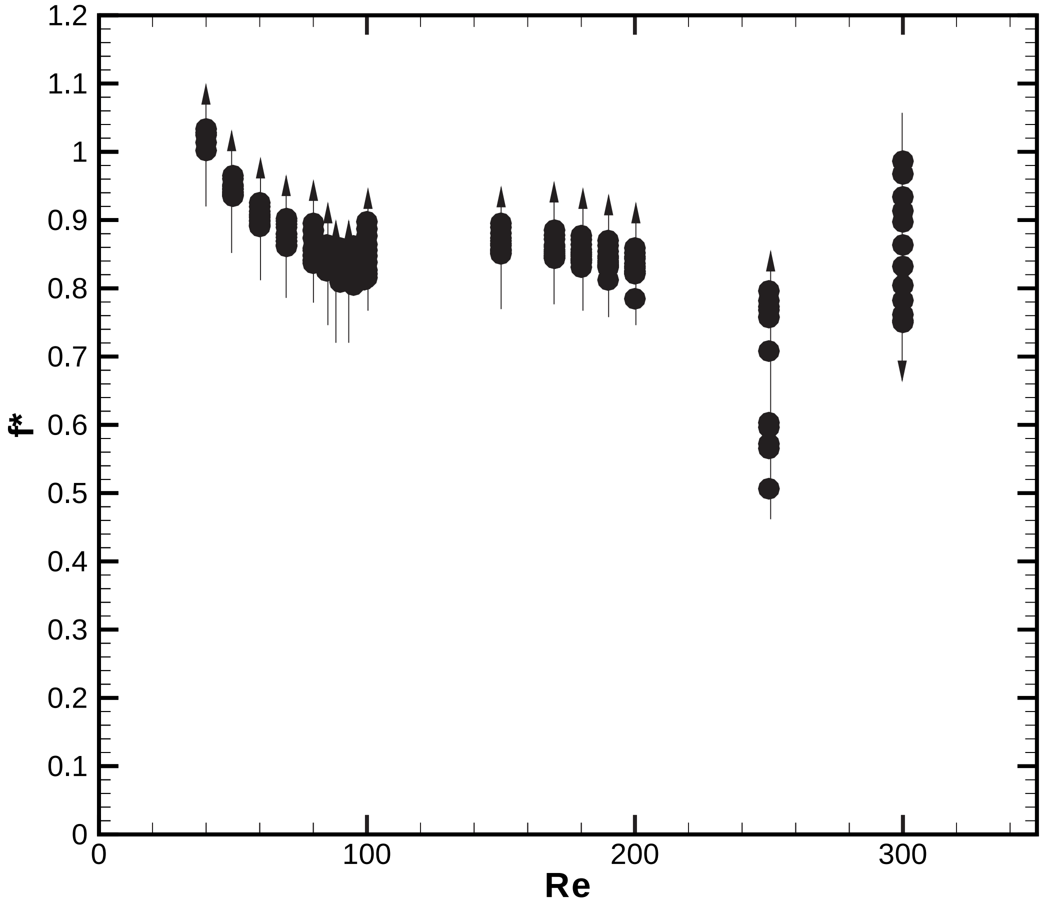

Figure 4.11: Frequency ratio, $f^* = f_{osc}/St$ (where St is the Strouhal shedding frequency for a fixed cylinder) as a function of Reynolds number. The arrows indicate increasing mass ratio.

phenomenon, and the significant fluctuations in A^* observed at these higher Reynolds number values where $m^* < m^*_{crit}$ Indeed, the highest amplitude response for the case of $Re = 250$ corresponds to $f^* \simeq 0.5$. By contrast, for the case of $Re = 300$, the high amplitude oscillations ($m^* < m^*_{crit}$) correspond to frequency ratio values $f^* \to 1$, as would be anticipated. As found in section 4.2, at this Reynolds number, the amplitude of oscillation was found to decrease smoothly with increasing mass ratio, and did not exhibit discontinuous fluctuations as a function of mass ratio for $m^* < m^*_{crit}$.

How the cylinder oscillation amplitudes increase for f^* moving away from unity is yet to be explained. It is hypothesized that it may be a two-dimensional effect, as experimentally, three-dimensional structures should reduce the correlation length along the cylinder span and may act to reduce the amplitude of oscillation. From our results, it appears that the case of Reynolds numbers $Re \geqslant 300$ represents a different state to $Re = [200, 250]$. Fully three-dimensional simulations may be able to account for three-dimensional effects at these higher Reynolds numbers, and accurately determine both the cylinder response and the critical mass ratio; however this is left to a future study.

4.4 Fluid Force Coefficient Results

The fluid force coefficients acting on the freely oscillating cylinder are analyzed in this section. However, as the forcing is coupled to the motion of the cylinder (primarily through the viscous component of the force coefficient), the force coefficient acting on a fixed cylinder in the Reynolds number range $Re = [50, 250]$ is also analyzed in an attempt to determine why a critical mass ratio was not observed in the region $Re = [100, 190]$.

4.4.1 Fixed Cylinder Results

Henderson (1995) performed simulations of the flow past a fixed circular cylinder, on a two-dimensional domain in the Reynolds number range $Re = [10, 1000]$. From these studies, he was able to determine both the viscous and pressure components of the drag force coefficient, as a function of Reynolds number. His results indicate that the viscous force coefficient component decreases for all Reynolds numbers considered, and that the total drag force coefficient also decreased for Reynolds numbers, $Re \lesssim 100$. However, in the range $Re \simeq [100, 200]$, the pressure component of the drag force coefficient increases with Reynolds number such that the total drag force coefficient remains approximately independent of Reynolds number in this range. For higher Reynolds numbers, the total drag force coefficient increases with increasing Reynolds number. It is speculated, from the results reported in section 4.2, that the distinct drop in A^*_{max} as Re is increased from $Re = 95$ to 100 may be due to the decrease in the viscous component of the drag force coefficient, noted for the fixed cylinder.

Henderson's study has been repeated, so that the fluid force coefficient information can also be determined in the range $Re = [50, 200]$ for the case of a fixed cylinder. Figure 4.12 shows the mean drag as a function of Reynolds number from both the current study, and from Henderson's study. In all cases, the current results were within 2% of those found by Henderson (1995). However the current results were consistently

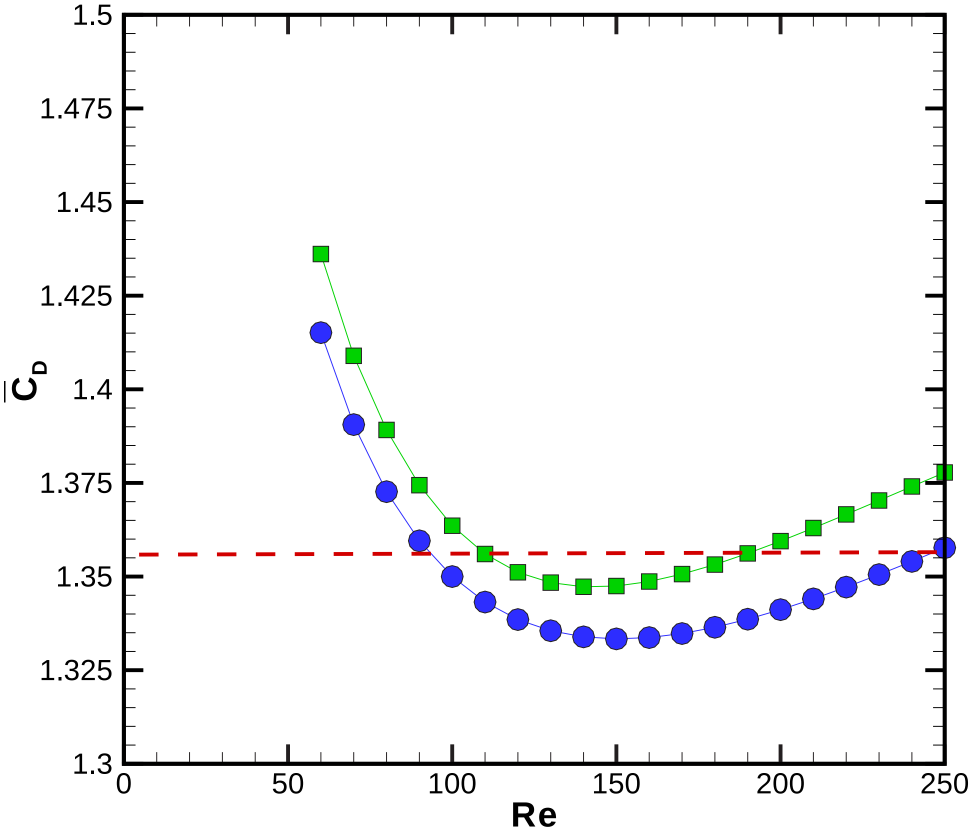

Figure 4.12: Mean Drag as a function of Reynolds number; □, present results, ○ Henderson (1995)'s results. In the Reynolds number range below the dashed line, a jump to large amplitude oscillations was not observed.

higher than those reported by Henderson (1995). Unfortunately Henderson did not give details of the mesh used in his study, and it is assumed that the discrepancy is due to blockage effects. The present fixed cylinder results were found to correspond more closely to the oscillation amplitude results described in section 4.2. In the present study, the Reynolds number regime where m^*_{crit} was not determined (for the oscillating cylinder) corresponds very well to the region where $\overline{C_D} < 1.36$ for the fixed cylinder case, as may be deduced by comparing figure 4.12 with figure 4.5.

Figure 4.13 shows the fluctuating lift and drag as a function of Reynolds number for the case of a fixed cylinder. Surprisingly, the fluctuating force coefficients increase monotonically with Reynolds number throughout the range $Re = [50, 200]$. There is no variation away from this monotonic increase for Reynolds numbers in the range

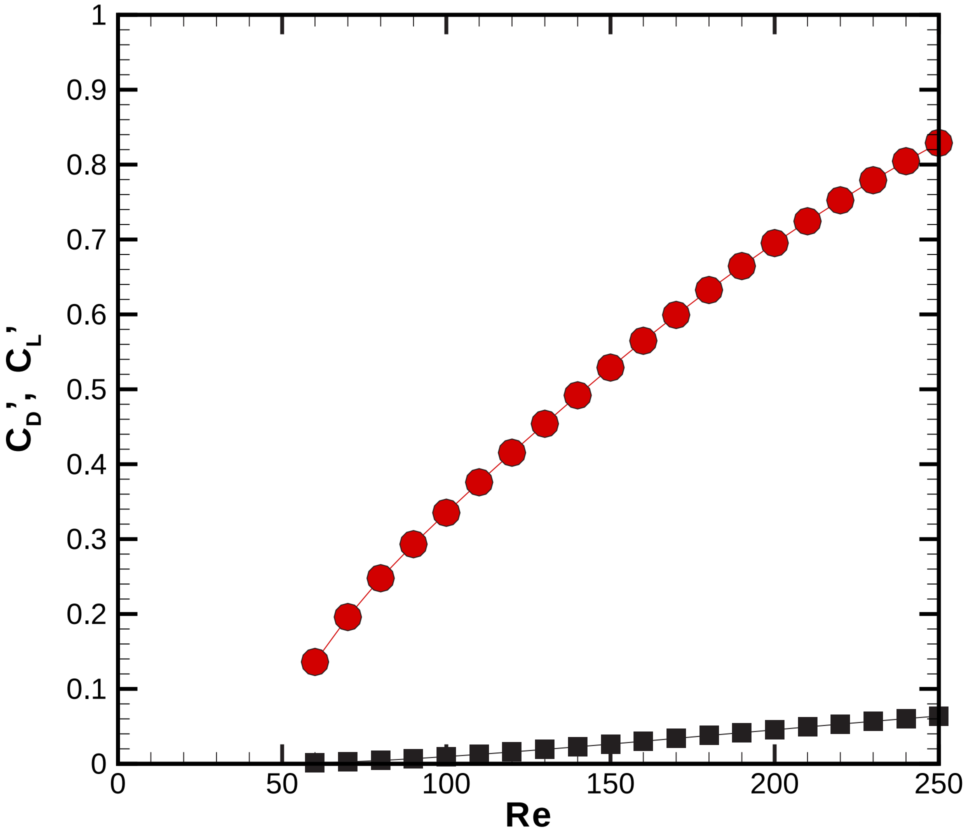

Figure 4.13: Fluctuating lift and drag coefficient components as a function of Reynolds number, for the case of a fixed cylinder; ○ fluctuating lift force coefficient, ■ fluctuating drag force coefficient

$Re = [100, 190]$.

From these results, it is hypothesized that the fluid structures inducing the increase in mean drag as a function of Reynolds number for $Re > 190$ must be inherently unstable to slight movement of the cylinder. However, this hypothesis has not been tested in this study as only steady state, saturated oscillation results have been analyzed. In order to test the above hypothesis, the growth of cylinder oscillation amplitude from a cylinder at rest for Reynolds numbers, $Re > 190$ would have to be analyzed. From such an analysis, the variation in the wake structures, due to the increase in cylinder oscillations could be determined. This is left to a later study.

4.4.2 Oscillating Cylinder Results: Mean Drag

The mean drag coefficient is plotted as a function of mass ratio in figure 4.14 for Reynolds numbers in the range $Re = [50, 250]$. For Reynolds numbers within the viscous regime ($Re = [50, 95]$), the mean drag increases inversely with m^* for all $m^* < m^*_{crit}$. For $m^* > m^*_{crit}$, the mean drag remains reasonably constant up to the highest mass ratios considered in this study.

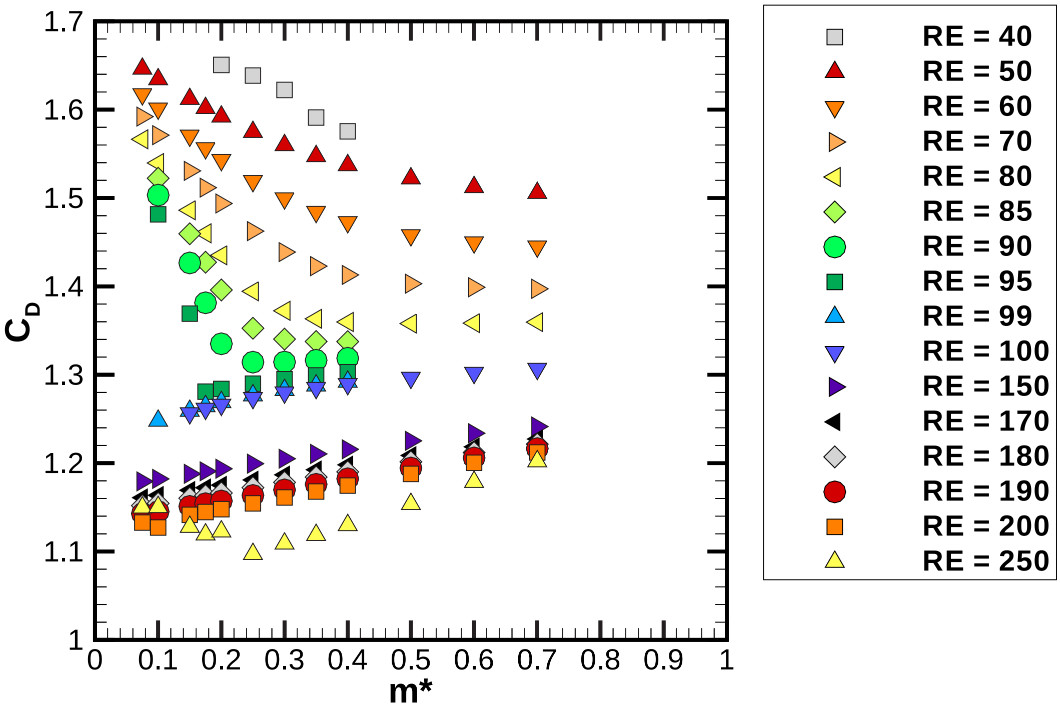

Figure 4.14: Mean drag as a function of mass ratio for the case of a freely oscillating cylinder, for $Re = [40, 250]$.

The relationship of $\overline{C_D}$ to Reynolds number for all $m^* > m^*_{crit}$ in the viscous range was approximated by the linear least squares fit,

$$\overline{C_D} = -0.0044 \cdot Re + 1.7177 \tag{4.4}$$

with a coefficient of determination, $R^2 = 0.998$.

The rate of increase of $\overline{C_D}$ as m^* decreases below m^*_{crit} was found to vary with Reynolds number. For low Reynolds number simulations $Re \simeq 50$, the increase in $\overline{C_D}$ was a smooth function of m^*. By contrast, for higher Reynolds numbers (for example $Re = 95$) the gradient of $\overline{C_D}$ to m^* increased markedly as $m^* < m^*_{crit}$.

For each Reynolds number in the range $Re = [50, 95]$, the mean drag was fitted to a quadratic least squares fit, which had the general form,

$$\overline{C_D} = (A \cdot m^{*2} + B \cdot m^*)^{-1/m^*} \tag{4.5}$$

The parameter A was found to vary with Reynolds number as,

$$A = -2 \times 10^{-5} Re^2 + 0.0062 Re - 0.5937, \tag{4.6}$$

and the parameter B was found to be constant ($B = 0.98$). In all cases, equation 4.5 had a coefficient of determination of $R^2 = 0.96$ or greater.

For $Re = [100, 190]$, no distinct increase in $\overline{C_D}$ was noted as m^* was reduced to the lowest value considered in this study. Instead, the mean drag was found to increase slightly with increasing mass ratio in this Reynolds number range.

A slight discontinuous increase in the mean drag was found for $Re = 200$ as the mass ratio was decreased down to $m^* = 0.075$. This discontinuity was more prominent as the Reynolds number was increased to $Re = 250$; in this case the discontinuity occurred for $m^* = 0.2$. For both the case of $Re = 200$ and the case $Re = 250$, the mass ratio at which the discontinuity in $\overline{C_D}$ occurred coincided with the critical mass ratio found for that Reynolds number.

For all mass ratios considered, the mean drag in the higher Reynolds number range was found to be significantly less than that found in the viscous range.

The findings detailed above indicate that the mean drag varies with cylinder oscillation amplitude. It is hypothesized that larger oscillation amplitudes induces a wider mean wake profile which further induces a greater mean drag.

4.4.3 Oscillating Cylinder Results: Peak Lift

The peak lift coefficient results provide information linking the force coefficients acting on the cylinder to the corresponding motion of the cylinder. The link between the lift coefficient and the subsequent motion of the cylinder is made by analyzing the equation of motion, which for a freely oscillating cylinder with $k = c = 0$, may be written in dimensional terms as:

$$m\ddot{y} = F_L, \tag{4.7}$$

where, F_L is the lift coefficient acting on the cylinder. Assuming that the oscillations are sinusoidal (as is the case with all oscillations in the viscous range), then the motion of the cylinder can be written as:

$$\begin{aligned} y &= Y\sin(\omega t), & (4.8) \\ \ddot{y} &= -\omega^2 Y\sin(\omega t), & (4.9) \end{aligned}$$

and the lift coefficient acting on the cylinder may be written as:

$$F_L = \hat{F_L}\sin(\omega t - \phi). \tag{4.10}$$

As there is no external damping or spring stiffness, the phase lag (ϕ) is either 0^o or 180^o, and for finite amplitude oscillations, $\phi = 180^o$. Therefore, equation 4.10 may be rewritten as:

$$F_L = -\hat{F_L}\sin(\omega t). \tag{4.11}$$

Substituting equation 4.9 and equation 4.11 into the equation of motion, and rewriting in non-dimensional form, the normalized amplitude of oscillation may be written as:

$$A^* = \frac{\hat{C_L}}{2\pi^3 m^* \cdot St^2 \cdot f^{*2}}. \tag{4.12}$$

This equation corresponds to the frequency equation defined by both Govardhan & Williamson (2000) and Govardhan & Williamson (2003). From section 4.3, it may be seen that the denominator in equation 4.12 is very small, making the equation stiffly stable. Small variations in $\hat{C_L}$, as a result of a changed mass ratio, may result in dramatic changes in the amplitude of oscillation. This goes some way to explaining the dramatic ‘jump’ in the amplitude observed both in this study and in Govardhan & Williamson (2003) as the mass ratio approaches the critical mass ratio.

From the results in section 4.2.2, two regions exist where the critical mass ratio is identified below which large amplitude oscillations are observed. The above observation implies that, for each Reynolds number considered, for mass ratios in the vicinity of the critical mass ratio, the gradient $(dA^*)/(dm^*)$ must be negative. From equation 4.12 this implies that,

$$\frac{d\hat{C_L}}{dm^*} < \frac{d(2\pi^3 m^* \cdot St^2 \cdot f^{*2})}{dm^*} \qquad \text{for } m^* \to m^*_{crit}. \tag{4.13}$$

The variation in $\hat{C_L}$ is described below both for the case of the viscous range and the higher Reynolds number range.

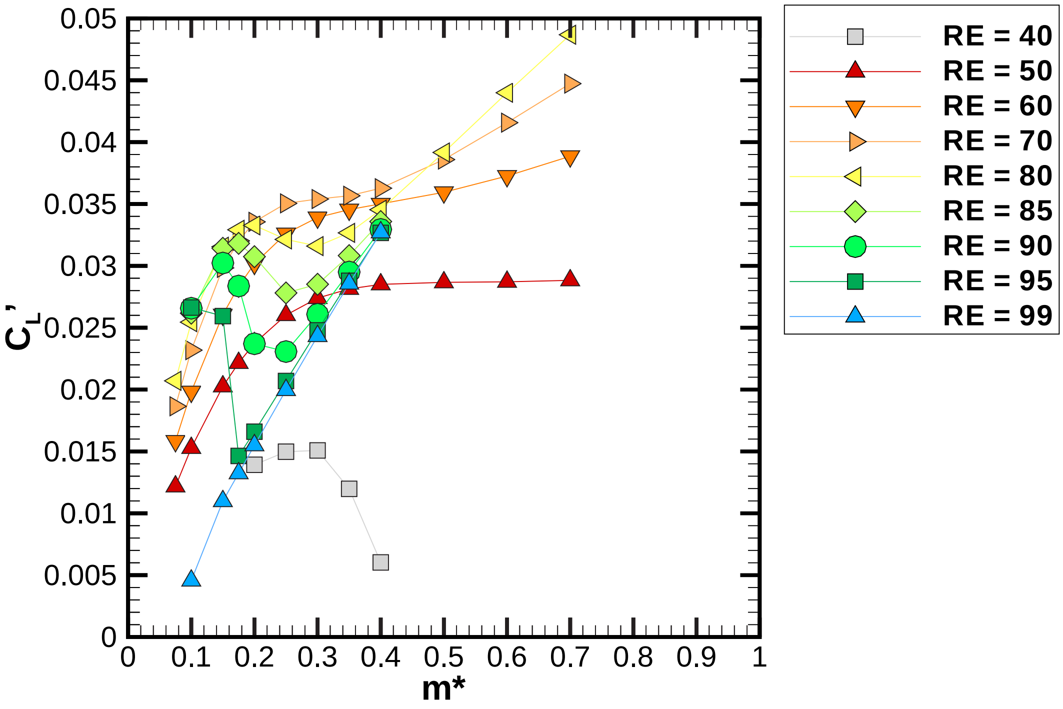

Figure 4.15: Fluctuating lift coefficient as a function of mass ratio for the case of a freely oscillating cylinder for Reynolds numbers in the viscous range, $Re = [40, 99]$.

The maximum lift coefficient, plotted as a function of mass ratio, is shown in figure 4.15 for all Reynolds numbers in the viscous range ($Re = [40, 99]$). As with the amplitude of oscillation results, the peak lift results for $Re = 40$ is distinctly different to the results for higher Reynolds numbers. For $Re = 40$, $\hat{C_L}$ reaches a peak value at $m^* \simeq 0.3$, prior to decreasing rapidly with mass ratio for $m^* > 0.3$.

By contrast, for the case of $Re = 50$, the peak lift coefficient increases with mass ratio for small mass ratios prior to asymptotically approaching a value of $\hat{C_L} \simeq 0.288$. At higher Reynolds number values ($Re = [60, 70]$, the overall form of the peak lift as a function of mass ratio is the same, however, $\hat{C_L}$ does not asymptote to a fixed value. Instead, as the mass ratio reaches $m^* \simeq 0.3$, $\hat{C_L}$ reaches a constant value, prior to increasing again as a function of m^* at higher values of m^*. In the Reynolds number range $Re = [40, 70]$, $\hat{C_L}$ increased as a function of Reynolds number for all mass ratios investigated.

At still higher Reynolds numbers (but still in the viscous range ($Re = [80, 95]$)), the variation of $\hat{C_L}$ with m^* at low mass ratios ($m^* \leqslant 0.15$) remains the same as for lower Reynolds numbers. However, a local minimum is observed as the mass ratio is increased; the mass ratio at which the local minimum is observed decreases with increasing Reynolds number and appears to coincide reasonably well with the critical mass ratio calculated in section 4.2.2. Within this Reynolds number range, as m^* is increased beyond m^*_{crit}, $\hat{C_L}$ increases linearly with mass ratio. The gradient with which $\hat{C_L}$ increases with m^* increases slightly with Reynolds number. For the case of $Re = 99$, no local minimum in $\hat{C_L}$ was noticed. At this Reynolds number, $\hat{C_L}$ increased linearly as a function of m^* for all m^* investigated.

It is surprising that, for small mass ratios, $\hat{C_L}$ increases with mass ratio, while (from the results of section 4.2) the amplitude of oscillation decreases with mass ratio number over the same range of $m^* \leqslant m^*_{crit}$. How this apparent anomaly is possible may be clarified by re-examining equation 4.13. Resolving this apparent anomaly requires that the denominator on the right hand side of equation 4.12 must increase at a faster rate as a function of m^* than $\hat{C_L}$, for all mass ratios $m^* < m^*_{crit}$ in the viscous range. The increase in the term $2\pi^3 m^* \cdot St^2 \cdot f^{*2}$ as a function of mass ratio is greater than the increase in the $\hat{C_L}$ term, subsequently causing the amplitude of oscillation to decrease with mass ratio.

The higher Reynolds number range

Figure 4.16 shows the variation of peak lift coefficient as a function of mass ratio in the higher Reynolds number range $Re = [100, 250]$. For all Reynolds numbers in the range $Re = [100, 190]$, corresponding to the Reynolds number range where no critical mass ratio was observed, $\hat{C_L}$ increased linearly with mass ratio. The rate of change of $\hat{C_L}$ increased with increasing Reynolds number. For the case of $Re = 200$, $\hat{C_L}$ did not increase between $m^* = 0.075$ and $m^* = 0.1$ corresponding to the critical mass ratio as described in the previous section for Reynolds numbers in the viscous regime. It appears that for $Re = 200$, the increase in A^* as $m^* < m^*_{crit}$ is due to an increase in $\hat{C_L}$ as the mass ratio is reduced below the critical mass ratio. The trend found for

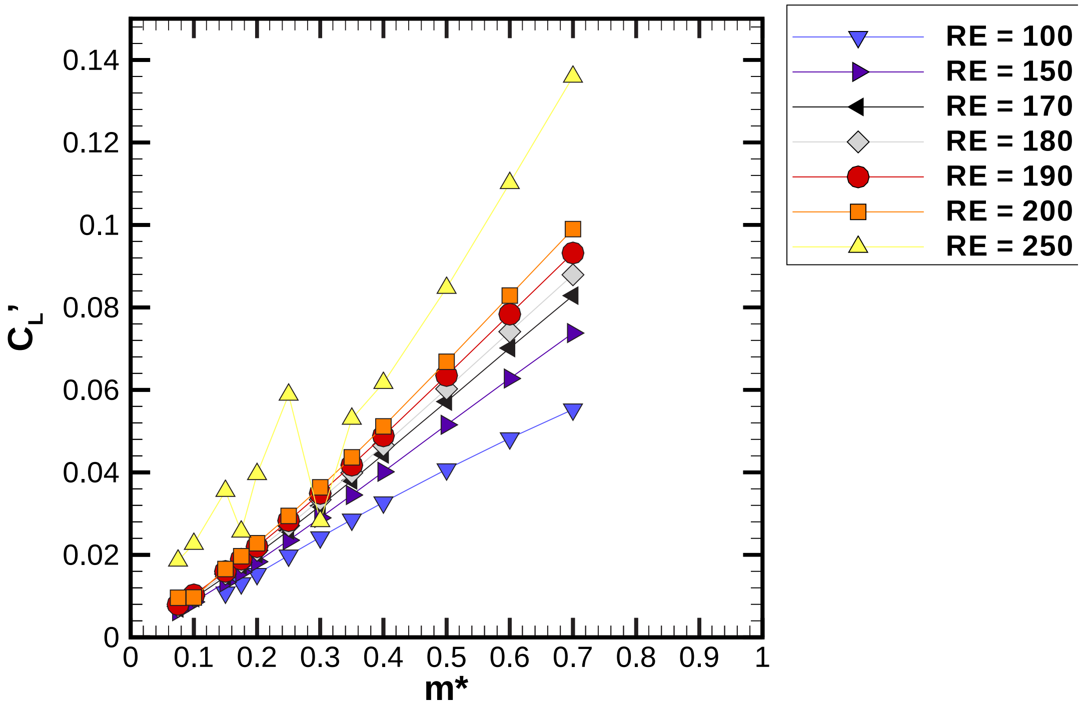

Figure 4.16: Fluctuating lift coefficient as a function of mass ratio for the case of a freely oscillating cylinder, for Reynolds numbers in the higher Reynolds number range, $Re = [100, 250]$.

$Re = 200$ is significantly amplified for the case of $Re = 250$. Here $\hat{C_L}$ increases sharply as the mass ratio is decreased below m^*_{crit}. For $m^* < m^*_{crit}$, $\hat{C_L}$ varies discontinuously with mass ratio. It is hypothesized that this variation is due to the beating effect noted in section 4.3 for these mass ratios at this Reynolds number.

4.5 Conclusion

Both the oscillation and force coefficient response has been analyzed using two-dimensional simulations as a function of both Reynolds number and mass ratio in the range $Re = [30, 300], \quad m^* = [0.075, 0.7]$. No oscillations were observed for $Re < 40$ in agreement with the findings of Taneda (1956) who found no perturbations in the wake of a fixed cylinder for $Re \lesssim 36$.

In the range $Re = [40, 99]$, appreciable oscillations were observed for mass ratios $m^* < m^*_{crit}$, in qualitative agreement with the experimental findings of Govardhan & Williamson (2003) at much higher Reynolds numbers. Surprisingly, no appreciable oscillations were observed for the range $Re = [100, 190]$. From the findings of Henderson (1995) and the present investigation, for the flow past a fixed cylinder, this Reynolds number regime corresponds to the range where the mean drag exhibits a local minimum. For $Re > 190$, a critical mass ratio was once again found, below which large amplitude oscillations were noted.

The present results differ somewhat from the findings of Shiels *et al.* (2001), however this may be due to their use of a vortex method which has difficulty in determining the linear viscous term in the Navier-Stokes equations, and as such may not be able to adequately resolve flow structures at the low Reynolds numbers investigated ($Re = 100$ in their case). It was further found that their results corresponded closely to the present findings at $Re = 80$.

The present results are in qualitative agreement with the finding of $m^*_{crit} = 0.54$ by Govardhan & Williamson (2003). For $Re > 190$, the critical mass ratio was found to increase with Reynolds number, reaching a maximum value of $m^*_{crit} = 0.4$ for $Re = 300$. As this was a two-dimensional study, higher Reynolds numbers were not considered. Determining the critical mass ratio as a function of Reynolds numbers between $Re = 300$ and the values investigated by Govardhan & Williamson (2003) is left for a future study.

Chapter 5

Two Dimensional simulations of the flow around a tethered cylinder

5.1 Introduction

As an extension to the case of the vortex-induced-vibration of a hydro-elastically mounted cylinder, the case of a tethered cylinder, whose motion is restricted to an arc by a restraining tether, is examined in this chapter. The tendency of a tethered buoy to oscillate when excited by waves is a well-known phenomenon. However, it has only recently been found that a submerged buoy will act in a similar fashion when exposed to a uniform flow at moderate Reynolds numbers, with a transverse peak-to-peak amplitude of approximately two diameters over a wide range of velocities. In this chapter, only the case of $m^* = 0.833$ and $L^* = 5.05$ will be investigated; these values were chosen to match preliminary experiments conducted simultaneously in the FLAIR water channel. The effect of varying both these parameters independently will be subsequently presented in chapters 6 and 7. The response of the tethered cylinder system was found to be strongly influenced by the mean layover angle as this parameter determined if the oscillations would be dominated by in-line oscillations, transverse oscillations or a combination of the two. Three branches of oscillation are noted, an in-line branch, a transition branch and a transverse branch. Within the transition branch, the cylinder oscillates at the vortex shedding frequency and modulates the drag force such that the drag signal is dominated by the lift frequency. It is found that the mean amplitude response is greatest at high reduced velocities, i.e. when the cylinder is oscillating predominantly transverse to the fluid flow. Furthermore, the oscillation frequency is synchronized to the vortex shedding frequency of a stationary cylinder, except at very high reduced velocities. Of interest is the finding that the cylinder exhibited a net negative lift coefficient for all reduced velocities investigated, it is speculated in this chapter that this is due to the constraint on the cylinder motion imposed by the restraining tether. Supporting evidence for this hypothesis is presented in chapter 6 and 7. Examination of the mean wake profile exhibits an asymmetry in the wake in line with the finding of a net lift coefficient. Visualizations of the pressure and vorticity in the wake reveal the mechanisms behind the motion of the cylinder.

5.2 Derivation of the Reduced Velocity Parameter

Following the work of Govardhan & Williamson (1997), Williamson & Govardhan (1997), and Jauvtis *et al.* (2001), results are presented as a function of reduced velocity, defined as:

$$u^* = \frac{U_\infty}{f_n D}, \tag{5.1}$$

which incorporates the inlet velocity, U_∞, cylinder diameter, D, and natural frequency of the system, f_n. Note that the natural frequency of the system is a function of the tension in the tether and varies with the drag, lift and buoyancy, unlike that of a hydro-elastically mounted cylinder which is independent of hydrodynamic forces. The following derivation determines the equation for the natural frequency from the polar form of the equations of motion. The equations of motion in terms of polar moment are written below:

$$J\ddot{\theta} = F_\theta \cdot L \tag{5.2}$$

where J is the polar moment of inertia, F_θ is the force acting on the cylinder in the direction of motion, and L is the tether length. Note that θ has both a mean component ($\overline{\theta}$) and an time dependent component (θ').

We can rewrite F_θ as:

$$F_\theta = F_D \cdot \cos(\theta) - (F_L + B) \cdot \sin(\theta) \tag{5.3}$$

where F_D and F_L are the drag and lift force, respectively, and B is the buoyancy force which also takes into account the force of gravity.

We shall now rewrite $F_D = F_x$ and $F_L + B = F_y$ in order to simplify the force equation. Using the fact that θ has a mean component $\overline{\theta}$ and an oscillatory component

θ', we can rewrite equation 5.3 as:

$$F_\theta = F_x \cdot \cos(\overline{\theta} + \theta') - F_y \cdot \sin(\overline{\theta} + \theta') \tag{5.4}$$

Using trigonometric theory and grouping like terms of $\sin(\theta')$ and $\cos(\theta')$, equation 5.4 may be written as:

$$F_\theta = -\sin\theta' \cdot \left(F_x \cdot \sin\overline{\theta} + F_y \cdot \cos\overline{\theta}\right) + \cos\theta' \cdot \left(F_x \cdot \cos\overline{\theta} - F_y \cdot \sin\overline{\theta}\right) \tag{5.5}$$

Now we know that both of the forces have a mean and oscillatory component as well:

$$\begin{aligned} \overline{F_x} &= \overline{F_D}, \qquad F_x' = F_D' \\ \overline{F_y} &= \overline{F_L} + B, \quad F_y' = F_L' \end{aligned} \tag{5.6}$$

and using these definitions, equation 5.5 can be written as:

$$\begin{aligned} F_\theta = &- \sin\theta' \cdot \left((\overline{F_D} + F_D') \cdot \sin\overline{\theta} + (\overline{F_L} + B + F_L') \cdot \cos\overline{\theta}\right) \\ &+ \cos\theta' \cdot \left((\overline{F_D} + F_D') \cdot \cos\overline{\theta} - (\overline{F_L} + B + F_L') \cdot \sin\overline{\theta}\right) \end{aligned} \tag{5.7}$$

By separating the mean and oscillatory forces, equation 5.7 can be rewritten:

$$\begin{aligned} F_\theta = &- \sin\theta' \cdot \left(\overline{F_D} \cdot \sin\overline{\theta} + (\overline{F_L} + B) \cdot \cos\overline{\theta} + F_D' \cdot \sin\overline{\theta} + F_L' \cdot \cos\overline{\theta}\right) \\ &+ \cos\theta' \cdot \left(\overline{F_D} \cdot \cos\overline{\theta} - (\overline{F_L} + B) \cdot \sin\overline{\theta} + F_D' \cdot \cos\overline{\theta} - F_L' \cdot \sin\overline{\theta}\right) \end{aligned} \tag{5.8}$$

and from the balance of forces (see figure 5.1)

$$\overline{F_D} \cdot \sin\overline{\theta} + (\overline{F_L} + B) \cdot \cos\overline{\theta} = \overline{T} \tag{5.9}$$

$$\overline{F_D} \cdot \cos\overline{\theta} - (\overline{F_L} + B) \cdot \sin\overline{\theta} = 0 \tag{5.10}$$

where $\overline{T}$ is the mean tension over a cycle. Using equations 5.9 and 5.10, equation 5.8 becomes:

$$\begin{aligned} F_\theta = &- \sin\theta' \cdot \left(\overline{T} + F_D' \cdot \sin\overline{\theta} + F_L' \cdot \cos\overline{\theta}\right) \\ &+ \cos\theta' \cdot \left(F_D' \cdot \cos\overline{\theta} - F_L' \cdot \sin\overline{\theta}\right) \end{aligned} \tag{5.11}$$

Finally, by assuming small amplitude oscillations, such that $\sin\theta' \simeq \theta'$ and $\sin\theta' \simeq 1$ F_θ can be written in a linearized form as:

$$\begin{aligned} F_\theta = &- \theta' \cdot \left(\overline{T} + F_D' \cdot \sin\overline{\theta} + F_L' \cdot \cos\overline{\theta}\right) \\ &+ \left(F_D' \cdot \cos\overline{\theta} - F_L' \cdot \sin\overline{\theta}\right) \end{aligned} \tag{5.12}$$

Returning now to equation 5.2 and remembering that θ has both a mean and oscillatory component, the equation of motion may be written as:

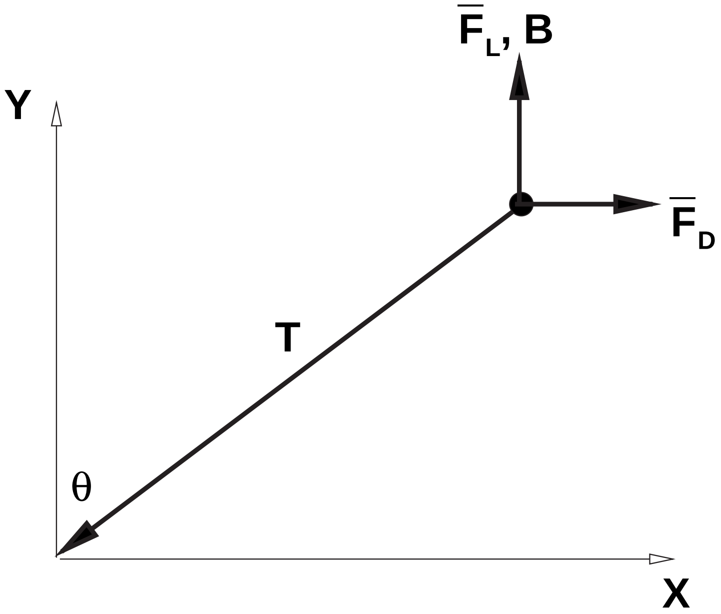

Figure 5.1: Mean force balance for the tethered cylinder

$$J\ddot{\theta}' = -\theta' \cdot \left(\overline{T} + F_D' \cdot \sin\overline{\theta} + F_L' \cdot \cos\overline{\theta}\right) \cdot L + \left(F_D' \cdot \cos\overline{\theta} - F_L' \cdot \sin\overline{\theta}\right) \cdot L \tag{5.13}$$

or:

$$J\ddot{\theta}' + \theta' \cdot \left(\overline{T} + F_D' \cdot \sin\overline{\theta} + F_L' \cdot \cos\overline{\theta}\right) \cdot L = \left(F_D' \cdot \cos\overline{\theta} - F_L' \cdot \sin\overline{\theta}\right) \cdot L \tag{5.14}$$

The term $\left(\overline{T} + F_D' \cdot \sin\overline{\theta} + F_L' \cdot \cos\overline{\theta}\right) \cdot L$ acts like the spring restoring force in the equations of motion for a freely oscillating cylinder, except that in this case it is non-linear as it alters through F_D' and F_L'.

In order to determine an equation for the natural frequency, equation 5.14 is linearized by assuming that the mean tension $\overline{T}$ is much greater than the non-linear term $(F_D' \cdot \sin\overline{\theta} + F_L' \cdot \cos\overline{\theta})$, and this non-linear term may be neglected. The linearized form of the equation of motion is then written in polar form as:

$$J\ddot{\theta}' + \theta' \cdot \overline{T} \cdot L = \left(F_D' \cdot \cos\overline{\theta} - F_L' \cdot \sin\overline{\theta}\right) \cdot L \tag{5.15}$$

The natural frequency of the tethered cylinder system is determined by solving the homogeneous form of equation 5.15, and is equal to:

$$f_n = \frac{1}{2\pi}\sqrt{\frac{\overline{T}L}{J}}. \tag{5.16}$$

From the definition, $J = m \cdot L^2$, equation 5.16 can be written as:

$$f_n = \frac{1}{2\pi}\sqrt{\frac{\overline{T}}{mL}}. \tag{5.17}$$

$\overline{T}$ can be decomposed in terms of the drag and buoyancy forces, and written in non-dimensional form as:

$$\overline{C_T} = \frac{\overline{T}}{\frac{1}{2}\rho_w U^2 D} = \sqrt{\overline{C_D}^2 + \left(\frac{\pi}{2} \cdot \frac{1}{Fr^2} \cdot (1 - m^*)\right)^2}. \tag{5.18}$$

By substituting equations 5.17 and 5.18 into the definition for the reduced velocity (equation 5.1), and rewriting in non-dimensional form, we obtain

$$u^* = \frac{2\pi^{\frac{3}{2}}}{\sqrt{2}} \left(\frac{(m^* + C_a)L^*}{\left(\overline{C_D}^2 + [\frac{\pi}{2} \cdot \frac{1}{Fr^2} \cdot (1 - m^*)]^2\right)^{\frac{1}{2}}} \right)^{\frac{1}{2}}, \tag{5.19}$$

where C_a is the added mass coefficient (see Govardhan & Williamson (2000) for details), and is equal to 1 for a circular cylinder.

For mean layover angles, $\overline{\theta}$, less than approximately 30^o, Equation 5.19 may be simplified by neglecting the mean drag coefficient, as the buoyancy force dominates drag force in this layover range. If this simplification is made, Equation 5.19 reduces to the same form as that found by Williamson & Govardhan (1997) describing the reduced velocity for the flow past a tethered sphere.

The above derivation highlights two limitations in using the reduced velocity to describe the flow conditions. Unlike the case of the hydro-elastically mounted cylinder, both f_n and u^* are functions of the fluid forces acting on the cylinder, and are non-linear. The above definition of the linearized form of f_n and u^* (equations 5.17 and 5.19 respectively) assumes that θ' is small (typically less than 20^o), and that $\overline{T} >> (F'_D \cdot \sin\overline{\theta} + F'_L \cdot \cos\overline{\theta})$.

5.3 Mean Layover Angle Results

Figure (5.2) shows the mean layover angle obtained through the numerical simulations, as well as results from the water channel experiments, both as a function of reduced velocity. The numerical simulations are found to closely match the experimental values for $u^* < 12$. Valid results from the experimental rig were limited to this reduced velocity range (corresponding to a Reynolds number range of ($Re = 1000 - 3500$)); for $u^* > 12$, the mean layover angle was such that the boundary layer on the channel base

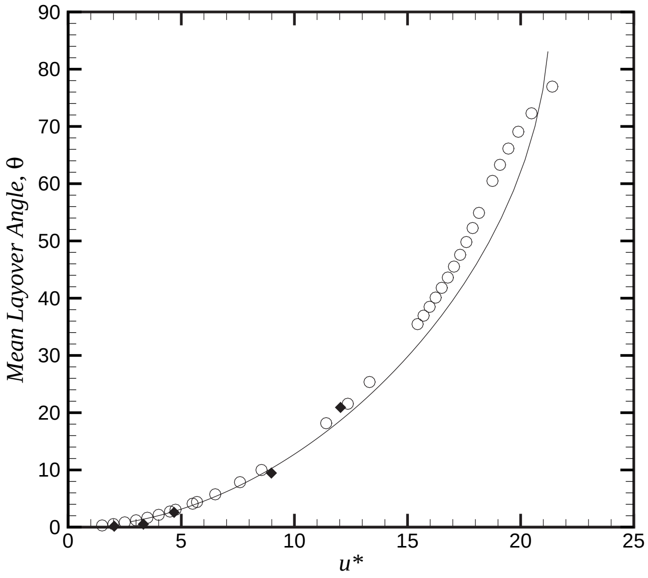

Figure 5.2: Mean layover angle, $\overline{\theta}$, as a function of reduced velocity, u^*; ○ numerical simulation, ⧫ experimental results,– analytical estimate (note the analytical estimate assumes a fixed $C_D = 1.34$, which is equivalent to the drag coefficient for a fixed cylinder at *Re*= 200).

interfered with both the cylinder motion and the hydrodynamic forces acting on the cylinder. The mean drag acting on cylinder was not measured directly in experiments. Instead, by assuming the mean lift tended to zero, the drag may be determined from the mean layover angle from the following equation

$$\overline{\theta} = \tan^{-1}\left(\frac{\overline{C_D}}{\overline{C_L} + (1 - m^*) \cdot \pi/2 \cdot 1/Fr^2}.\right) \tag{5.20}$$

An analytical estimate of the mean lay-over angle was also made from Equation (5.20) and is plotted in Figure (5.2) as a solid line. Here, the drag coefficient was held constant ($C_D = 1.34$), and was equal to the drag coefficient for a stationary cylinder at the corresponding Reynolds number of *Re*= 200 (Henderson (1995)). For $u^* < 5$, the predicted response using Equation (5.20) describes both the numerical and experimental values of $\overline{\theta}$ accurately. In the reduced velocity range, $5 < u^* \leq 18.5$, the rate of increase of $\overline{\theta}$ with respect to u^* gradually deviates away from the predicted curve. Beyond $u^* = 18.5$, this rate of increase rapidly diminishes and crosses the predicted curve at $u^* \simeq 20$. Beyond $u^* = 20$, the curve over-predicts $\overline{\theta}$. Equation (5.20) is essentially the ratio of drag to buoyancy force. Assuming constant buoyancy for a given mass ratio, any deviation in $\overline{\theta}$ away from that predicted from Equation (5.20) implies a variation in the drag force away from that found for a fixed circular cylinder. For a given u^*, $\overline{\theta}_{numerical} > \overline{\theta}_{predicted}$ implies that the mean drag is greater than that of a fixed cylinder and $\overline{\theta}_{numerical} < \overline{\theta}_{predicted}$ implies that the mean drag is less than that of a fixed cylinder.

5.4 Mean Drag Coefficient Results

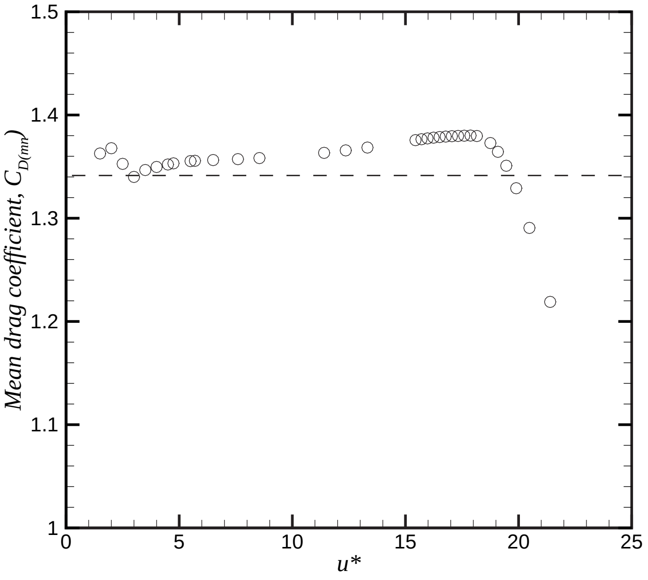

Figure 5.3: Mean drag coefficient,C_D, as a function of reduced velocity, u^*; ○ numerical simulation of tethered cylinder, $--$ for a fixed cylinder at Re= 200.

The drag coefficient is presented in Figure (5.3) as a function of u^*. As anticipated from the previous discussion, the drag coefficient gradually increases from that of a fixed cylinder in the range $5 < u^* < 18.5$ before rapidly decreasing below that of a fixed cylinder for $u^* > 19$. A small peak is observed at $u^* = 2.5$. At low reduced velocities and therefore low layover angles, the buoyancy force dominates the drag force and predictions using Equation (5.20) accurately estimate $\overline{\theta}$. Any variation in the drag may be associated with an increased amplitude in the oscillation of the tethered cylinder. Figure 5.3 indicates that two local maxima in the oscillation amplitude should be observed at $u^* = 2.5$ and 19. The small deviation in the mean drag as a function of reduced velocity indicates that the cylinder oscillations should be small for the entire range of reduced velocity investigated.

5.5 Mean Lift Coefficient Results

The mean lift, plotted both as a function of reduced velocity and mean layover angle, is presented in figure 5.4 and figure 5.5, respectively. For a large range of the reduced velocities investigated, a net negative lift was observed. The mean lift is always quite small, with a local minimum in the mean lift of $\overline{C}_L \simeq -0.05$ occurring at $u^* \simeq 19$. At this reduced velocity, C_D exhibited a local maximum. The mean lift was only observed to approach zero when $\overline{\theta} \geqslant 70^o$.

From section 1.2, it is hypothesized that the negative mean lift is due to an asymmetry in the mean wake profile about the centreline. To confirm this hypothesis, section 5.9.1 will show the existence of an asymmetry in the mean wake profile for the case of $u^* = 15.4$ and 19. The case of $u^* = 21$, corresponding to $\overline{\theta} = 78^o$, exhibited a symmetric wake.

It is further hypothesized that the asymmetry in the mean wake profile is due to the combined in-line and transverse components of motion imposed by the restraining tether. This hypothesis is examined in section 5.8 and further in chapter 7 where the effect of the tether length is examined in detail.

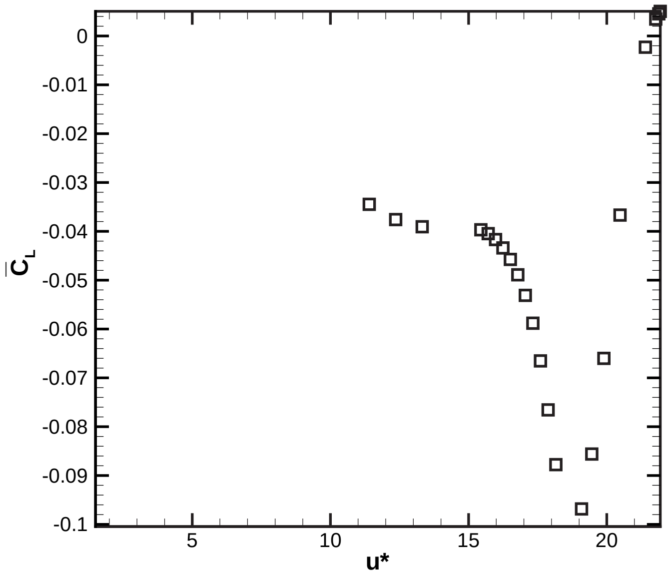

Figure 5.4: Mean lift as a function of reduced velocity

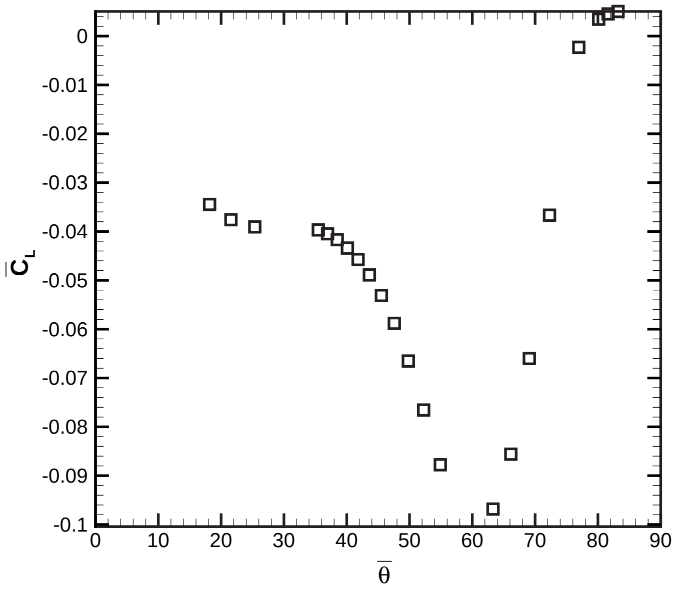

Figure 5.5: Mean lift as a function of mean layover angle.

5.6 Amplitude of Oscillation

The normalized amplitude of oscillation in the direction of cylinder motion ($A^* = \frac{A}{D}$) is presented in Figure (5.6) along with the in-line ($x^* = \frac{x}{D}$) and transverse ($y^* = \frac{y}{D}$) components, each as a function of the reduced velocity. As anticipated, two distinct peaks are observed in A^*; the first, occurring at $u^* = 2.5$, is very small in amplitude and is dominated almost entirely by the in-line component. This dominance implies that the forcing is comprised almost entirely of the drag force component. It appears that the peak is due to a resonance between the natural frequency, f_n, of the system and the drag signal, f_D, which (at this reduced velocity) is twice the lift frequency, f_L. Assuming the Strouhal number for a stationary cylinder, $St \simeq 0.2$, the natural frequency and the drag signal are equivalent at $u^* \simeq 2.5$, in agreement with the assumption of a resonance between the two frequencies. The peak amplitude of the oscillations at $u^* = 2.5$ (dominated by an in-line component) is far lower than the second peak found at $u^* = 19$ (dominated by a transverse component). The relative amplitudes of the in-line and transverse branches are in agreement with King (1974), who studied the in-line vortex-induced oscillation of a hydro-elastically mounted cylinder. He found two in-line branches of oscillation in the reduced velocity range, $u^* \simeq 1 - 3$ with maximum

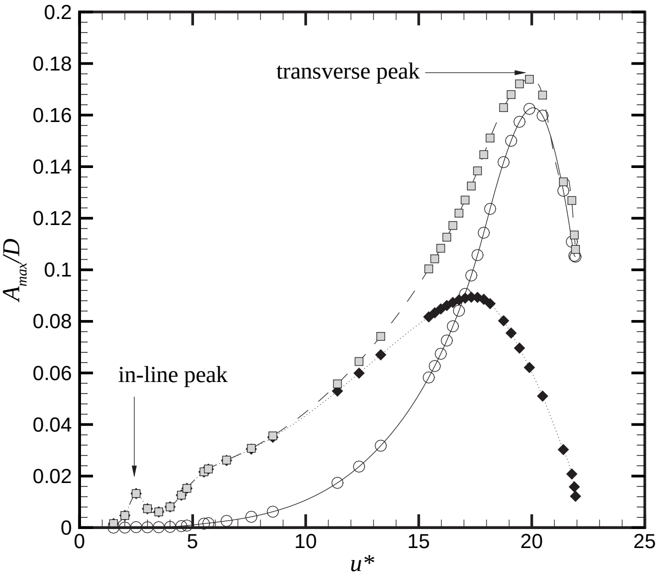

Figure 5.6: Normalized amplitude of oscillation as a function of reduced velocity; ◆, in-line component of normalized oscillation amplitude; ○, transverse component of normalized oscillation amplitude; □, normalized oscillation amplitude in the direction of motion.

in-line oscillations peaking at $A^* = 0.12D$. The first branch has a symmetric shedding wake, while the wake structure of the second branch resembles a Karman vortex street.

At a reduced velocity, $u^* = 17$, corresponding to a mean lay-over angle, $\overline{\theta} = 45^o$, the transverse component of oscillation, y^*, begins to dominate the in-line component. The in-line component of oscillation peaks at $u^* = 17.5$ prior to decreasing rapidly. Throughout the reduced velocity range, $u^* = 5 - 19$, A^* continues to increase and is increasingly dominated by the transverse component.

A second peak in A^* is observed at a reduced velocity, $u^* \simeq 20$. At this reduced velocity the mean lay-over angle is $\overline{\theta} \simeq 70^o$, and the oscillations are dominated by the transverse component (y^*), which accounts for 93% of the oscillation amplitude in the direction of motion. For reduced velocities greater than 20, both A^* and y^* decrease rapidly with u^*. At these high layover angles, the cylinder behaves in a fashion similar to a low mass-damped, hydro-elastically mounted cylinder undergoing transverse vortex-induced vibration as described by Khalak & Williamson (1999) and Govardhan & Williamson (2000). The high value of u^*, combined with $m^* = 0.833$, implies that the oscillations occur on the lower branch of oscillation and that the cylinder oscillations become de-synchronized from the vortex shedding frequency. At $u^* = 22$, this phenomenon is observed, the oscillation time series is chaotic and appears uncorrelated to the vortex shedding frequency. The cylinder oscillation at these high reduced velocities ($u^* > 20$) is therefore in agreement with the findings of Govardhan & Williamson (2000).

Three force coefficients can be identified that describe the transient forces acting on the cylinder to induce motion; the drag coefficient, C_D, the lift coefficient, C_L, and the force coefficient acting in the direction of motion, C_{Tan}. The instantaneous value of C_{Tan} is defined by:

$$C_{Tan} = C_D \cos(\overline{\theta} + \theta') - (C_L + \frac{\pi}{2} \cdot \frac{1}{Fr^2}(1 - m^*)) \sin(\overline{\theta} + \theta') \qquad (5.21)$$

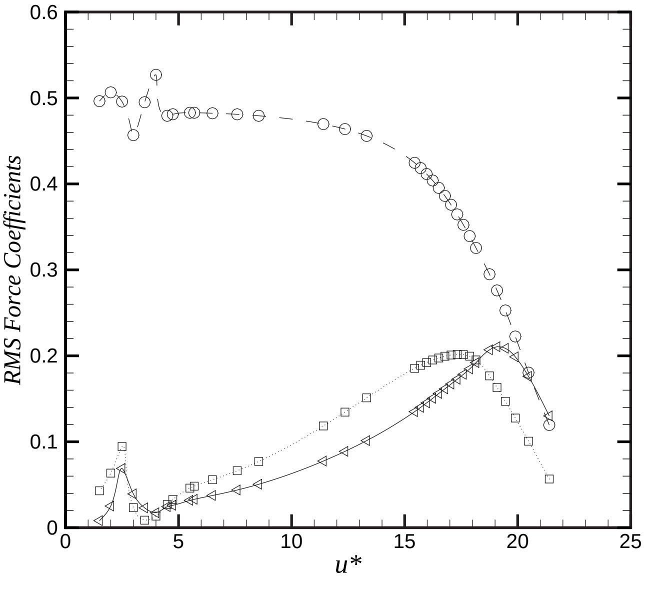

Figure 5.7: RMS force coefficients as a function of reduced velocity; ○ RMS Lift, □ RMS Drag, ◁ RMS C_{TAN} (force coefficient in the direction of motion).

A plot of the RMS values of the amplitudes of each of these coefficients is presented in Figure (5.7), as a function of the reduced velocity. In the reduced velocity range, $u^* = 1 - 4$, all three RMS force coefficients exhibit significant fluctuations. As anticipated, both RMS C_D and RMS C_{Tan} exhibit a local peak at $u^* = 2.5$. Of interest is RMS C_D, whose peak value at $u^* = 2.5$ appears to be larger in amplitude than RMS C_{Tan}. A more refined analysis of this parameter space would reveal if this is correct. By considering the mean layover angle at this reduced velocity ($\overline{\theta} = 0.875$ degrees), it would be assumed that the cylinder oscillates in the in-line direction, and the oscillations are almost entirely independent of the fluctuating lift force. This is clearly not the case, and Equation (5.21) indicates that the instantaneous amplitude of the lift force is considerably greater than the instantaneous amplitude of the drag force, and acts to reduce the total force contribution in the direction of motion. From Figure (5.7), this is indeed the case; the RMS lift is over five times that of the RMS drag for $u^* \lesssim 10$. As with the in-line amplitude of motion, the RMS drag force peaks at $u^* \simeq 17.5$ before decaying. The RMS C_{Tan} peaks at $u^* \simeq 19$ before decaying, its maximum value barely exceeding the maximum drag value. For $u^* > 20$, the RMS lift dominates the RMS C_{Tan} and both decay up to the highest reduced velocity investigated.

5.7 Frequency of Oscillation

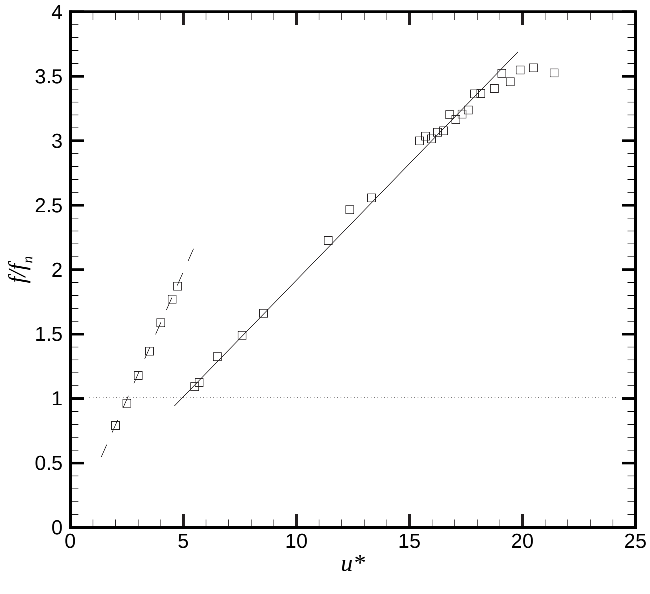

Figure 5.8: Frequency of oscillation, normalized against the natural frequency of the tethered body system (f/f_n), where f is the oscillation frequency, and f_n is the natural frequency of the system; as a function of the reduced velocity. The dashed line is the drag frequency for a fixed cylinder at Re= 200, the solid line is the lift frequency for a fixed cylinder at Re= 200.

Figure (5.8) shows the fundamental frequency of oscillation, normalized against the natural frequency of the tethered cylinder system, as a function of the reduced velocity. In this figure, the solid line is the Strouhal number for a fixed cylinder (St_1), corresponding to the fixed cylinder lift frequency, and the dotted line is twice the Strouhal number of the shedding frequency for a fixed cylinder (St_2), corresponding to the fixed cylinder drag signal.

For $u^* < 5$, the principal frequency of oscillation is synchronized with St_2, i.e. the in-line force frequency for a fixed cylinder. This is anticipated as the cylinder is dominated by the in-line component of oscillation. At $u^* \simeq 2.5$, St_2 is synchronized with the natural frequency of the tethered body system, accounting for the peak in both the oscillation amplitude and the RMS in-line force at this reduced velocity (figures (5.6) and (5.7)).

In the reduced velocity range, $u^* = 2.5 - 3.5$, there is a reduction in the oscillation amplitude and RMS fluid forces (see figures (5.6) and (5.7)). This is due to the oscillation frequency no longer being synchronized with the natural frequency of the tethered cylinder system. From figure (5.6), the oscillation amplitude increases rapidly with increasing reduced velocity in the range, $u^* = 3.5 - 5$. At $u^* = 5$, St_1 is synchronous with the natural frequency of the system and the dominant oscillation frequency switches to St_1. Beyond $u^* = 5$, as the oscillation frequency departs from f_n, there is a sudden decrease in the gradient of oscillation amplitude as a function of reduced velocity (as shown in Figure 5.6), however the dominant oscillation frequency remains close to St_1.

Only two regions of synchronization or “lock-in” are found when one considers the classical definition of lock-in, i.e. a synchronization of the vortex shedding frequency (f_V) and body oscillation frequency (f) with the natural frequency of the system (f_n), so that $f^* = \frac{f}{f_n}$ is close to unity, which is valid for hydro-elastically mounted cylinders of large $m^* = O(100)$. The first, at $u^* = 2.5$, results in a local peak of the oscillation amplitude, the second at $u^* = 5$ results in a change in gradient in the oscillation amplitude vs u^*. If the ratio between the fluid forcing frequency and the shedding frequency from a fixed cylinder is considered (Govardhan & Williamson (2000)), a lock in regime clearly exists for a much broader range of $u^* = 1 - 19$. This form of lock in behaviour is similar to the response of a freely vibrating cylinder at very low mass-damping (Khalak & Williamson (1999)). This is in contrast with a low mass-ratio tethered sphere in which the oscillation frequency has been found not to correspond to either the vortex shedding frequency or natural frequency within the same reduced velocity range (Govardhan & Williamson (1997)).

The transition in the principal frequency from synchronization with St_2 to synchronization with St_1 would, at first glance, imply a transition in the dominant force component from drag to lift. However, this transition occurs at a surprisingly low reduced velocity when the mean layover angle is considered. At $u^* = 5$, the mean layover angle, $\overline{\theta} = 4.2^o$, and it would be assumed that the drag force would continue to dominate the oscillations in preference to the lift force. Analysis of figure (5.6) also implies that C_{Tan} is dominated by the drag force up to $u^* \simeq 17$, well beyond the point of frequency transition, and analysis of figure (5.7) clearly confirms this assumption. This leads to the conclusion that the drag signal is dominated by the same frequency as the lift for $u^* > 4$. As the reduced velocity increases beyond 17, the dominant driving force switches to the lift force; however, the frequency of oscillation does not change as the principal frequency of the lift remains equivalent to the principal frequency of the drag force.

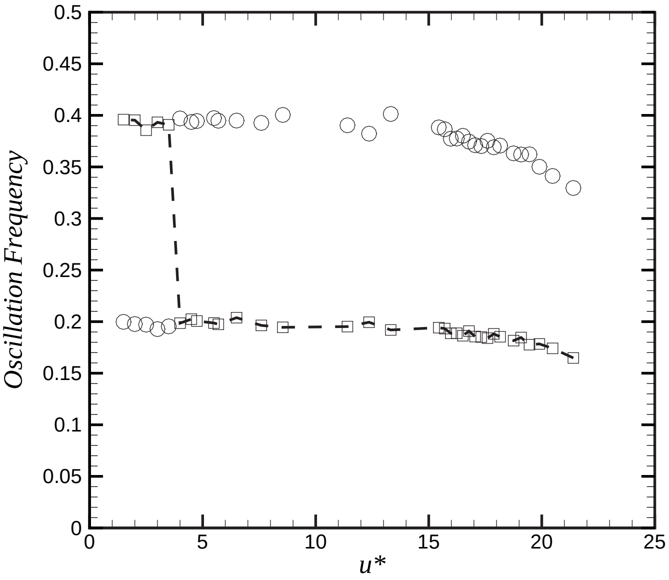

Figure 5.9: Principal (f_1) and secondary (f_2) components of the cylinder oscillation as a function of reduced velocity. □ principal frequency of oscillation, ○ secondary frequency of oscillation.

The abrupt switch in dominant frequency at $u^* = 5$ is apparent in figure (5.9). For $u^* < 5$, the dominant normalized frequency, f_1, is 0.4 (or the drag signal) and the secondary normalized frequency, f_2, is 0.2 (the lift frequency). At $u^* = 5$, f_1 and f_2

switch values, such that for $u^* > 5$, f_1 is 0.2 and f_2 is 0.4. A decrease in both f_1 and f_2 of the cylinder oscillation is observed for $u^* > 19$ as the oscillations become de-synchronized with the wake flow field.

5.8 Time History of Oscillation

Three branches of oscillation have so far been discussed and are clearly visible in figures (5.6) and (5.7). The first branch ($u^* \simeq 2.5$) is due to a resonance between the drag signal and the natural frequency of the system. The second branch occurs in the reduced velocity range, $u^* = 5 - 19$, peaking at $u^* = 19$. In the previous section, it was hypothesized that the change in the oscillation frequency is due to a resonance between the natural frequency of the tethered body system and the subharmonic of the drag signal. For $u^* > 19$, the oscillations are dominated by the lift force, and the tethered cylinder appears to behave as a hydro-elastically mounted cylinder.

Time histories of the fluid forces and cylinder motion for $u^* = 2.5, 3.5$ and 5.0 are presented in figure 5.10, 5.11, and 5.12 respectively. At $u^* = 2.5$, the drag signal clearly has twice the frequency of the lift signal, suggesting a Karman type wake shedding and indicating that the local peak in A^* observed at this reduced velocity compares with the second instability region of in-line oscillation observed by King (1974). Both C_{Tan} and A^* exhibit the same frequency as the drag force term with a slight modulation in amplitude due to the lift term.

As the reduced velocity is increased to 3.5, a significant alteration is observed. As anticipated, the drag force diminishes markedly in amplitude as the drag force is no longer synchronized with the natural frequency of the tethered cylinder system. However, every second peak of the drag signal is substantially greater in amplitude than the neighboring peaks. The normalized amplitude of oscillation (A^*) shows the same behavior, indicating that the natural frequency of the system is indeed influencing the subharmonic of the drag force.

As the reduced velocity is further increased to $u^* = 5.5$, the drag is clearly dominated by St_1 and is in phase with the lift. This may explain the increase in the amplitude of oscillation as both the RMS lift and drag forces act in unison to drive the cylinder oscillations. Both A^* and C_{Tan} are also dominated by the St_1 frequency lending support to this theory.

Beyond $u^* = 19$, the drag signal remains dominated by St_1, however the St_2 com-

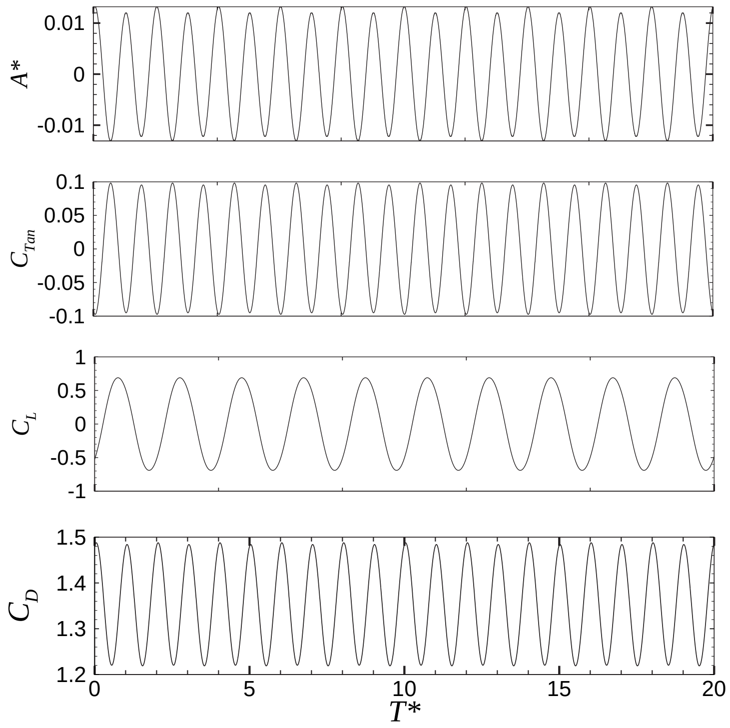

Figure 5.10: Variation of amplitude and force coefficients against normalized time for $u^* = 2.5$.

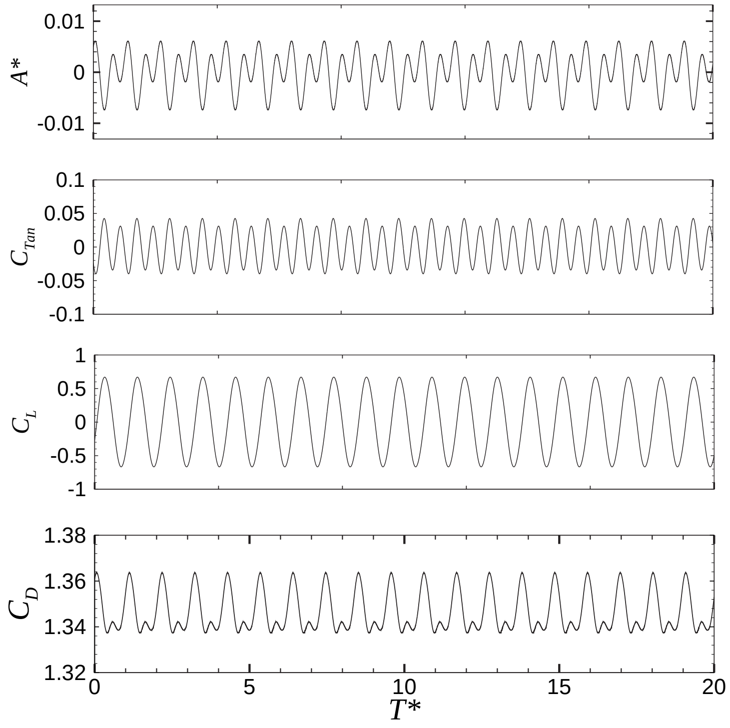

Figure 5.11: Variation of amplitude and force coefficients against normalized time for $u^* = 3.5$.

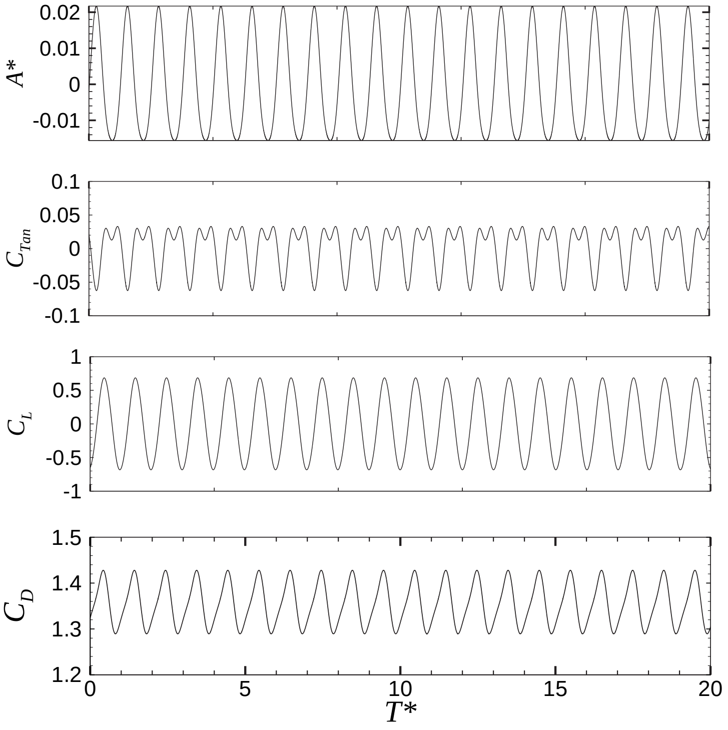

Figure 5.12: Variation of amplitude and force coefficients against normalized time for $u^* = 5.5$.

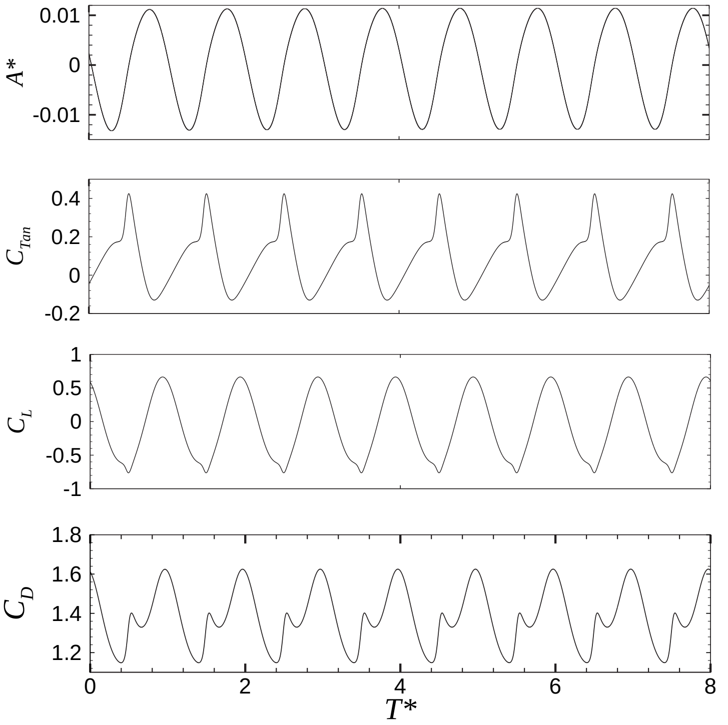

Figure 5.13: Variation of amplitude and force coefficients against normalized time for $u^* = 22$.

ponent is more noticeable when compared to lower reduced velocities. The time history for $u^* = 22$ is presented in figure 5.13. Every second drag peak has a higher amplitude then its neighboring peak indicating that a significant component of the St_1 frequency still exists in the drag signal. At this reduced velocity, the cylinder behaves similar to a low mass-damped cylinder oscillating transverse to the flow field. The phase angle between the cylinder motion and C_{TAN} is 180^o. For a very low mass-damped freely oscillating cylinder (Govardhan & Williamson (2000)), the phase angle between the displacement and forcing was 180^o only for the lower branch of amplitude response. This similarity provides an explanation for the reduction in A^* and the de-synchronization from the vortex shedding frequency for $u^* > 19$, as the cylinder is now oscillating in the lower branch of shedding as described by Govardhan & Williamson (2000) for a hydro-elastically mounted cylinder.

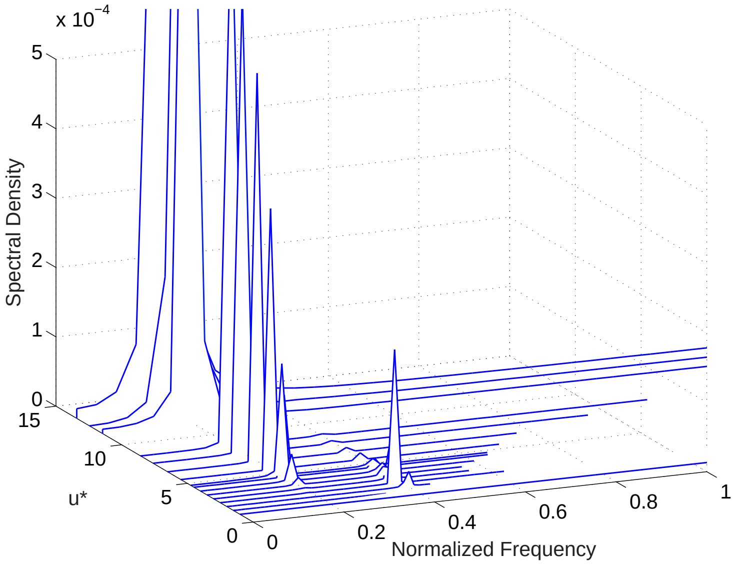

Figure 5.14: Spectral density of the cylinder oscillation as a function of reduced velocity.

Figure (5.14) depicts the spectral density of the cylinder oscillation as a function of the reduced velocity. For $u^* \leq 5$, no peak is apparent for the St_1 frequency, and the St_2 frequency dominates the cylinder oscillations. For $u^* > 5$, a local peak in the frequency synchronous with the St_1 frequency is apparent. A local peak in the frequency synchronous with the St_2 frequency is observed for all reduced velocities studied.

5.9 Flow Field Analysis

The vorticity and pressure fields are examined in this section, for a variety of reduced velocities. Section 5.9.1 analyzes the mean vorticity field for the reduced velocity values $u^* = 15.4$, 19 and 21. From this analysis, an asymmetry in the wake is noted for $u^* = 15.4$ and 19, corresponding to the net negative lift found previously. Snapshots of the vorticity field taken at the top and bottom position of the cylinder motion are compared for the same three reduced velocities in section 5.8, which associates variation in the inception of vortex structures in the wake to the instantaneous motion of the cylinder. Finally, in section 5.9.3, instantaneous pressure fields are analyzed for $u^* = 3.5$ and 5.5 in order to explain the change in the drag frequency noted in section 5.7.

5.9.1 Mean Vorticity Fields

Figures 5.15(a), 5.15(b) and 5.15(c) show the mean vorticity fields measured over one cycle of oscillation for $u^* = 15.4$, 19 and 21 respectively. Analysis of these figures indicates a distinct asymmetry in the wake for $u^* = 15.4$ and 19. The wake formation region for these reduced velocities is significantly shorter than for $u^* = 21$. Here, the formation length is measured as the distance from the mean position of the rear surface of the cylinder to the position downstream where the mean u velocity component is zero. The values of the formation length are detailed in table 1. The variation in the formation length as a function of u^*, and the variation in the downstream location of the positive and negative vortex cores, are due to the asymmetric forces imposed by the motion of the cylinder during the shedding cycle.

A difference in the downstream extent of the positive shedding vortex compared to the negative shedding vortex is observed for both $u^* = 15.4$ and 19. This difference appears to reduce with increasing reduced velocity. It is speculated that this is due to the reduction in the in-line component of oscillation as the reduced-velocity is increased.

For $u^* = 15.4$ and 19, the centroid of the time-mean vortex structure is 0.6 diameters downstream of the mean position of the rear surface of the cylinder. As the reduced-velocity is increased to $u^* = 21$, the centroid of the time-mean vortex cores increases to 1.05 cylinder diameters downstream of the mean position of the rear surface of the cylinder. Bearman (1965) found that, for the flow past a blunt body fitted with a splitter plate, the position of the fully formed vortex downstream of the body was inversely proportional to the base pressure coefficient. Assuming that a similar trend

	$u^* = 15.4$	$u^* = 19$	$u^* = 21$
$Core^+$	0.615	0.594	1.038
$Core^-$	0.415	0.532	1.038
Formation length	1.196	1.118	1.787
Wake thickness	1.688	1.656	1.788

Table 5.1: Position of time-mean positive and negative vortex cores downstream of the cylinder, formation length, and wake thickness 2δ, where δ is the boundary layer thickness measured at $(Core^+ + Core^-)/2$

applies to the time-mean vortex structures in the wake of a circular cylinder, from the results listed in table 5.1, it would therefore anticipated that the mean drag acting on the cylinder would therefore decrease as the reduced-velocity is increased from $u^* = 19$ to $u^* = 21$. This is finding is observed in figure 5.3.

5.9.2 Vorticity Field Analysis

Figures 5.16, 5.17 and 5.18 show contours of vorticity at the top and bottom of the oscillation cycle for $u^* = 15.4, 19$ and 21, respectively. These reduced velocity values are considered as they fall in the vicinity of the transverse peak shown in figure 5.6 above; the case of $u^* = 19$ has the largest amplitude oscillations found for the reduced-velocity range investigated ($u^* = [1, 25]$). For each reduced-velocity, the first frame (frame a) coincides with the most counter-clockwise position of the cylinder (referred to as the top of the oscillation cycle), and the second frame (frame b) coincides with the bottom of the oscillation cycle.

As there is no external damping term in the equations of motion (equation 5.2), and an appreciable amplitude in the reduced velocity range investigated, the phase lag between the force acting on the cylinder and the resultant displacement is 180^o. Therefore, for each reduced velocity, the first frame (frame a) coincides with the maximum positive peak in the fluctuating fluid forces acting on the cylinder.

Figure 5.16 shows contours of vorticity (ω_z) for the reduced-velocity, $u^* = 15.4$. At this reduced-velocity, the mean layover angle $\overline{\theta} = 35.5$ and the oscillations are dominated by the in-line component (see figure 5.6). At the top of the cylinder oscillation cycle (figure 5.16(a)), four vortex structures are observed. Two of these vortices (labelled

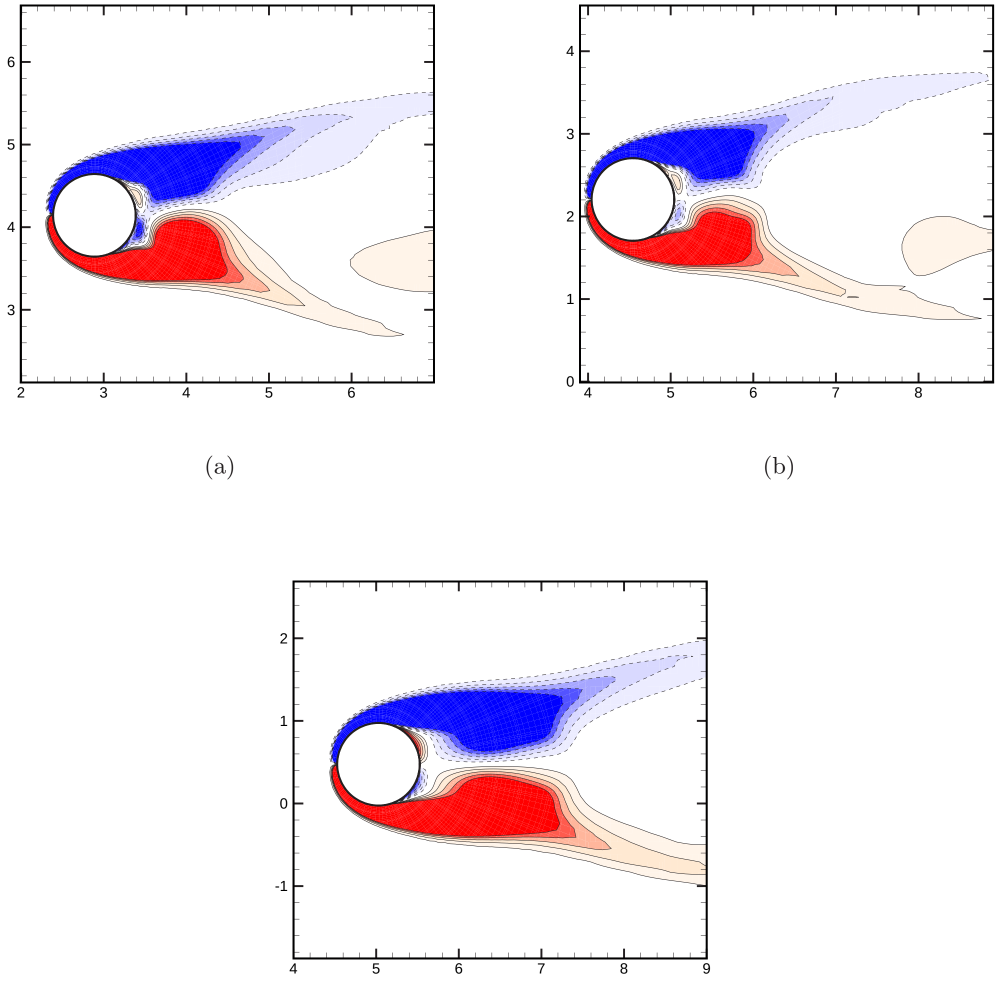

(a)

(b)

(c)

Figure 5.15: Contours of the time-mean span-wise vorticity in the wake of a tethered cylinder for (a) $u^* = 15.4$, (b) $u^* = 19$, and (c) $u^* = 21$. Contours are evenly spaced over the range (blue) $-1 \leqslant \overline{\omega_z} \leqslant 1$ (red); with $\Delta\overline{\omega_z} = 0.2$.

A and B) represent the shedding negative and positive vortex structures, respectively. In response to the pressure gradient induced by the presence of both vortices A and B, and the no-slip condition on the surface of the cylinder, two secondary vortices (labelled C and D, representing positive and negative vortex structures, respectively) are generated in the vicinity of the rear surface of the cylinder. Figure 5.16(a) represents a positive peak in the fluctuating hydrodynamic forces acting in the direction of cylinder motion; the combined effect of the size and location of vortex A and vortex B directly behind the cylinder induce a low pressure region. In figure 5.16(b), the cylinder is once again momentarily stationary (now located at the bottom of the oscillation cycle), the

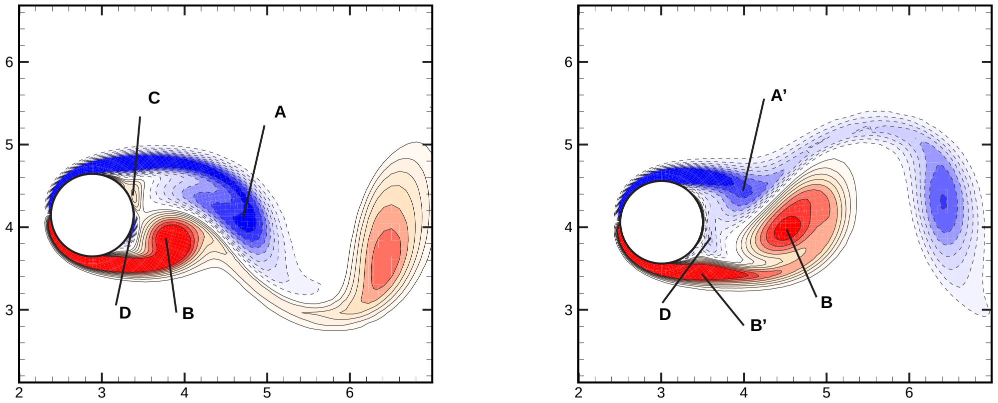

(a)

(b)

Figure 5.16: Contours of span-wise vorticity in the wake of a tethered cylinder for $u^* = 15.4$ corresponding to (a) the top of the oscillation cycle and (b) the bottom of the oscillation cycle. The flow is from left to right. Contours are evenly spaced over the range (blue) $-1 \leqslant \omega_z \leqslant 1$ (red); with $\Delta\omega_z = 0.2$.

fluctuating fluid forces acting on the cylinder have reached a maximum negative value. Comparing the flow field at the top and bottom of the cycle, a subtle asymmetry in the wake is noted. At the top of the cycle, vortex A is far more elongated than vortex B at the bottom of the cycle. The asymmetry is also apparent when observing figure 5.16(b) where vortex D is observed to dominate the entire near wake region.

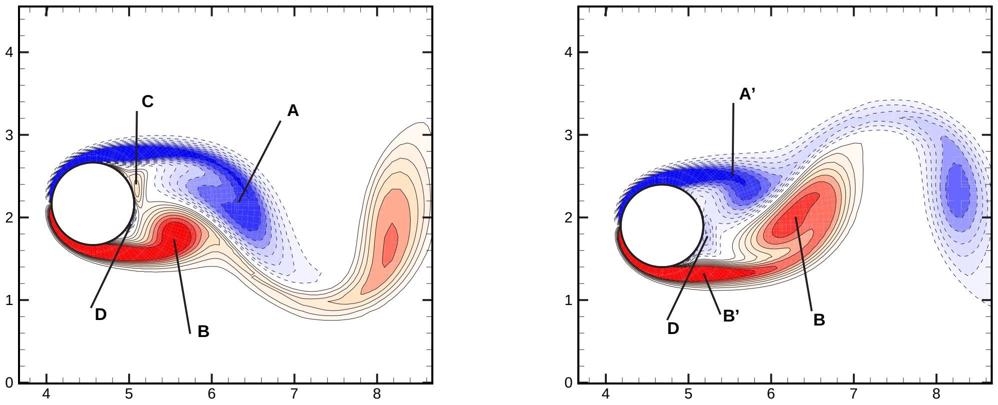

(a)

(b)

Figure 5.17: Contours of span-wise vorticity in the wake of a tethered cylinder for $u^* = 19$; (a) corresponds to the top of the cycle, (b) corresponds to the bottom of the oscillation cycle. The flow is from left to right. Contours are evenly spaced over the range (blue) $-1 \leqslant \omega_z \leqslant 1$ (red); with $\Delta\omega_z = 0.2$.

As the reduced-velocity is increased to $u^* = 19$ (figure 5.17), representing the largest amplitude oscillations over the range of reduced velocities studied ($u^* = [1, 25]$), the cylinder wake structure is very similar to the case of $u^* = 15.4$ at every stage of the oscillation cycle, indicating that the mode of cylinder oscillation is similar. At this reduced velocity, the mean layover angle has increased to $\overline{\theta} = 63.3^o$ and the cylinder oscillation is now dominated by the transverse component. The vortex structures have increased significantly in size; this occurs for two reasons. First, as the reduced-velocity is increased, the period of oscillation also increases and the vortex structures have more time to develop over an oscillation cycle. Second, at this particular reduced velocity ($u^* = 19$) the amplitude of oscillation of the cylinder is significantly greater than for the case of $u^* = 15.4$. This is also associated with an increase in the fluctuating acceleration acting on the cylinder, which increases the size of the vortices being shed from the cylinder. It is assumed that the increase in oscillation amplitude is due to the increase in the Froude number, with a subsequent reduction in the mean vertical force ($\overline{F_y}$) which results in the mean layover angle increasing and the cylinder oscillation being less constrained by the in-line component.

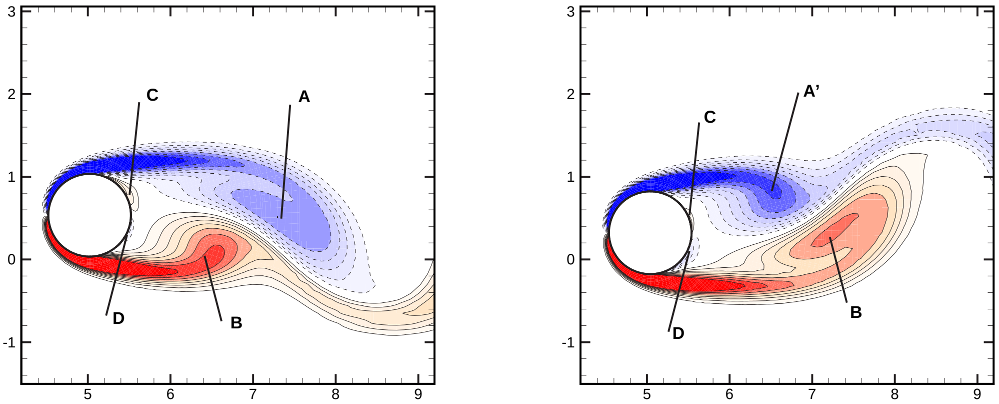

(a)

(b)

Figure 5.18: Contours of span-wise vortex structures in the wake of a tethered cylinder for $u^* = 21$, (a) corresponds to the top of the cycle, (b) corresponds to the bottom of the oscillation cycle, the flow is from left to right. Contours are evenly spaced over the range (blue) $-1 \leqslant \omega_z \leqslant 1$ (red); with $\Delta\omega_z = 0.2$.

As the reduced velocity is further increased to $u^* = 21$, there is a significant change in the wake structure, relative to the two previous cases. Here the mean layover angle $\overline{\theta} = 83^o$ and the motion is dominated by the transverse component. At this reduced velocity, the in-line component of the oscillation amplitude is $x_{amp} \simeq 0.012D$, whereas the transverse component of the oscillation amplitude is $y_{amp} \simeq 0.1D$. The near wake structure (comprising vortex C and D) is considerably more symmetric.

In summary, a mode of wake formation has been identified (and will be referred to as the 'transition mode') from the vortex structures in the wake of the oscillating cylinder for $u^* = 15.4$ and 19. From the findings of Ryan *et al.* ((2003), for this cylinder mass ratio and tether length ratio, the transition mode would appear to exist over the range $u^* = [5, 19]$ and involves a transition from cylinder oscillations dominated by the in-line component (at low reduced velocities) to oscillations dominated by the transverse component (at high reduced velocities).

In the transition mode, the in-line motion of the cylinder appears to be critical to the vortex shedding structures in the wake, and produces a subtle but distinct asymmetry in the shedding wake not observed for the flow past a freely oscillating cylinder (see Govardhan & Williamson (2000)). The in-line component of motion acts to reduce the length of the formation region, inducing larger forces in both the in-line and transverse directions to act on the cylinder. As the mean layover angle, $\overline{\theta}$, exceeds 45^o, the oscillations are increasingly dominated by the transverse component, and the in-line component of oscillation rapidly diminishes.

As the reduced-velocity is increased from $u^* = 15.4$ to $u^* = 19$, the transverse oscillations of the cylinder are less constrained by the resultant in-line oscillations. The overall effect is an increase in the amplitude of cylinder oscillation as the reduced-velocity is increased to $u^* = 19$.

As the reduced-velocity is further increased to $u^* = 21$, the in-line component of oscillation is not sufficient to maintain the transition mode. The shedding vortices convect away from the cylinder at a faster rate and the length of the formation region increases. The forces acting on the cylinder diminish and the amplitude of oscillation decreases markedly, in agreement with the findings of Bearman (1965). The cylinder is now oscillating in a fashion similar to a low mass-damped hydro-elastically mounted cylinder oscillating in the lower branch of oscillation (as described by Govardhan & Williamson (2000)).

To quantitatively compare the force acting on the cylinder as a function of its relative position, the limit cycles of the cylinder position (θ') as a function of the normalized moment acting on the tethered cylinder system (M) for the three values of

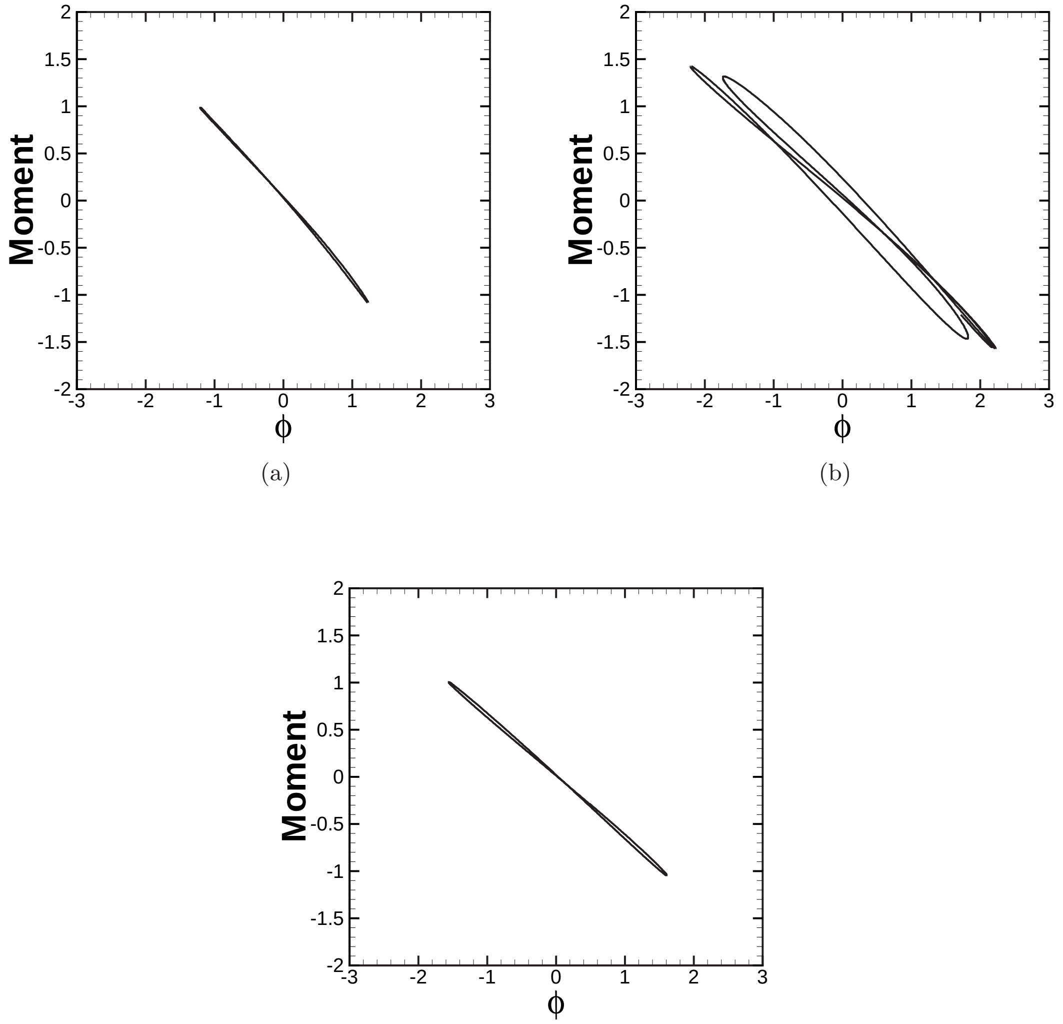

(a)

(b)

(c)

Figure 5.19: Cylinder displacement θ' as a function of the normalized moment acting on the tethered cylinder system, for the reduced velocities; (a), $u^* = 15.4$; (b), $u^* = 19$; and (c), $u^* = 21$. Each limit cycle is traversed in a clock-wise direction

u^* investigated above are presented in figure 5.19.

For each reduced velocity, the moment (and hence the force acting on the cylinder) is clearly 180^o out of phase with the cylinder position, θ', hence the maximum value of θ' coincides with the minimum value of M and vice versa.

For $u^* = 15.4$, asymmetry in the moment acting on the cylinder when comparing the top and bottom of the cycle. This asymmetry is considerably amplified for $u^* = 19$. For $u^* = 21$ the oscillation cycle is clearly more symmetric. As each cycle in figure 5.19 forms a closed limit cycle, the mean forces acting on the cylinder in the direction of motion must equate to zero over one cycle, and the cylinder will therefore oscillate about the mean angle $\overline{\theta}$.

5.9.3 Pressure Field Analysis

The transition from a St_2 to a St_1 dominated drag cycle may be better described by the analysis of pressure plots of the flow field over one period of the cylinder shedding cycle. Contour plots of the pressure fields are presented in figures 5.20 and 5.21.

Figure 5.20 shows the pressure field for a cylinder at the top of the cylinder cycle, defined as the uppermost position of the cylinder counter clockwise from the mean layover angle. The image on the left and right correspond to $u^* = 2.5$ and $u^* = 5.5$, respectively. Comparing the two images, the wake structures are in the same phase of spatial position. For both reduced velocities, the wake is of a von Karman type. At this phase of the oscillation cycle, the drag coefficient is at a minimum for both reduced velocities, and there are few differences between the two pressure fields.

Figure 5.21 depicts the pressure flow field taken $\frac{1}{4}$ of a shedding cycle later. In this case, the cylinder oscillating at $u^* = 2.5$ has reached the bottom of its cycle (i.e. it is halfway through its oscillation cycle) and is essentially stationary with respect to the pivot point. However, the cylinder oscillating at $u^* = 5.5$ is only $\frac{1}{4}$ through its oscillation cycle and is moving in the flow field direction with a maximum velocity with respect to the pivot point. As with figure 5.20, the wake pressure fields for both the reduced velocities are remarkably similar, however the stagnation pressure acting at the front of the cylinder for $u^* = 2.5$ is significantly greater than for $u^* = 5.5$. It would appear that the motion of the cylinder, oscillating at its natural frequency at $u^* = 5.5$, reduces the intensity of the stagnation pressure point over half of its cycle providing a drag signal component at the cylinder oscillation frequency (St_1). The drag cycle retains a component of the St_2 frequency due to the Karman type shedding wake for the entire range of reduced velocities investigated. The St_1 frequency is simply superimposed over this for $u^* > 3.5$.

Time histories of the base pressure coefficient (C_{PB}) and the leading-edge pressure coefficient (C_{PLE}) for $u^* = 2.5$ and $u^* = 5.5$ are shown in figures 5.22 and 5.23. As may be observed in figure 5.22, both C_{PB} and C_{PLE} are synchronized with the St_2 frequency. As the reduced velocity is increased to $u^* = 5.5$ (figure 5.23), C_{PB} remains dominated by the St_2 frequency, however the St_1 frequency is also apparent. By contrast, C_{PLE} is dominated by the St_1 frequency, in a fashion similar to the drag signal at this reduced

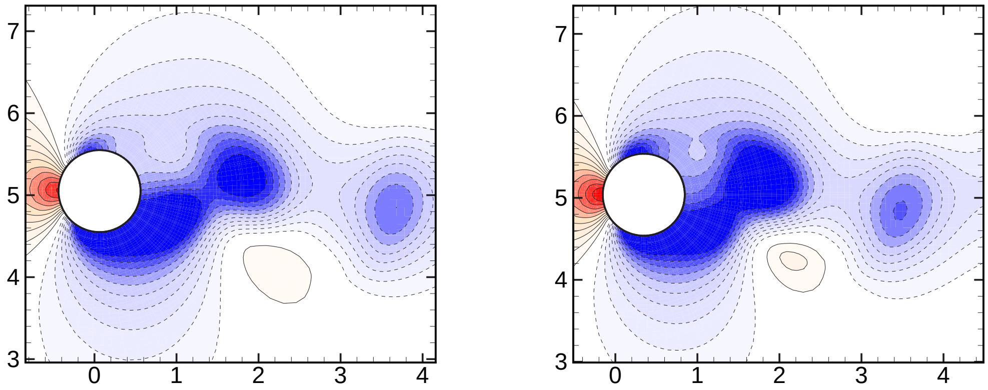

Figure 5.20: Pressure coefficient contours about the tethered cylinder at (left) $u^* = 2.5$ and (right) $u^* = 5.5$ for the uppermost position (most counter clockwise position from the mean layover angle) of the cylinder in its cycle. Contours are evenly spaced over the range (blue) $-0.5 \leqslant C_P \leqslant 0.5$ (red); with $\Delta C_P = 0.05$.

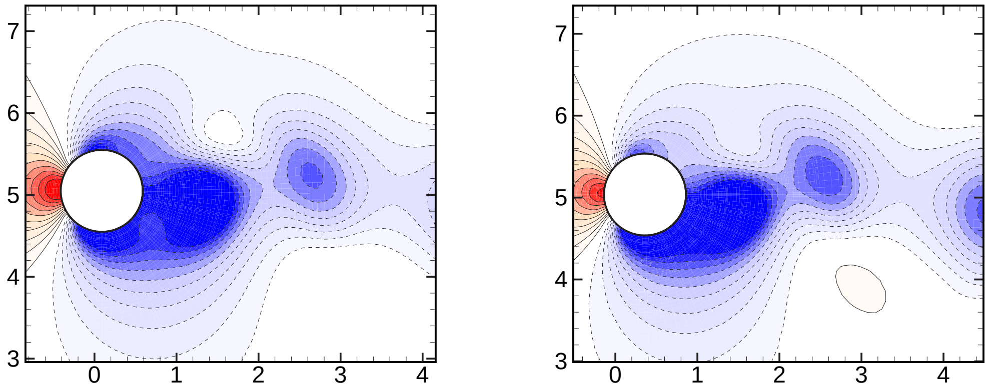

Figure 5.21: Pressure coefficient contours about the tethered cylinder at (left) $u^* = 2.5$ and (right) $u^* = 5.5$, $\frac{1}{4}$ of a shedding cycle after the cylinder reaches its uppermost position. Contours are evenly spaced over the range (blue) $-0.5 \leqslant C_P \leqslant 0.5$ (red); with $\Delta C_P = 0.05$.

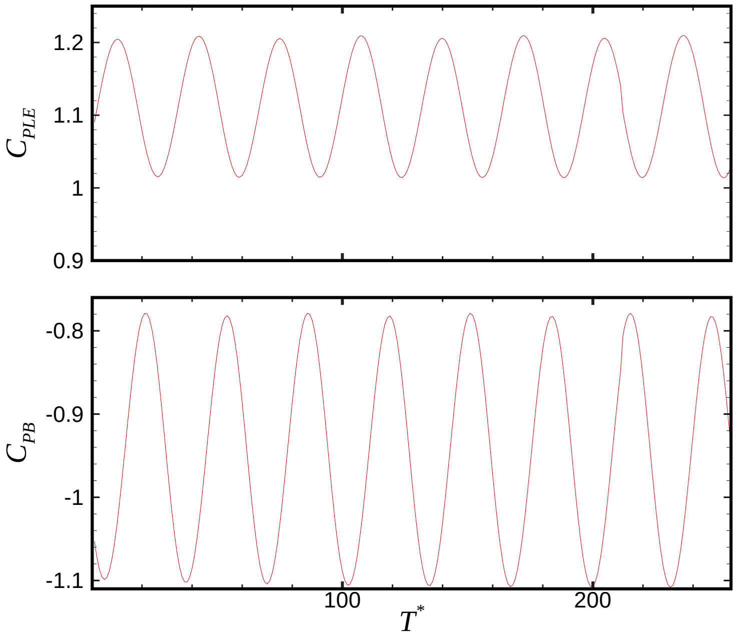

Figure 5.22: (Top) leading edge stagnation point pressure coefficient (C_{PLE}) and (Bottom) base pressure coefficient (C_{PB}) as a function of normalized time, for $u^* = 2.5$.

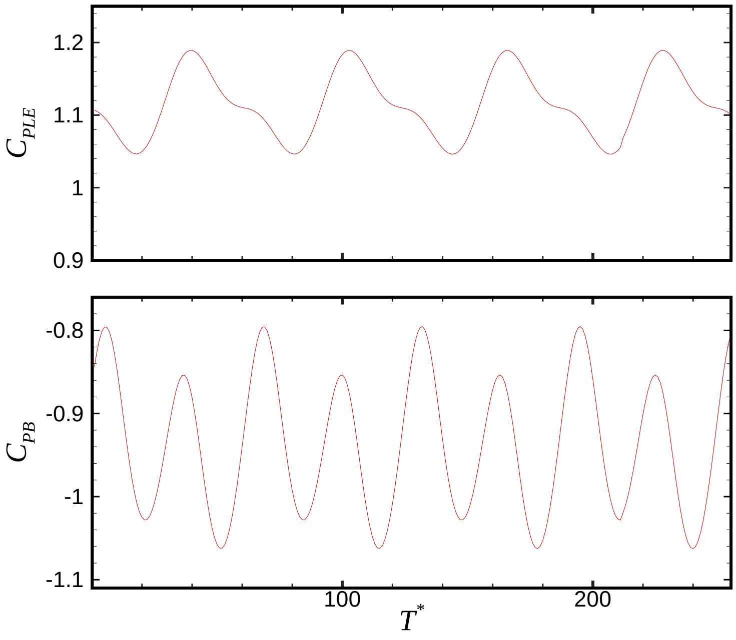

Figure 5.23: (Top) leading edge stagnation point pressure coefficient (C_{PLE}) and (Bottom) base pressure coefficient (C_{PB}) as a function of normalized time, for $u^* = 5.5$.

velocity.

At higher reduced velocities, the cylinder oscillation remains synchronized with the lift frequency (St_1) and sufficient horizontal motion is retained to reduce the pressure at the leading edge stagnation point over half the oscillation cycle up to a reduced velocity of $u^* = 19$. Beyond $u^* = 19$, the cylinder's horizontal motion is less dominant as the cylinder oscillates principally in the transverse direction, and the dominant drag signal reverts to St_2 for these high reduced velocities.

Of interest is that the shedding into the wake is clearly a 2S branch of shedding, as is the shedding for all reduced velocities investigated. This finding is especially relevant at this high reduced velocity as it is in contrast with the experimental findings of Govardhan & Williamson (2000), who found 2P shedding for a low mass-damped hydroelastically mounted cylinder allowed to oscillate in the transverse direction. However the research of Blackburn *et al.* (2001) reveals that two-dimensional low Reynolds number simulations are insufficient to capture 2P shedding branches as these shedding modes appear to be strongly influenced by three-dimensional effects.

5.10 Predictions of the St_1 component in the Drag Response

The influence of the cylinder velocity on the calculated drag force over one cycle of oscillation was determined for $u^* = 5.5$, where the cylinder oscillations may be considered in-line with the flow direction.

In the reduced velocity range $u^* = 5.5 - 19$, the cylinder oscillation provides a variation in the flow field velocity with respect to the cylinder and hence an effective change in the local Reynolds number, that is, the Reynolds number based on the flow relative to the cylinder. The maximum local Reynolds number occurs at the point in the oscillation cycle where the cylinder is moving upstream with the greatest velocity. The minimum local Reynolds number occurs when the cylinder is moving downstream with the greatest velocity. The calculated maximum and minimum local Reynolds numbers at $u^* = 5.5$ were found to be $Re_{max} = 205.4$ and $Re_{min} = 194.7$, respectively. From the relationship between the Reynolds number and the drag coefficient, C_D, determined by Henderson (1995), this implies a maximum variation in the drag coefficient of 0.003 over one cycle. Therefore the drag coefficient may be considered effectively constant over a cycle of oscillation for $u^* = 5.5$. However, even though the drag coefficient is approximately constant, the drag force may vary substantially. The maximum drag force corresponds to the maximum local Reynolds number and the minimum drag force corresponds to the minimum local Reynolds number.

For all the reduced velocities considered in this study, the drag force acting on the cylinder is 180^o out-of-phase with the cylinder velocity. Combining this with the definition of the drag coefficient, the ratio of maximum drag coefficient to minimum drag coefficient may be written as:

$$\frac{C_{D_{max}}}{C_{D_{min}}} = \left[\frac{Re^2_{max}}{Re^2_{min}}\right] \cdot F_{D_{ratio}} \simeq 1. \tag{5.22}$$

Here $F_{D_{ratio}} = \frac{F_{D_{max}}}{F_{D_{min}}}$ is the ratio of maximum to minimum drag force acting on the cylinder. Since the drag coefficient varies little over this Reynolds number range, equation (5.22) can be rearranged as:

$$F_{D_{ratio}} = \frac{Re^2_{min}}{Re^2_{max}} \tag{5.23}$$

For $u^* = 5.5$ the drag ratio was $F_{D_{ratio}} = 1.107$. By substituting this, and the values for the maximum and minimum Reynolds number quoted earlier into Equation (5.23), we see that the variation in effective Reynolds number accounts for 81% of the observed variation in the drag ratio. The remainder is due to non-linear effects including the Karman type wake shedding. To confirm this result, the spectral density of the drag is presented in figure (5.24). Two peaks are observed, occurring at St_1 and St_2. The larger of the two peaks, St_1, is due to the cylinder oscillation, and accounts for 82 % of the amplitude of the drag trace, in close agreement with the predictions made above.

5.11 Conclusions

Two-dimensional simulations of the flow past a tethered cylinder have been performed for the reduced velocity range, $u^* = 1-22$, for a cylinder mass ratio $m^* = 0.833$. In this range of u^*, three distinct branches have been identified. The first branch, peaking at $u^* = 2.5$, is essentially an in-line branch and is driven by a resonance between the in-line forces and the natural frequency of the cylinder system. The second branch, occurring over the range $u^* = 5-19$, is initiated in the range $u^* = 3.5-5$ by resonance between the natural frequency of the tethered body system and the subharmonic of the drag force which peaks at $u^* = 5$. At higher reduced velocities, the motion of the cylinder modifies the drag response, such that the drag and lift have the same dominant frequency and are

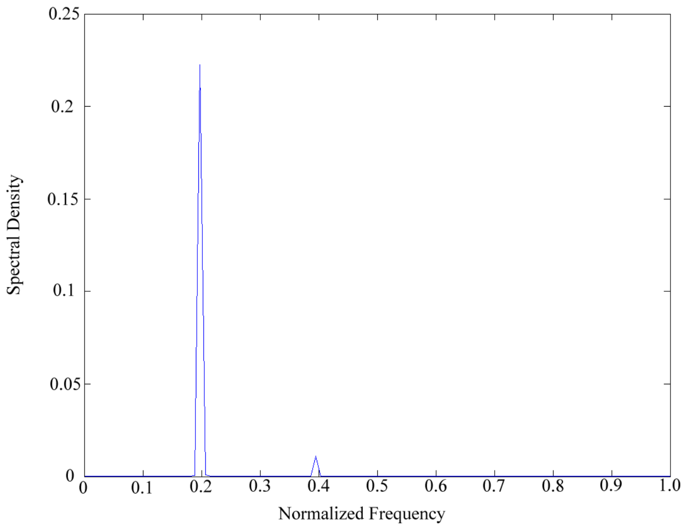

Figure 5.24: Spectral density of the drag force for $u^* = 5.5$.

in phase. The cylinder oscillates at the drag/lift frequency over the extent of the second branch. The motion of the cylinder alters the frequency of the leading-edge stagnation pressure. As a result, the drag signal is altered, such that the drag signal is dominated by the lift frequency, and both the drag and lift are in-phase. The third branch occurs for $u^* > 19$ and is dominated by transverse oscillations. The cylinder response for this branch is similar to that observed by Govardhan and Williamson (2000) for a low mass-damped hydro-elastically mounted cylinder oscillating transverse to the flow field. The cylinder oscillations reduce dramatically with increasing u^*, and the oscillations are no longer synchronized at the vortex shedding frequency from a fixed cylinder.

Two-dimensional numerical simulations of the flow past a tethered cylinder with mass ratio $m^* = 0.833$ have been performed. The Navier-Stokes and dynamic equations of motion of the cylinder are solved using a spectral element method. The fluid forces acting on the cylinder, as well as the tension in the tether, are computed and used to determine the resulting cylinder motion. A large peak in the cylinder oscillation was noted for a reduced-velocity $u^* \simeq 19$. Analysis of the vortex structures in the wake of the cylinder, for the case of $u^* = 15.4$, reveals that the in-line motion of the body in the reduced-velocity range $u^* = [5, 19]$ reduces the length of the formation region, and increases the forces acting on the cylinder. As the reduced-velocity is increased to $u^* = 19$, the change in the mean layover angle allows a greater transverse amplitude of oscillation for a given in-line amplitude, and hence the overall amplitude of oscillation is increased. For both these reduced velocities, the near wake, and the moment acting on the cylinder over one period, are observed to be asymmetric. As the reduced-velocity is further increased to $u^* = 21$, there is insufficient in-line motion to enable enhanced interaction of the body motion with the wake vortex structures, and the formation length increases markedly.

Chapter 6

The Effect of Changed Mass Ratio on the Flow around a Tethered Cylinder

6.1 Introduction

Two dimensional simulations were conducted at a Reynolds number of 200 for a variety of mass ratios in the range $m^* = [0.1, 0.8]$. For all the simulations conducted in this section, the tether length was held constant at $L^* = 5.00$. An extensive range of Froude numbers were investigated ($0 \leqslant Fr \leqslant 50$) corresponding to a mean layover range of $0 \leqslant \overline{\theta} \leqslant 89.99$. As discussed in section 6.2.1, the reduced velocity range is limited by the $\overline{C_D}$ and $\overline{C_L}$ and is different for each mass ratio.

A distinct jump in the amplitude was noted for $m^* \lesssim 0.38$ as the Froude number was increased beyond $Fr \simeq 0.8$ from below. A corresponding jump in the mean layover angle and mean drag coefficient was noted. The mean lift was found to be negative for all but the highest Froude numbers investigated for all mass ratios considered.

6.2 Mean Layover Angle Results

Figure 6.1 shows the predicted mean layover angle, $\overline{\theta}$, as a function of the reduced velocity, u^*. For $u^* \lesssim 10$, the data points collapse for all the mass ratios investigated. In general, the mean layover angle varies inversely with m^* for any given reduced velocity beyond $u^* \simeq 10$. A jump in the mean layover angle is noted for $m^* \leqslant 0.36$ as the reduced velocity is increased beyond $u^* \simeq 10$. Close analysis of the jump region for $m^* \leqslant 0.36$ reveals a slight overlap of u^*. For every mass ratio that experiences a jump in $\overline{\theta}$, the reduced velocity prior to the jump is greater than the reduced velocity after

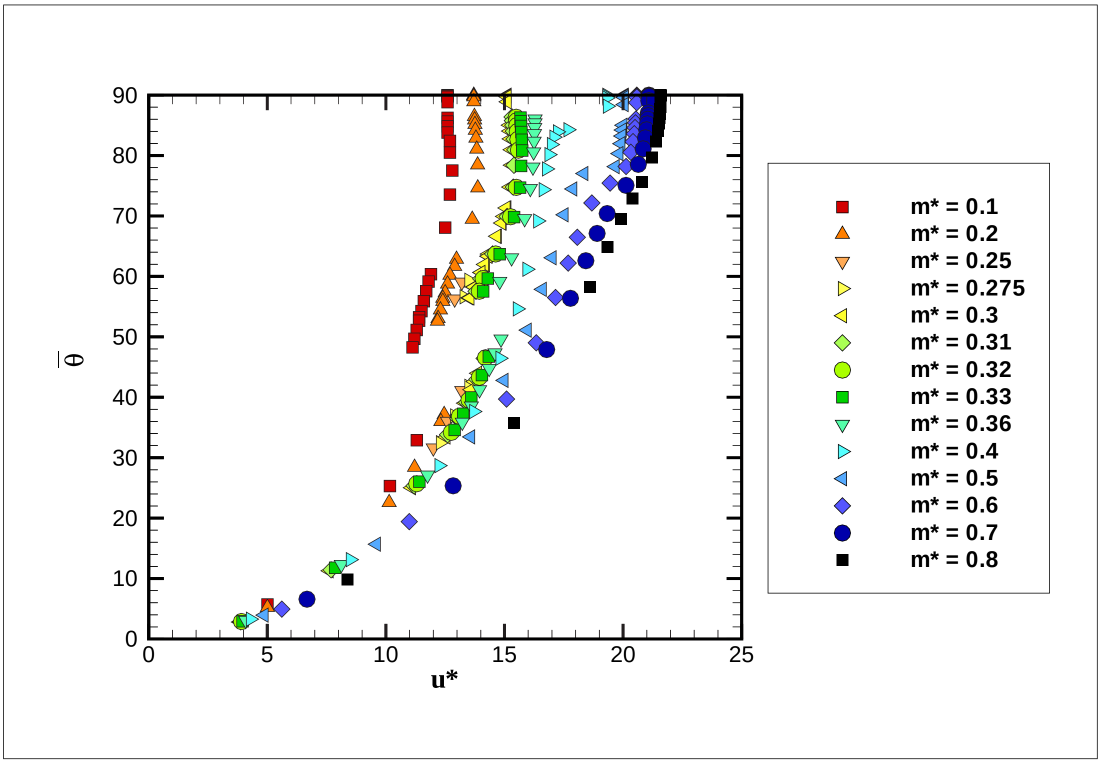

Figure 6.1: Mean layover angle as a function of reduced velocity for $m^* = [0.1, 0.8]$ and $L^* = 5.0$

the jump. The relationship between the mean layover angle and the reduced velocity is not one to one, and the fluid controlling parameter needs to be reinterpreted in the form of a new variable. The mean value of u^* across which a jump in $\overline{\theta}$ occurs is shown in 6.2, as a function of m^*. The relationship between u^*_{jump} with m^* has been fitted to a quadratic equation using the method of least squares, resulting in:

$$\overline{u^*}_{jump} = 16.789m^{*2} + 6.018m^* + 10.447, \tag{6.1}$$

with a coefficient of determination $R^2 = 0.99$. Equation 6.1 indicates that for the lower limit $m^* \to 0$, the jump will not occur for $u^* \lesssim 10.5$ for the Reynolds number and tether length ratio investigated.

The layover angles just before and just after the jump occurs is presented in figure 6.3 as a function of the mass ratio. The mean layover angle about which the cylinder passes during the jump as a function of mass ratio has been fit to an exponential least squares fit,

$$\overline{\theta}_{jump} \simeq 35.85 \cdot e^{1.145 \cdot m^*} \tag{6.2}$$

with a coefficient of determination $R^2 = 0.9898$. Equation 6.2 indicates that as $m^* \to 0$

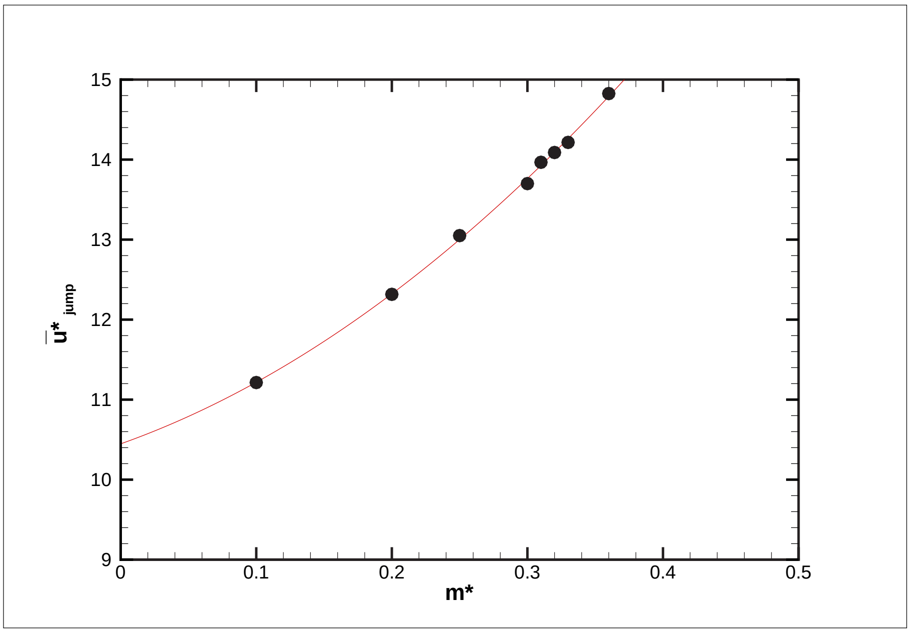

Figure 6.2: Critical reduced velocity through which the jump in mean layover angle occurs as a function of mass ratio for $m^* = [0.1, 0.4]$ and $L^* = 5.0$

there is a lower limit of $\overline{\theta}_{jump}$ below which a jump will not be observed regardless of mass ratio. For $Re = 200$ and $L^* = 5$, this critical mean layover angle is $\overline{\theta}_{crit} \simeq 36^o$, this point is clarified in subsequent sections.

The size of the jump reduces slightly with increasing mass ratio, varying between 15.5^o for $m^* = 0.1$ and 9.5^o for $m^* = 0.36$. While not clear from figure 6.1 alone, no jump was observed for $m^* \geqslant 0.4$.

An entirely separate discontinuity is observed for mass ratios $m^* \geqslant 0.4$, where a jump in the reduced velocity is noted as $\overline{\theta} \simeq 80^o$. This is most apparent for $m^* = 0.4$. For larger m^* it is revealed by a subtle change in gradient as $\overline{\theta} \rightarrow 90^o$.

The mean layover angle may be related to the fluid forces acting on the cylinder through a mean force balance, giving the equation:

$$\overline{\theta} = \tan^{-1}\left(\frac{\overline{C_D}}{\overline{C_L} + (1 - m^*) \cdot \pi/2Fr^2}\right) \tag{6.3}$$

From equation 6.3, for fixed values of $\overline{C_D}$ and $\overline{C_L}$, a continuous change in the Froude number results in a continuous change in the reduced velocity. From equation 6.3, it may therefore be assumed that any discontinuous change in the $u^* - \overline{\theta}$ relationship is a direct result of a discontinuous change in either $\overline{C_D}$ and/or $\overline{C_L}$. In particular, the jump in $\overline{\theta}$ for $m^* \leqslant 0.38$ is due either to a discontinuous increase in $\overline{C_D}$ and/or a discontinuous decrease in $\overline{C_L}$. For $m^* \geqslant 0.4$, the jump in u^* is due either to a discontinuous decrease in $\overline{C_D}$ or a discontinuous increase in $\overline{C_L}$. Evidence supporting this hypothesis is presented in section 6.3.

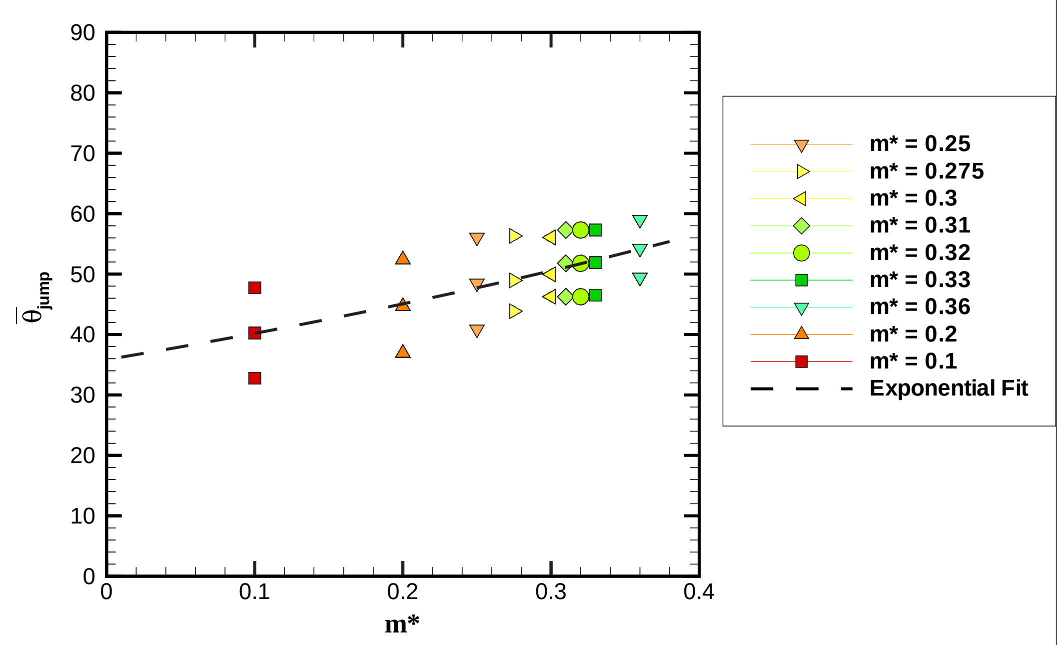

Figure 6.3: Maximum, minimum and averaged mean layover angles through which the jump occurs as a function of mass ratio for $m^* = [0.1, 0.4]$ and $L^* = 5.0$

6.2.1 A maximum reduced velocity

Figure 6.1 shows that for each m^*, an upper limit exists for the maximum reduced velocity possible. This maximum value of u^* may also be inferred from analysis of equation 5.19 which is rewritten below,

$$u^* = \frac{2\pi^{3/2}}{\sqrt{2}} \cdot \left(\frac{(m^* + C_A)L^*}{\sqrt{\overline{C_D}^2 + \left[\overline{C_L} + \frac{\pi(1-m^*)}{2Fr^2}\right]^2}} \right)^{1/2}, \tag{6.4}$$

as $Fr \rightarrow \infty$, the term $\left[\overline{C_L} + \frac{\pi(1-m^*)^2}{2Fr^2}\right]^2 \rightarrow \overline{C_L}^2$, and the equation for the reduced velocity (corresponding to the maximum possible reduced velocity) is simplified to,

$$u^*_{max} = \frac{2\pi^{3/2}}{\sqrt{2}} \cdot \left(\frac{(m^* + C_A)L^*}{\sqrt{\overline{C_D}^2 + \overline{C_L}^2}} \right)^{1/2}, \tag{6.5}$$

As the value of $\overline{C_D}$ is finite for $u^*, Fr \neq 0$, there is a limit on the maximum possible reduced velocity. From equation 6.2.1, u^*_{max} increases with increasing m^* and L^*.

6.2.2 A new controlling parameter

The reduced velocity shows several shortcomings as a parameter to describe the flow conditions. From section 5.2, the definition of u^* assumes small oscillations and that the peak values of the Drag and Lift coefficients are small relative to their mean values. The reduced velocity does not vary linearly with the Froude number; for small Froude numbers, small variations in the Froude number are reflected by disproportionate variations in the reduced velocity. As the Froude number becomes large, $u^* \rightarrow u^*_{max}$ which depends on the flow parameters $\overline{C_D}$ and $\overline{C_L}$ and the physical parameters m^* and L^*. In light of these shortcomings, a new controlling parameter has been suggested to the author (private communications, Josie Carberry), which has been developed in order to achieve a collapse of $\overline{\theta}$ results over the range of mass ratios investigated . The new parameter, referred to as Fr' is derived by first considering the definition of the Froude number,

$$Fr = \frac{U}{\sqrt{gD}} = \frac{F_I}{F_g} = \frac{\text{Inertia}}{\text{gravity}}, \tag{6.6}$$

where the gravity term may be written as:

$$F_g = g \cdot \rho \frac{\pi D^2}{4} L_C, \tag{6.7}$$

and the inertial term may be written as:

$$F_I = \frac{\pi}{4} \cdot U^2 \rho_w D L_C. \tag{6.8}$$

As all the tethered cylinders investigated in this study are positively buoyant, the vertical force acting on the cylinder due to hydrostatic forces and gravity may be written as,

$$B = -g \cdot (\rho - \rho_w) \cdot \frac{\pi D^2}{4} L_C. \tag{6.9}$$

Here, the leading negative sign on the right hand side, indicates that the buoyancy force acts opposite to the gravity force. Fr' may be written as,

$$Fr' = \frac{U}{\sqrt{gD \cdot (1 - m^*)}} = \frac{\text{Inertia}}{\text{Buoyancy}}. \tag{6.10}$$

From equation 6.10, Fr' is essentially the inverse of the non-dimensional form of the buoyancy force.

Figure 6.4 plots $\overline{\theta}$ as a function of Fr'. The mean layover angle results collapse onto a single line regardless of mass ratio for $Fr' \lesssim 0.5$. For higher values of Fr', and for $m^* \geqslant 0.5$, $\overline{\theta}$ collapses onto a single line for all Fr'. For $m^* \leqslant 0.36$, a discontinuous increase is noted at $Fr' \simeq 0.5$; above this Froude number, $\overline{\theta}$ collapses onto a new line. Of interest is $m^* = 0.4$ which, while it does not exhibit a jump in $\overline{\theta}$, it's response increases away from higher mass ratio simulations for $Fr' \geqslant 1$.

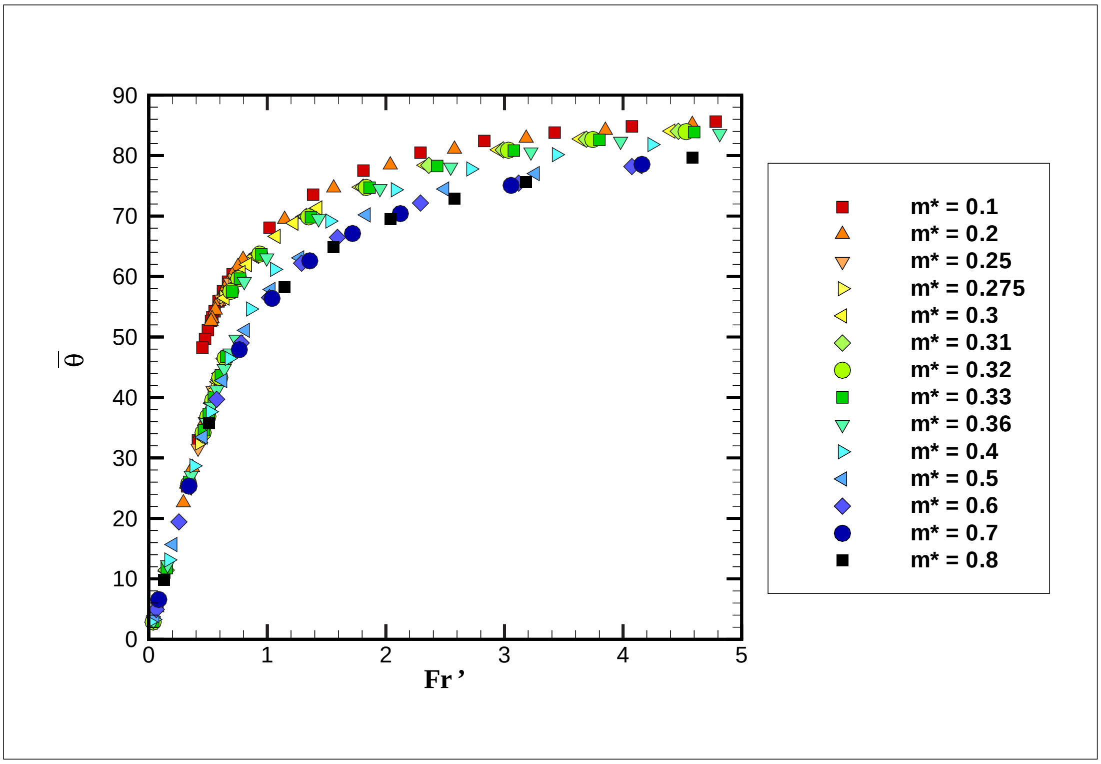

Figure 6.4: Mean layover angle as a function of the modified Froude number Fr' for $m^* = [0.1, 0.8]$ and $L^* = 5.0$

6.3 Mean Force Coefficient Results

6.3.1 Mean Drag Coefficient Results

The mean drag, $\overline{C_D}$, is plotted in figure 6.5 as a function of reduced velocity. As anticipated by the analysis in section 6.2, a discontinuous jump in $\overline{C_D}$ is observed for $m^* \leqslant 0.36$. The extent of the jump in $\overline{C_D}$ varies inversely with the mass ratio.

For mass ratios which experience a jump in both $\overline{\theta}$ and $\overline{C_D}$, a slight reduction in the drag ratio is noted as u^* is increased beyond u^*_{jump}; this minimum in $\overline{C_D}$ is referred to as $C_{D(low)}$. As u^* is further increased, $\overline{C_D}$ increases above $C_{D(low)}$, before reaching a

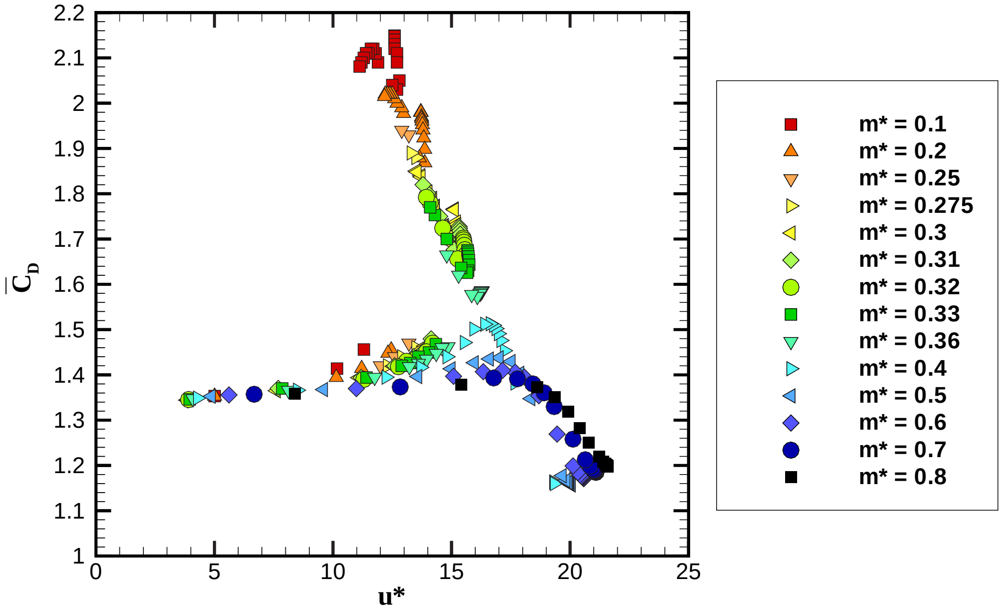

Figure 6.5: Mean drag coefficient as a function of the reduced velocity for $m^* = [0.1, 0.8]$ and $L^* = 5.0$

maximum value of $C_{D(high2)}$ at u^*_{max}. This trend can clearly be seen in figure 6.6 which shows a close up of $\overline{C_D}$ as a function of u^*. The difference between $\overline{C_D}_{High2}$ and $\overline{C_D}_{Low}$ varies inversely with the mass ratio. From figure 6.6, $C_{D(low)}$ and $\overline{C_D}_{High2}$ appear to be implicitly associated with the jump in $\overline{C_D}$ as neither feature is observed for mass ratios which do not exhibit a jump in $\overline{\theta}$ and C_D. The two cases of $m^* = 0.36$ and 0.4 (the critical mass ratio below which the jump occurs lies between these two values) have distinct drag profiles as a function of reduced velocity. For $m^* = 0.36$, there is a slightly higher value of C_D as u^* is increased beyond the value at which $\overline{C_D}_{Low}$ occurs. By contrast, for $m^* = 0.4$, the mean drag coefficient rapidly diminishes at high reduced velocity values.

6.3.2 A Critical Mass Ratio

A particular mass ratio exists where $\overline{C_{D_{low}}} = \overline{C_{D_{high2}}}$ From the previous findings, this mass ratio will correspond to the critical mass ratio below which a jump in both $\overline{C_D}$ and $\overline{\theta}$ will be observed. In order to determine an accurate value of m^*_{crit} below which the jump will occur, the author has found the critical mass ratio that corresponds to

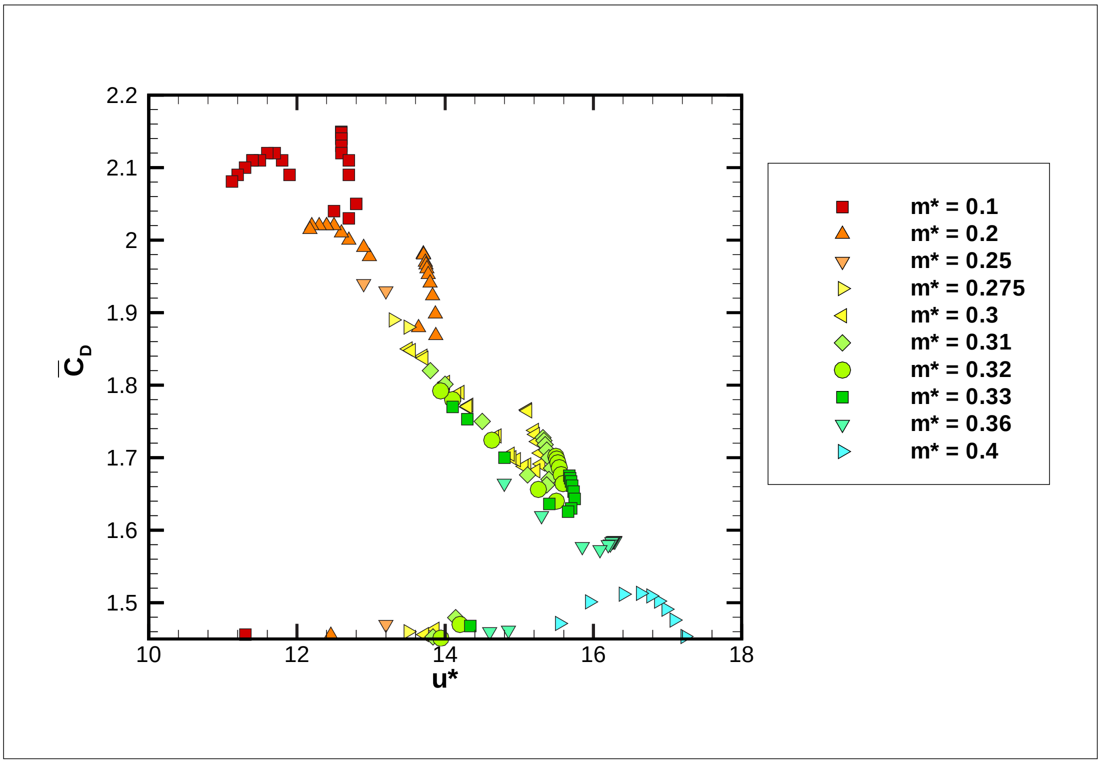

Figure 6.6: Mean drag coefficient as a function of the reduced velocity for $m^* = [0.1, 0.4]$ and $L^* = 5.0$

$\overline{C_D}_{High2} = \overline{C_D}_{Low}$.

Both $\overline{C_D}_{High2}$ and $\overline{C_D}_{Low}$ are plotted as a function of $m^* \leqslant 0.36$ in figure 6.7. $\overline{C_D}_{Low}$ has a linear trend with an equation,

$$\overline{C_D}_{Low} \simeq -1.772 \cdot m^* + 2.2128, \tag{6.11}$$

with a coefficient of determination $R^2 = 0.999$. $\overline{C_D}_{High2}$ has a quadratic trend with an equation,

$$\overline{C_D}_{High2} \simeq -3.4189 \cdot m^{*2} - 0.5645 \cdot m^* + 2.2374, \tag{6.12}$$

with a coefficient of determination $R^2 = 0.999$. Equating equation 6.11 to equation 6.12 results in $m^*_{crit} = 0.373$. Below this mass ratio, a jump in the mean layover angle will be observed, as will a jump in the mean drag coefficient. The value of m^*_{crit} found here is significantly above that for a freely oscillating cylinder for the same Reynolds number. From chapter 4, m^*_{crit} for a freely oscillating cylinder is $m^*_{crit} = 0.01$. Assuming that the same phenomenon is responsible for the jump in $\overline{C_D}$ in both cases, the difference in m^*_{crit} may be explained by either the fact that, for the case of the tethered cylinder, the cylinder motion has an imposed curvature due to the restraining tether; or the fact

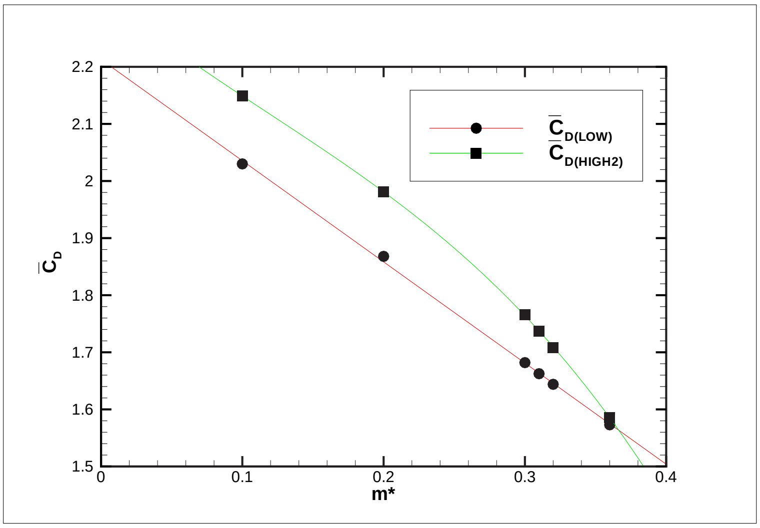

Figure 6.7: $C_{D_{Low}}$ and $C_{D_{High2}}$ as a function of mass ratio for $m^* = [0.1, 0.36]$ and $L^* = 5.0$

that, for the tethered cylinder, the cylinder is oscillating at an angle to the flow. An analysis of the effect of a changed tether length in chapter 7 attempts to answer this question.

Referring back to figure 6.5, we can see that for $m^* > m^*_{crit}$ there is a gradual increase in $\overline{C_D}$ with increasing reduced velocity up to $u^* \simeq 17$; beyond this, $\overline{C_D}$ decreases rapidly. For $u^* \gtrsim 18$, the mean drag reduces below that for a fixed cylinder at the same Reynolds number. From equation 6.2.1, this reduction in the mean drag allows u^* to increase beyond the u^*_{max} imposed by a fixed drag coefficient (see section 6.2.1). The highest reduced velocity observed for each mass ratio increases with increasing mass ratio.

Figure 6.8 plots the mean drag as a function of the Froude number. Of interest is the fact that the jump in $\overline{C_D}$ occurs at $Fr \simeq 0.8$ for all $m^* < m^*_{crit}$. The Froude number at which $\overline{C_D}_{Low}$ occurs is also constant for $m^* < m^*_{crit}$ at $Fr \simeq 1.4$. Just prior to the jump ($Fr \simeq 0.6$), the mean drag is the same value for all mass ratios investigated. Analysis of figure 6.9 reveals that the mean drag remains remarkably constant for each mass ratio in the range $Fr = [5, 50]$.

Figure 6.10 shows the mean drag as a function of the mean layover angle. This clearly shows that the jump in both are related. For $m^* < m^*_{crit}$, $\overline{C_D}_{Low}$ occurs at $\overline{\theta} \simeq 77^o$ regardless of mass ratio. A dramatic reduction in the mean drag is also noted for $m^* = 0.4$ and 0.5, at $\overline{\theta} \simeq 80^o$; this is associated with the discontinuous increase in

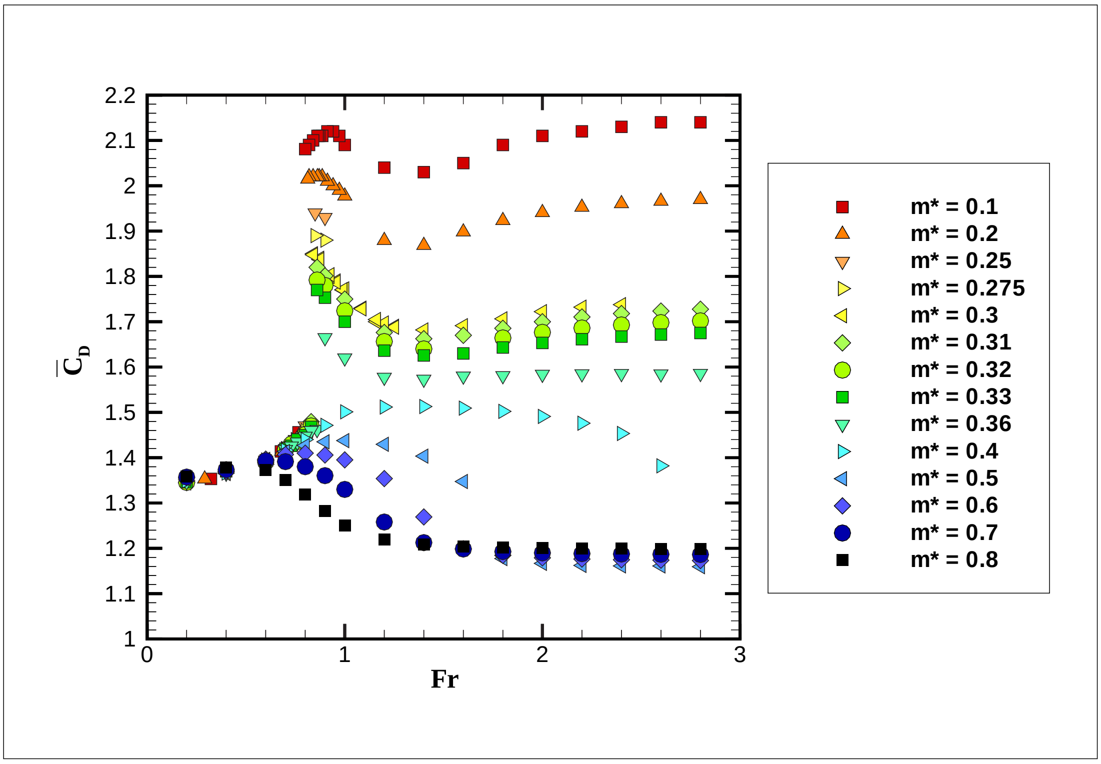

Figure 6.8: Mean drag coefficient as a function of Froude number in the range $Fr = [0, 3]$ for $m^* = [0.1, 0.8]$ and $L^* = 5.0$

the reduced velocity noted for these mass ratios.

6.3.3 Mean Lift Coefficient Results

The mean lift coefficient is plotted against the Froude number in figure 6.10. For all mass ratios considered, the mean lift was negative for an appreciable range of Froude number. It is hypothesized in section 6.6 that this negative mean lift is due to the cylinder oscillating at an appreciable amplitude at an angle to the flow. Unlike the work of Jauvtis & Williamson (2003), the cylinder is forced to oscillate asymmetrically about the centre of its cycle by the restraining tether. This in turn induces an asymmetry in the wake formation. The asymmetry in the wake induces a net lift force.

The range of Froude numbers over which a negative lift coefficient is observed varies inversely with mass ratio. For $m^* > m^*_{crit}$, the local minimum in $\overline{C_L}$ was found to vary inversely with the mass ratio between $Fr = [0.4 - 0.8]$. For $m^* < m^*_{crit}$, the local minimum in $\overline{C_L}$ occurs at $Fr \simeq 0.8$, corresponding to the Froude number at which the jump in $\overline{\theta}$ and $\overline{C_D}$ is noted. The local minimum in $\overline{C_L}$ represents a discontinuous decrease in $\overline{C_L}$ as the Froude number is increased from $Fr < 0.8$.

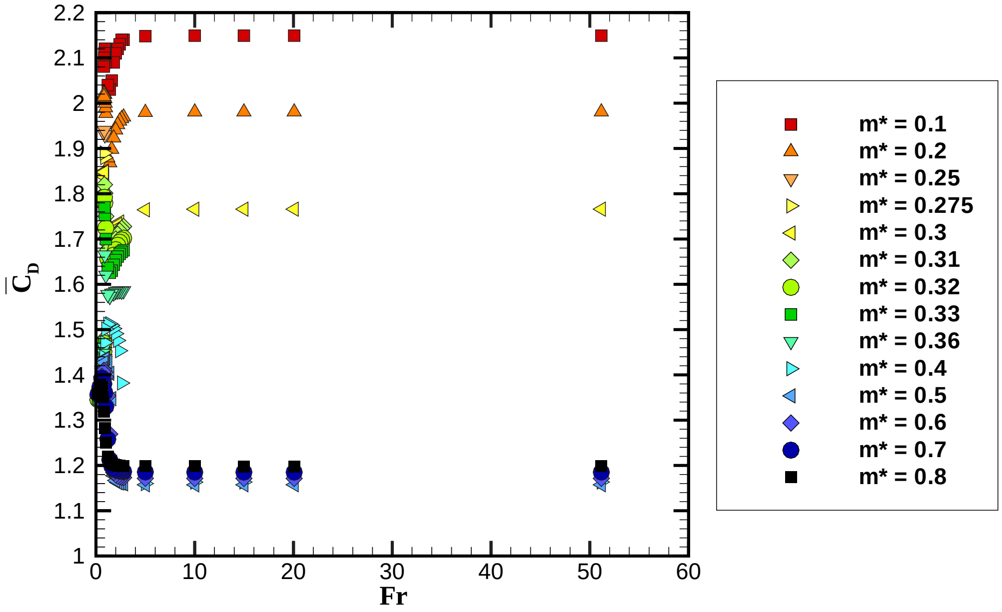

Figure 6.9: Mean drag coefficient as a function of Froude number in the range $Fr = [0, 50]$ for $m^* = [0.1, 0.8]$ and $L^* = 5.0$

A distinct difference in the mean lift response as a function of the Froude number is noted when comparing $m^* < m^*_{crit}$ with $m^* > m^*_{crit}$. The local minimum in $\overline{C_L}$ has been determined for each mass ratio investigated. These results have been plotted in the form of $m^*/\overline{C_L}$ as a function of m^* in figure 6.12. For $m^* > m^*_{crit}$, the data have been approximated by the linear least squares fit,

$$-m^*/\overline{C}_{L(Min)} = 36.515 \cdot m^* - 12.216 \tag{6.13}$$

with a coefficient of determination $R^2 = 0.99$. This equation predicts a minimum mean lift of -0.04 (which is considered to be negligibly small) for $m^* = 1$. This conclusion is consistent with the hypothesis that the net mean lift is a function of the mean layover angle. For $m^* = 1$, the mean layover angle is 90^o, and the net mean lift should approach zero. This result has been verified by predicting the flow for the case of $m^* = 1$ for a variety of Froude numbers. From equation 5.20, for $m^* = 1$, the change in Froude number does not change the reduced velocity directly. As the Reynolds number is held constant at 200 for all simulations, the same time series result was observed with a zero mean lift, and a symmetric wake profile for all simulations with $m^* = 1$.

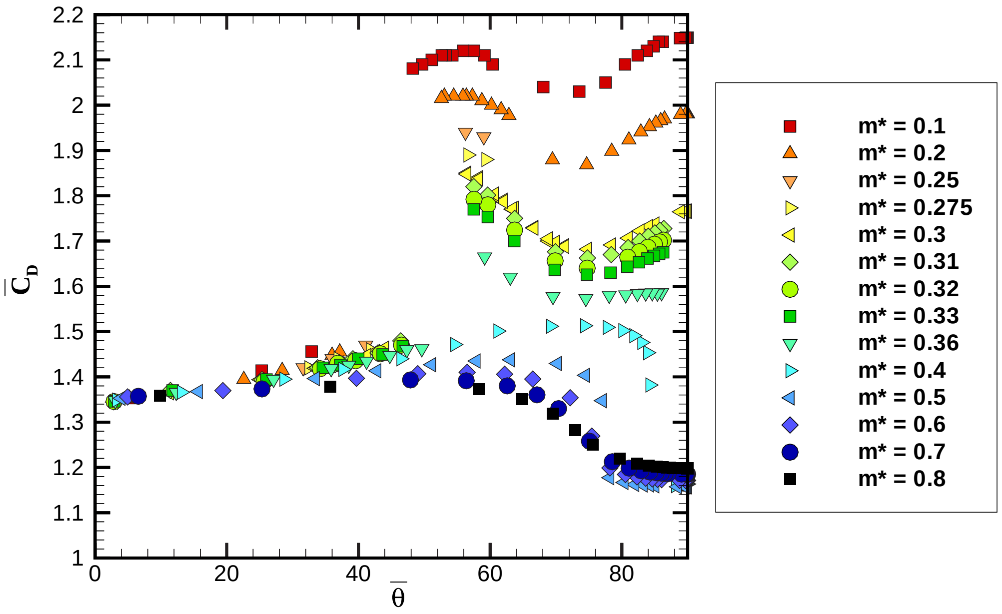

Figure 6.10: Mean drag coefficient as a function of mean layover angle for $m^* = [0.1, 0.8]$ and $L^* = 5.0$

For $m^* < m^*_{crit}$, the data has been approximated by a quadratic least squares fit,

$$-m^*/\overline{C}_{L(Min)} = 6.3788 \cdot m^{*2} + 0.7714 \cdot m^* + 0.1446 \tag{6.14}$$

with a coefficient of determination $R^2 = 0.999$. Equation 6.14 predicts $\overline{C}_{L(Min)} \to 0$ as $m^* \to 0$. Indeed, the minimum mean lift for $m^* = 0.1$ is slightly less than $m^* = 0.2$. Simulations approaching $m^* = 0$ have been performed ($m^* = 0.01$). For this mass ratio the minimum mean lift was equal to $\overline{C_{L_{min}}} = -0.346$. By equating Equation 6.13 and 6.14, the value of m^*_{crit} may be predicted, resulting in (for this tether length ratio and Reynolds number) $m^*_{crit} = 0.37$, in agreement with the prediction discussed earlier.

It was found that $\overline{C_L} \simeq 0$ for high Froude numbers, corresponding to $\overline{\theta} \simeq 90^o$, for all mass ratios investigated. Figure 6.13 plots $\overline{C_L}$ as a function of the mean layover angle. For $m^* < m^*_{crit}$, the value of $\overline{\theta}$ at which the local minimum of $\overline{C_L}$ occurs increases with increasing mass ratio. As the minimum in $\overline{C_L}$ occurs at the position of the jump for these mass ratios, this finding is in direct agreement with figure 6.3 discussed earlier. For $m^* > m^*_{crit}$, the value of $\overline{\theta}$ corresponding to the local minimum of $\overline{C_L}$ increases inversely with mass ratio.

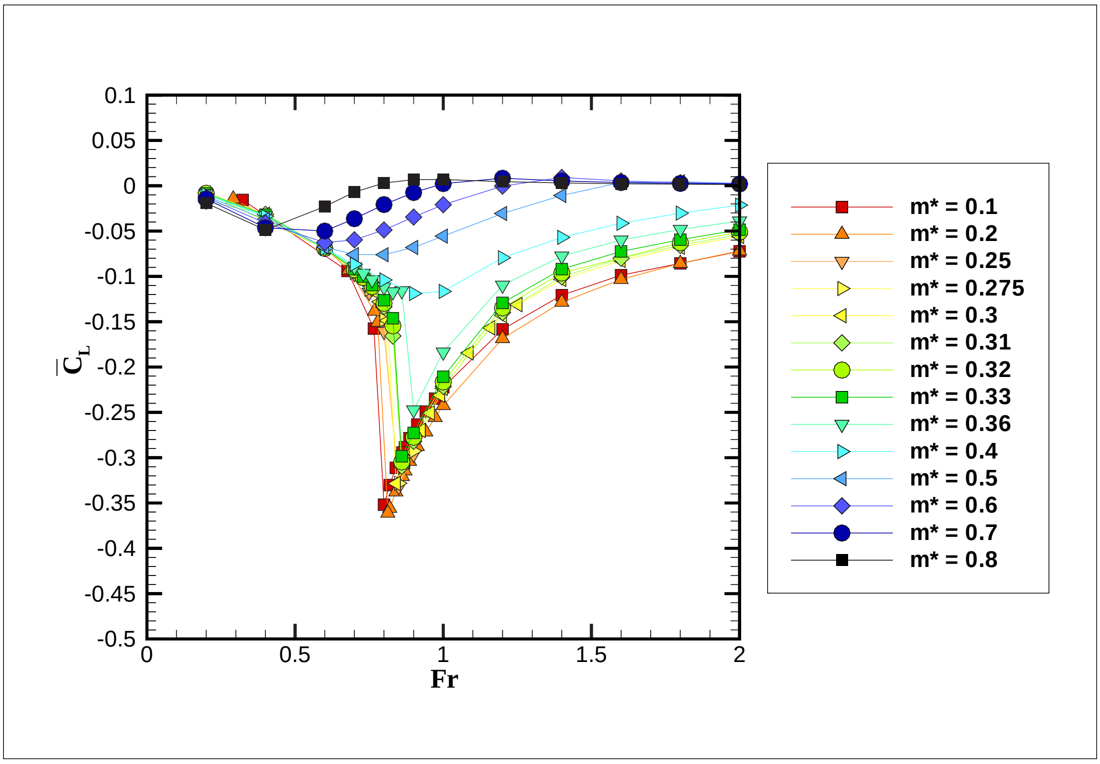

Figure 6.11: Mean lift coefficient as a function of Froude number in the range $Fr = [0, 2]$ for $m^* = [0.1, 0.8]$ and $L^* = 5.0$

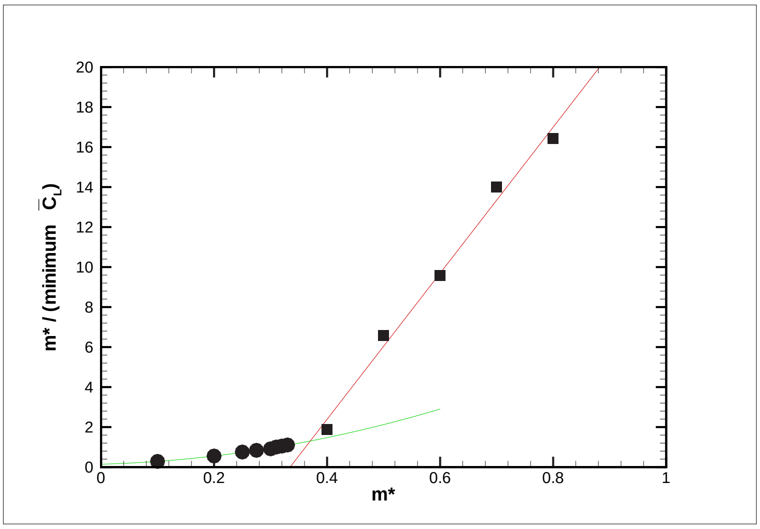

Figure 6.12: $m^*/C_{L(min)}$ as a function of mass ratio for $m^* = [0.1, 0.8]$ and $L^* = 5.0$

In summary, a discontinuous jump has been found in $\overline{\theta}$, $\overline{C_D}$ and $\overline{C_L}$, which corresponds to a local minimum in $\overline{C_L}$, for $m^* < m^*_{crit}$. The value of m^*_{crit} has been estimated in two distinct ways: first, by determining the mass ratio where $\overline{C}_{D(Low)} = \overline{C}_{D(High2)}$;

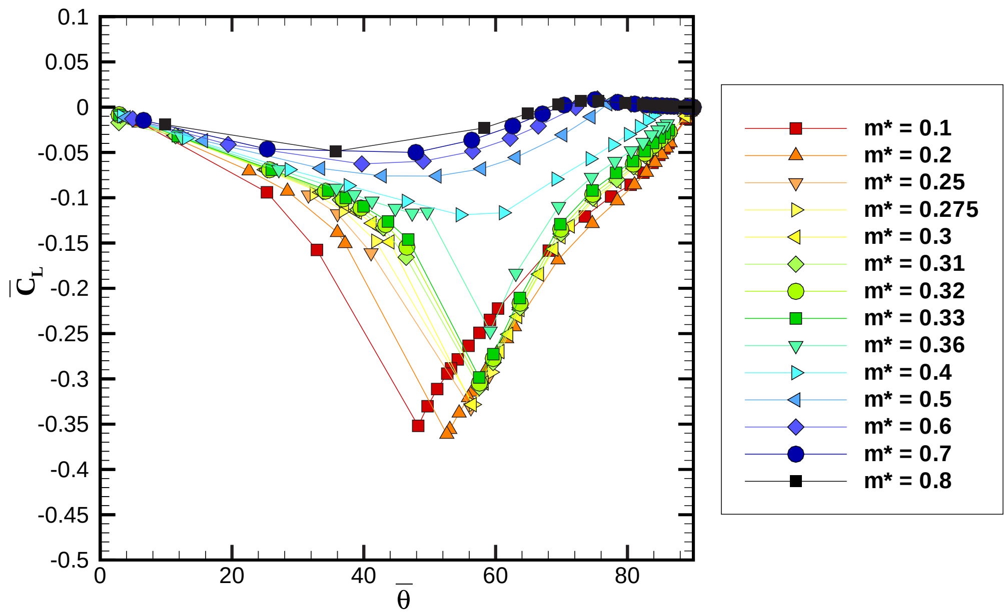

Figure 6.13: Mean lift coefficient as a function of mean layover angle for $m^* = [0.1, 0.8]$ and $L^* = 5.0$

second, by determining the mass ratio where the value of $\overline{C}_{L(Min)}$ is obtained from the intersection of equation 6.13 and equation 6.14. Both methods obtain $m^*_{crit} = 0.37$ for this tether length and Reynolds number. This value of m^*_{crit} is considerably greater than that found for a freely oscillating cylinder at the same Reynolds number. It is hypothesized that this increase in m^*_{crit} is due to enforced motion of the cylinder along an arc imposed by the restraining tether, and is therefore a function of the tether length. This hypothesis is tested in chapter 7.

It is recognized that the jump in $\overline{\theta}$ for $m^* < m^*_{crit}$ is due to a discontinuous change in both $\overline{C_D}$ and $\overline{C_L}$. The mean drag was found to discontinuously increase and the mean lift to discontinuously decrease as the Froude number was increased beyond $Fr \simeq 0.8$ for all $m^* < m^*_{crit}$. This discontinuous change represents a change in the wake structure and it is hypothesized that the increase in $\overline{C_D}$, in particular, is implicitly related to a jump in the amplitude of oscillation. This hypothesis is supported by the evidence presented in section 6.4.

It is hypothesized that the large local minimum found for $\overline{C_L}$ can be related to the flow structure. For a finite value of $\overline{C_L}$, it is hypothesized that the wake must convect at an angle to the free stream; this is confirmed in section 6.6.

6.4 Oscillation Results

6.4.1 Amplitude of Oscillation Results

The amplitude of oscillation, defined as $A^* = \theta' \cdot L^*$, is plotted in figure 6.14 as a function of the reduced velocity. As predicted in the previous section, a jump in A^* is noted for $m^* < m^*_{crit}$ at the same reduced velocity where the jump in $\overline{\theta}, \overline{C_D}$ and $\overline{C_L}$ was noted in the previous section. The difference in response for $m^* < m^*_{crit}$ as compared to $m^* > m^*_{crit}$ is clearly apparent from this figure. For $m^* < m^*_{crit}$, the amplitude of oscillation is observed to jump discontinuously prior to decreasing slightly as u^* is increased further. As u^* is increased further still, A^* increases once more to reach a maximum value as $u^* \to u^*_{max}$ (corresponding to $\overline{\theta} \to 90^o$). This is distinct to the response noted for $m^* > m^*_{crit}$ which does not experience a jump. For $m^* > m^*_{crit}$, the amplitude of oscillation gradually increases to a maximum value prior to decreasing to a small amplitude ($A^* \simeq 0.1$) for high u^*. For high mass ratios $m^* \geqslant 0.5$, little variation in the value of A^* is observed at the highest reduced velocity considered (corresponding to the fully laid over case, $\overline{\theta} \simeq 90^o$).

The maximum amplitude was determined for each mass ratio, and is plotted as m^*/A^* as a function of m^* in figure 6.15. For $m^* < m^*_{crit}$, the data was approximated using least squares to the quadratic,

$$m^*/A^* = 2.5355 \cdot m^{*2} + 1.1943 \cdot m^* + 0.0482 \tag{6.15}$$

with a coefficient of determination $R^2 = 0.998$. However, it is presumed that this equation would not approximate the amplitude well for very small mass ratios, as it predicts that $A^* \to 0$ as $m^* \to 0$. This prediction is contrary to the findings for the mass ratios considered here. The case of $m^* = 0.01$ was investigated, the oscillations were found to have a peak amplitude $A^*_{max} = 0.52598$ at u^*_{max}. It appears from this that $A^*_{max} \to 0.55$ as $m^* \to 0$ for the tether length and Reynolds number considered in this study.

For $m^* > m^*_{crit}$, the data were approximated by a least squares linear fit,

$$m^*/A^* = 7 \cdot m^* - 1.7725 \tag{6.16}$$

with a coefficient of determination $R^2 = 0.998$. Equation 6.16 predicts the amplitude will asymptote to $A^* = 0.14$ as $m^* \to \infty$. This is in qualitative agreement with the

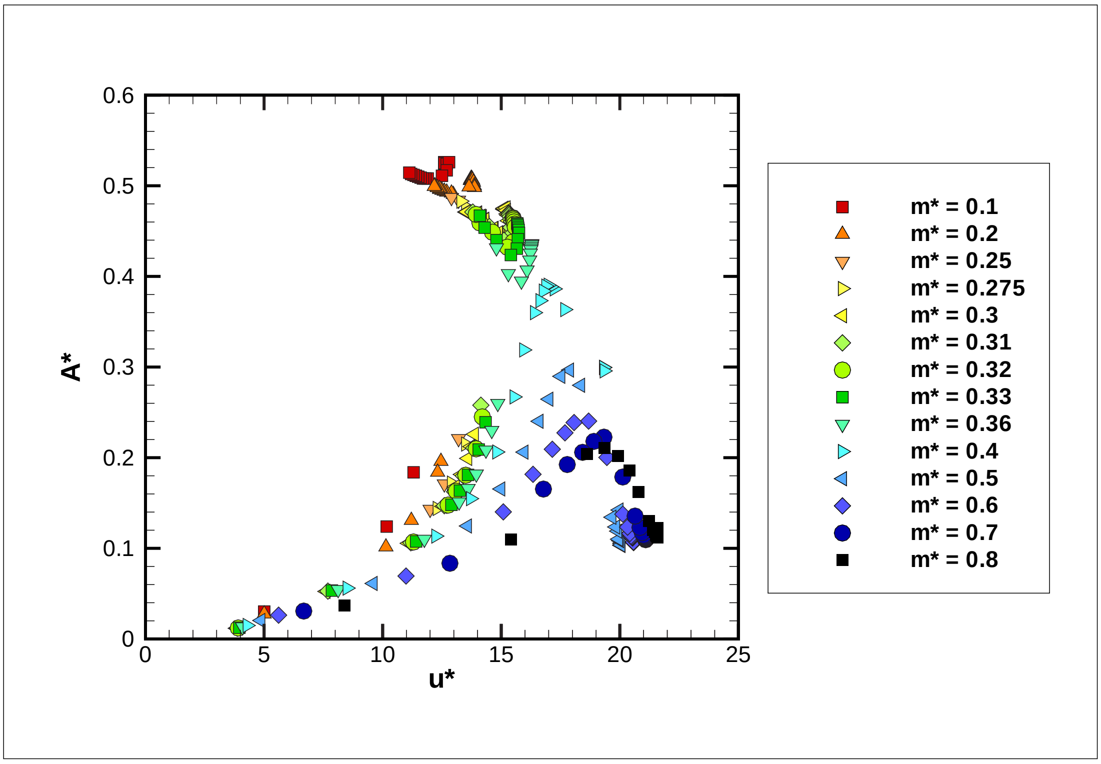

Figure 6.14: Amplitude of oscillation, in the direction of motion, as a function of reduced velocity for $m^* = [0.1, 0.8]$ and $L^* = 5.0$

findings for the mass ratio range considered in this study. However, it is possible that this fit is valid only in the range of mass ratios investigated here, as it is assumed that very large mass ratio cylinders ($m^* >> 1$) would exhibit extremely small amplitude oscillations. Equations 6.15 and 6.16 intersect at $m^* = m^*_{crit}$.

Figure 6.16 plots A^* as a function of Fr. For $m^* < m^*_{crit}$, the discontinuous jump in A^* occurs at $Fr \simeq 0.8$ regardless of mass ratio. The value of Fr at which the jump occurs appears to increase slightly with mass ratio, however the jump was noted to occur prior to $Fr = 0.9$ for all $m^* < m^*_{crit}$ in this study. Of interest is that for $Fr \simeq 0.78$ the amplitude of oscillation is the same for all mass ratios considered.

The amplitude of oscillation maintained a constant value for all Froude numbers in the range $Fr = [2.5, 50]$. For $m^* < m^*_{crit}$, this amplitude was always greater than $A^* = 0.4$. For the case of $m^* = 0.4$, the amplitude did not reduce to $A^* \simeq 0.1$ as for higher mass ratios, but maintained an amplitude of $A^* \simeq 0.3$ up to and including $Fr = 50$. For higher mass ratios, $A^* \to 0.1$ for high Froude numbers.

Figure 6.17 shows A^* as a function of $\overline{\theta}$. The jump in $\overline{\theta}$ noted in the previous section is clearly related to the jump in amplitude described here. For $0.3 \leqslant m^* \leqslant 0.36$, the

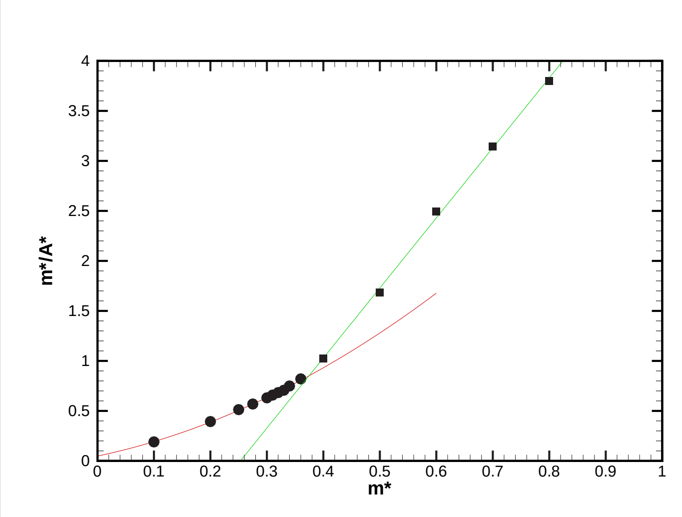

Figure 6.15: m^*/A^* as a function of mass ratio for $m^* = [0.1, 0.8]$ and $L^* = 5.0$

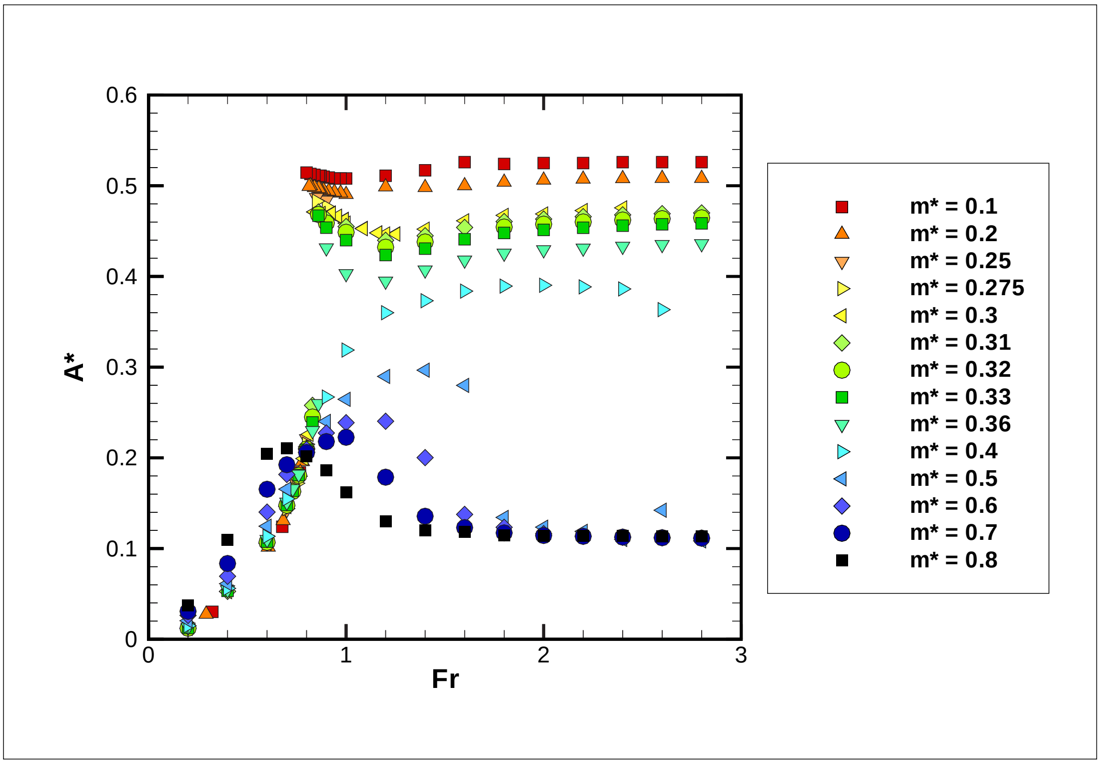

Figure 6.16: Amplitude of oscillation, in the direction of motion, as a function of Froude number in the range $Fr = [0, 3]$ for $m^* = [0.1, 0.8]$ and $L^* = 5.0$

slight reduction in amplitude noted in figure 6.14 appears to occur at $\overline{\theta} \simeq 75^o$. For $m^* < 0.3$, this reduction appears to occur at slightly lower values of $\overline{\theta}$. For $m^* = 0.4$, a significant reduction in A^* is noted as $\overline{\theta} \to 85^0$. For higher mass ratios, this reduction

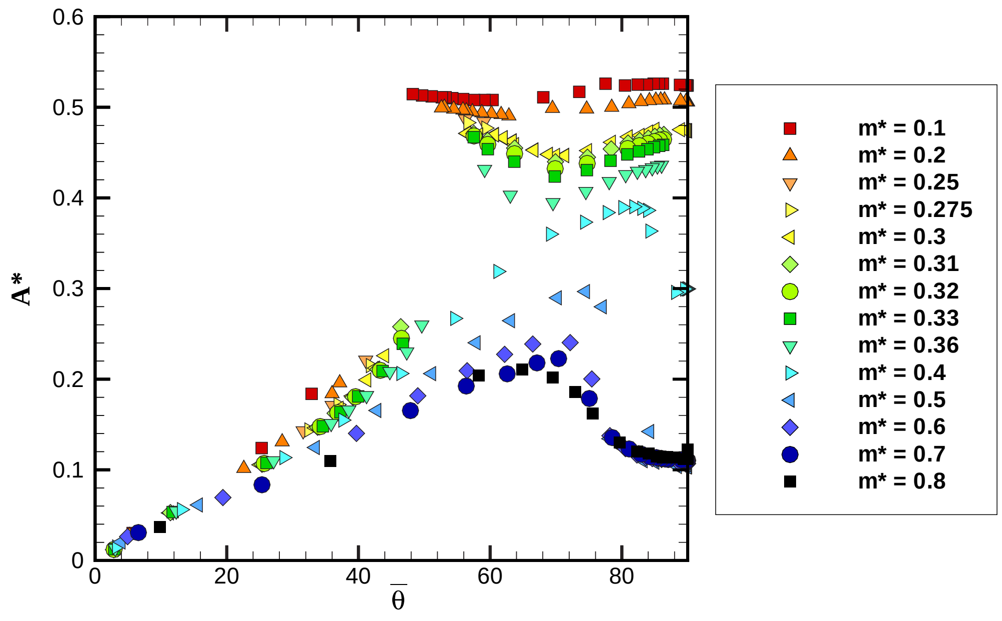

Figure 6.17: Amplitude of oscillation, in the direction of motion, as a function of mean layover angle for $m^* = [0.1, 0.8]$ and $L^* = 5.0$

in A^* occurs at progressively lower mean layover angles.

A significant increase in $\overline{C_D}$ was noted for $m^* < m^*_{crit}$ as the Froude number was increased beyond $Fr_{crit} \simeq 0.8$. It was conjectured in section 6.3 that the jump in $\overline{C_D}$ is related to a jump in the amplitude of oscillation. Figure 6.18 shows $\overline{C_D}$ as a function of A^*. For $m^* < m^*_{crit}$, a jump in both $\overline{C_D}$ and A^* is apparent and a high drag is only observed for a high value of A^*. The difference in response between $m^* < m^*_{crit}$ and $m^* > m^*_{crit}$ is clearly apparent. For $m^* > m^*_{crit}$, both the drag and amplitude increase gradually with reduced velocity, prior to decreasing as u^* is increased further. By contrast, for $m^* < m^*_{crit}$, both the drag and amplitude experience a jump, prior to decreasing and then increasing once more.

6.4.2 RMS Force Results

Figure 6.19 shows the RMS drag coefficient as a function of the Froude number. Not surprisingly a jump in $C_{D_{RMS}}$ is observed for $m^* < m^*_{crit}$ at $Fr \simeq 0.8$. The value of $C_{D_{RMS}}$ was measured at a Froude number slightly higher than Fr_{jump} for each mass

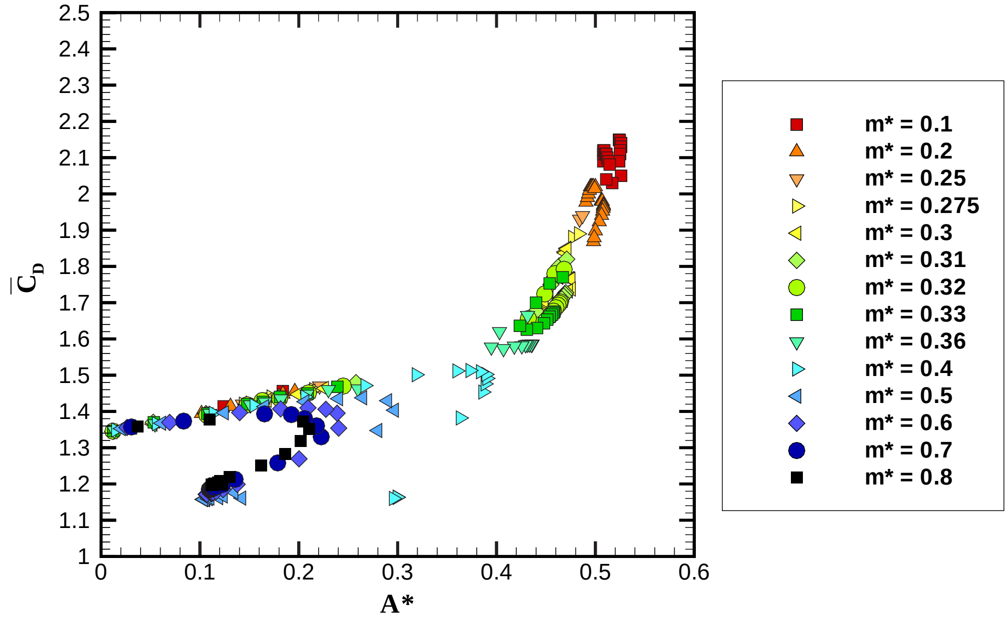

Figure 6.18: Mean drag coefficient as a function of the amplitude of oscillation, in the direction of motion, for $m^* = [0.1, 0.8]$ and $L^* = 5.0$

ratio $m^* < m^*_{crit}$ and was approximated by the quadratic least squares fit:

$$C_{D_{RMS(jump)}} = -1.36 \cdot m^{*2} - 0.142 \cdot m^* + 0.667 \tag{6.17}$$

with a coefficient of determination, $R^2 = 0.999$. Equation 6.17 indicates that $C_{D_{RMS(jump)}}$ approaches 0.667 as m^* approaches 0, which represents the maximum value of $C_{D_{RMS(jump)}}$ possible for this tether length and Reynolds number.

At high Froude numbers ($Fr \gtrsim 3$), the value of $C_{D_{RMS}}$ remains constant up to and including the highest Froude number investigated ($Fr = 50$) for each mass ratio investigated. The value of $C_{D_{RMS}}$ at high Froude numbers is dependent on the mass ratio. $C_{D_{RMS}}$ was measured at $Fr = 50$ for each $m^* < m^*_{crit}$; the results have been approximated by the linear least squared fit:

$$C_{D_{RMS(Fr=50)}} = -1.26 \cdot m^* + 0.7 \tag{6.18}$$

with a coefficient of determination, $R^2 = 0.998$. This equation indicates that at $Fr \gtrsim 3$, $C_{D_{RMS}} \to 0.7$ as $m^* \to 0$.

The ratio of $C_{D_{RMS(jump)}}/C_{D_{RMS(Fr=50)}}$ was also determined for $m^* \leqslant m^*_{crit}$, and a quadratic polynomial was fit to the results using the method of least squares:

$$C_{D_{RMS(jump)}}/C_{D_{RMS(Fr=50)}} = 3.884 \cdot m^{*2} + 0.6849 \cdot m^{*} + 1 \tag{6.19}$$

with a coefficient of determination, $R^2 = 0.999$. This trend shows that $C_{D_{RMS(jump)}}$ will be greater than $C_{D_{RMS(Fr=50)}}$ for all mass ratios $m^*_{crit} > m^* > 0$.

For $m^* \geqslant 0.5$, the value of $C_{D_{RMS}}$ at $Fr = 50$ was found to vary linearly with mass ratio as:

$$C_{D_{RMS(Fr=50)}} = 0.0181 \cdot m^* + 0.002 \tag{6.20}$$

with a coefficient of determination, $R^2 = 0.998$. This trend indicates that $C_{D_{RMS}}$ is always in the range [0.1,0.2] for $m^* = [0.5, 0.8]$ for high Froude numbers. Of interest is that $C_{D_{RMS}}$ at high Froude numbers increases slightly with mass ratio.

The case of $m^* = 0.4$ represents a unique mass ratio as it fits neither equation 6.18 or 6.20 well. It appears that $m^* = 0.4$ retains some of the features of $m^* < m^*_{crit}$, in that it retains a reasonably high value of $A^* = 0.299$ and $C_{D_{RMS}} = 0.044$ for $Fr = 50$.

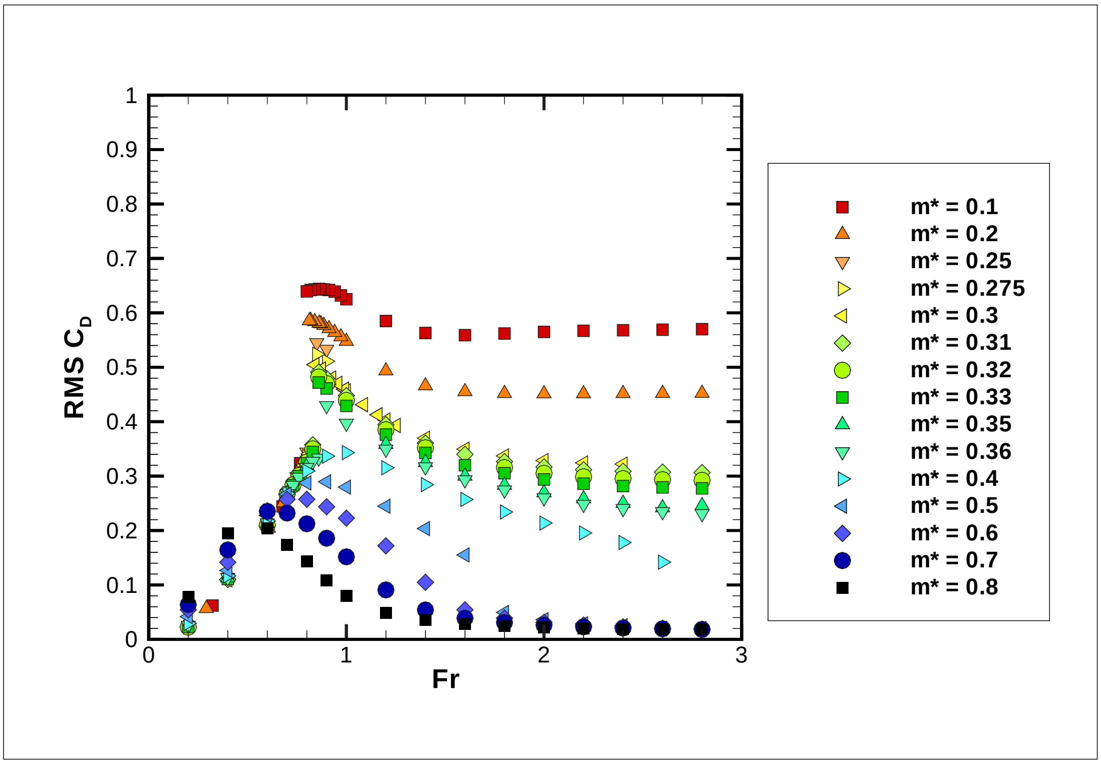

Figure 6.19: RMS drag coefficient as a function of Froude number in the range $Fr = [0, 3]$ for $m^* = [0.1, 0.8]$ and $L^* = 5.0$

Figure 6.20 shows the RMS lift coefficient as a function of the Froude number for $m^* < m^*_{crit}$. A jump in $C_{L_{RMS}}$ is noted at $Fr \simeq 0.8$ in line with previous results.

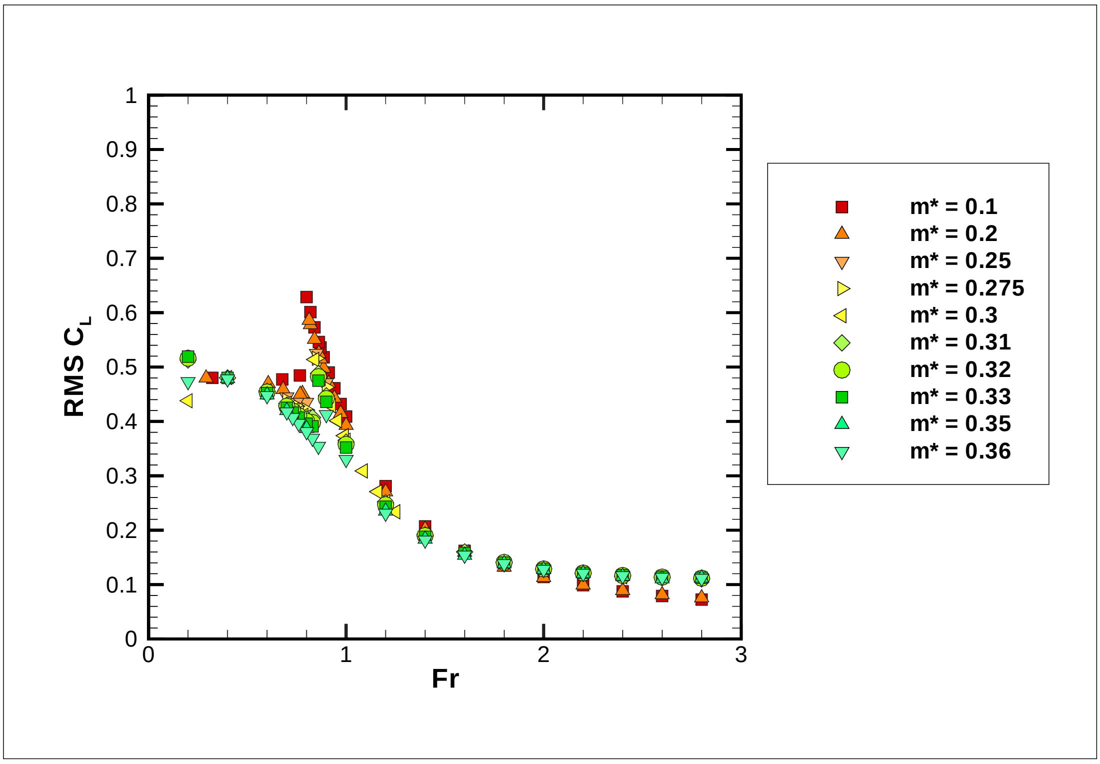

Figure 6.20: RMS lift coefficient as a function of Froude number in the range $Fr = [0, 3]$ for $m^* = [0.1, 0.36]$ and $L^* = 5.0$

Figure 6.20 clearly shows the range of Froude number over which this jump occurs ($Fr_{jump} = 0.8$ for $m^* = 0.1$, $Fr_{jump} = 0.86$ for $m^* = 0.36$). For $Fr > Fr_{jump}$, the data collapse extremely well to the curve:

$$C_{L_{RMS}} = 0.436 \cdot Fr^{-3.37} + 0.048, \quad Fr > Fr_{jump}. \tag{6.21}$$

with a coefficient of determination, $R^2 = 0.98$. This equation can be used to determine the highest value of $C_{L_{RMS}}$ for all $m^* < m^*_{crit}$

It is interesting to note that $C_{L_{RMS}}$ asymptotes to $C_{L_{RMS}} \simeq 0.1$ regardless of m^* for $Fr > 3$. A small but significant difference in $C_{L_{RMS}}$ is observed at $Fr = 3$ between $m^* \leqslant 0.2$ and $m^* \leqslant 0.25$. Interestingly, at high Froude numbers, the larger mass ratio has the higher value of $C_{L_{RMS}}$.

Figure 6.21 shows $C_{L_{RMS}}$ as a function of Froude number for $m^* > m^*_{crit}$. The data appear to collapse as $Fr \to 0$ ($C_{L_{RMS}} \to 0.5$). As the Froude number is increased, the data spread as a function of mass ratio, with $C_{L_{RMS}}$ being larger for lighter m^* values in the range $Fr = [0.4, \simeq 1.4]$.

At high Froude numbers, the value of $C_{L_{RMS}}$ asymptotes to a constant value. Com-

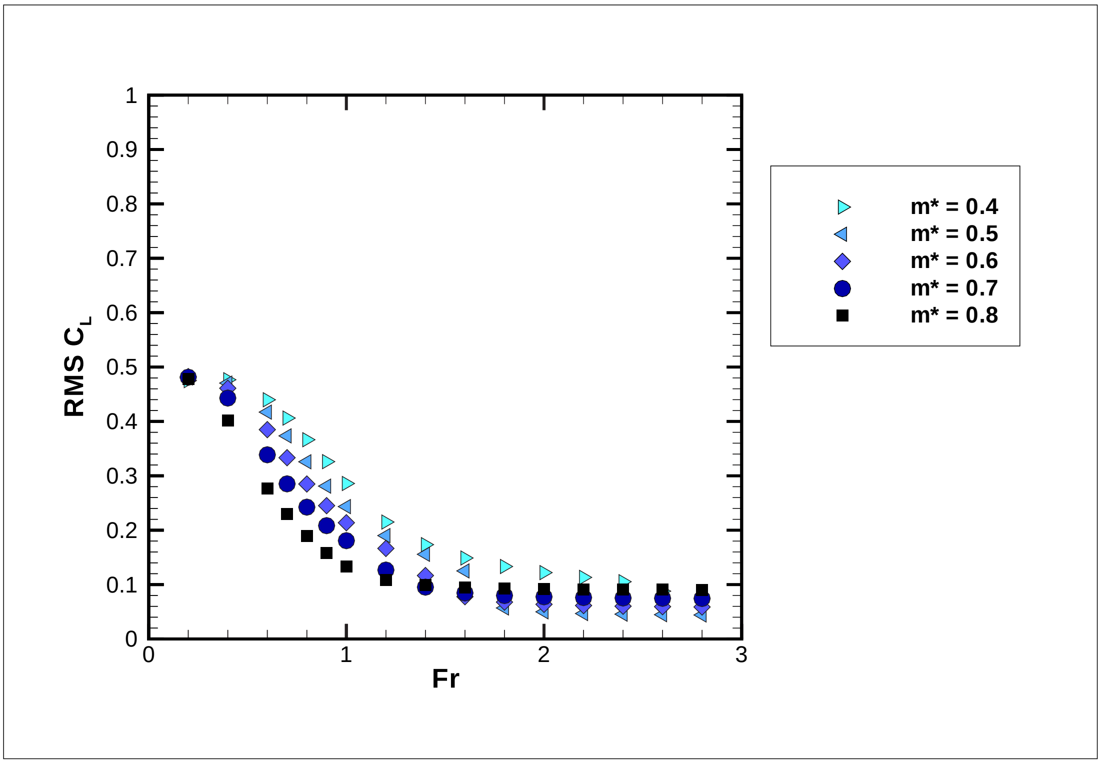

Figure 6.21: RMS lift coefficient as a function of Froude number in the range $Fr = [0, 3]$ for $m^* = [0.4, 0.8]$ and $L^* = 5.0$

paring figure 6.20 and 6.21 we see that $C_{L_{RMS}} \simeq [0.04, 0.1]$ at high Froude numbers ($Fr \gtrsim 3$) for all mass ratios considered.

In summary, the jump in mean position and mean fluid forces noted in section 6.4 coincides with a jump in $A^*, C_{D_{RMS}}$ and $C_{L_{RMS}}$. A critical Froude number exists ($Fr \simeq 0.7$) where the results collapse very well for all the mass ratios discussed here. For $m^* < m^*_{crit}$, the jump is found for Froude numbers slightly greater than this critical Froude number.

Both A^* and $C_{D_{RMS}}$ asymptote to a finite value of very high Froude numbers for $m^* < m^*_{crit}$. The value to which these parameters asymptote is a function of m^*. For $m^* > m^*_{crit}$, $A^* \rightarrow 0.1$ and $C_{D_{RMS}} \rightarrow 0$ for high Froude number, regardless of mass ratio.

6.5 Frequency Analysis

Figure 6.22 shows f/f_n as a function of u^*, where f is the fundamental frequency of oscillation, and f_n is the natural frequency of the tethered cylinder system. Unlike the case of the freely oscillating cylinder, the natural frequency varies with the fluid forces acting on the cylinder (see section 5.2). The frequency ratio, f/f_n, collapses linearly when plotted against the reduced velocity, for all mass ratios considered in this study,

$$f/f_n = 0.16 \cdot u^* + 0.2126. \tag{6.22}$$

This result indicates that the fundamental frequency of oscillation locks on to the Strouhal shedding frequency found for a fixed cylinder at $Re = 200$.

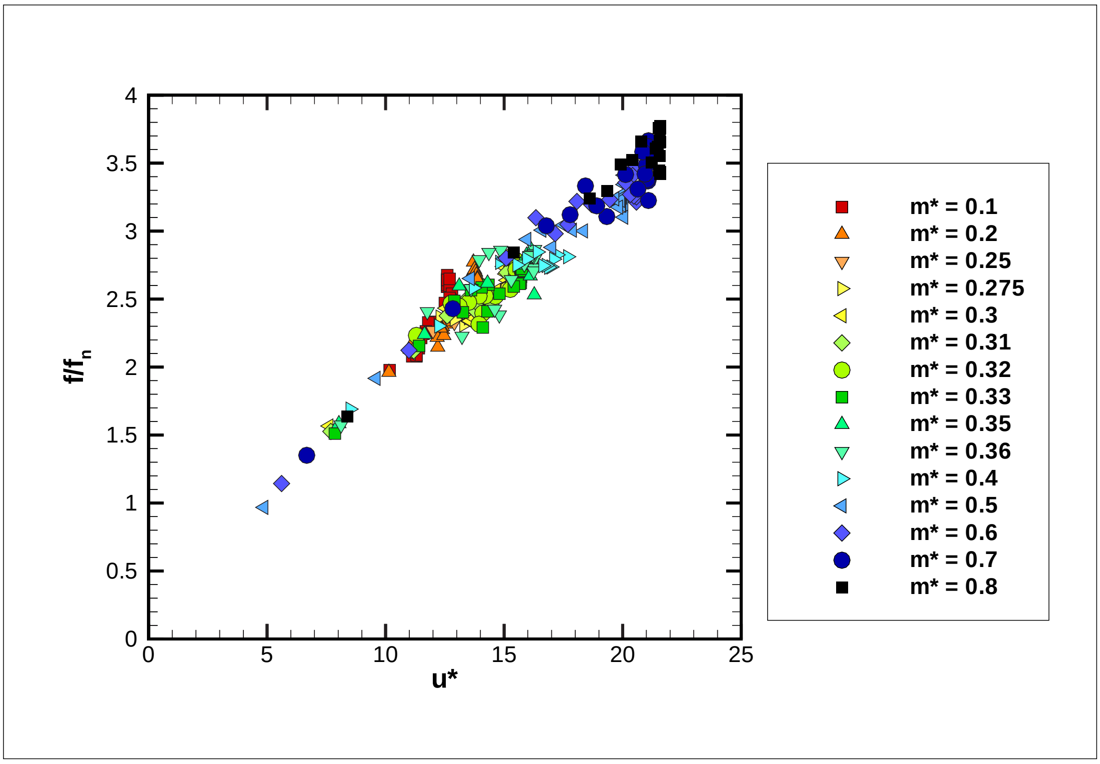

Figure 6.22: frequency ratio, f/f_n, as a function of reduced velocity for $m^* = [0.1, 0.8]$ and $L^* = 5.0$

6.6 The Vortex-Shedding Process in the Wake of a Tethered Cylinder

As noted in section 6.3.3, a non-zero mean lift coefficient is observed for a majority of the cases investigated, although for low Froude numbers and very high Froude numbers, the mean lift is close to zero. The finite mean lift is clearly due to the influence that the moving cylinder has on the surrounding fluid. While the wake structures and the cylinder form a coupled system, this section will describe the flow from the perspective of the influence of the cylinder motion on the formation and propagation of fluid structures in the wake. However, it should be remembered that the wake structures continually influence the forces acting on the cylinder and its subsequent motion in a feedback loop.

This section will concentrate on analyzing the case of a cylinder oscillating with a high amplitude. Specifically, snapshots of the vortex shedding cycle will be investigated for the case of $m^* = 0.1$ and $Fr = 0.8$. The case of low amplitude oscillations has previously been considered in section 5.9.2.

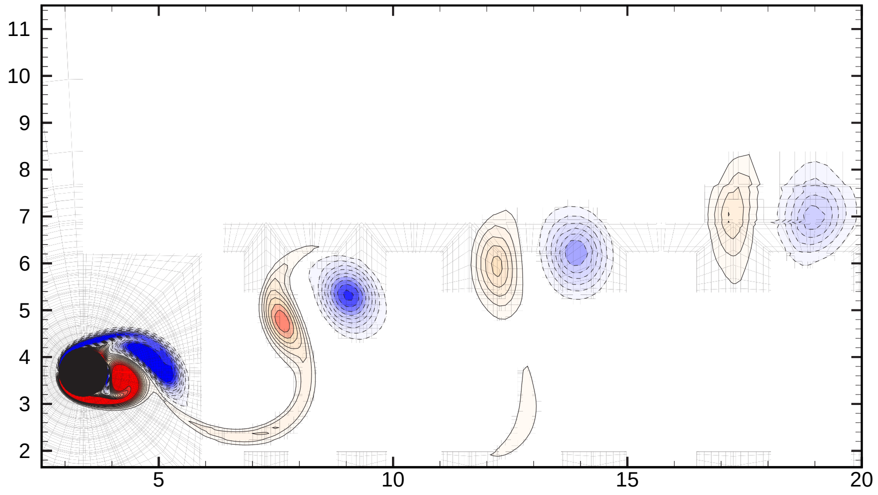

Figure 6.23: Vorticity field ω_z for $m^* = 0.1$, $L^* = 5.0$ and $Fr = 0.8$, for the cylinder at the top of the oscillation cycle. Contours are evenly spaced over the range (blue) $-5.0 \leqslant \omega_z \leqslant 5.0$ (red); with $\Delta\omega_z = 0.5$.

Figure 6.23 shows a snapshot of the vortex structures in the wake of the tethered cylinder. The cylinder is at the top of its cycle, defined as the most counter-clockwise position, and is momentarily stationary. Two related features of the shedding wake distinguish the flow past a tethered cylinder from either the flow past a fixed cylinder or the flow past a freely oscillating cylinder. First, the wake is shedding at an angle to the inflow. In itself, this is indicative of the mean negative lift acting on the tethered cylinder. Second, the fluid structures are shed in vortex pairs. These structures induce a jet of fluid to travel in the positive y direction, inducing both the mean negative lift and the angle at which the wake is shed. The motion of the cylinder is responsible for inducing the vortex pairing.

Figure 6.24 to 6.27 show closeup snapshots of vorticity in the wake at quarter cycle intervals. Figure 6.24 shows the shedding structures, taken for the case of the cylinder moving midway between the bottom position and the top position of the oscillation

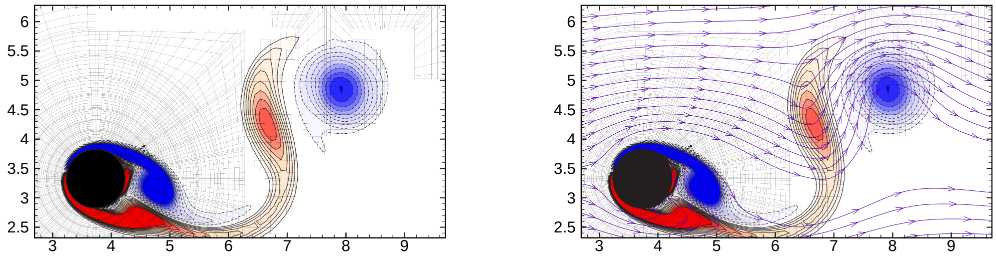

Figure 6.24: Vorticity field ω_z for $m^* = 0.1$, $L^* = 5.0$ and $Fr = 0.8$, for the cylinder moving between the bottom of the oscillation cycle and the top of the oscillation cycle. Contours are evenly spaced over the range (blue) $-5.0 \leqslant \omega_z \leqslant 5.0$ (red); with $\Delta\omega_z = 0.5$.

cycle. The cylinder is instantaneously moving both upstream and in the positive y direction. At this position in the oscillation cycle, both a negative and a positive vortex structure are forming behind the cylinder. The instantaneous streamlines indicate that the motion of the cylinder is inducing an upstream and positive y component of velocity in the fluid directly behind the cylinder. This acts to move the positive vortex core upstream and in the positive y direction, and increases the intensity of the negative vortex core.

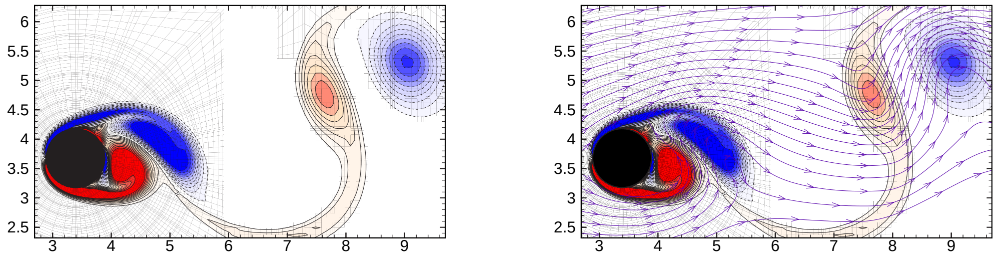

Figure 6.25: Vorticity field ω_z for $m^* = 0.1$, $L^* = 5.0$ and $Fr = 0.8$, for the cylinder at the top of the oscillation cycle. Contours are evenly spaced over the range (blue) $-5.0 \leqslant \omega_z \leqslant 5.0$ (red); with $\Delta\omega_z = 0.5$.

Figure 6.25 shows the instantaneous vortex structures a quarter of a cycle later. Here, the cylinder is at the top of its cycle (i.e. the most counter-clockwise position) and is stationary. The negative vortex core has commenced convecting downstream. The motion of the cylinder prior to this snapshot has drawn the positive vortex core upstream and in the positive y direction, such that it is now directly behind the cylinder. Importantly, when compared to the case of a stationary cylinder, the positive vortex is closer to the newly shed negative vortex core. The negative vortex core is stretched around the positive vortex core, and from the instantaneous streamlines, a jet of fluid has formed between the two vortex cores. The jet is travelling both in the upstream and positive y direction.

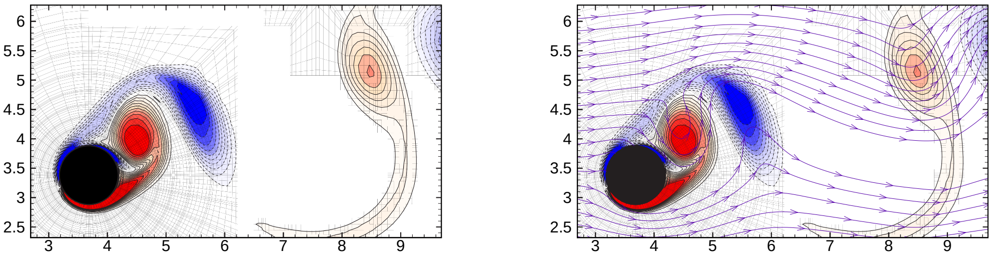

Figure 6.26: Vorticity field ω_z for $m^* = 0.1$, $L^* = 5.0$ and $Fr = 0.8$, for the cylinder moving from the top of the oscillation cycle to the bottom of the oscillation cycle. Contours are evenly spaced over the range (blue) $-5.0 \leqslant \omega_z \leqslant 5.0$ (red); with $\Delta\omega_z = 0.5$.

In Figure 6.26, the cylinder is midway between the top and bottom of the oscillation cycle, and is moving in a downstream and negative y direction. The positive vortex core has shed away from the cylinder, and is positioned downstream and above the rear cylinder surface. While the positive vortex core has shed, it remains close to the cylinder surface. As may be seen from the instantaneous streamlines, the position of the positive vortex core inhibits the growth of the developing negative vortex core, which is located at the cylinder surface. The jet between the shed positive and negative vortices is now directed principally in the positive y direction. In this snapshot, the shed negative vortex core is still considerably elongated in the cross-stream direction.

In figure 6.27, the cylinder is at the bottom of its oscillation cycle and is instantaneously stationary. The positive vortex core has convected further downstream allowing the developing negative vortex core to grow slightly. However, from the instantaneous streamlines, the growth of the developing negative core is still inhibited by the position of the positive vortex core. At this point, the positive vortex core has been stretched in the cross-stream direction and is becoming more diffuse. By contrast, the negative vortex core maintains its intensity over a small area, and is becoming less elongated. It appears that the combined action of the jet acting in the positive y direction, and the free-stream velocity combine to maintain the intensity of the negative vortex core.

Returning briefly to figure 6.24, it may be seen that the combined action of the jet and the free-stream velocity continue to maintain a small intense negative vortex core

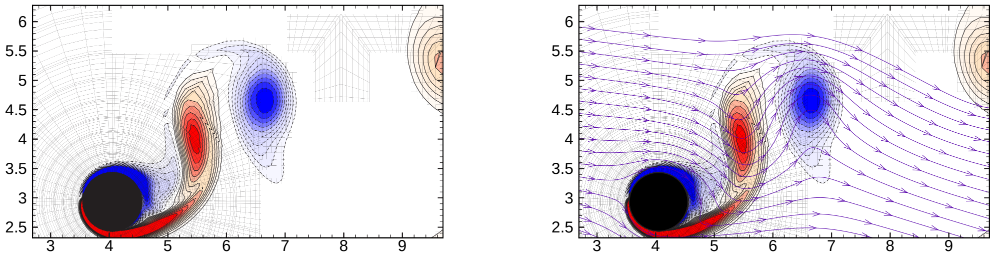

Figure 6.27: Vorticity field ω_z for $m^* = 0.1$, $L^* = 5.0$ and $Fr = 0.8$, for the cylinder at the bottom of the oscillation cycle. Contours are evenly spaced over the range (blue) $-5.0 \leqslant \omega_z \leqslant 5.0$ (red); with $\Delta\omega_z = 0.5$.

as the vortex pair convect downstream.

In summary, the motion of the cylinder as it moves from the bottom to the top of the oscillation cycle acts to induce the positive vortex core upstream and in the positive y direction. The subsequent position of the positive vortex core induces a jet between itself and the newly shed negative vortex core. The position of the positive vortex core also inhibits the growth of the developing negative vortex core. This results in a delay of the shedding of the negative vortex cores and allows vortex pairing in the wake. A jet forms between each shed vortex pair, which induces a momentum shift from the in-flow direction to the cross-flow direction, inducing a negative mean lift. From this analysis the following hypothesis may be formed:

> “The negative mean lift is due to the inclined angle to the free-stream at which the cylinder oscillates.”

As discussed in section 1.6.3, very few studies have analyzed the motion of a cylinder confined to oscillate at an angle other than 90^o or 0^o to the flow field. Of these, only the numerical work of Kocabiyik (2003) has identified a finite mean lift force. Kocabiyik (2003) restricted the motion of the cylinder such that upstream oscillations coincided with a negative y oscillation and downstream oscillations coincided with a positive y oscillation (i.e. the angle of oscillation of the cylinder was essentially 180^o from that described in the present study). She found a positive mean lift occurred for a wide range of oscillation amplitudes. It is left to a future study to determine if the same results can be achieved experimentally, and over what range of Reynolds numbers a finite mean lift may be maintained.

6.7 Comparison with Experimental Results

In this section the numerical results analyzed in depth in section 6.2 to 6.6 are compared with the experimental findings of Dr Josie Carberry, who conducted her experiments using a tethered cylinder rig set up in the FLAIR water channel as described in section 2.5.8. Experimentally, the mass ratio's examined were $m^* = [0.54, 0.97]$ and the tether length chosen was $L^* = 5$. The water channel allowed results in the range $Re = [1000, 8000]$, corresponding to Froude numbers in the range $Fr = [0, 1.2]$ and reduced velocities in the range $u^* = [0, 26]$. As mentioned in section 2.5.8, the motion of the cylinder was captured using a PAL video camera which allowed 25 frames per second in temporal resolution. The camera was sufficiently zoomed onto the moving cylinder that a spatial accuracy of $\pm 0.5mm$ (representing 3.1% of the cylinder diameter) after parallax errors were taken into consideration.

The tethered cylinder system was not instrumented to measure fluid forcing. However, by assuming that the mean lift coefficient was zero, the mean drag and reduced velocity could be calculated from knowledge of the mean layover angle, which was measured using the PAL tracking system. As mentioned, both in section 5.5 and 6.3.3, a finite negative mean lift coefficient has been noted for the numerical simulations.

Assuming the negative mean lift observed numerically at $Re = 200$ is also observed experimentally at higher Reynolds numbers, the assumption that $\overline{C_L}$ is zero leads to errors in the experimental calculation of both $\overline{C_D}$ and u^* as follows. Numerically, the mean drag was calculated directly, however, it can also be calculated from the equation:

$$\overline{C_{D_N}} = \tan\overline{\theta} \cdot \left(\overline{C_{L_N}} + (1 - m^*)\frac{\pi}{2} \cdot Fr^2\right). \tag{6.23}$$

By contrast, experimentally, the mean drag coefficient was calculated as:

$$\overline{C_{D_E}} = \tan\overline{\theta} \cdot \left((1 - m^*)\frac{\pi}{2} \cdot Fr^2\right). \tag{6.24}$$

By not including the negative mean lift coefficient, the mean drag calculated from the experimental findings is higher than the actual drag acting on the cylinder.

The reduced velocity is calculated numerically from equation 5.19, which is rewritten below:

$$u_N^* = \frac{2\pi^{\frac{3}{2}}}{\sqrt{2}} \left(\frac{(m^* + C_a)L^*}{\left(\overline{C_{D_N}}^2 + [\overline{C_{L_N}} + \frac{\pi}{2} \cdot \frac{1}{Fr^2} \cdot (1 - m^*)]^2\right)^{\frac{1}{2}}} \right)^{\frac{1}{2}}. \tag{6.25}$$

Experimentally, the mean lift coefficient is removed and the equation becomes:

$$u_E^* = \frac{2\pi^{\frac{3}{2}}}{\sqrt{2}} \left(\frac{(m^* + C_a)L^*}{\left(\overline{C_{D_E}}^2 + [\frac{\pi}{2} \cdot \frac{1}{Fr^2} \cdot (1 - m^*)]^2\right)^{\frac{1}{2}}} \right)^{\frac{1}{2}}. \tag{6.26}$$

From equation 6.25, an increase in $\overline{C_D}$ acts to decrease u^*, and a decrease in $\overline{C_L}$ acts to increase u^*. Numerically, both an increase in $\overline{C_D}$ and a decrease in $\overline{C_L}$ were reported as $\overline{\theta}$ and A^* discontinuously increased. The change in $\overline{C_D}$ and $\overline{C_L}$ tend to cancel each other out and only a small decrease in u^* is noted across the jump. However, experimentally, a jump in $\overline{\theta}$ will produce a large jump in $\overline{C_D}$, and, as $\overline{C_L}$ is assumed to be zero, the jump in $\overline{\theta}$ and A^* will result in a significant decrease in u^*. From the numerical findings, it is believed that this decrease may be erroneous.

6.7.1 Mean Layover Results

Figure 6.28 compares both the experimental and numerical findings of the mean layover angle as a function of u^*. Experimentally, a significant reduction in u^* is noted as $\overline{\theta} \geqslant 60^o$ for all mass ratios investigated. A jump in $\overline{\theta}$ is observed for $m^* \leqslant 0.76$, although at $m^* = 0.76$ the jump in $\overline{\theta}$ is only minor. This critical mass ratio is significantly higher than the value found numerically where $m^*_{crit} = 0.37$. However, from the findings presented in chapter 4, for the case of a freely oscillating cylinder, the critical mass ratio at $Re = 200$ is only $m^*_{crit} \simeq 0.1$ compared with the experimental findings of Govardhan & Williamson (2000) for the much higher Reynolds number range $Re = [2000, 10000]$ where $m^*_{crit} \simeq 0.54$.

Both experimentally and numerically, the critical mass ratio found for the case of a tethered cylinder is significantly higher when compared to that found for a freely oscillating cylinder at the same Reynolds number. The effect of tether length on m^*_{crit} will be investigated in chapter 7.

By plotting $\overline{\theta}$ as a function of Fr', where Fr' has been previously defined as:

$$Fr' = Fr \cdot \frac{1}{\sqrt{1 - m^*}}, \tag{6.27}$$

both the experimental and numerical results collapse extremely well (see figure 6.29). This is a superior parameter to compare numerical and experimental findings of the mean layover angle results, as it has been calculated directly in both cases.

Both results show a similar jump in $\overline{\theta}$ for $m^* < m^*_{crit}$. Clearly, the jump in $\overline{\theta}$ occurs at higher layover angles experimentally when compared to the numerical simulations.

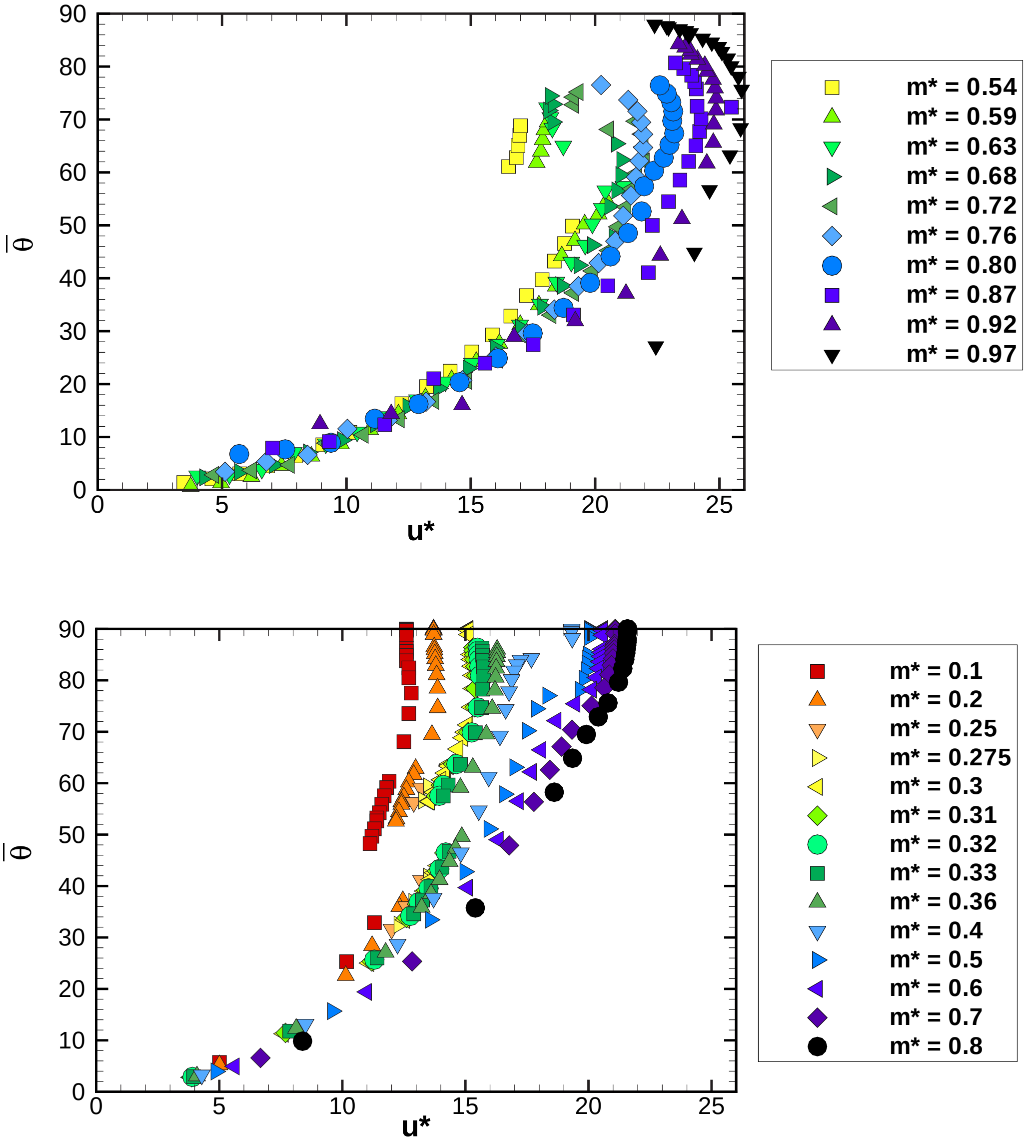

Figure 6.28: Comparison of the mean layover angle as a function of reduced velocity for, (top) Experimental ($Re = [1000, 8000]$ and, (bottom) numerical studies ($Re = 200$), both for $L^* = 5.0$.

The experimental results were limited by the maximum flow speed allowed by the facilities, and therefore the highest mean layover angles observed experimentally for $m^* < m^*_{crit}$ was $\overline{\theta} \simeq 78^o$. By contrast, numerical results were obtained up to $u^* \simeq 90^o$ for all mass ratios considered.

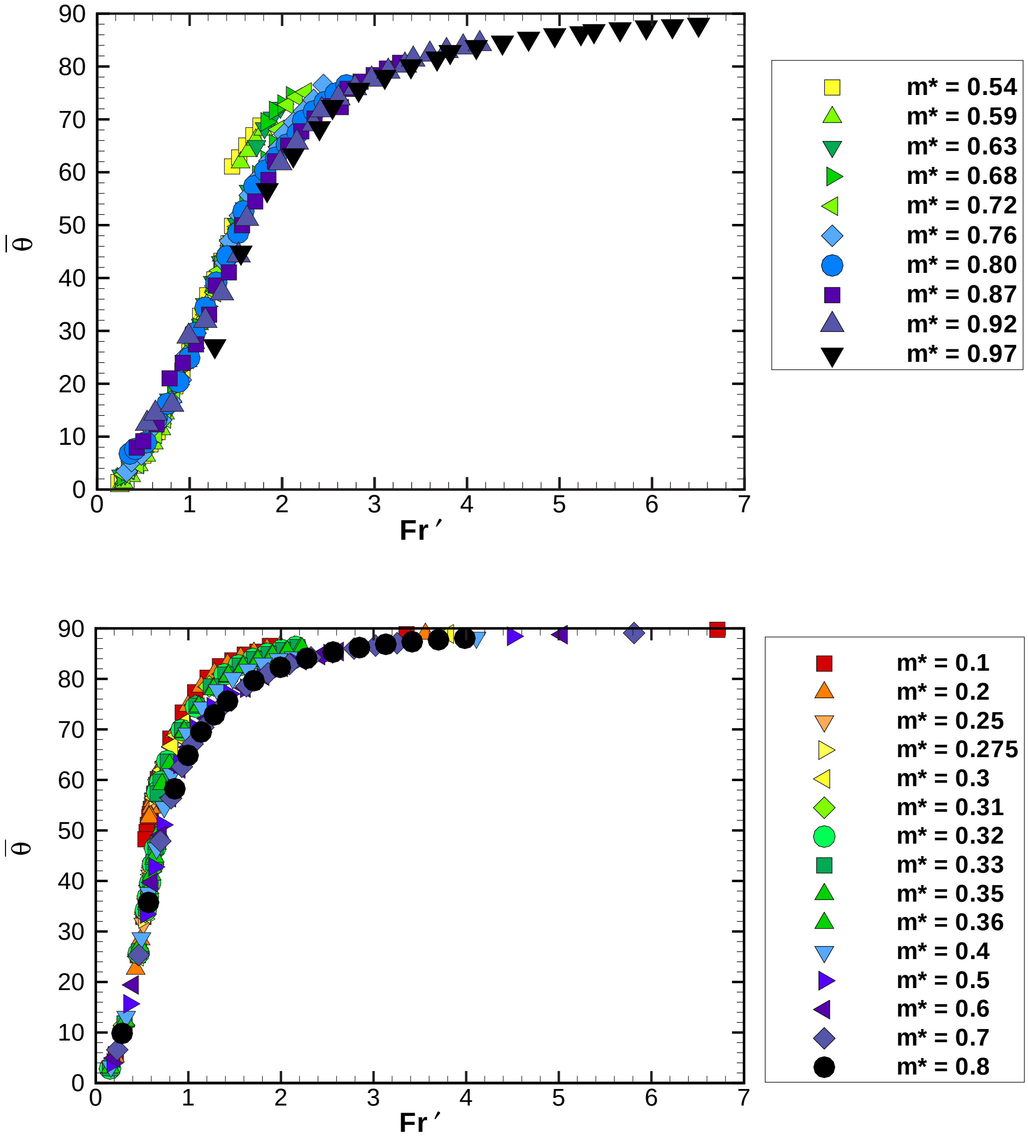

Figure 6.29: Comparison of the mean layover angle as a function of modified Froude number Fr' for, (top) Experimental ($Re = [1000, 8000]$ and, (bottom) numerical studies ($Re = 200$), both for $L^* = 5.0$.

6.7.2 Mean Drag Results

The mean drag coefficient, calculated both numerically and experimentally, is shown in figure 6.30 as a function of reduced velocity. Experimentally, for small reduced velocities ($u^* \lesssim 13$), the cylinder was found to stick against the side walls of the water channel, with the fluid providing insufficient momentum to move the cylinder. As a result, the calculated values of $\overline{C_{D_E}}$ at these low reduced velocities are scattered and in some cases

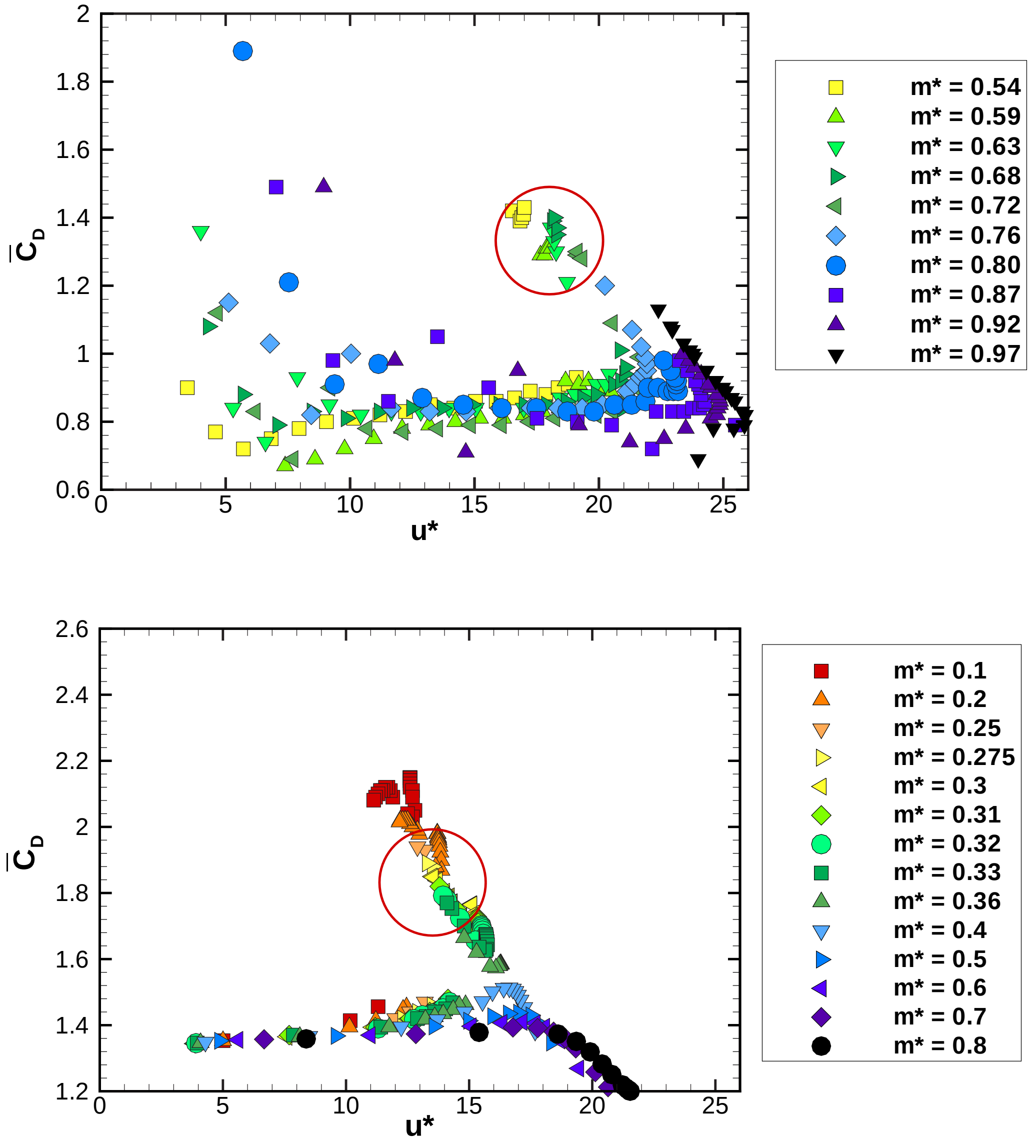

Figure 6.30: Comparison of the mean drag coefficient as a function of the reduced velocity for, (top) Experimental ($Re = [1000, 8000]$) and, (bottom) numerical studies ($Re = 200$), both for $L^* = 5.0$.

extremely high. It is believed that the true value of $\overline{C_{D_E}}$ acting on the cylinder at these low reduced velocities is significantly smaller.

A jump in $\overline{C_D}$ (which is highlighted in the figure by the circle) for $m^* < m^*_{crit}$ is observed both numerically and experimentally. Numerically, a reduction in the mean drag is noted as u^* is increased beyond $u^* \simeq 17$. Experimentally this effect is not noted; this may be due to the technique employed to calculate $\overline{C_{D_E}}$. Over the entire range,

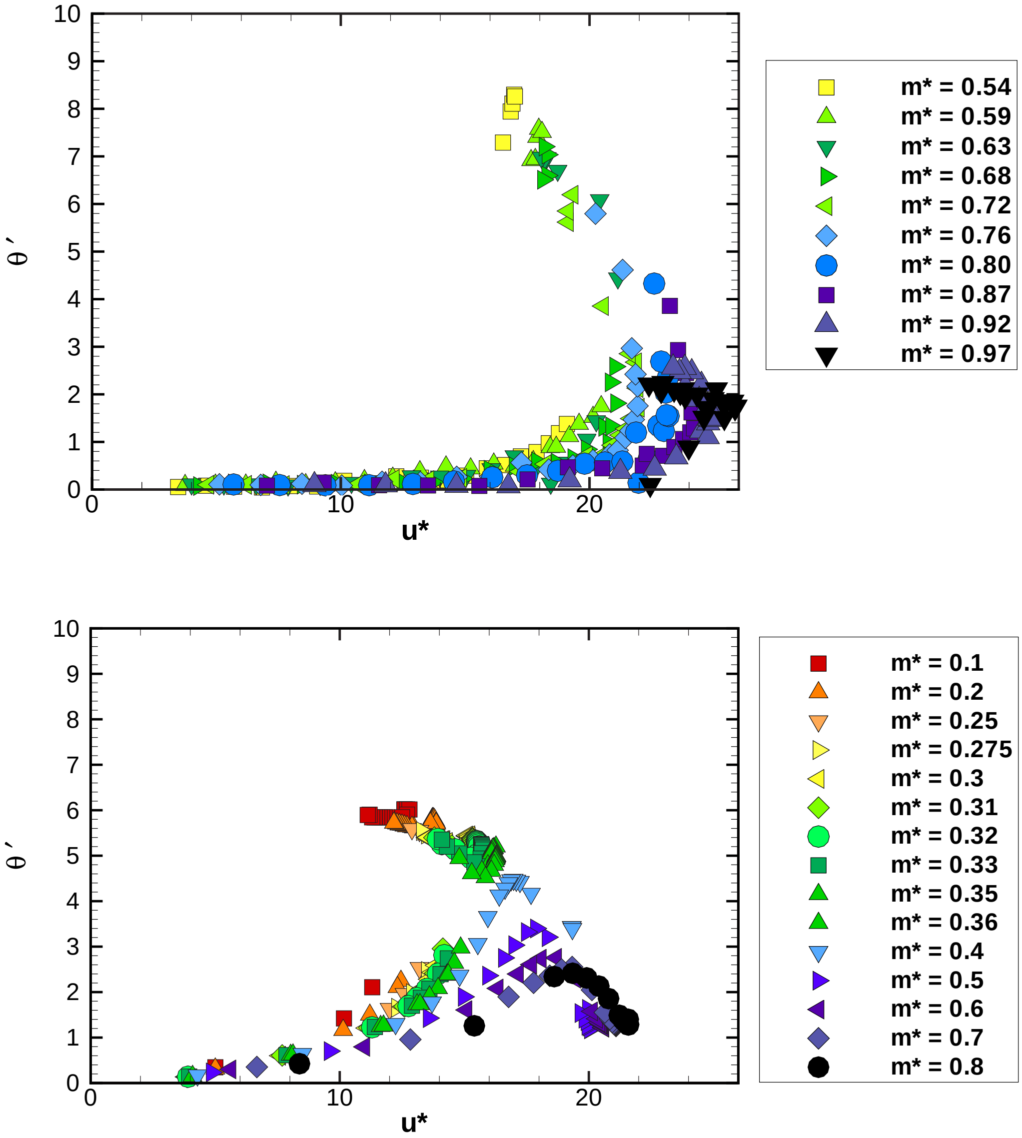

Figure 6.31: Comparison of the angular amplitude of oscillation, θ' as a function of the reduced velocity for, (top) Experimental ($Re = [1000, 8000]$) and, (bottom) numerical studies ($Re = 200$), both for $L^* = 5.0$.

the mean drag calculated numerically is somewhat higher than $\overline{C_{D_E}}$. This is attributed to the difference in Reynolds number between the two sets of results; when comparing $Re = 200$ to $Re = [1000, 10000]$ for the flow past a fixed cylinder, a similar decrease is noted.

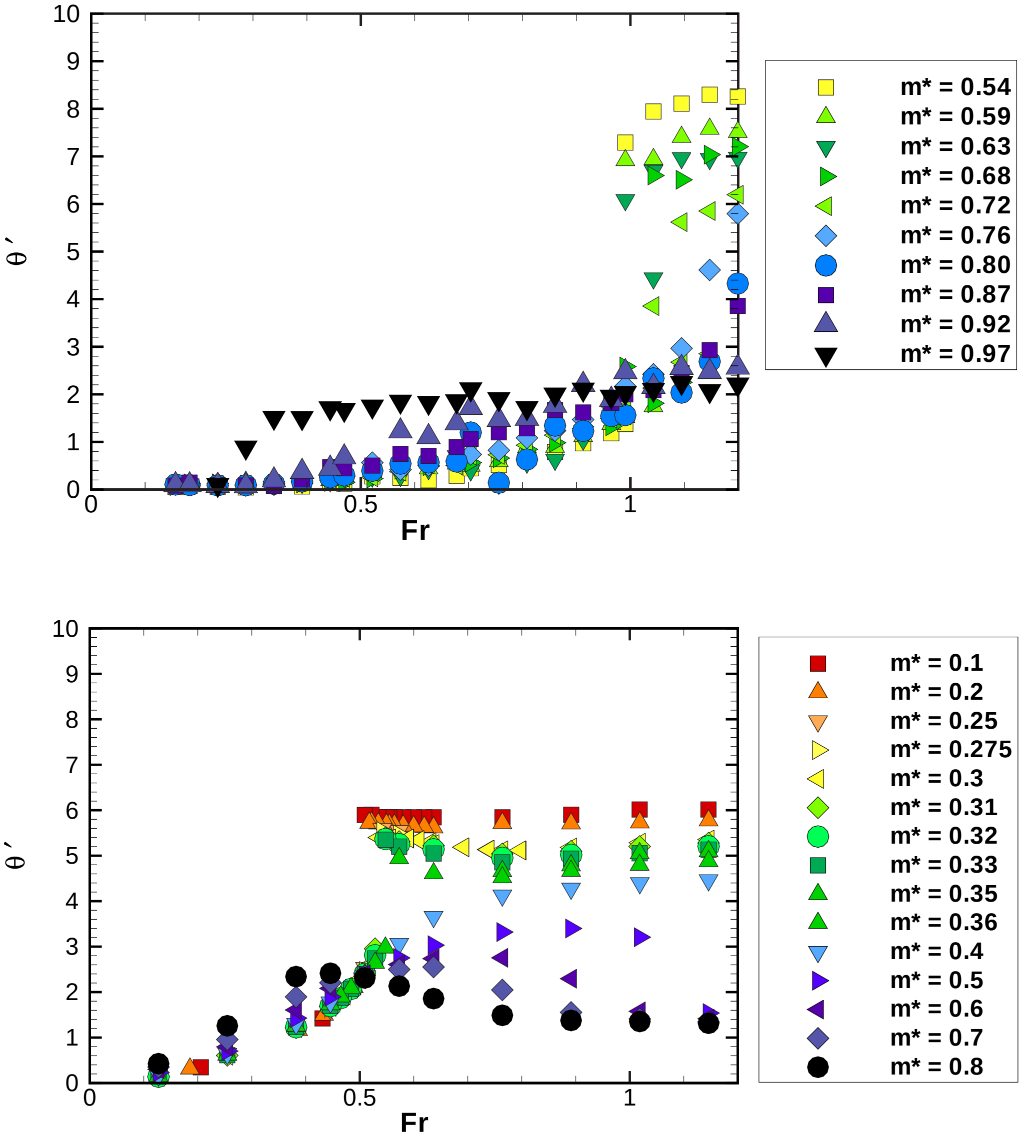

Figure 6.32: Comparison of the angular amplitude of oscillation, θ' as a function of the Froude number for, (top) Experimental ($Re = [1000, 8000]$) and, (bottom) numerical studies ($Re = 200$), both for $L^* = 5.0$.

6.7.3 Oscillation Results

The oscillation amplitude results, presented as $\hat{\theta}$, are shown in figure 6.31 as a function of u^* for both the numerical and experimental results.

Experimentally, the maximum oscillations are 50% greater in magnitude than the highest oscillation amplitudes observed numerically. It is believed that this is a Reynolds number effect, as numerically the fluid simulated is effectively more viscous then that analyzed experimentally and acts to damp out the cylinder motion.

The overall forms of the experimental and numerical results are very similar except at high values of u^*, where for $m^* > m^*_{crit}$ the numerically calculated amplitude decreases. Experimentally at high u^*, the oscillation amplitude appears to maintain a constant value for $m^* > m^*_{crit}$.

Finally, comparing the oscillation results as a function of Froude number (see figure 6.32), a critical Froude number is observed both numerically and experimentally at which the jump in $\hat{\theta}$ is observed to occur for all $m^* \leqslant m^*_{crit}$. Numerically, this critical Froude number occurs at $Fr \simeq 0.8$, whereas experimentally it occurs closer to $Fr = 1$. In both cases, just prior to the critical Froude number, the amplitude of oscillation reduces, and is independent of m^*.

6.7.4 Time History Results

Numerically, as has been shown in section 6.4, for $m^* \leqslant m^*_{crit}$, the oscillation amplitude is relatively small for small Froude numbers before increasing discontinuously at $Fr \simeq 0.8$. Beyond this Froude number, the cylinder oscillated at a considerably higher amplitude. A similar result has been noted for the experimental results; however the critical Froude number where a jump in amplitude is observed is closer to $Fr = 1$.

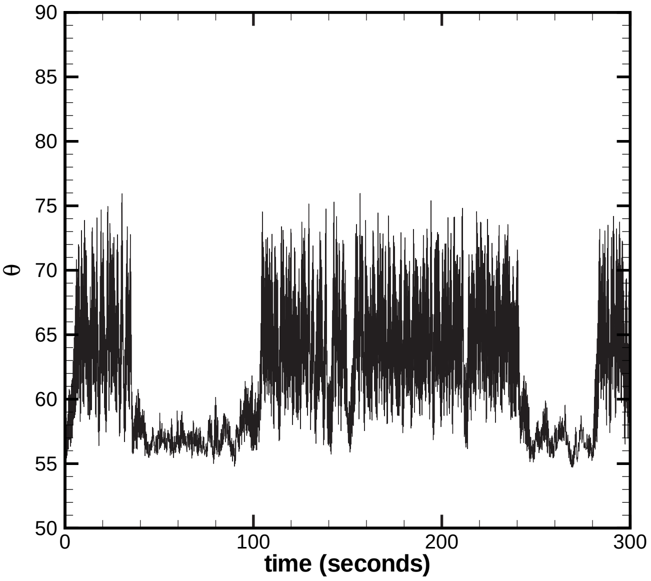

Figure 6.33: Oscillation time trace for experiments with $m^* = 0.64$, $L^* = 5.0$ and $Fr = 1.04$.

For specific cases of mass ratio, $m^* \rightarrow m^*_{crit}$, at Froude numbers near $Fr = 1$, the cylinder was observed to switch between oscillating at a small amplitude and oscillating at a higher amplitude. An example of this is shown in figure 6.33 with $m^* = 0.64$ and $Fr = 1.04$. It is speculated that experimentally at this Froude number and mass ratio the cylinder oscillation regime is unstable, and small changes in the flow field may result in a period of large or small oscillation respectively. It is further speculated that such a transition is not observed numerically due to the relatively low Reynolds number examined.

6.7.5 Vortex Structures in the Wake

Preliminary PIV results from the experiments performed by Josie Carberry have been obtained and two images are presented here with numerical results for comparison. Experimentally, the mass ratio considered was $m^* = 0.64$. Figure 6.34 shows a snapshot of the vorticity field comparing results for low amplitude oscillations for both the numerical simulations and the experimental results. The two snapshots have been taken at the same phase of shedding and cylinder position in the oscillation cycle. In both cases the wake resembles a standard Karman vortex street which would be seen in the wake of a stationary cylinder. Three features indicate distinct differences between the experimental and numerical findings. The first is that the vortex structures found experimentally show smaller vortex structures which may be due to the contour levels used and noise in the flow. Second, the vortex structures found experimentally are much smaller than those found in the numerically simulated wake. The boundary layer thickness is similarly smaller for the experimental results. This is a direct result of the discrepancy in the Reynolds number between the numerical and experimental results.

Figure 6.35 shows the vortex field for larger oscillation amplitudes (In this case for $m^* < m^*_{crit}$ and for $Fr > 0.8$ numerically and $Fr > 1.0$ experimentally). Once again, for both the experimental case and the numerical case, each image represents a snapshot of the vorticity field. The cylinder position and the shedding is in phase between the numerical and experimental result. In this case, the wake from the numerical simulation is found to shed at an appreciable angle to the flow direction for oscillations of this amplitude (see section 6.6). The experimental results are very similar to the numerical finding and it appears that the experimental wake is also directed at an angle to the flow. From the results presented in section 6.6, this may indicate that the cylinder has a

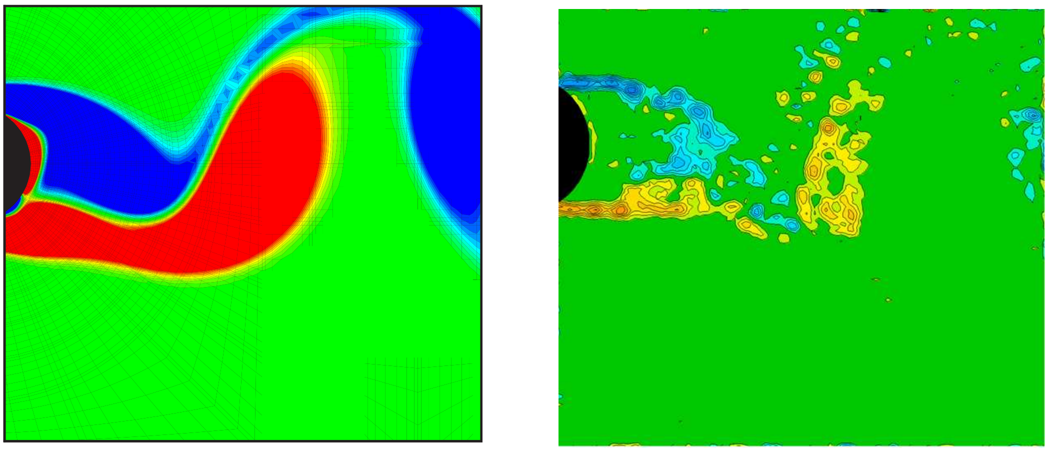

(a) (b)

Figure 6.34: Comparison of the span-wise vorticity field, ω_z for a cylinder undergoing low amplitude oscillations; (left) numerical and, (right) experimental studies, both for $L^* = 5.0$.

finite (and in this case negative) mean lift for the experimental results, in line with the findings of the numerical simulations. The author is cautious to suggest that this is the only possible conclusion. The PIV results are preliminary and the three-dimensional nature of the wake results in two-dimensional slices having very patchy vorticity fields. It is intended that future work will analyze the wake structures experimentally in more detail.

6.8 Conclusions

The results presented in this chapter demonstrate the existence of a critical mass ratio, which in this case was found to be 0.37, below which a large jump in A^*, $\overline{\theta}$ and $\overline{C_D}$ is observed. The jump occurs in the vicinity of $Fr = 0.8$ for the Reynolds number investigated. The critical mass ratio found for the tethered cylinder represents a dramatic increase in m^*_{crit} when compared to the case of a freely oscillating cylinder at the same Reynolds number.

A new controlling parameter $Fr' = Fr \cdot 1/\sqrt{1 - m^*}$ enables the results from all the mass ratios investigated to collapse along a single line.

For a majority of cases, a negative mean lift was observed and this has been related to the vortex shedding process.

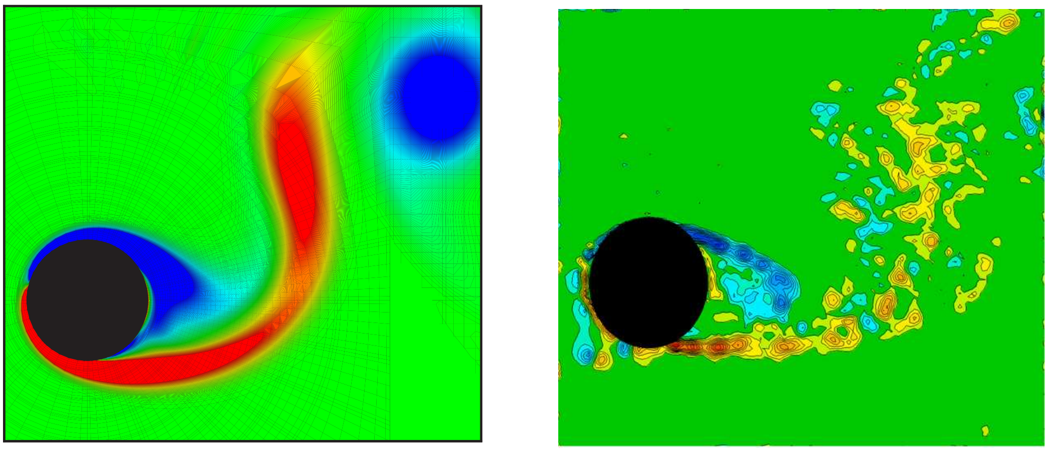

(a) (b)

Figure 6.35: Comparison of the span-wise vorticity field, ω_z for a cylinder undergoing high amplitude oscillations; (left) numerical and, (right) experimental studies, both for $L^* = 5.0$.

Comparison between the numerical results and Dr Josie Carberry's experimental results indicated that the same trends exist for both sets of data despite the significant difference in Reynolds number. Of interest is whether a negative mean lift is observed experimentally. As the experimental rig was not instrumented to measure force, this remains an unanswered question and is the source of future work.

Chapter 7

The Effect of Changed Tether Length on the Response of a Tethered Cylinder

7.1 Introduction

The effect of the normalized tether length parameter ($L^* = L/D$) on the response of the tethered cylinder is investigated in this chapter. Initially, all studies have been restricted to $m^* = 0.2$; however subsequent investigations have determined the critical mass ratio, m^*_{crit} (as defined in section 6.3.2 for a tethered cylinder) as a function of tether length.

The value of $m^* = 0.2$ was chosen, as, for the case of $L^* = 5$, the large amplitude oscillation branch was noted for $Fr \geq 0.8$ for this mass ratio. This branch of tethered cylinder response exhibits large oscillation amplitudes of up to $0.5D$, and it is therefore interesting to examine if this mode exists for both larger and smaller tether lengths.

Tether length ratios in the range $L^* = [0.1, 10]$ were investigated. As the tether length is measured from the centre of the cylinder, $L^* < 0.5$ represents a cylinder which is pivoted internally, and $L^* = 0.5$ represents a cylinder which is pivoted at a point on its surface. The limiting case of L^* for very small tethers is $L^* \to 0$, where $L^* = 0$ represents a fixed cylinder. At these very small tether lengths, simplifications used so far in determining the moment of inertia of the tethered body are no longer valid. The equation used by previous investigators (see section 5.2) for a tethered sphere assume that the moment of inertia is given by:

$$J = m \cdot L^2. \tag{7.1}$$

Equation 7.1 was also used in our investigations for a tethered cylinder where $L^* >> D$.

However, the exact value of the moment of inertia for a tethered cylinder can be obtained from any standard physics textbook (for example Giancoli (1989)) as,

$$J = m \cdot L^2 + (1/8)m \cdot D^2, \tag{7.2}$$

which can be rewritten in terms of the length ratio, L^*, as,

$$J = m \cdot D^2 \left(L^{*2} + 1/8\right). \tag{7.3}$$

From equation 7.3, if $L^* >> 1/64$, then equation 7.1 is a valid simplification of the moment of inertia, as has been used in previous investigations. However, in order to discuss the results of this chapter, the exact value of the moment of inertia (equation 7.3) must be used.

Substituting equation 7.3 into the derivation of the natural frequency of a tethered cylinder system (see section 5.2 for the complete derivation), the natural frequency of oscillation becomes,

$$f_n = \sqrt{\frac{T \cdot L^*}{m \cdot D(L^{*2} + 1/8)}}. \tag{7.4}$$

It should be kept in mind that derivation in section 5.2 determines the linearized form of the natural frequency by assuming a small angular amplitude of oscillation (assumed to be $\theta' \leq 20^o$).

From equation 7.4, the reduced velocity is defined as

$$u^* = \frac{u}{f_n D} = \sqrt{\frac{m^* \cdot \pi(L^{*2} + 1/8)}{2C_T \cdot L^*}}, \tag{7.5}$$

where C_T is the tension coefficient as defined in section 5.2. As with the moment of inertia, both the natural frequency and the reduced velocity defined in equation 7.4 and 7.5 approach the values previously used as $L^* \to \infty$. In practice, the error induced by using the definitions given in section 5.2 is less than 1% for any tether length ratio, $L^* \geq 3.6$.

At greater tether lengths (the largest investigated here being, $L^* = 10$), the tethered cylinder behaves as a freely oscillating cylinder restricted to oscillate at an angle to the flow field, where the angle of oscillation is defined by the equation,

$$\overline{\theta} = \tan^{-1}\left(\frac{\overline{C_D}}{\overline{C_L} + (1 - m^*) \cdot \pi/(2Fr^2)}\right). \tag{7.6}$$

For large tether lengths, the curvature of the cylinder path, represented by θ', varies with the amplitude of oscillation in the direction of motion, A^*, as,

$$\theta' = \tan^{-1}\left(\frac{A^*}{L^*}\right). \tag{7.7}$$

Therefore, as the tether length increases, the amount of curvature inherent in a given oscillation amplitude decreases. For example, for $L^* = 15$, and $A^* = 0.5$, the angular amplitude, θ' is only 1.9^o. This may be compared with the same amplitude, A^*, for tether length, $L^* = 5$ ($\theta' \simeq 5^o$) and for a tether length $L^* = 1$ ($\theta' \simeq 26.6^o$).

Of particular interest in this study is the effect of both very large and very small tether lengths on the subsequent motion of the cylinder.

The small values of L^* investigated provide information on the behaviour of a cylinder pivoted internally, and the results have practical applications in marine and offshore engineering fields. Of interest is the amplitude and frequency response as $L^* \to 1/64$. Of interest too is the vortex structures in the wake of an internally pivoted cylinder, as large amplitude oscillations A^* require large angular oscillations, necessitating large in-line and transverse components of oscillation.

The study of large tether lengths provides a link between research on a tethered cylinder and prior studies on freely oscillating cylinders with low mass and damping (see for example Khalak & Williamson (1999) and Govardhan & Williamson (2000)). Of particular interest is the effect of the tether length on the critical mass ratio, m^*_{crit}, when compared to that found for a freely oscillating cylinder at the same Reynolds number (see chapter 4), and if the imposed oscillation angle has any significant effect on the cylinder response.

7.2 Mean Layover Angle Results

Figure 7.1 shows the mean layover angle as a function of reduced velocity for $L^* = [1, 10]$. Each study was performed with $m^* = 0.2$. A jump in the mean layover angle is clearly apparent for $L^* = 5.0$ as has been discussed in the previous chapter. While not apparent from the results in this figure, the cases of $L^* = [2, 7.5]$ all experience a jump in the mean layover angle for this mass ratio. Interestingly, the case of $L^* = 10$ did not, this is further discussed in section 7.7. Regardless of whether a jump in $\overline{\theta}$ is observed or not, the overall form of the relationship between $\overline{\theta}$ and u^* appears very similar regardless of tether length. The most marked difference between each case is the rate of increase of $\overline{\theta}$ as a function of u^*. Another observation is that the maximum reduced velocity u^*_{max}, as defined in section 6.2.1 varies significantly with tether length. Close observation of figure 7.1 reveals that for the mass ratio investigated, the highest reduced velocity does not in general correspond to the highest mean layover angle recorded. For $L^* = 1.0$, the

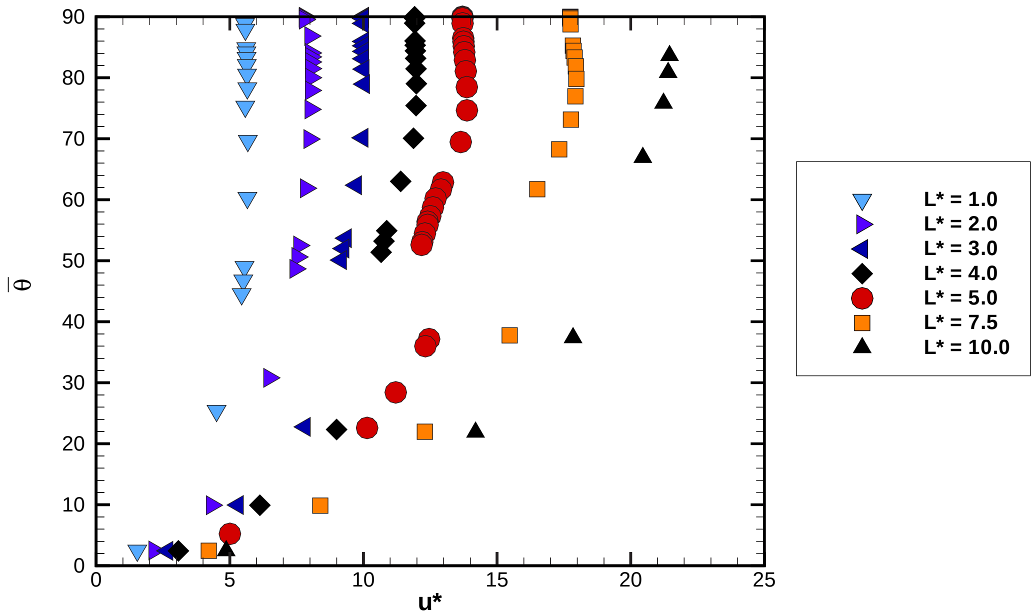

Figure 7.1: Mean layover angle as a function of reduced velocity for $m^* = 0.2$ and $L^* = [1, 10]$

largest reduced velocity recorded was $u^* = 5.67$ (corresponding to $\overline{\theta} \simeq 70^o$), whereas for $L^* = 10.0$, the largest reduced velocity recorded was $u^* = 21.45$ (corresponding to $\overline{\theta} \simeq 84^o$). Following the method presented in section 6.2.1, we can determine u^*_{max} from equation 7.5 to be:

$$u^*_{max} = \sqrt{\frac{m^* \cdot \pi(L^{*2} + 1/8)}{2 \cdot L^* \sqrt{\overline{C_D}^2 + \overline{C_L}^2}}}. \tag{7.8}$$

To account for the effect of L^* on u^*_{max}, a new parameter, η, was developed in an attempt to collapse the data, where:

$$\eta = u^* \cdot \sqrt{\frac{L^*}{L^{*2} + 1/8}} = \sqrt{\frac{\pi m^*}{2 C_T}} \tag{7.9}$$

Figure 7.2 plots the mean layover angle as a function of η. The results collapse to follow a general trend, however there is still some difference in the response as a function of L^*. As the mass ratio investigated is the same for all tether lengths investigated, the variation observed in figure 7.2 can only be due to a variation in $\overline{C_T}$, and as a consequence, implies a variation in $\overline{C_D}$ and $\overline{C_L}$ as a function of tether length. In the previous two chapters, it was shown that $\overline{C_D}$ and $\overline{C_L}$ varied as a consequence of oscillation amplitude. Therefore, from figure 7.2, a slight variation in cylinder oscillation characteristics as a function of tether length is implied.

Finally, the parameter Fr' was used successfully, both numerically and experimentally to collapse the mean layover results onto one line regardless of mass ratio in the previous chapter. By its definition (see section 6.2.2), for a fixed mass ratio, all the results should collapse onto one line when plotted against $Fr' = U_\infty/\sqrt{gD \cdot (1 - m^*)}$ regardless of tether length. Figure 7.3 shows the mean layover angle as a function of Fr'. Despite a wide range of tether length investigated, all the results collapse onto one line. A small variation is noted for large layover angles ($\overline{\theta} \gtrsim 70^o$); this may be due to the fact that there is no jump in $\overline{\theta}$ for $L^* = 10$. Therefore, for the same Fr', the mean layover angle is slightly reduced for this tether length. The results shown in figure 7.3 show an inflection at $\overline{\theta} \simeq 45^o$ at $Fr' \simeq 1$. Below $Fr' \simeq 1$ the rate of change of $\overline{\theta}$ is considerably greater than for $Fr' > 1$.

7.3 Mean Force Coefficient Results

7.3.1 Mean Drag Coefficient Results

Figure 7.4 shows the mean drag as a function of reduced velocity for $L^* = [1, 10]$ and $m^* = 0.2$. For a majority of tether lengths investigated, a jump in $\overline{\theta}$ was observed as the reduced velocity was increased beyond a critical value. The critical value of u^* at which the jump occurs increases as a function of tether length corresponding to the reduced velocity at which a jump is observed in $\overline{\theta}$ (as presented in the previous section). The size of the jump in $\overline{C_D}$ decreases with tether length, such that at $L^* = 7.5$, the jump in $\overline{C_D}$ represents only a 27% increase.

Of interest is that for this mass ratio and Reynolds number, there is no discontinuous jump in $\overline{C_D}$ as a function of reduced velocity observed for $L^* = 1.0$ or 2.0. In these cases, the mean drag rises steeply but continuously as a function of reduced velocity. It is postulated that the reason that no ‘jump’ in the drag is noted for these tether length ratios, is that the maximum reduced velocity is very small, and the rapid increase in $\overline{C_D}$ only appears to be continuous.

From figure 7.4, the maximum mean drag coefficient recorded remains very high down to $L^* = 1$. As the mean drag was shown to vary with oscillation amplitude in chapter 5, it is interesting to determine the maximum mean drag as a function of tether length for both the limiting cases of $L^* \to 0$ and $L^* \to \infty$, as this may reflect

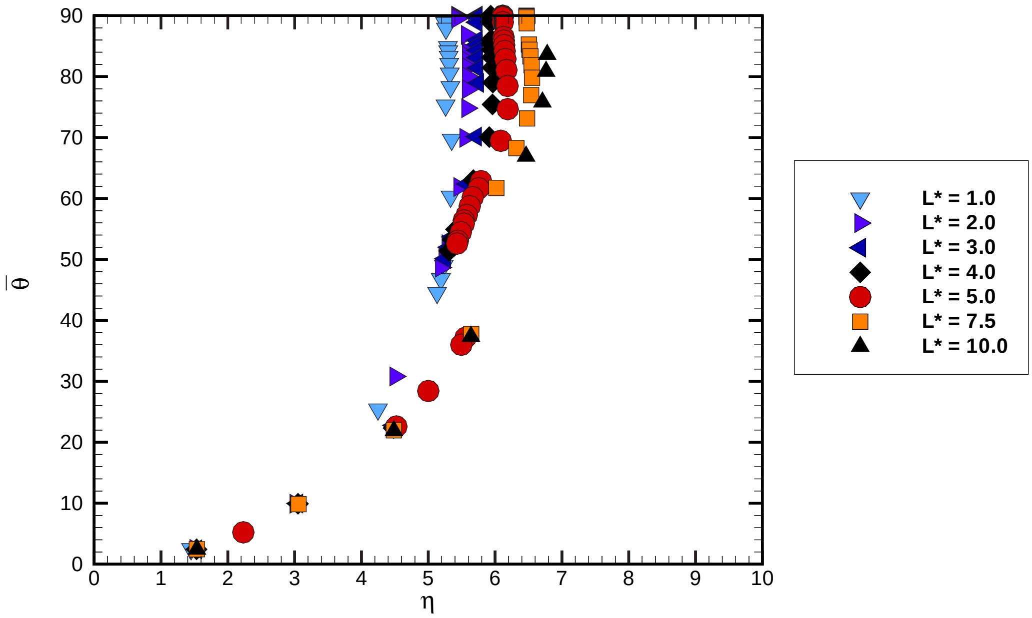

Figure 7.2: Mean layover angle as a function of η for $m^* = 0.2$ and $L^* = [1, 10]$

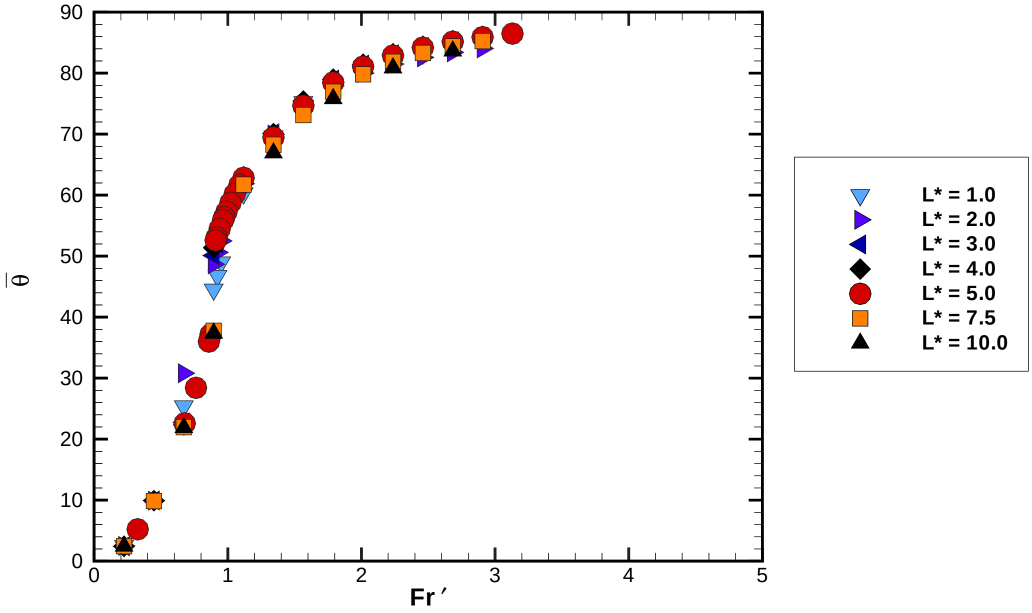

Figure 7.3: Mean layover angle as a function of the modified Froude number, Fr', for $m^* = 0.2$ and $L^* = [1, 10]$

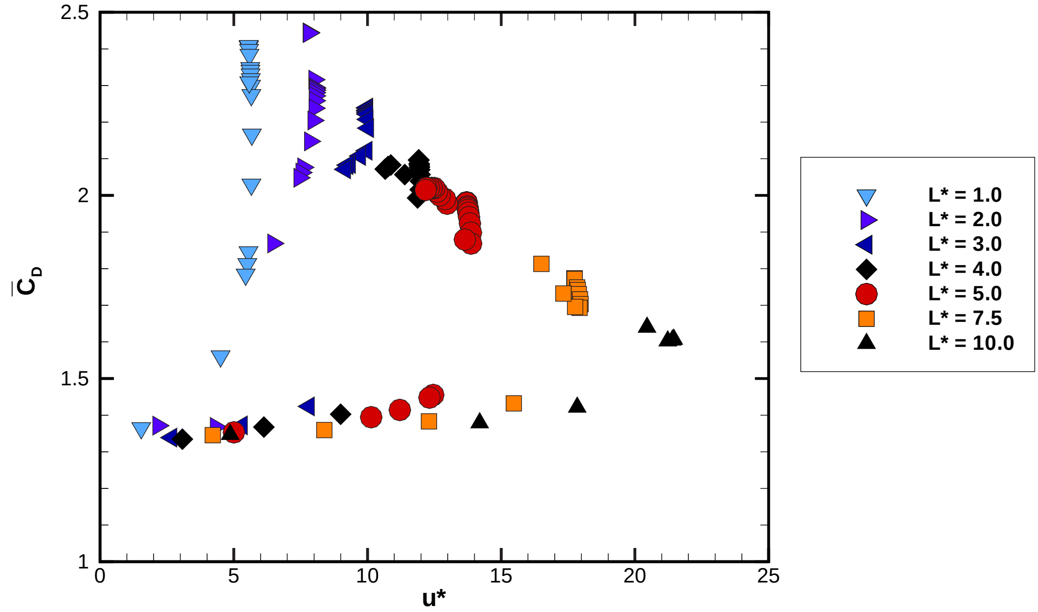

Figure 7.4: Mean drag coefficient as a function of reduced velocity for $m^* = 0.2$ and $L^* = [1, 10]$

the maximum amplitude of oscillation expected as a function of tether length. Figure 7.5 shows the maximum mean drag coefficient as a function of tether length for the range $L^* = [0.1, 10]$. For very small tether lengths ($L^* = [0.1, 0.3]$), the maximum mean drag coefficient is very small, remaining reasonably constant at $\overline{C_{D(max)}} = 1.4$. Comparing this value to the mean drag for a fixed cylinder, this represents only a 4% increase. It is therefore assumed that for these very small tether lengths (representing an internal pin), the maximum amplitude of oscillation is very small. This finding is verified in section 7.4.1. As the tether length is increased further ($L^* = [0.4, 1.0]$), $\overline{C_{D(max)}}$ increases rapidly with L^*.

A discontinuous change in the relationship between $\overline{C_{D(max)}}$ and L^* occurs as L^* increases from 1 to 2. For the range $L^* = [2, 10]$, the maximum mean drag decreases with L^* as:

$$\overline{C_{D(max)}} = 1.6071 \cdot e^{-0.127L^*} + 1.15, \tag{7.10}$$

with a coefficient of determination, $R^2 = 0.99$. In equation 7.10, the constant 1.15, is the mean drag coefficient calculated for a freely oscillating cylinder with $m^* = 0.2$ at $Re = 200$, for an infinite reduced velocity and no damping (see chapter 4). Equation 7.10 reveals that the maximum mean drag coefficient decreases with tether length, such that, for the case of $L^* \to \infty$, the mean drag response approaches the case of a freely oscillating cylinder with no damping and $u^* = \infty$.

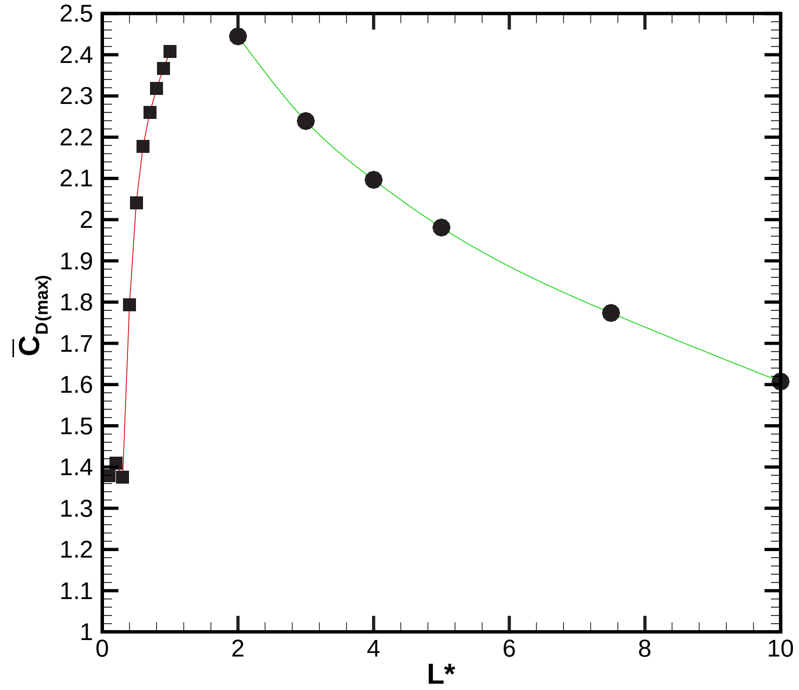

Figure 7.5: Maximum value of $\overline{C_D}$ as a function of L^* for $m^* = 0.2$.

The mean drag is plot against the mean layover angle in figure 7.6. For length ratios in the range $L^* = [3, 7.5]$, a local peak in the mean drag occurs for $\overline{\theta} \simeq 50 - 60^o$. As the mean layover angle is increased beyond this value, the mean drag decreases once more. At $\overline{\theta} \simeq 70 - 80^o$, a local minimum in $\overline{C_D}$ is observed, before the mean drag coefficient increases once more to reach a second maximum at $\overline{\theta} = 90^o$ (this being the maximum mean layover angle investigated). For $L^* = [1, 2]$ no local maximum is observed at $\overline{\theta} \simeq 50, 60$, and the value of $\overline{C_D}$ at $\overline{\theta} = 90^o$ represents the largest mean drag coefficient. When determining the maximum mean drag coefficient for $L^* < 1$ in figure 7.5, the trend that $\overline{C_D}$ at $\overline{\theta} = 90^o$ represents the largest mean drag coefficient was taken into consideration; for these tether length values, only very high Froude numbers (corresponding with $\overline{\theta} = 90^o$) were simulated.

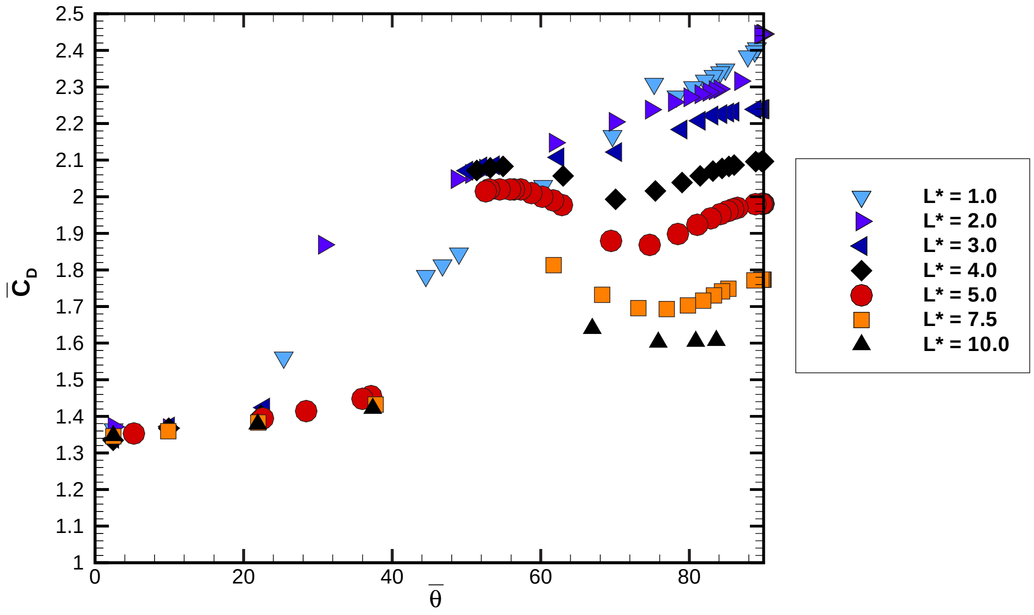

Figure 7.6: Mean drag coefficient as a function of mean layover angle for $m^* = 0.2$ and $L^* = [1, 10]$.

7.3.2 Mean Lift Coefficient

Figure 7.7 shows the mean lift coefficient as a function of Fr' for $L^* = [1, 10]$ and $m^* = 0.2$. As has been shown in the previous two chapters, a negative mean lift coefficient is noted for a majority of reduced velocities investigated. For all tether lengths investigated, there was a value of Fr' at which a local minimum in $\overline{C_L}$ was observed. The value of Fr' at which this local minimum is observed varies slightly with tether length, however it is always found in the range $Fr' = [0.8, 1]$. Interestingly, a very small *positive* mean lift coefficient was found for the case of $L^* = 1$ and 2 for $Fr' = [2, 10]$. This implies that for these two cases, there is a difference in the shedding process in this range of Fr' when compared to longer tether length cases with the same in-flow conditions. Section 7.6 analyzes the wake patterns as a function of tether length. It is found that the recording of a positive mean lift occurs in conjunction with a highly asymmetrical wake, for both cases of $L^* = 1.0$ and 2.0, as $\overline{\theta} \rightarrow 90^o$. It is believed that this small positive mean lift is due to the asymmetry of the shedding wake at these tether lengths. For higher values of Fr', corresponding to $\overline{\theta} \rightarrow 90^o$, the mean lift approaches zero for all tether lengths considered.

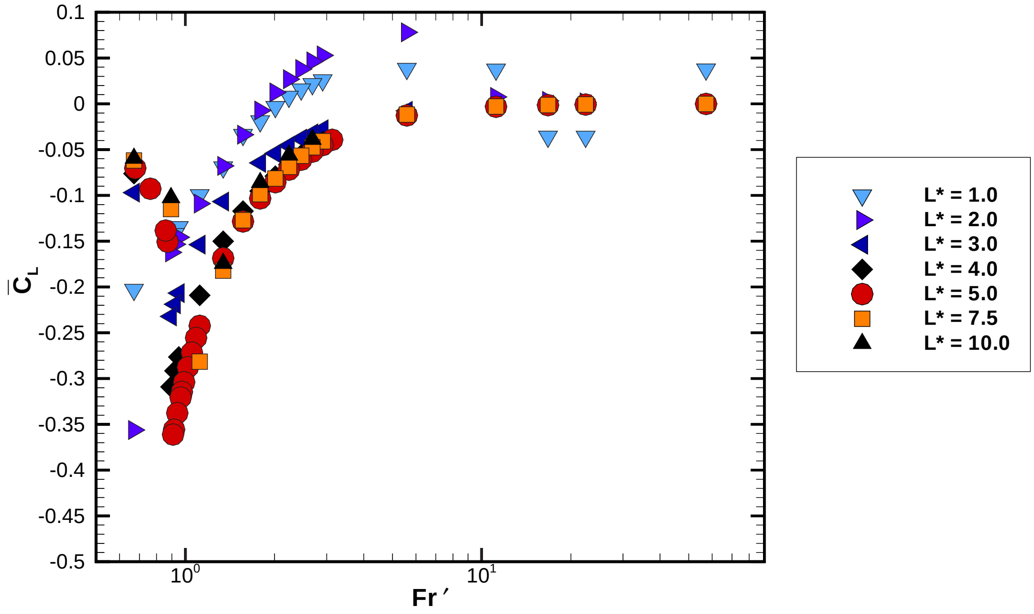

Figure 7.7: Mean lift coefficient as a function of the modified Froude number, Fr' for $m^* = 0.2$ and $L^* = [1, 10]$.

The mean lift coefficient is plotted against the mean layover angle in figure 7.8. From this figure it is clear that the local minimum in the mean lift occurs at $\overline{\theta} \simeq 50^o$ regardless of tether length, except for the particular case of $L^* = 1.0$. For the case of $L^* = 1.0$, a local minimum in $\overline{C_L}$ is observed at $\overline{\theta} \simeq 25^o$. This tether length was the shortest investigated over a range of $\overline{\theta}$. Simulation of smaller L^* tether lengths were only performed at $\overline{\theta} \simeq 90^o$, as for $m^* = 0.2$, they exhibited a maximum in the amplitude of oscillation at this layover angle.

In the range $L^* = [2.0, 5.0]$, the minimum $\overline{C_L}$ decreases linearly with increasing tether length:

$$\overline{C_L} = -0.0663L^* - 0.0335, \qquad (7.11)$$

with a coefficient of determination, $R^2 = 0.993$. Clearly, there must be an upper limit of L^* beyond $L^* = 5.0$, where this linear relationship no longer holds. However, for the present results, an insufficient number of simulations have been performed in the range $\overline{\theta} = [40, 70]$ for $L^* > 5.0$ to accurately determine the upper limit of L^* where equation 7.11 still holds.

In chapter 6, it was hypothesized that the negative mean lift coefficient could be due to a combination of the oscillation amplitude, and the angle between the flow direction

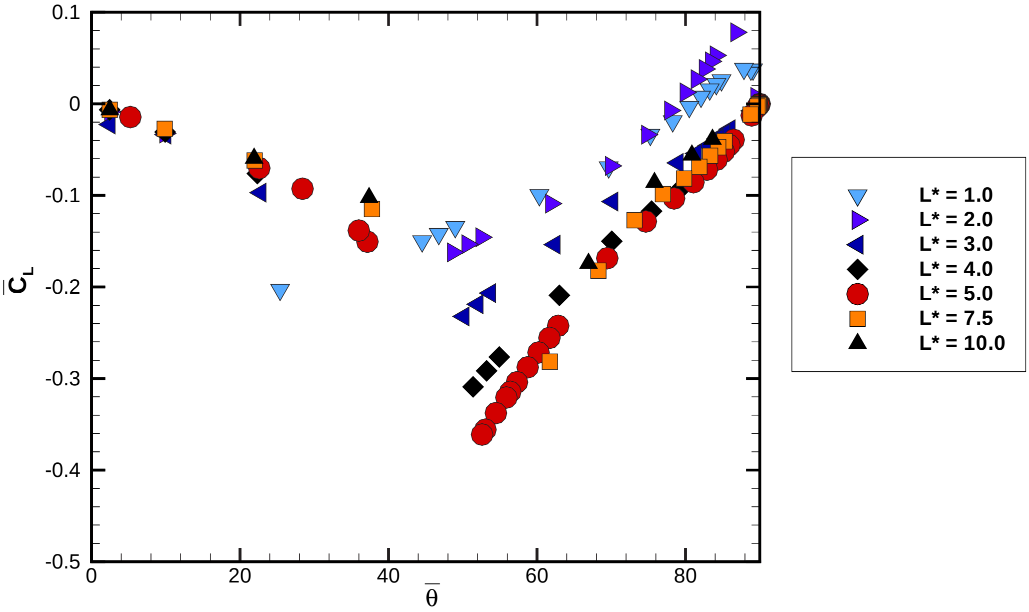

Figure 7.8: Mean lift coefficient as a function of the mean layover angle for $m^* = 0.2$ and $L^* = [1, 10]$.

and the cylinder motion. An alternative hypothesis is that it could be due to the imposed curvature on the motion of the cylinder by the tether. The observation that the local minimum in $\overline{C_L}$ occurs at $\overline{\theta} \simeq 50^o$, regardless of tether length in the range $L^* = [2.0, 5.0]$, lends weight to the first hypothesis. The variation in the minimum value of $\overline{C_L}$, as a function of L^* in the range $L^* = [2.0, 5.0]$, indicates a variation in the amplitude of oscillation in this range of L^*. This variation in amplitude is discussed in the next section.

7.4 Oscillation Results

7.4.1 Amplitude of Oscillation Results

Figure 7.9 shows the amplitude of oscillation, A^*, as a function of the modified Froude number, Fr', for tether lengths in the range $L^* = [1.0, 10.0]$ and $m^* = 0.2$. For all tether lengths investigated, a rapid increase in A^* was noted as Fr' was increased beyond $Fr' \simeq 1$. The dramatic increase in A^* as a function of Fr' corresponds to the rapid increase noted for $L^* = 5$ and $m^* < m^*_{crit}$ in chapter 6.

In chapter 6, for $m^* \leqslant m^*_{crit}$ and $L^* = 5.0$, the increase in A^* as a function of Fr was described as discontinuous. From figure 7.9, the increase in A^*, as a function

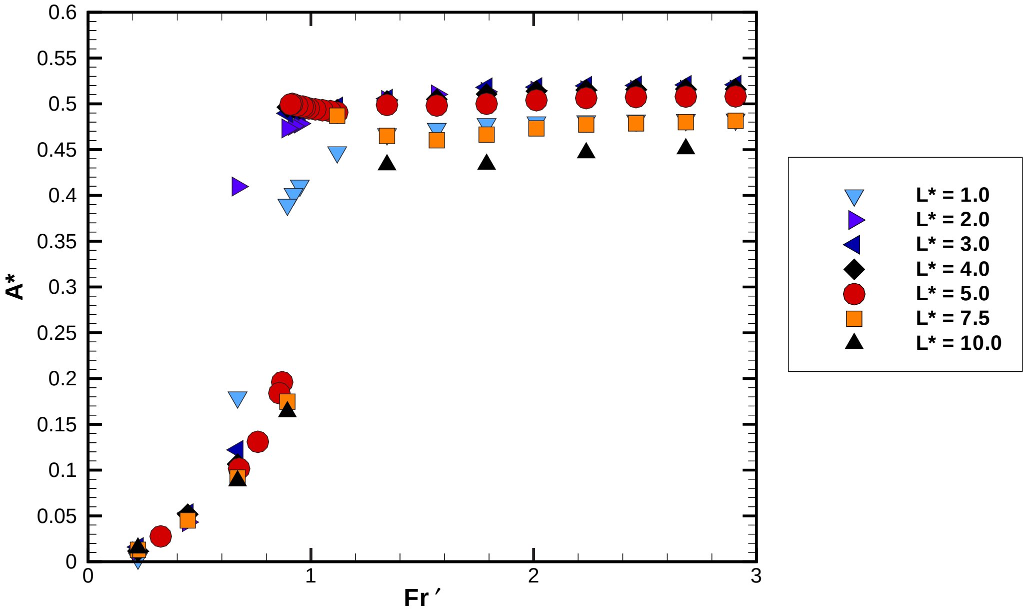

Figure 7.9: Amplitude of oscillation, in the direction of motion, as a function of the modified Froude number, Fr', for $m^* = 0.2$ and $L^* = [1, 10]$.

of Fr', is clearly discontinuous for $L^* = [3.0, 7.5]$. However, for $L^* = 1.0$ and 2.0, the amplitude increases rapidly but smoothly as a function of Fr'. For $L^* = 10.0$, there is insufficient resolution at $Fr' \simeq 1.0$ to determine if the jump is continuous or discontinuous. As will be shown in section 7.7, for $L^* = 10.0$, m^*_{crit} is very close to and possible marginally smaller than the case of $m^* = 0.2$ shown here. Should m^*_{crit} be less than 0.2 for $L^* = 10.0$, then the amplitude should increase smoothly, in a fashion similar to the case of $m^* = 0.4$ and $L^* = 5.0$ shown previously in section 6.4.

For $Fr' > 1.0$, the amplitude of oscillation quickly reaches a steady value invariant of further increases in Fr'. Once this invariant value is reached it is maintained up to and including the highest Fr' investigated (here $Fr'_{max} = 57$), and corresponds to the highest amplitude observed for the range of Fr' investigated. Of interest is that this maximum value of A^* varies only slightly with tether length. A high maximum amplitude is observed even at small tether lengths as low as $L^* = 1.0$. It is recognized that there must be a lower limit of L^* below which large amplitude oscillations are not observed.

To investigate how A^*_{max} varies with L^* for $L^* < 1.0$, several cases in the range $L^* = [0.1, 1]$ were investigated at $Fr = [5, 50]$, corresponding to $\overline{\theta} = [87^o, 89^o]$. In

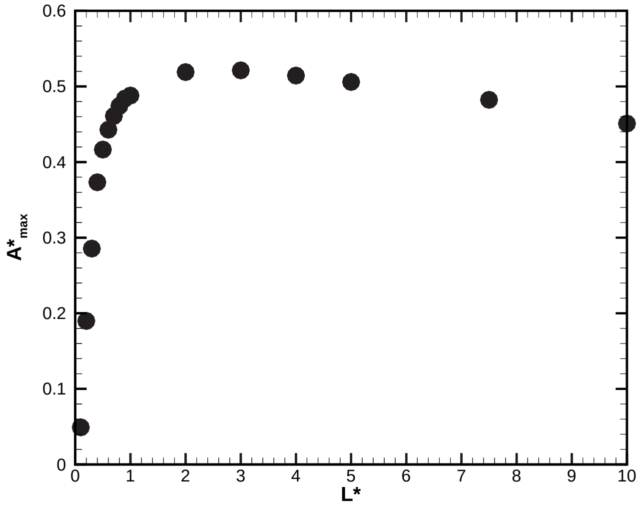

Figure 7.10: Maximum amplitude of oscillation, in the direction of motion, as a function of L^*, for $m^* = 0.2$.

this range of Froude numbers, for a given tether length, the amplitude of oscillations remains essentially constant with variation in amplitude of less than 5% for any given tether length investigated. It is believed (from the analysis of the cases of tether length $L^* > 1.0$) that this Froude number range should correspond to the highest amplitude of oscillation observed for these low tether lengths. The results are shown in figure 7.10. Two distinct regimes exist. In the first regime ($L^* = [0.1, 1.0]$), the amplitude of oscillation increases rapidly with tether length. For $L^* \geqslant 2.0$ (representing the second regime) the amplitude decreases slowly with increasing tether length. The maximum amplitude observed across all tether lengths investigated occurs at $L^* = 3.0$. Comparing figure 7.5 to figure 7.10, a similarity in the response of $\overline{C_{D(max)}}$ as a function of L^*, and A^*_{max} as a function of L^*, is observed. This supports the hypothesis that the mean drag coefficient may be related directly to the amplitude of oscillation, as discussed previously in section 5.4.

As with the maximum $\overline{C_D}$ response, the change in A^*_{max} response as a function of L^* in the range $L^* = [1, 2]$ indicates a possible change in the system response at a critical L^* within this transition range. In section 7.7, the calculated critical mass ratio as a function of L^* indicates that $m^*_{crit} \geqslant 1.0$ for $L^* \leqslant 1.23$. As shall be further discussed in section 7.6, the system response for $m^*_{crit} \geqslant 1.0$ is inherently different to that for $m^*_{crit} \leqslant 1.0$, and may explain why there is a change in response in the range

$L^* = [1, 2]$.

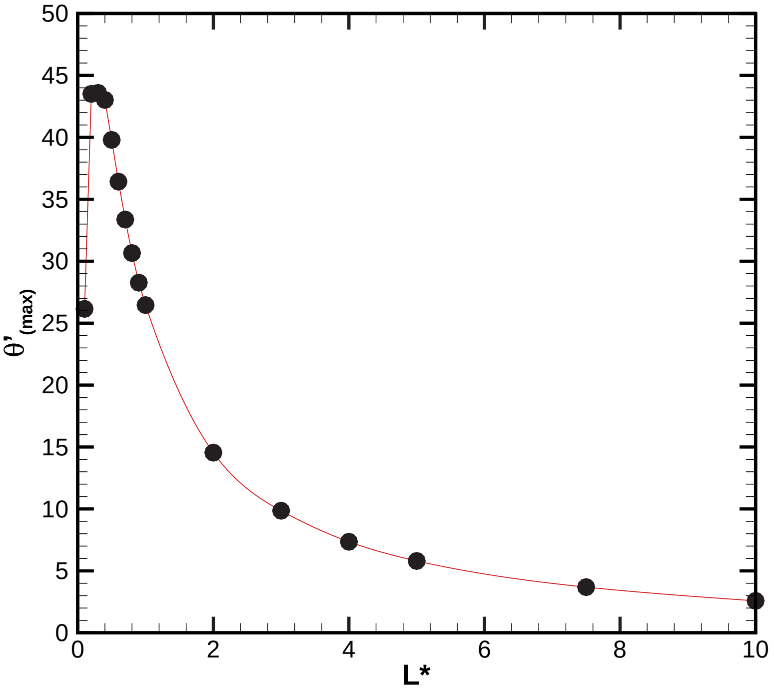

Figure 7.11: Maximum amplitude of oscillation, in polar coordinates, as a function of L^*, for $m^* = 0.2$.

Despite the linear amplitude being very small for small tether lengths (for example $A^*_{max} = 0.05$ for $L^* = 0.1$), the maximum polar amplitude of oscillation remains very high, even for the shortest tether length investigated in this study, as shown in figure 7.11. The highest maximum polar amplitude of oscillation, θ'_{max}, occurs at $L^* = 0.3$, with $\theta'_{max} = 43.6$ at this tether length. Recalling the definition of the polar moment of inertia, which is rewritten below:

$$J = m \cdot D^2(L^{*2} + 1/8), \tag{7.12}$$

we see that the tether length $L^* = 0.3$ corresponds to the critical value where $L^{*2} \simeq 1/8$. For tether lengths, $L^* < 0.3$, the critical scaling length in equation 7.3 is the cylinder diameter. For $L^* > 0.3$, the critical scaling length is the tether length. Therefore the case of $L^* = 0.3$ represents a critical case and this may explain why θ'_{max} has a local maximum at this tether length.

As discussed in section 5.2, in order to linearize the equations leading to the definition of u^* and the natural frequency of the tethered system, the terms $\sin\theta'$ and $\cos\theta'$ were replaced with θ' and 1 respectively. This linearization is only successful if θ' is small (for example, if $\theta' = 20^o$ the error induced by the linearization is about 6%). From figure 7.11, this implies that the linearization process in the determination of the natural frequency and the reduced velocity is invalid for $L^* \lesssim 1$. The natural frequency and reduced velocity calculated for these tether lengths have errors inherent in their calculation.

Finally, figure 7.12 shows the amplitude of oscillation, A^*, as a function of mean layover angle for $L^* = [1, 10]$ and $m^* = 0.2$. The amplitude of oscillation remains reasonably constant at $A^* \simeq [0.4, 0.5]$ for $\overline{\theta} = [50, 60]$, for all tether lengths investigated. As has been mentioned, while a distinct increase in A^* is noted for $L^* = [1.0, 2.0]$, it is distinguished from larger tether length cases as this increase in A^* is smooth.

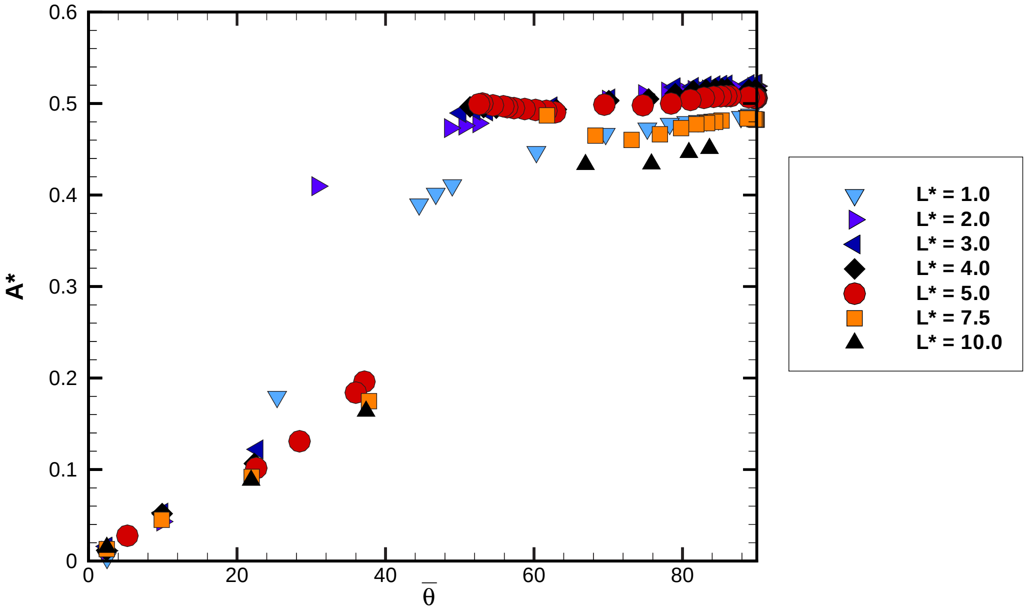

Figure 7.12: Amplitude of oscillation, in the direction of motion, as a function of the mean layover angle, for $m^* = 0.2$ and $L^* = [1, 10]$.

7.4.2 RMS Force Coefficients results

The RMS drag coefficient is plotted as a function of Fr' in figure 7.13, for $L^* = [1, 10]$ and $m^* = 0.2$. A jump in $C_{D(RMS)}$ is noted for $Fr' = 1.0$ for all tether lengths investigated. For $L^* = 1.0$ and $L^* = 2.0$, the increase in $C_{D(RMS)}$ as a function of

Fr' is smooth (as is expected given the previous results) and increases slowly with increasing Fr' beyond $Fr' = 1$. The rate of increase of $C_{D(RMS)}$ as a function of Fr' is greater for $L^* = 1.0$ than for $L^* = 2.0$. For $L^* = 3.0$, $C_{D(RMS)}$ has a discontinuous increase at $Fr' \simeq 1.0$. At slightly higher Fr', the RMS drag coefficient decreases before reaching a value independent of further increases of Fr'. Tethered cylinders with longer tether lengths experience the same phenomenon as for $L^* = 3.0$, however the value of $C_{D(RMS)}$ at high Fr' decreases as a function of L^*.

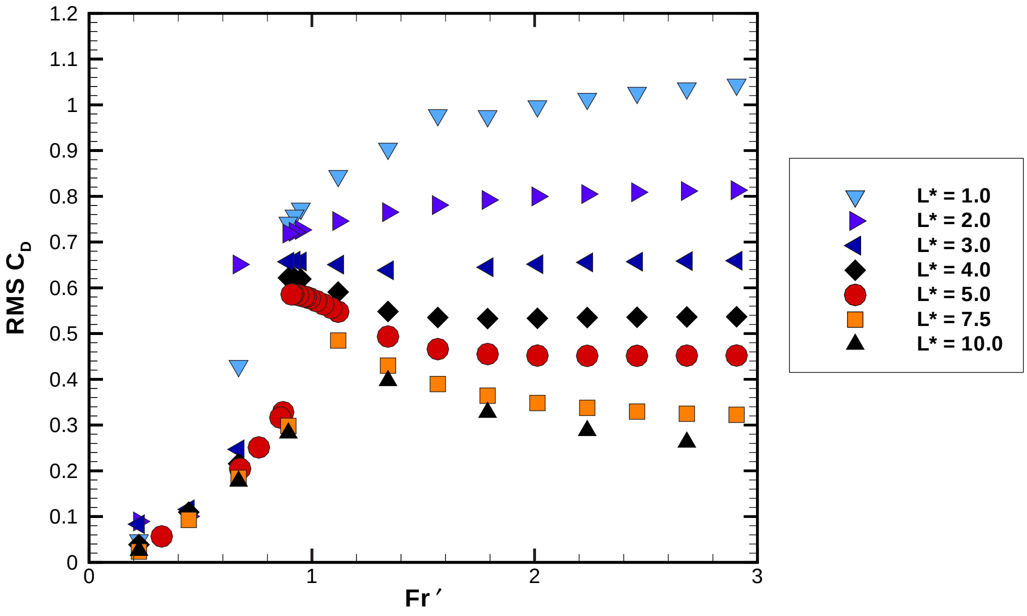

Figure 7.13: RMS drag coefficient as a function of the modified Froude number, Fr', for $m^* = 0.2$ and $L^* = [1, 10]$.

The RMS drag coefficient is plotted as a function of $\overline{\theta}$ in figure 7.14. For $L^* \gtrsim 3.0$, the jump in $C_{D(RMS)}$ appears to coincide with the jump in $\overline{\theta}$ noted in section 7.2. The constant value of $C_{D(RMS)}$ at high Fr' noted for $L^* \geqslant 3$ corresponds to the constant value of $C_{D(RMS)}$ observed at $\overline{\theta} \rightarrow 90^o$ in figure 7.14. The range of $\overline{\theta}$ over which this constant value of $C_{D(RMS)}$ occurs appears to decrease with increasing L^*.

The RMS lift coefficient is plot as a function of Fr' in figure 7.15, for $L^* = [1, 10]$ and $m^* = 0.2$. For $L^* = 1.0$ and $L^* = 2.0$, $C_{L(RMS)}$ increases smoothly as a function of Fr' over the range investigated. For both these values of L^*, $C_{L(RMS)}$ exhibits a local maximum at $Fr' \simeq 0.8$ before asymptotically decreasing to a constant value of $C_{L(RMS)}$at higher Fr'. For $L^* \geqslant 3$, the $C_{L(RMS)}$ collapse onto one line when plotted

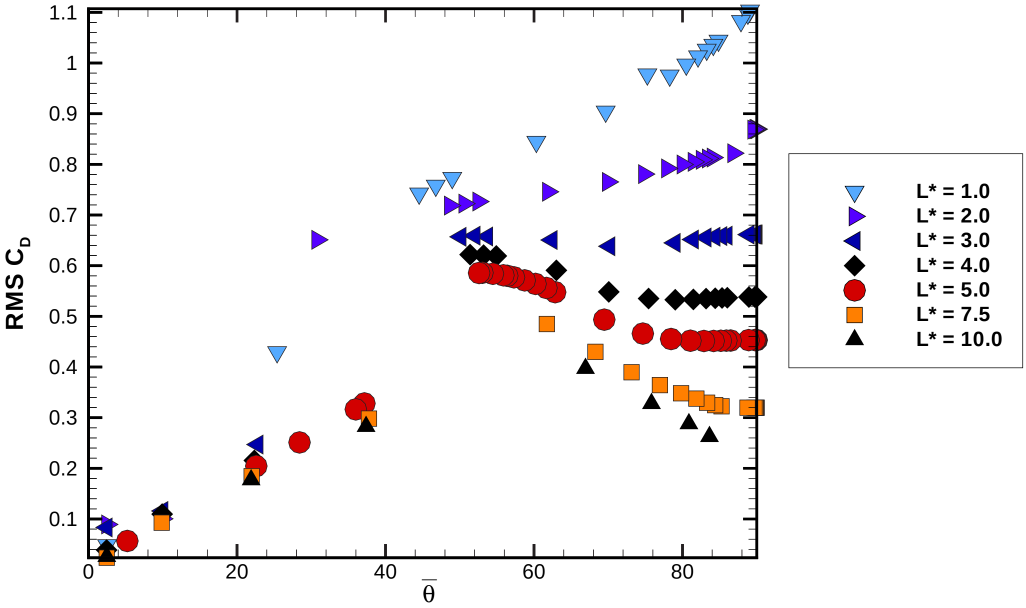

Figure 7.14: RMS drag coefficient as a function of the mean layover angle, for $m^* = 0.2$ and $L^* = [1, 10]$.

against Fr'. A jump is noted for all $L^* \geqslant 3$ at $Fr' \simeq 1.0$ before $C_{L(RMS)}$ asymptotically decreases to a constant value.

The fact that $C_{L(RMS)}$ collapses onto one line regardless of L^* for $L^* \geqslant 3$ indicates that $C_{L(RMS)}$ should also collapse as a function of $\overline{\theta}$. This is indeed the case, as shown in figure 7.16. The fact that $C_{L(RMS)}$ collapses as a function of $\overline{\theta}$ regardless of tether length for $L^* = [3, 10]$ indicates that it is purely a function of the angle to the mean flow field at which the cylinder oscillates. By contrast, as no collapse of $C_{L(RMS)}$ is predicted for $L^* < 3.0$; for these tether lengths, the induced curvature on the motion of the cylinder begins to alter the shedding structures in the wake. The form of the shed vortices in the wake is shown in section 7.6 to be a function of tether length.

7.5 Frequency Analysis

For each tether length investigated, the time trace of the cylinder displacement was sinusoidal, regardless of Froude number. Therefore, the change in character of the oscillation response may be described in entirety by analysis of the amplitude and frequency of oscillation.

The ratio of the frequency of shedding (f) to the natural frequency of the tethered

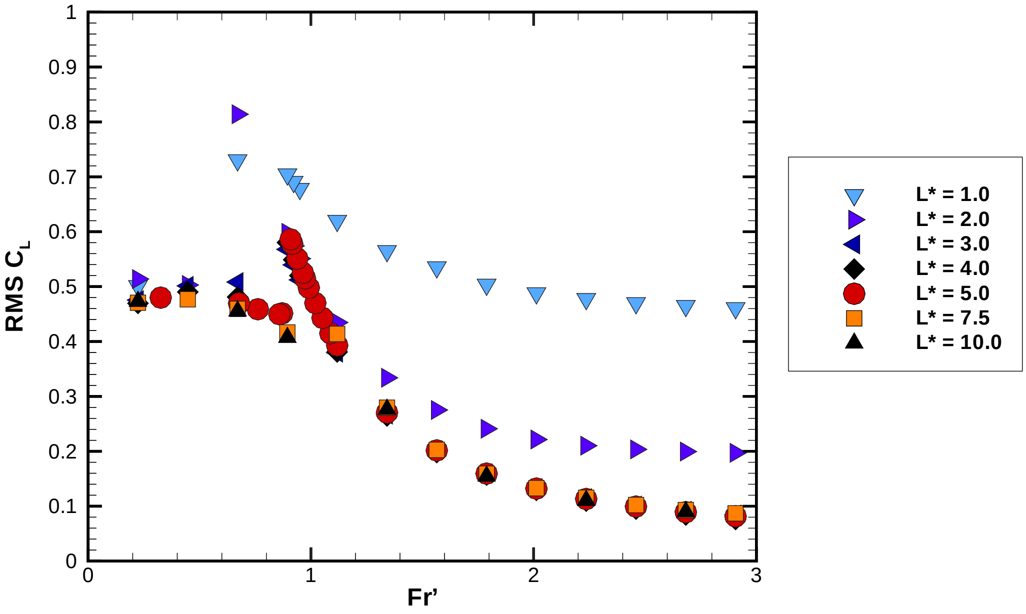

Figure 7.15: RMS lift coefficient as a function of the modified Froude number, Fr', for $m^* = 0.2$ and $L^* = [1, 10]$.

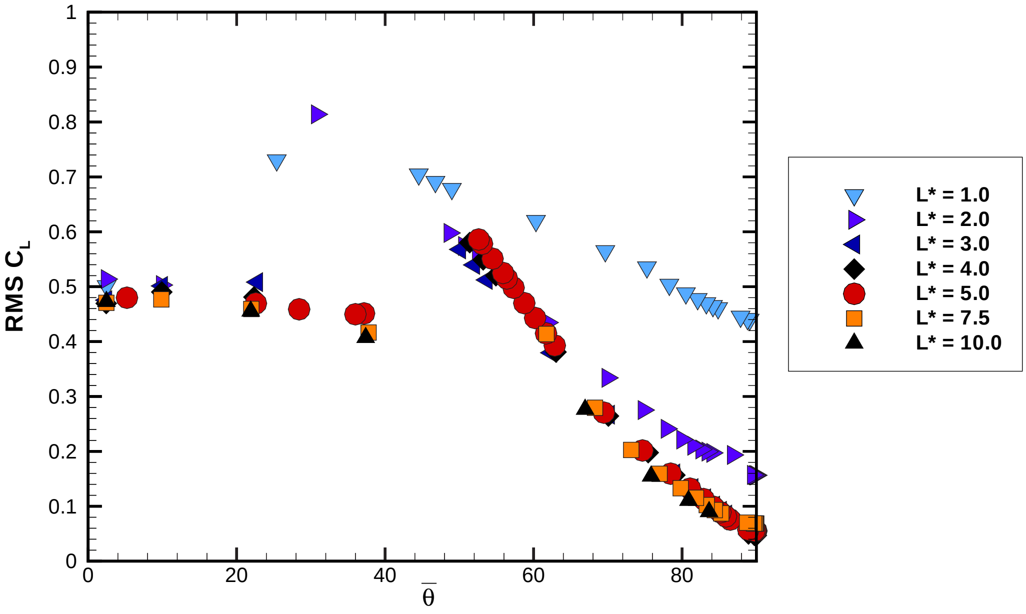

Figure 7.16: RMS lift coefficient as a function of the mean layover angle, for $m^* = 0.2$ and $L^* = [1, 10]$.

system (f_n), is shown as a function of tether length for $L^* = [0.1, 1]$ in figure 7.17. In each case the largest value of f/f_n coincides with the largest Froude number investigated ($Fr = 50$ for each case, corresponding to $\overline{\theta} \simeq 90^o$). For $L^* < 2$, the calculation of f_n is approximate, as $\theta' \geqslant 20^o$ (as discussed in section 7.4.1).

As the largest value of Fr corresponds to both the largest amplitude of oscillation and the largest value of f/f_n, it is the maximum value of f/f_n that is of interest when analyzing figure 7.17.

$f/f_{n(max)}$ has a local minimum at $L^* = 0.3$, coinciding to where $L^{*2} = 1/8$. For all tether lengths in the range $L^* = [0.2, 1.0]$, the maximum value of f/f_n approaches 1. As shown in the next section, it is these tether lengths which experience a different wake state, when compared to longer tether length results.

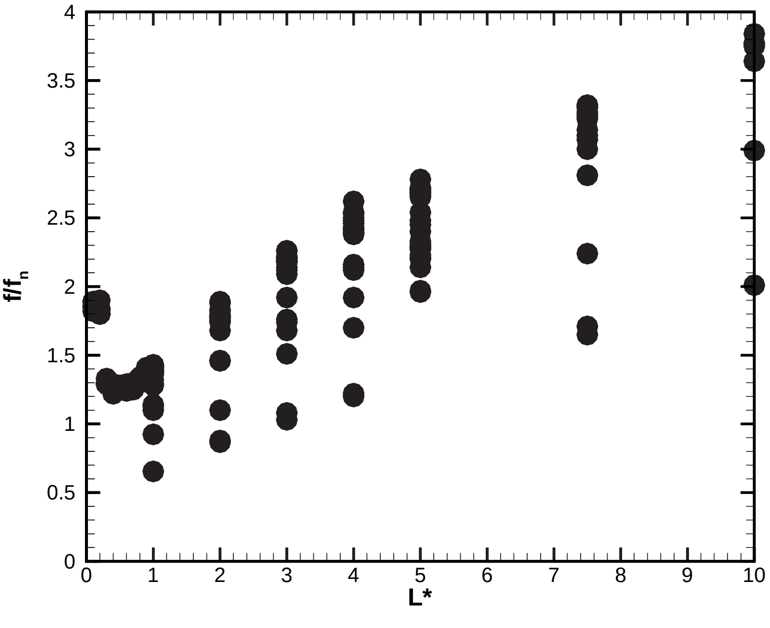

Figure 7.17: Frequency ratio, f/f_n, where f is the oscillation frequency, and f_n is the natural frequency of the tethered cylinder system; as a function of tether length for $m^* = 0.2$

7.6 The Effect of Tether Length on Vortex Structures in the Wake

Snapshots of the vortex structures in the wake of the tethered cylinder are shown in figures 7.18, 7.19 and 7.20 for a range of tether lengths, $L^* = [0.1, 10]$. In each image, the cylinder is at the top of its oscillation cycle and is instantaneously stationary. For each case, $m^* = 0.2$ and the Froude number chosen was $Fr = 50$, corresponding to $\overline{\theta} \simeq 90^o$. Because $\overline{\theta} \simeq 90^o$, the oscillations are symmetric about the cylinders mean position and, from figure 7.8, the mean lift approaches zero for all cases investigated. This mean layover angle was chosen so that the effect of L^* could be analyzed without the complications induced by a finite mean lift coefficient and the accompanying vortex pairing in the wake and mean angle at which the wake is shed.

For $L^* = 0.1$, the vortex structures observed are not dissimilar to the Karman vortex street observed in the wake of a fixed cylinder. This is not surprising given that the amplitude of oscillation is very small ($A^* = 0.05$, $\theta' = 28^o$) and is not expected to affect the shedding process appreciably.

As the tether length is increased to $L^* = 0.3$, the vortex structures in the wake are considerably different to the case of $L^* = 0.1$. In this snapshot, the positive shedding vortex core is shed at a considerable angle to the flow direction. Downstream, the negative and positive vortex cores coalesce to form two distinct shear layers. This 'double' shear layer becomes unstable at about fifteen diameters downstream. Beyond this instability point, the shear layer rolls up in the form of a Karman vortex street of lower frequency. The vortex structures in this Karman wake are considerably larger than the structures shed from the cylinder for either the case of a fixed cylinder or for the case with $L^* = 0.1$. The transition of the double shear layer occurs very close to the outlet. It is left for future studies to determine the effect (if any) of the location of the outlet on the wake structures and the position of the double shear layer instability. The double shear layer is similar to that observed by Dusek *et al.* (1994), who observed this vortex structure in the wake of a circular cylinder in the range $Re = [50, 300]$. They found that the local shedding vortex core is strained by surrounding vortices into an elliptical cross-section. They further found that this elliptical vortex core rotates due to self-induced velocities such that it's major axis is in-line with the flow field. As the vortices convect downstream, consecutive vortices of the same sign form a continuous shear layer. Further downstream, they noted that the double shear layer becomes unstable and gives rise to a secondary vortex street with a lower shedding frequency. The present findings are in agreement with these findings.

As the tether length is further increased to $L^* = 0.5$, representing the case where the cylinder is pivoting about a point on its surface, the shear structures are observed to continue all the way to the outlet. When compared to the case of $L^* = 0.1$ and 0.3, a subtle difference in the vortex structures is observed, in the vicinity of the cylinder. For the case of $L^* = 0.5$, the forming negative vortex structure is between the cylinder and the newly shed positive vortex structure. The shed positive vortex structure has a very weak 'arm' of positive vorticity which is entrained around and above the recently shed negative vortex core. The resulting wake is significantly wider than for the case of either $L^* = 0.1$ or $L^* = 0.3$. It is hypothesized that the increase in $\overline{C_D}$ as a function of L^* in this range may be directly attributed to the increase in wake width as a function of L^* in the same range.

Figure 7.19(a) shows a snapshot of the vortex structures for $L^* = 1.0$. The wake appears to be wider than for the shorter tether lengths discussed above. As with $L^* = 0.5$, a component of positive vorticity is stretched around and above the newly shed negative vortex core. Further downstream (at about seven diameters downstream), a very weak positive vortex core is observed above the negative vortex core. This would provide a very weak thrust in the negative y direction. As for $L^* = 0.2$, 0.3 and 0.5, the wake reverts to a double shear layer which remains up to and including the outlet boundary. Towards the outlet, the width of the wake is observed to reduce slightly.

As the tether length is increased to $L^* = 1.5$ (figure 7.19(b)), a significant change in the wake is observed when compared to the case of $L^* < 1.5$. As with $L^* = 0.5$ and 1.0, a component of positive vorticity is observed above the negative vortex cores and the wake appears to have a 'P+S' structure as described by Williamson & Roshko (1988) and observed by Blackburn & Henderson (1999) for the case of a freely oscillating cylinder at low Reynolds numbers. In agreement with the current findings (see section 7.3.2), Blackburn & Henderson (1999) report a very small mean positive lift for this wake structure. The small positive vortex cores above the negative vortex cores convect downstream faster than the negative vortex cores, and therefore appear to skip the third negative vortex core in this snapshot. No shear structure is observed in this case, however, towards the outlet, the wake appears to form a secondary Karman vortex street in a fashion similar to the case where $L^* = 0.3$.

For a tether length, $L^* = 2.0$, the wake appears to commence shedding in a fashion similar to a Karman vortex wake observed in the wake of a stationary cylinder. However, roughly seven diameters downstream, the wake reverts to a double shear layer. The double shear layer in turn becomes unstable seventeen diameters downstream. The double shear layer is more complicated than that found for $L^* = [0.3, 1.0]$. From seventeen diameters downstream up to the outlet, the wake appears to form a secondary Karman vortex street.

For $L^* = 5.0$ and $L^* = 10.0$ (figure 7.20), the formation length is considerably greater than for shorter tether lengths and appears to increase with tether length. For both these cases the wake has reverted to a reasonably 'standard' Karman wake, as would be observed for the wake of a stationary cylinder. However, for the case of $L^* = 5.0$, an instability appears to exist about 20 to 25 diameters downstream of the cylinder.

7.6.1 The Vortex Shedding Process for $L^* = 0.5$

In the previous section, for $L^* = [0.3, 2.0]$, a 'double' shear layer has been noted with vortex structures in the wake which are significantly different to that observed in the wake of stationary cylinder. This section analyzes the interaction between the flow field and the oscillating cylinder which results in the formation of these structures. While it is recognized that the wake structures and the moving cylinder form a coupled system, as with section 6.6, this section will describe the flow from the perspective of the influence of the cylinder motion on the formation and propagation of fluid structures in the wake. However, it should be recognized that the wake structures have a feedback effect on the subsequent motion of the cylinder.

This section concentrates on the case of $L^* = 0.5$ and $m^* = 0.2$. Specifically, snapshots of the vortex shedding cycle will be investigated for the case of $Fr = 50$, corresponding to $\overline{\theta} \simeq 90^o$. This Froude number was chosen so that the vortex shedding process resulting in the 'double' shear layer could be analyzed without the complication of the cylinder oscillating at an angle $\overline{\theta} < 90^o$ to the free-stream. Analysis in section 6.6 showed that the case of the cylinder oscillating at an inclined angle to the free-stream induces a non-zero mean lift, and vortex pairing in the wake.

While, in the present study, the case of the double shear layer formation only appears to occur for a very small range of L^* and only one value of $\overline{\theta}$, it has also been noted to occur for low Reynolds number simulations of a freely oscillating cylinder, restricted to oscillate transverse to the flow field (private communications, Justin Leontini). Similar vortex structures have been noted in the wake of a stationary elliptic cylinder (for example see Johnson *et al.* (2001)), and for the flow around a thin flat plate, placed

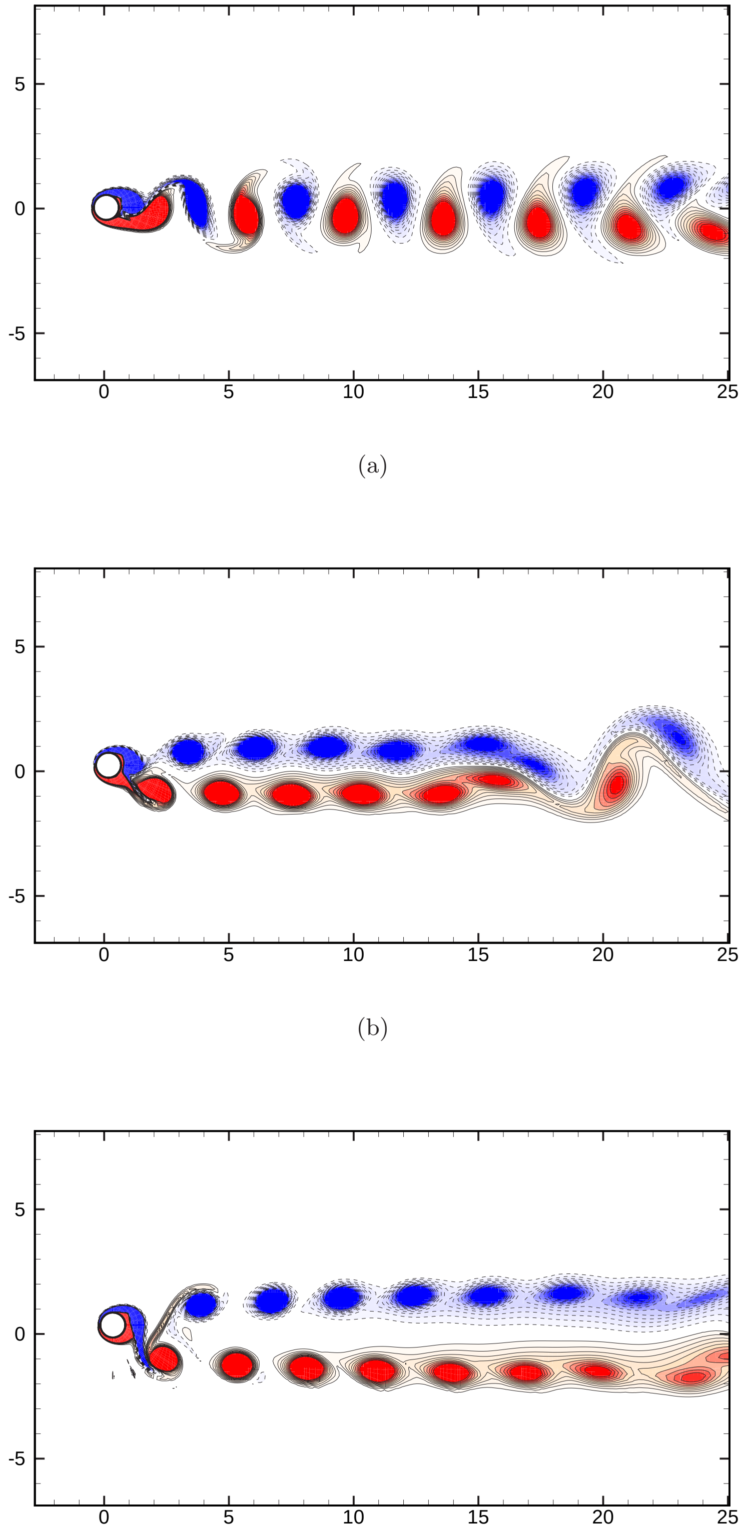

(a)

(b)

(c)

Figure 7.18: Instantaneous snapshots of the span-wise vorticity field, ω_z, as a function of tether length. Contours are evenly spaced over the range (blue) $-1 \leqslant \omega_z \leqslant 1$ (red). All images are at the instant when the cylinder reaches the top of the oscillation cycle; (a) $L^* = 0.1$; (b) $L^* = 0.3$; (c) $L^* = 0.5$.

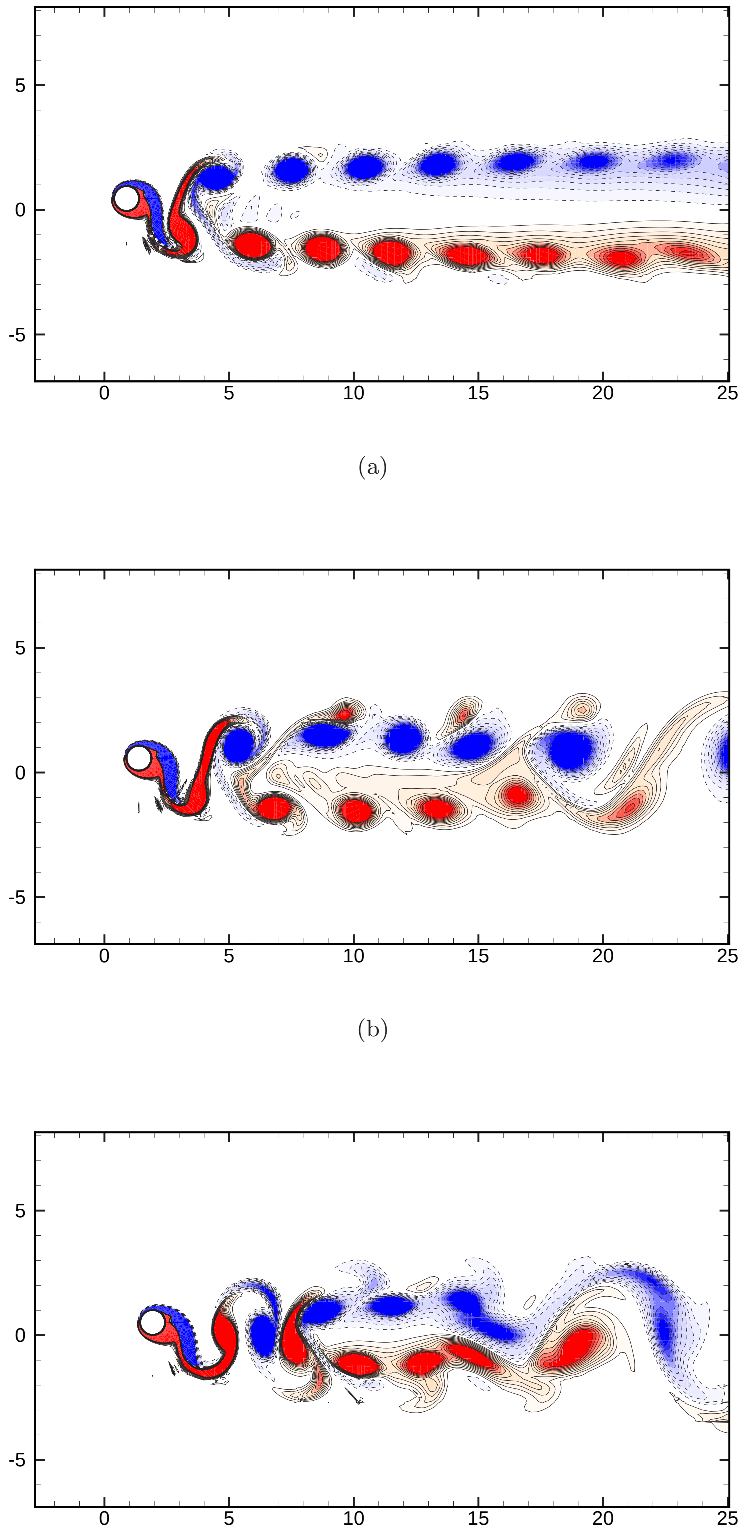

(a)

(b)

(c)

Figure 7.19: Instantaneous snapshots of the span-wise vorticity field, ω_z, as a function of tether length. Contours are evenly spaced over the range (blue) $-1 \leqslant \omega_z \leqslant 1$ (red). All images are at the instant when the cylinder reaches the top of the oscillation cycle; (a) $L^* = 1.0$; (b) $L^* = 1.5$; (c) $L^* = 2.0$.

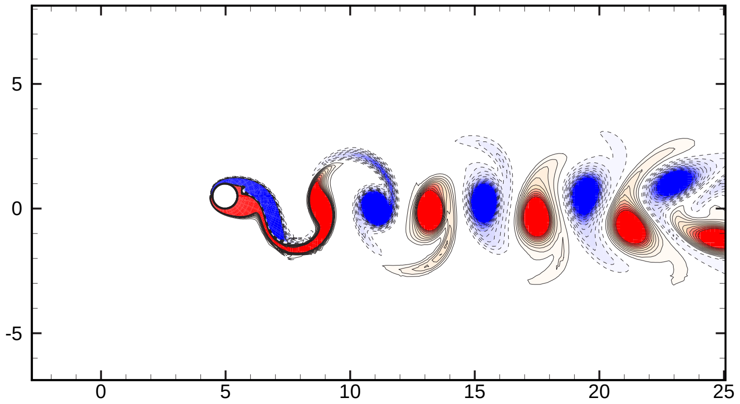

(a)

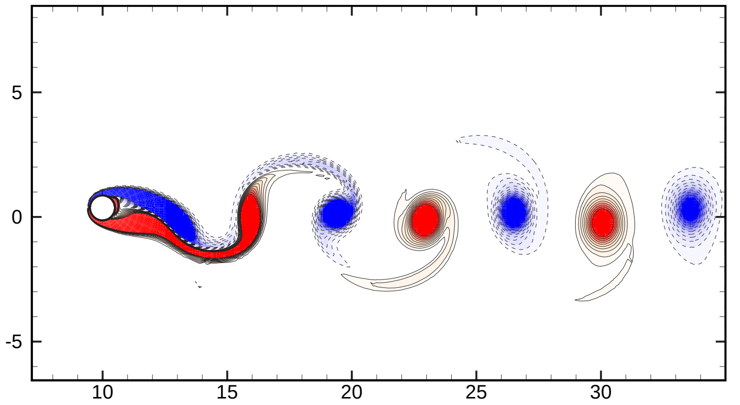

(b)

Figure 7.20: Instantaneous snapshots of the span-wise vorticity field, ω_z, as a function of tether length. Contours are evenly spaced over the range (blue) $-1 \leqslant \omega_z \leqslant 1$ (red). All images are at the instant when the cylinder reaches the top of the oscillation cycle; (a) $L^* = 5.0$; (b) $L^* = 10.0$.

normal to the flow field (Najjar & Balachandar (1997)).

Figures 7.21 to 7.24 show closeup snapshots of vorticity in the wake at quarter cycle intervals. Figure 7.21 shows the shedding structures, taken for the case of the cylinder moving midway between the bottom position and top position of the oscillation cycle. The cylinder is instantaneously moving both upstream and in the positive y direction. At this instant, a positive vortex is being shed, and a negative vortex core is forming adjacent to the cylinder. Both the shed positive vortex core and the forming negative vortex structures are located at an angle with the free stream direction of 30^0, where measurements are taken from the rear stagnation point. The instantaneous streamlines indicate that the motion of the cylinder is in the positive y direction. This transverse component of motion acts to move the negative vortex core in the negative y direction, and a jet structure is observed between the two vortices. The jet is travelling in the negative y direction. The cylinder motion in the upstream direction appears to have a minimal effect on the vortex structures, however it may act to intensify the negative vortex structure, with a resultant effect that the jet between the two vortex structures is intensified.

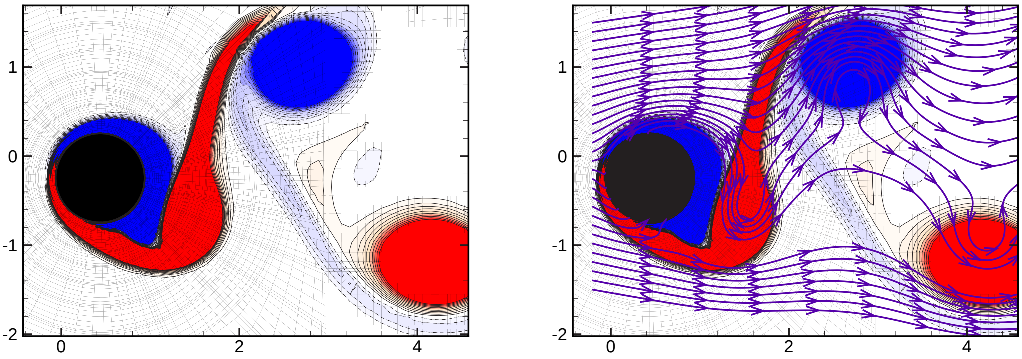

Figure 7.21: Instantaneous snapshots of the span-wise vorticity field, ω_z, for $m^* = 0.2$, $L^* = 0.5$ and $Fr = 50$, for the cylinder moving between the top of the oscillation cycle and the bottom of the oscillation cycle. Contours are evenly spaced over the range (blue) $-1 \leqslant \omega_z \leqslant 1$ (red).

Figure 7.22 shows the instantaneous vortex structures a quarter of a cycle later. The cylinder is at the top of its cycle (i.e. the most counter-clockwise position) and, at this instant, is stationary. Here the positive vortex has shed and is convecting downstream, and the negative vortex structure has just shed from the cylinder. The jet which formed between the positive and negative vortex structures a quarter of a cycle earlier has now acted to draw a component of the negative vortex structure away from the cylinder, in the negative y direction. This elongated structure wraps around the newly shed positive vortex core. Analysis of the instantaneous streamlines shows the jet between the positive and negative vortex structures still exists and acts to propel the positive vortex in the negative y direction, increasing the width of the wake when compared to the wake shed from a stationary cylinder.

In figure 7.23 the cylinder is midway between the top and bottom of the cycle, and

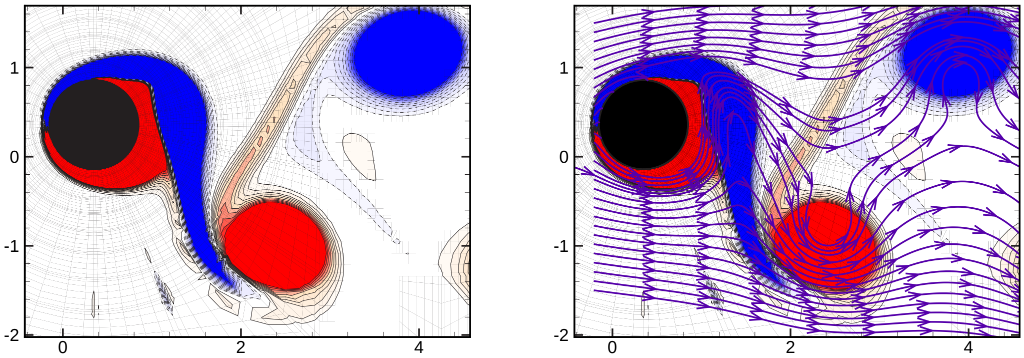

Figure 7.22: Instantaneous snapshots of the span-wise vorticity field, ω_z, for $m^* = 0.2$, $L^* = 0.5$ and $Fr = 50$, for the cylinder at the top of the oscillation cycle. Contours are evenly spaced over the range (blue) $-1 \leqslant \omega_z \leqslant 1$ (red).

is moving downstream and in the negative y direction. The positive vortex continues to convect downstream and in the negative y direction. The jet between the component of negative vorticity wrapped around the positive vortex core, retains a very strong component of velocity in the negative y direction. The negative vortex core has shed away from the cylinder and is beginning to convect downstream, and in the positive y direction. In this snapshot, the negative vortex now has two distinct regions, the negative vortex core which has just shed, and the 'tongue' of negative vorticity wrapped around the positive vortex as a result of the jet. The flow field appears to be a mirror image of that described in figure 7.21.

In figure 7.24, the cylinder is at the bottom of its oscillation cycle and is instantaneously stationary. Both the negative and positive vortex cores have convected downstream, and the negative vortex structure which is wrapped around the positive vortex core has weakened significantly. Without the induced jet between the positive vortex core and this negative vortex structure, the motion of the positive core in the negative y direction is diminished, and the wake width remains relatively constant further downstream. Analysis of figure 7.24 reveals that, further downstream, adjacent vortices of the same sign merge, to form the double shear layer described earlier.

Returning briefly to figure 7.22, and comparing this image to figure 7.24, it is clear that the shedding cycle is symmetric about the mean position of the cylinder.

In summary, the transverse component of motion of the cylinder as it moves from the bottom to the top of the oscillation cycle acts to move the forming negative vortex

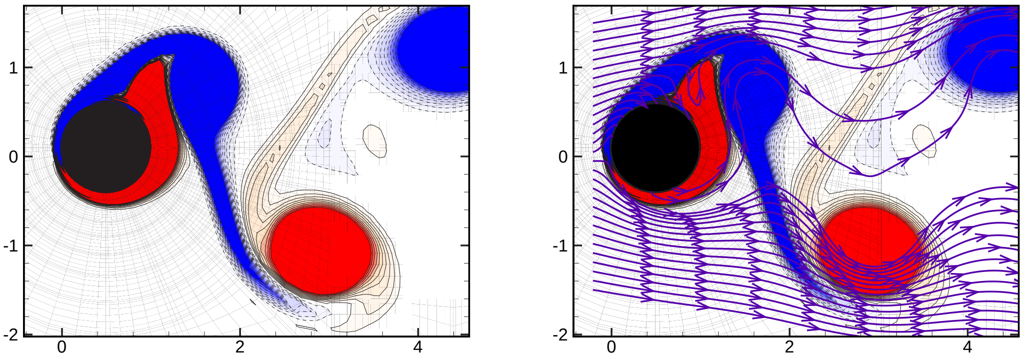

Figure 7.23: Instantaneous snapshots of the span-wise vorticity field, ω_z, for $m^* = 0.2$, $L^* = 0.5$ and $Fr = 50$, for the cylinder moving between the bottom of the oscillation cycle and the top of the oscillation cycle. Contours are evenly spaced over the range (blue) $-1 \leqslant \omega_z \leqslant 1$ (red).

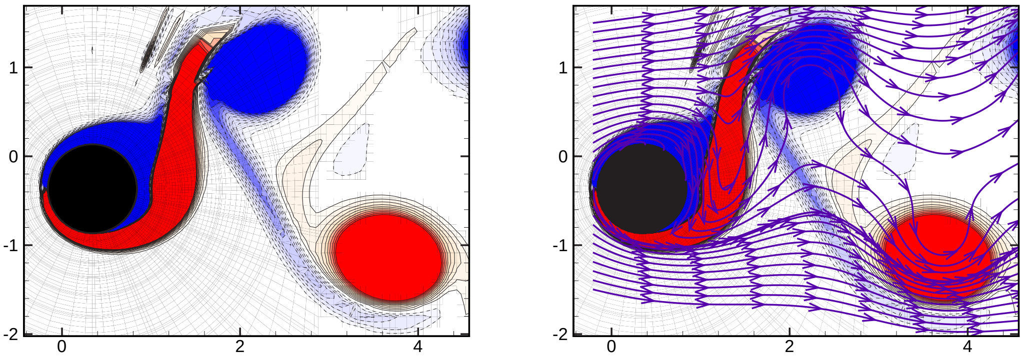

Figure 7.24: Instantaneous snapshots of the span-wise vorticity field, ω_z, for $m^* = 0.2$, $L^* = 0.5$ and $Fr = 50$, for the cylinder at the bottom of the oscillation cycle. Contours are evenly spaced over the range (blue) $-1 \leqslant \omega_z \leqslant 1$ (red).

across to the bottom rear surface of the cylinder. This induces a jet between the forming negative vortex and the newly shed positive vortex. As the cylinder reaches the top of its cycle, the positive vortex core has convected slightly downstream, and has entrained an elongated negative vortex region, which wraps around the vortex core. Between the positive vortex core and the negative vortex region, a jet is induced, with velocity components in the negative y and downstream direction. This jet acts to convect the positive vortex core in the negative y direction. These findings are in broad agreement with the findings of Dusek *et al.* (1994). From this analysis, the following hypothesis may be formed:

> “The double shear layer wake is formed due to the motion of the cylinder moving the forming vortex region from one side of the wake to the other and increasing the lateral spacing of vortex structures.”

It is further hypothesized that the same mechanism creates the double shear layer wake observed numerically for the case of a freely oscillating cylinder confined to oscillate transverse to the flow field at low Reynolds numbers by Justin Leontini (private communication). However, it is left for future studies to provide supporting evidence for this conjecture.

It is noted that there is a similarity between the near wake structure of the double shear layer described here, and the $2P$ mode described by Williamson & Roshko (1988) among others. For example, the wrapping of the highly strained negative vortex structure around the positive vortex core of opposite sign may allow a small negative vortex core to detach from the highly strained region and convect with the positive vortex core downstream. This is indeed evident on one side of the wake for $L^* = 1.5$. Whether the double shear layer mode is a low Reynolds number form of $2P$ shedding is left for future studies.

Finally, referring back to figure 7.17, it is noted that the double shear layer wake only occurs when the ratio of $f/f_n \to 1$. That is, the natural frequency of the tethered system must coincide closely with the oscillation frequency to allow the mechanism leading to the double shear layer wake. Of interest, referring to the work of Govardhan & Williamson (2000), both the initial and upper branches (which both exhibit $2P$ shedding) have $f/f_n \to 1$, whereas for the lower branch (which exhibits $2S$ shedding), $f/f_n \to 1.1$.

7.7 The Critical Mass Ratio as a Function of Tether Length

In chapter 6, the critical mass ratio found was $m^*_{crit} = 0.38$ for $L^* = 5.0$. For mass ratios below this critical value, a jump in $\overline{\theta}$, A^* and the mean and RMS fluid forces was observed as the Froude number was increased beyond $Fr \simeq 0.8$. The clearest evidence of choosing $m^*_{crit} = 0.38$ is in figure 6.8, which shows $\overline{C_D}$ as a function of Fr for $L^* = 5.0$ and $m^* = [0.1, 0.8]$. For very high Froude numbers ($Fr = [5, 50]$, and for $m^* > m^*_{crit}$, the mean drag collapsed to a very small value ($\overline{C_D} \simeq 1.2$) regardless of mass ratio. By contrast for $m^* < m^*_{crit}$, $\overline{C_D}$ maintained a high, finite value over all Froude numbers considered in the range $Fr = [5, 50]$. Of particular interest is that for $m^* > m^*_{crit}$, the mean drag was marginally greater for larger mass ratios. Therefore, the smallest recorded mean drag at these high Froude numbers was found for m^* just marginally greater than m^*_{crit}.

In chapter 4, for the case of a freely oscillating cylinder, with $k = 0$ and $c = 0$, the critical mass ratio was found to be much lower, $m^*_{crit} = 0.1$. In this case, the definition of m^*_{crit} is slightly different, as it is the mass ratio below which large peak to peak oscillations occur. However, the two mass ratio values may be related by considering that the case of a freely oscillating cylinder with $k = 0$ and $c = 0$ effectively represents the same problem as a tethered cylinder with $L^* \to \infty$ and very high Froude numbers (corresponding to $\overline{\theta} \to 90^o$). The question of why there is a discrepancy in m^*_{crit} between the two cases arose. As the tether length represents the controlling parameter between the two studies, it was decided to determine the effect of tether length on m^*_{crit}.

To determine the critical mass ratio for each tether length, simulations over a broad range of m^* ($m^* = [0.1, 1.0]$) were conducted at $Fr = 0.8$ and $Fr = 50$ for several tether lengths. The mean drag was calculated for each simulation, and an estimate of the critical mass ratio was made by determining the mass ratio which exhibited the smallest value of $\overline{C_D}$ (typically $\overline{C_D} \to 1.2$). For each tether length, a more refined study was undertaken with four mass ratios close to the estimated value of m^*_{crit}; this allowed for estimates of m^*_{crit} to be made with $\Delta m^* = \pm 0.05$. Finally, a check of the amplitude response was made to determine that $m^* < m^*_{crit}$ exhibited large amplitude oscillations and $m^* > m^*_{crit}$ exhibited small amplitude oscillations. The results are shown, as a function of L^* in figure 7.25 for $L^* = [2, 15]$.

The value of the critical mass ratio was found to exponentially decay with L^* and is well represented by the equation:

$$m^*_{crit} = 1.3313 \cdot e^{-0.3163L^*} + 0.1, \tag{7.13}$$

with a coefficient of determination, $R^2 = 0.995$. Therefore, from equation 7.13, for $L^* \to \infty$, $m^*_{crit} \to 0.1$ which is the same value found for the freely oscillating case in chapter 4.

A second finding is that $m^*_{crit} \geqslant 1$ for $L^* \leqslant 1.23$. This finding correlates extremely well with the previous finding in $\overline{C_D}$, A^*, and the vortex shedding structures in the

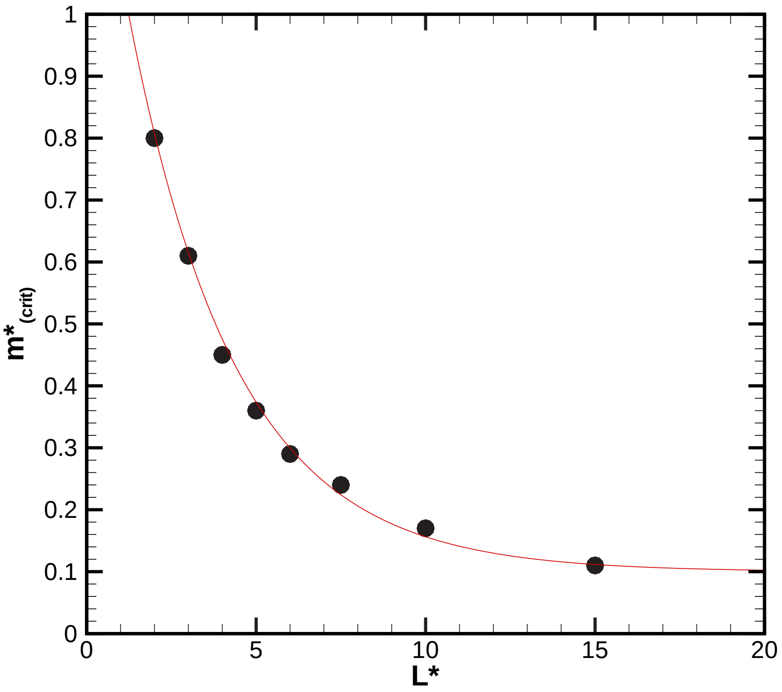

Figure 7.25: Critical mass ratio, m^*_{crit} as a function of tether length, for $L^* = [2, 15]$.

wake, to suggest that there is a critical tether length, $L^* \simeq 1.23$ below which the flow conditions are inherently different to tethered cylinders with longer tether lengths.

7.8 Conclusion

By choosing Fr' as the controlling parameter, the mean layover angle results were found to collapse on to a single line for $L^* = [1.0, 10.0]$. The amplitude of oscillation was found to increase significantly as Fr' was increased beyond 1. Beyond this value, the amplitude of oscillation remained reasonably constant at $A^* \simeq 0.5$ for $L^* = [1, 10]$. By referring solely to these two results, it may be inferred that there is barely any change in the cylinder response for $L^* = [1, 10]$. However, analysis of the force results shows a significant decrease in the maximum $\overline{C_D}$ as a function of L^*. Close examination of the oscillation results shows a similar decrease in A^*_{max} as a function of L^* in the range $L^* = [3, 10]$.

A significant change in the vortex structures in the wake of the cylinder has been noted as a function of L^*. For $L^* = [0.1, 2.0]$, a 'double' shear layer has been identified, which appears to show many of the characteristics of the ‘P+S’ and ‘2P’ modes described by Williamson & Roshko (1988) for the case of the forced oscillations of a cylinder, transverse to the flow field. Similar structures were once again identified by Govardhan & Williamson (2000) for the case of a freely oscillating cylinder. The ‘2P’ mode has not been previously identified for two-dimensional simulations, and it is not clear from the present results if this is a true ‘2P’ mode or a ‘P+S’ mode, which has previously been identified numerically by Blackburn & Henderson (1999) for the case of the forced oscillations of a cylinder, transverse to the flow field.

Finally, the effect of tether length on the critical mass ratio has been identified. The value of the critical mass ratio was found to decay exponentially with tether length, such that as $L^* \rightarrow \infty$, m^*_{crit} approaches the value found for the freely oscillating cylinder with $k = 0$ and $c = 0$ in chapter 4.

Chapter 8

Conclusions and Recommended Future Work

8.1 Conclusions

Two distinct studies are reported in this thesis. The first study investigates the transition to three-dimensionality of fluid structures in the wake of a bluff body. By varying the aspect ratio of the body but maintaining the form of both the leading and trailing edges; the effect of body aspect ratio on the flow structures in the wake is investigated. Aspect ratios in the range $AR = [2.5, 17.5]$ were investigated for flows with Reynolds numbers in the range $Re = [300, 700]$. A Floquet stability analysis study was performed to determine the order in which instability modes become linearly unstable, the critical Reynolds number of transition, and the structure of the three-dimensional modes.

Three instability modes were identified, and are referred to herein as Mode A, Mode B', and mode S'. Both Mode A and Mode B' show similarities in wake structure to Modes A and B identified for the case of a circular cylinder. Mode S' show similarities to the Mode S instability identified by Robichaux *et al.* (1999) for the case of a square cross-section cylinder.

For very short bodies, Mode A is the first instability to become critically unstable, and it is presumed that the transition scenario is the same as previously described for the flow around a circular cylinder (see section 1.3.3 for details). For larger aspect ratio bodies ($AR > 7.5$), Mode B' undergoes transition at a lower Reynolds number than Mode A. Mode B' differs from Mode B described for the case of a circular cylinder, as it has a much longer wavelength and the near wake structure of mode B' differs in comparison to that found for Mode B. The difference in critical Reynolds numbers of inception for Mode A and Mode B' increases with plate aspect ratio. For the aspect ratio body ($AR = 17.5$), Mode S', is also more unstable than Mode A. A full three-dimensional simulation is performed which produce a quasi-asymptotic state consistent with the findings of the Floquet analysis. The results indicate that the path to turbulence for a bluff body of significant aspect ratio is distinctly different to that already described for a circular, or square cross section cylinder.

The second study focuses on the vortex-induced-vibration for both the case of a cylinder free to oscillate transverse to the flow field at $u^* = \infty$, and for the case of a tethered cylinder free to oscillate at finite reduced velocities.

Chapter 4 details the results of two-dimensional simulations of a freely oscillating cylinder at $u^* = \infty$, for cylinder mass ratios in the range $m^* = 0.075, 0.7$; and Reynolds numbers in the range $Re = [40, 300]$. The purpose of the study was to determine if a critical mass ratio existed, below which large amplitude oscillations would be observed, in this Reynolds number range. This phenomena has already been reported for much higher Reynolds numbers by Govardhan & Williamson (2000), and for the specific case of $Re = 100$ by Govardhan & Williamson (2003).

A critical mass ratio was found for the Reynolds number ranges $Re = [40, 99]$ and $Re = [190, 300]$. In between these two Reynolds number ranges, no appreciable oscillations were observed for all the mass ratios investigated in the present study. In the first Reynolds number range, the critical mass ratio decreases with increasing Reynolds number. In the second Reynolds number range the critical mass ratio increases with increasing Reynolds number, reaching a maximum of $m^*_{crit} = 0.4$ at $Re = 300$, and appears to be approaching the value of $m^*_{crit} = 0.54$ found by Govardhan & Williamson (2000) at higher Reynolds numbers.

Chapters 5, 6 and 7 detail the investigations of the flow past a tethered circular cylinder. In each case the numerical simulations were performed on a two-dimensional domain and the Reynolds number was held constant at $Re = 200$.

In chapter 5, an initial study is made for the particular case of $m^* = 0.833$ and $L^* = 0.505$ for reduced velocities in the range $u^* = [1, 22]$. Three distinct branches of oscillation were observed. The first branch, peaking at $u^* = 2.5$ is essentially an in-line branch, and is driven by a resonance between the in-line forces and the natural frequency of the tethered cylinder. The second branch, occurring in the reduced velocity range $u^* = [5, 19]$ has components of oscillation in the in-line and transverse directions. It is initiated in the range $u^* = [3.5, 5]$ by a resonance between the natural frequency of the tethered body system and he subharmonic of the drag force. The third branch occurs for $u^* > 19$ and is dominated by transverse oscillations. The cylinder response for this branch is similar to that observed by Govardhan & Williamson (2000) for a low mass-damped hydro-elastically mounted cylinder oscillating transverse to the flow field. Analysis of the wake structure was made for $u^* = 15.4$, 19 and 21. For both $u^* = 15.4$ and 19, the near wake was asymmetric and a net negative lift was observed. As the reduced velocity is increased to $u^* = 21$, the wake is far more symmetric and the mean lift approaches zero.

Chapter 6 examines the effect of mass ratio on the interaction between a tethered cylinder and the flow field. Mass ratios in the range $m^* = [0.1, 0.8]$ were investigated, and the tether length was kept constant at $L^* = 5$. A critical mass ratio is found (in this case $m^*_{crit} = 0.38$), below which a large jump in A^*, $\overline{\theta}$ and $\overline{C_D}$ is observed. The jump in these parameters occurs at a Froude number, $Fr = 0.8$. The critical mass ratio observed for this particular tether length is considerably higher when compared to the case of a freely oscillating cylinder at the same Reynolds number. For a majority of cases, a net negative lift was observed, and this has been related to the shedding structures in the wake of the tethered cylinder which exhibit vortex pairing. Comparison is made between the numerical results and the experimental results performed at a much higher Reynolds number range. Despite the difference in Reynolds number, common trends are observed between the two studies.

Chapter 7 examines the effect of tether length on the interaction between a tethered cylinder and the flow field. Tether lengths in the range $L^* = [0.1, 10]$ were investigated, and the mass ratio was held constant at $m^* = 0.2$. Very little variation in the oscillation amplitude was observed as the tether length was varied in the range $L^* = [1, 10]$. However the mean drag was observed to decrease with increasing tether length. Analysis of the vortex structures in the wake of the tethered cylinder reveals a ‘double’ shear layer, in place of the standard Karman vortex street for tethered cylinders with tether length $L^* = [0.1, 2.0]$. The ‘double’ shear layer appears to exhibit many of the characteristics of the ‘P+S’ and ‘2P’ modes described by Williamson & Roshko (1988). Finally, the effect of tether length on the critical mass ratio is identified. The value of the critical mass ratio is found to decay exponentially with increasing tether length, such that as $L^* \rightarrow \infty$, the value of m^*_{crit} approaches the value found for a freely oscillating cylinder at the same Reynolds number.

8.2 Recommended Future Work

While this work has answered several questions, it has also raised several issues which are themselves worthy of further investigation; commencing with the initial study regarding wake transition to three-dimensionality:

- The effect of varying the geometry of both the leading- and trailing-edge of a generic bluff body may provide further information on the spatial and temporal properties of three-dimensional structures leading to turbulence.
- A fully non-linear three-dimensional study of would provide information on the interaction of both linear and non-linear instabilities in the cylinder wake.

The study of vortex-induced-vibration of both a hydro-elastically mounted, and tethered cylinder have also led to suggestions for future work:

- A fully three-dimensional study of the freely oscillating cylinder at higher Reynolds numbers would be able to provide information relating the current work to the work of Govardhan & Williamson (2003).
- In the case of the tethered cylinder, further study of the case of an internally pivoted cylinder at higher Reynolds numbers, than that studied here would provide information of interest to the offshore industry.

Bibliography

ALBAREDE, P. & MONKEWITZ, P. A. 1992 A model for the formation of oblique shedding and “chevron” patterns in cylinder wakes. *The Physics of Fluids A* **4**, 744–756.

ANAGNOSTOPOULOS, P. 1989 Numerical solution for laminar two-dimensional flow about a fixed and transversely oscillating cylinder in a uniform stream. *Journal of Computational Physics* **85**, 434–456.

ANAGNOSTOPOULOS, P. & BEARMAN, P. W. 1992 Response characteristics of a vortex-excited cylinder at low reynolds numbers. *Journal of Fluids and Structures* **6**, 39–50.

BARKLEY, D. & HENDERSON, R. D. 1996 Three-dimensional floquet stability analysis of the wake of a circular cylinder. *Journal of Fluid Mechanics* **322**, 215–241.

BATCHELOR, G. K. 1967 *An Introduction to Fluid Dynamics*. Cambridge University Press. Cambridge, UK.

BAYLY, B. J. 1986 Three-dimensional instability of elliptical flow. *Physical Review Letters* **57**, 2160–2163.

BEARMAN, P. 1965 Investigation of the flow behind a two-dimensional model with a blunt trailing edge and fitted with splitter plates. *Journal of Fluid Mechanics* **21**, 241–255.

BEARMAN, P. W. 1969 On vortex shedding from a circular cylinder in the critical reynolds number regime. *Journal ofFluid Mechanics* **37**, 577–585.

BEARMAN, P. W. 1984 Vortex shedding from oscillating bluff bodies. *Annual Review of Fluid Mechanics* **16**, 195–222.

Berger, E. 1964 Transition of the laminar vortex flow to the turbulent state of the karman vortex street behind an oscillating cylinder at low reynolds number. *Jahrbuch 1964 de Wiss. Gess. L. R.* p. 164.

Berger, E. & Wille, R. 1972 Periodic flow phenomena. *Annual Review Fluid Mechanics* **4**, 313–340.

Blackburn, H. M., Govardhan, R. & Williamson, C. 2001 A complementary numerical and physical investigation of vortex-induced vibration. *Journal of Fluids and Structures.* **15**, 481–488.

Blackburn, H. M. & Henderson, R. D. 1996 Lock-in behavior in simulated vortex-induced vibration. *Experimental Thermal and Fluid Science.* **12**, 184–189.

Blackburn, H. M. & Henderson, R. D. 1999 A study of two-dimensional flow past an oscillating cylinder. *Journal of Fluid Mechanics.* **385**, 255–286.

Blackburn, H. M. & Karniadakis, G. 1993 Two- and three-dimensional simulations of vortex-induced vibration of a circular cylinder. In *Proceedings of the Third International Offshore and Polar Engineering Conference, Singapore, 6-11 June*, pp. 715–720.

Blackburn, H. M. & Lopez, J. M. 2003 On three-dimensional quasiperiodic floquet instabilities of two-dimensional bluff body wakes. *Physics of Fluids* **15**, L57–L60.

Blackburn, H. M. & Lopez, J. M. To Appear The onset of three-dimensional standing and modulated travelling waves in a periodically driven cavity flow. *Journal of Fluid Mechanics* .

Blackburn, H. M., Marques, F. & Lopez, J. M. To Appear On three-dimensional instabilities of two-dimensional flows with a z2 spatio-temporal symmetry. *Journal of Fluid Mechanics* .

Blevins, B. 1990 *Flow-induced vibrations*. Van Nostrand Reinhold.

Bloor, M. S. 1964 The transition to turbulence in the wake of a circular cylinder. *Journal of Fluid Mechanics* **19**, 290–304.

Braza, M., Chassaning, P. & Ha-Minh, H. 1986 Numerical study and analysis of the pressure and velocity fields in the near wake of a cylinder. *Journal of Fluid Mechanics* **165**, 79.

Brede, M., Eckelmann, H., Konig, M. & Noack, B. R. 1994 Discrete shedding modes of the circular cylinder wake in a jet with a homogeneous core. *Physics of Fluids* **6**, 2711–2715.

Brede, M., Eckelmann, H. & Rockwell, D. 1996 On secondary vortices in a cylinder wake. *Physics of Fluids* **8**, 2117–2124.

Brika, D. & Laneville, A. 1993 Vortex induced vibrations of a long flexible circular cylinder. *Journal of Fluid Mechanics.* **250**, 481–508.

Canuto, C., Hussaini, M. Y., Quarteroni, A. & Zang, T. A. 1988 *Spectral Methods in Fluid Dynamics*, 2nd edn. Springer-Verlag.

Carberry, J. J. ???? Wake states of a submerged oscillating cylinder and of a cylinder beneath a free-surface. PhD thesis.

Chapra, S. & Canale, R. 1998 *Numerical MEthods for Engineers*. McGraw-Hill Singapore.

Corcos, G. M. & Lin, S. J. 1984 The mixing layer: Deterministic models of a turbulent flow. part 2. the origin of the three-dimensional motion. *Journal of Fluid Mechanics* **139**, 67–95.

Coutanceau, M. & Bouard, R. 1977 Experimental determination of the main features of the viscous flow in the wake of a circular cylinder in uniform translation. part 1. steady flow. *Journal of Fluid Mechanics* **79**, 231–256.

Danielson, D. A. 1997 *Vectors and Tensors in Engineering and Physics*. Addison-Wesley Publishing.

Dusek, J., Fraunie, P. & Le Gal, P. 1994 Local analysis of the onset of instability in shear flows. *Physics of Fluids* **6**, 172–186.

Eisenlohr, H. & Eckelmann, H. 1989 Vortex splitting and its consequences in the vortex street wake of cylinders at low reynolds number. *Physics of Fluids A* **1**, 189–192.

Eloy, C. & Le Dizes 1999 Three-dimensional instability of burgers and lamb-oseen vortices in a strain field. *Journal of Fluid Mechanics* **378**, 145–166.

Eloy, C. & Le Dizes 2001 Stability of the rankine vortex in a multipolar strain field. *Physics of Fluids* **8**, 660–676.

Evangelinos, C. & Karniadakis, G. E. 1999 Dynamics and flow structures in a turbulent wake of rigid and flexible cylinders subject to vortex-induced vibration. *Journal of Fluid Mechanics* **400**, 91–124.

Feng, C. 1968 The measurements of vortex-induced vibrations of a long flexible circular cylinder. Master's thesis, University of British Columbia.

Friehe, C. A. 1980 Vortex shedding from cylinders at low reynolds numbers. *Journal of Fluid Mechanics* **100**, 237–241.

Gaster, M. 1969 Vortex shedding from slender cones at low reynolds numbers. *Journal of Fluid Mechanics* **38**, 565–576.

Gaster, M. 1971 Vortex shedding from circular cylinders at low reynolds numbers. *Journal of Fluid Mechanics* **46**, 749–756.

Gerich, D. & Ecklemann, H. 1982 Influence of end plates and free ends on the shedding frequency of circular cylinders. *Journal of Fluid Mechanics* **122**, 109–121.

Gerrard, J. H. 1978 The wakes of cylindrical bluff bodies at low reynolds numbers. *Philos. Trans. R. Soc. London Ser. A* **288**, 351–382.

Giancoli, D. C. 1989 *Physics for Scientists and Engineers*, 2nd edn. Prentice Hall.

Govardhan, R. N. & Williamson, C. H. K. 1997 Vortex-induced motions of a tethered sphere. *Journal of Wind Engineering.* **69-71**, 375–385.

Govardhan, R. N. & Williamson, C. H. K. 2000 Modes of vortex formation and frequency response of a freely vibrating cylinder. *Journal of Fluid Mechanics* **420**, 85–130.

Govardhan, R. N. & Williamson, C. H. K. 2003 Resonance forever: existence of a critical mass and an infinite regime of resonance in votex-induced vibration. *Journal of Fluid Mechanics* **473**, 147–166.

Griffin, O. M. 1980 Vortex-excited cross-flow vibrations of a single cylindrical tube. *ASME Journal of Pressure Vessel Technology* **102**, 158–166.

Griffin, O. M. & Ramberg, S. E. 1974 The vortex street wakes of vibrating cylinders. *Journal of Fluid Mechanics* **66**, 553–576.

Griffin, O. M. & Ramberg, S. E. 1982 Some recent studies of vortex shedding with application to marine tubulars and risers. *ASME Journal of Energy Resources Technology* **104**, 2–13.

Griffin, O. M. & Ramberg, S. E. 1994 Timing of vortex formation from an oscillating cylinder. *Physics of Fluids* **6**, 3677–3682.

Griffin, O. M., Skop, R. A. & Ramberg, S. E. 1982 The resonant vortex-excited vibrtions of structures and cable systems. In *7th Offshore Technology Conference, Houston, Texas, U.S.A.*, , vol. OTC Paper 2319.

Hama, F. R. 1957 Three-dimensional vortex pattern behind a circular cylinder. *Journal of Aeronaut. Sci.* **24**, 156.

Hammache, M. & Gharib, M. 1989 A novel method to promote parallel shedding in the wake of circular cylinders. *The Physics of Fluids, A.* **1**, 1611.

Harlemann, D. & Shapiro, W. 1961 The dynamics of a submerged moor sphere in oscillatory waves. *Coastal Engineering.* **2**, 746–765.

Henderson, R. 1995 Details of the drag curve near the onset of vortex shedding. *Physics of Fluids* **7**, 2102–2104.

Henderson, R. 1997 Nonlinear dynamics and pattern formation in turbulent wake transition. *Journal of Fluid Mechanics* **352**, 65–112.

Hourigan, K., Thompson, M. C. & Tan, B. T. 2001 Self-sustained oscillations in flows around long blunt plates. *Journal of Fluids and Structures* **15**, 387–398.

Hover, F. S., Miller, S. N. & Triantafyllou, M. S. 1997 Vortex-induced vibration of marine cables: Experiments using force feedback. *Journal of Fluids and Structures* **11**, 307–326.

Hover, F. S., Techet, A. H. & Triantafyllou, M. S. 1998 Forces on oscillating uniform and tapered cylinders in crossflow. *Journal of Fluid Mechanics* **363**, 97–114.

Iooss, G. & Joseph, D. D. 1990 *Elementary Stability and Bifurcation Theory*. Springer-Verlag.

Jauvtis, N., Govardhan, R. & Williamson, C. 2001 Multiple modes of vortex-induced vibration of a sphere. *Journal of Fluids and Structures.* **15**, 555–563.

Jauvtis, N. & Williamson, C. 2003 Vortex-induced vibration of a cylinder with two degrees of freedom. *Journal of Fluids and Structures* **17**, 1035–1042.

Jauvtis, N. & Williamson, C. H. K. 2002 Vortex-induced vibration of a cylinder in two-degrees of freedom. In *Conference on Bluff Body Wakes and Vortex-Induced vibrations, BBVIV3, Port Douglas, Australia, 17-20 December 2002*.

Johnson, S. A., Thompson, M. C. & Hourigan, K. 2001 Flow past elliptical cylinders at low reynolds numbers. In *Proceedings of 14th Australasian Fluid Mechanics Conference, Adelaide*, pp. 343–346.

Julien, S., Lasheras, J. & Chomaz, J. 2003a Three-dimensional instability and vorticity patterns in the wake of a flat plate. *Journal of Fluid Mechanics* **479**, 155–189.

Julien, S., Ortiz, S. & Chomaz, J.-M. 2003b Secondary instability mechanisms in the wake of a flat plate. *European Journal of Mechanics B/Fluids* p. to appear.

Karman, T. V. 1911 Flussigkeits- u. luftwiderstand. *Phys. Zeitschr.* **14**, 49.

Karniadakis, D. N. . G. E. 1996 Simulations of flow over a flexible cable. comparison of forced and flow-induced vibration. *Journal of Fluids and Structures* **10**, 439–453.

Karniadakis, G. E. & Henderson, R. D. 1998 *The Handbook of Fluid Dynamics*, chap. Spectral Element Methods for Incompressible Flows, pp. 29–1 – 29–41. CRC Press.

Karniadakis, G. E., Israeli, M. & Orszag, S. A. 1991 High-order splitting methods of the incompressible Navier-Stokes equations. *Journal of Computational Physics.* **97**, 414–443.

Karniadakis, G. E. & Trintafyllou, G. S. 1992 Three-dimensional dynamics and transition to turbulence in the wake of bluff objects. *Journal of Fluid Mechanics* **238**, 1–30.

Khalak, A. & Williamson, C. 1997 Fluid forces and dynamics of a hydroelastic structure with very low mass and damping. *Journal of Fluids and Structures* **11**, 973–982.

KHALAK, A. & WILLIAMSON, C. 1999 Motions, forces and mode transitions in vortex-induced vibrations at low mass-damping. *Journal of Fluids and Structures.* **13**, 813–851.

KING, R. 1974 Vortex excited oscillations of a circular cylinder in steady currents. In *Offshore Technology Conference, OTC 1948*.

KNOTT, M. 2003 Power from the waves. In *New Scientist (Australia)* (ed. A. Anderson), , vol. 2413, pp. 33–35. Gordon and Gotch Australia.

KOCABIYIK, S. 2003 A numerical study on the recti-linear oscillations of a circular cylinder in cross-flow: Flow patterns and loading. In *Proceedings of IUTAM Symposium On Integrated Modeling of Fully Coupled Fluid-Structure Interactions Using Analysis, Computations, and Experiments 1 June-6 June 2003, New Brunswick, U.S.A.*.

KOOPMAN, G. 1967 The vortex wakes of vibrating cylinders at low Reynolds numbers. *Journal of Fluid Mechanics.* **28**, 501–512.

LAMB, H. 1932 *Hydrodynamics*. Dover, New York.

LANDMAN, M. J. & SAFFMAN, P. G. 1987 The three-dimensional instability of strained vortices in a viscous fluid. *Physics of Fluids* **30**, 2339–2342.

LE DIZES & LAPORTE, F. 2002 Theoretical predictions for the elliptical instability in a two-vortex flow. *Journal of Fluid Mechanics* **471**, 169–201.

LEONARD, A. 1985 Computing three-dimensional incompressible flow with vortex elements. *Annu. Rev. Fluid Mech.* **17**, 523–559.

LEWEKE, T. & PROVANSAL, M. 1995 The flow behind rings: Bluff body wakes without end effects. *Journal of Fluid Mechanics* **288**, 265–310.

LEWEKE, T. & WILLIAMSON, C. H. K. 1998 Cooperative elliptic instability of a vortex pair. *Journal of Fluid Mechanics* **360**, 85–119.

LEWEKE, T. & WILLIMSON, C. H. K. 1998 Three-dimensional instabilities in wake transition. *European Journal of Mechanics B/Fluids* **17**, 571–586.

LIGHTHILL, M. J. 1963 *Laminar Boudary Layer*, chap. Introduction: Boundary Layer Theory, pp. 46–113. Oxford University Press.

LIGHTHILL, M. J. 1986 Wave loading on offshore structutes. *Journal of Fluid Mechanics* **173**, 667–681.

LIN, J. C., TOWFIGHI, J. & ROCKWELL, D. 1995 Instantenous structure of the near-wake of a circular-cylinder - on the effect of reynolds number. *Journal of Fluids and Structures* **9**, 409–418.

LU, X.-Y. & DALTON, C. 1996 Calculation of the timing of vortex formation from an oscillating cylinder. *Journal of Fluids and Structures* **10**, 527–541.

MEIBURG, E. & LASHERAS, J. C. 1987 Comparison between experiments and numerical simulations of three-dimensional transition in plane wakes. *The Physics of Fluids* **30**, 623.

MEIBURG, E. & LASHERAS, J. C. 1988 Experimental and numerical investigation of the three-dimensional transion in plane wakes. *Journal of Fluid Mechanics* **190**, 1.

MEIER-WINDHORST, A. 1939 Flatterschwingungen von zylindern im gleichmassigen flussigkeitsstrom. *Mitteilungen des Hydraulischen Instituts der Technischen Hochschule, Munchen* **9**, 3–39.

MENEGHINI, J. R. & BEARMAN, P. W. 1995 Numerical simulation of high amplitude oscillatory flow about a circular cylinder. *Journal of Fluids and Structures* **9**, 435–455.

MILLER, G. D. & WILLIAMSON, C. H. K. 1994 Control of three-dimensional phase dynamic ina cylinder wake. *Experimens in Fluids* **18**, 26.

MOE, G. & WU, Z. J. 1990 The lift force on a cylinder vibrating in a current. *ASME Journal of Offshore Mechanics and Arctic Engineering* **112**, 297–303.

MORTON, B. R. 1984 The generation and decay of vorticity. *Geophys. Astrophys. Fluid Dynamics* **28**, 277–308.

NAJJAR, F. M. & BALACHANDAR, S. 1997 Low-frequency unsteadiness in the wake of a normal flat plate. *Journal of Fluid Mechanics* **370**, 101–147.

NAUDASCHER, E. & ROCKWELL, D. 1993 *Flow-Induced Vibrations: An Engineering Guide*. Rotterdam: Balkema.

Noca, F. 1997 On the evaluation of time dependent fluid-dynamic forces on bluff bodies. PhD thesis, Graduate Aeronautical Laboratories, California Institute of Technology, Pasadena.

Noca, F., Shiels, D. & Jeon, D. 1997 Measuring instantaneous fluid dynamic forces on bodies, using only velociy fields and their derivatives. *Journal of Fluids and Structures* **11**, 345–350.

Noca, F., Shiels, D. & Jeon, D. 1999 A comparison of methods for evaluating time-dependent fluid dynamic forces on bodies, using only velocity files and their derivatives. *Journal of Fluids and Structures* **13**, 551–578.

Norberg, C. 1987 Effects of reynolds number and a low-intensity freestream turbulence on the flow around a circular cylinder. PhD thesis, Chalmers Univ. Technol. Publ. No 87/2, S-412-96. Goteborg, Sweden.

Norberg, C. 1994 An experimental investigation of the flow around a circular cylinder: Influence of aspect ratio. *Journal of Fluid Mechanics* **258**, 287–316.

Ogihara, K. 1988 Theoretical analysis on the transverse motion of a buoy by a surface wave. *Applied Ocean Research.* **2**, 51–56.

Ongoren, A. & Rockwell, D. 1988 Flow structure from an oscillating cylinder. part 2. mode competition in the near wake. *Journal of Fluid Mechanics* **191**, 225–245.

Perry, A. E., Chong, M. S. & Lim, T. T. 1982 The vortex-shedding process behind two-dimensional bluff bodies. *Journal of Fluid Mechanics* **116**, 77–90.

Pesce, C. & Fujarra, A. L. C. 2000 Vortex-induced vibratios and jump phenomenon: Experiments with a clamped flexible cylinder in water. *International Journal of Offshore and Polar Engineering* **10**, 26–33.

Pierrehumbert, R. T. 1986 Universal short-wave instability of two-dimensional eddies in an inviscid fluid. *Physical Review Letters* **57**, 2157–2159.

Prasad, A. & Williamson, C. H. K. 1997 The instability of the shear layer sepatating from a bluff body. *Journal of Fluid Mechanics* **333**, 375–402.

Pregnalato, C. J. 2003 Flow-induced vibrations of a tethered sphere. PhD thesis, Deptartment of Mechanical Engineering, Monash University.

Pregnalato, C. J., Thompson, M. C. & Hourigan, K. 2003a The flow-induced vibrations of a tethered sphere. *Journal of Fluid Mechanics* **To Appear**.

Pregnalato, C. J., Thompson, M. C. & Hourigan, K. 2003b Vortex dynamics and oscillation modes of a tethered sphere. *Journal of Fluid Mechanics* **To Appear**.

Provansal, M., Mathis, C. & Boyer, L. 1987 Bernard-von karman instability: transient and forced regimes. *Journal of Fluid Mechanics* **182**, 1–22.

Ramberg, S. E. 1983 The effects of yaw and finite length upon the vortex wakes of stationary and vibrating circular cylinders. *Journal of Fluid Mechanics* **128**, 81–107.

Ramberg, S. E. & Griffin, O. M. 1981 Hydroelastic response of marine cables and risers. In *Hydrodynamics in Ocean Engineering*, , vol. Norwegian Institute of Technology, Trondheim, Norway.

Rao, S. S. 1995 *Mechanical Vibrations*, 3rd edn. Addison-Wesley.

Robichaux, J., Balachandar, S. & Vanka, S. P. 1999 Three-dimensional floquet instability of the wake of square cylinder. *Physics of Fluids* **11**, 560–578.

Roshko, A. 1954 On the development of turbulent wakes from vortex streets. *N.A.C.A. Report No. 1191* .

Roshko, A. 1955 On the wake and drag of bluff bodies. *Journal of the Aeronautical Sciences* **22**, 124–132.

Roshko, A. 1961 Experiments on the flow past a circular cylinder at very high reynolds number. *Journal of Fluid Mechanics* **10**, 345–356.

Roshko, A. 1993 Perspectives on bluff body aerodynamics. *Journal of Wind and Industrial Aerodynamics* **49**, 79.

Ryan, K., Pregnalato, C., Thompson, M. & Hourigan, K. (2003) Flow-induced vibrations of a tethered circular cylinder. *Journal of Fluids and Structures* **Submitted**.

Ryan, K., Thompson, M. C. & Hourigan, K. To appear Three-dimensional transition in the wake of elongated bluff bodies. *Journal of Fluid Mechanics* .

Sakamoto, H. & Haniu, H. 1990 A study on vortex shedding from spheres in a uniform flow. *ASME Journal of Fluids Engineering* **112**, 386–392.

Saltara, F., Meneghini, J. R., Siqueira, C. R. & Bearman, P. W. 1998 The simulation of vortex shedding from an oscillating circular cylinder with turbulence modelling. In *Conference on Bluff Body Wakes and Vortex-Induced Vibrations, Washington, D.C., 21-23 June 1998* (ed. P. Bearman & C. H. K. Williamson).

Sarpkaya, T. 1978 Fluid forces on oscillating cylinders. *ASCE Journal of Waterway, Port, Coastal and Ocean Division* **104**, 275–290.

Sarpkaya, T. 1979 Vortex-induced oscillations. *Journal of Applied Mechanics* **46**, 241–258.

Sarpkaya, T. 1993 Offshore hydrodynamics. *ASME Journal of Offshore Mechanics and Arctic Engineering* **115**, 2–5.

Sarpkaya, T. 1995 Hydrodynamic damping, flow-induced oscillations, and biharmonic response. *ASME Journal of Offshore Mechanics and Arctic Engineering* **117**, 232–238.

Schewe, G. 1983 On the force fluctuations acting on a circular cylinder in crossflow from subcritical up to transcritical reynolds numbers. *Journal of Fluid Mechanics* **133**, 265–285.

Schiller, L. & Linke, W. 1933 Druck und reibungswiderstand des zylinders bei reynolds-aachen zahlen 5 000 bis 40 000. *Z. Flugtech. Motorluft.* **24**, 193.

Scruton, C. 1965 On the wind-excited oscillations of towers, stacks and masts. In *Proceeding of the Symposium on Wind Effects on Buildings and Structures*, , vol. London: Her Majesty's Stationery Office, Paper 16, pp. 798–836.

Shair, F. H., Grove, A. S., Petersen, E. E. & Acrivos, A. A. 1963 The effect of confining walls on the stability of the steady wake behind a circular cylinder. *Journal of Fluid Mechanics* **17**, 546–550.

Sheard, G., Thompson, M. & Hourigan, K. 2003 From spheres to circular cylinders: Stability and flow structures of bluff ring wakes. *Journal of Fluid Mechanics* **pending publication**, XX.

Sheridan, J., Carberry, J., Lin, J.-C. & Rockwell, D. 1998 On the near wake topology of an oscillating cylinder. *Journal of Fluids and Structures* **12**, 215–220.

Shi-Igai, H. & Kono, T. 1969 Study on vibration of submerged spheres caused by surface waves. *Coastal Engineering Japan* **12**, 29–40.

Shiels, D. 1998 Simulation of controlled bluff body flow with a viscous vortex method. PhD thesis, California Institute of Technology, Pasadena, California.

Shiels, D., Leonard, A. & Roshko, A. 2001 Flow-induced vibration of a circular cylinder at limiting structural parameters. *Journal of Fluids and Structures* **15**, 3–21.

Skop, R. A. 1974 On modelling vortex-excited oscillations. *Tech. Rep.*. NRL Memorandum Report 2927.

Skop, R. A. & Balasubramanian, S. 1973 A new twit on an old model for vortex-excited vibrations. *Journal of Fluids and Structures* **11**, 395–412.

Skop, R. A. & Griffin, O. M. 1973 An heuristic model for determining flow-induced vibrations of offshore structures. In *5th Offshore Technology Conference, Houstan, Ts, U.S.A.*, , vol. OTC Paper 1843.

Tan, B. T. 2001 Vortex shedding and interaction in flows around bluff plates. PhD thesis, Deptartment of Mechanical Engineering, Monash University.

Taneda, S. 1956 Experimental investigation of the wakes behind cylinders and plates at low reynolds numbers. *Journal of the Physical Society of Japan* **11**, 302–307.

Taneda, S. 1963 The stability of two-dimensional laminar wakes. *Journal of the Physical Society of Japan* **18**, 288–296.

Thompson, M., Hourigan, K. & Sheridan, J. 1994 Three-dimensional instabilities in the cylinder wake. In *Int. Colloq. Jets, Wakes, Shear Layers*. Melbourne, Aust.

Thompson, M., Leweke, T. & Provansal, M. 2001a Kinematics and dynamics of sphere wake transition. *Journal of Fluids and Structures* **15**, 575–585.

Thompson, M., Leweke, T. & Williamson, C. 2001b The physical mechanism of transition in bluff body wakes. *Journal of Fluids and Structures* **15**, 607–616.

Thompson, M. C., Hourigan, K. & Sheridan, J. 1996 Three-dimensional instabilities in the wake of a circular cylinder. *Experimental Thermal and Fluid Science* **12**, 190–196.

Thompson, M. C., Leweke, T. & Williamson, C. H. K. 2001c The physical mechanism of transition in bluff body wakes. *Journal of Fluids and Structures* **15**, 607–616.

Tritton, D. J. 1959 Experiments on the flow past a circular cylinder at low reynolds numbers. *Journal of Fluid Mechanics* **6**, 547–567.

Tritton, D. J. 1971 A note on vortex streets behind circular cylinders at low reynolds numbers. *Journal of Fluid Mechanics* **45**, 203–208.

Unal, M. F. & Rockwell, D. 1988 On vortex shedding from a cylinder: Part 1. the initial instability. *Journal of Fluid Mechanics* **190**, 491.

Van Dyke, M. 1982 *An Album of Fluid Motion*. The Parabolic Press.

Vickery, B. J. & Watkins, R. D. 1964 Flow-induced vibrations of cylindrical structures. In *Proceedings of the First Australian Conference on Hydraulics and Fluid Mechanics* (ed. R. Silvester). New York: Pergamon Press.

Waleffe, F. 1990 On the three-dimensional instability of strained vortices. *Physics of Fluids A* **2**, 76–80.

White, F. M. 1999 *Fluid Mechanics*, 4th edn. McGraw Hill.

Williamson, C. 1996a Three dimensional wake transition. *Journal of Fluid Mechanics* **328**, 345–407.

Williamson, C. & Govardhan, R. 1997 Dynamics and forcing of a tethered sphere in a fluid flow. *Journal of Fluids and Structures* **11**, 293–305.

Williamson, C. H. K. 1988a Defining a universal and continuous strouhal-reynolds number relationship for the laminar vortex shedding of a circular cylinder. *The Physics of Fluids* **31**, 2742–2744.

Williamson, C. H. K. 1988b The existence of two stages in the transition to three dimensionality of a cylinder wake. *The Physics of Fluids* **31**, 3165–3168.

Williamson, C. H. K. 1989 Oblique and parallel modes of vorte shedding in the wake of a circular cylinder at low reynolds numbers. *Journal of Fluid Mechanics* **206**, 579–627.

WILLIAMSON, C. H. K. 1996b Three-dimensional wake transition. *Journal of Fluid Mechanics* **328**, 345–407.

WILLIAMSON, C. H. K. 1996c Vortex dynamics in the cylinder wake. *Annual Review of Fluid Mechanics* **28**, 477–539.

WILLIAMSON, C. H. K. & ROSHKO, A. 1988 Vortex formation in the wake of an oscillating cylinder. *Journal of Fluids and Structures* **2**, 355–381.

WILLIAMSON, C. H. K. & ROSHKO, A. 1990 Measurements of base pressure in the wake of a cylinder at low reynolds numbers. *Zeitschrift fr Flugwissenschaften und Weltraumforschung* **14**, 38–46.

WU, J. C. 1981 Aerodynamic force and moment in viscous flows. *AIAA Journal* **19**, 432–441.

WU, J. C. & THOMPSON, J. F. 1973 Numerical soluitions of time-dependant incompressible navier-stokes equations using an integro-differenctial formulation. *Computers and Fluids* **1**, 197–215.

WU, J. Z. & WU, J. M. 1996 Vorticity dynamics on boundaries. *Advances in Applied Mechanics* **32**, 119–275.

ZDRAVKOVICH, M. M. 1982 Modification of vortex shedding in the synchronization range. *ASME Journal of Fluids Engineering* **104**, 513–517.

ZHANG, H., FEY, U., NOACK, B. R., KOENIG, M. & ECKELMANN, H. 1995 On the transition of the cylinder wake. *Physics of Fluids* **7**, 779–794.